Stony Brook University

Structure and Elasticity of $NaMgF_3$ and $CaIrO_3$ at High Pressures and Temperatures—the Perovskite and Post-Perovskite Structure Model of $MgSiO_3$ Investigated with Rietveld Structure Refinement and Ultrasonic Interferometry.

A Dissertation Presented

by

Charles David Martin

to

The Graduate School

in Partial Fulfillment of the Requirements

for the Degree of

Doctor of Philosophy

in

Geosciences

Stony Brook University

August 2007

Stony Brook University

The Graduate School

Charles David Martin

We, the dissertation committee for the above candidate for the Doctor of Philosophy degree, hereby recommend acceptance of this dissertation

John B. Parise, Dissertation Advisor
Professor, Department of Geosciences

Donald J. Weidner, Chairman of the Dissertation
Professor, Department of Geosciences

Robert C. Liebermann
Professor, Department of Geosciences

Jiuhua Chen
Associate Professor, Department of Geosciences

Wilson A. Crichton
Earth Scientist, European Synchrotron Radiation Facility

This dissertation is accepted by the Graduate School

Lawrence Martin
Dean of the Graduate School

Abstract of the Dissertation

Structure and Elasticity of $NaMgF_3$ and $CaIrO_3$ at High Pressures and Temperatures—the Perovskite and Post-Perovskite Structure Model of $MgSiO_3$ Investigated with Rietveld Structure Refinement and Ultrasonic Interferometry.

by

Charles David Martin

Doctor of Philosophy

in

Geosciences

Stony Brook University

2007

Perovskite-structured $MgSiO_3$ dominates the mineralogy of Earth's lower mantle. As a result, the physical properties and phase transitions of this mineral are key to understanding anomalous seismic observations of the mantle's lowermost 150-300 km—the D" region. Recent literature suggests a post-perovskite phase of $MgSiO_3$, experimentally observed at pressures and temperatures consistent with those expected to exist at D", is responsible for the observed discontinuity in seismic velocity. While characterizing the crystal-chemistry, structure, and elastic properties of these two mineral phases *in situ* at high pressure and temperature would immediately shed light on this

enigmatic region of the Earth, many conventional experimental apparatus are unable to reproduce these extreme conditions in the laboratory. Thus, measurements of the solubility of trace elements, the elastic changes with pressure and temperature, and the Clapeyron slope between perovskite and post-perovskite phases are in desperate need; however difficult or impossible to perform on $MgSiO_3$ directly. This dissertation addresses structure changes at high pressure and temperature occurring in materials analogous to $MgSiO_3$ with perovskite and post-perovskite structure, considering that conclusions drawn from this research will prove useful to a subsequent understanding of the elastic, rheological, and crystal-chemical properties of $MgSiO_3$.

Neighborite ($NaMgF_3$) is isostructural to orthorhombic (*Pbnm*) $MgSiO_3$ perovskite. On the basis of X-ray diffraction data, previous research by Yusheng Zhao has shown that increasing temperature, or potassium substitution for sodium in the structure, drives an evolution in the average structure (> 100 Å) towards a perovskite with cubic ($Pm\bar{3}m$) symmetry. Through utilization of pair-distribution function analysis and nuclear magnetic resonance spectroscopy, experimental techniques sensitive to short-range structure (< 20 Å), we show that when the average structure appears cubic with X-ray diffraction the local structure remains orthorhombic.

By measuring the velocity of ultrasonic waves (MHz) through millimeter-sized polycrystalline samples we characterize the elastic behavior of $NaMgF_3$ *in situ* at high pressure and temperature as X-ray diffraction shows a transition from orthorhombic to cubic in the average structure. Accompanying constant signal intensity from the acoustic buffer-rod, we observe attenuation before a disappearance of the ultrasonic signal from the sample as pressure-temperature conditions approach the phase transition.

While the perovskite/post-perovskite phase transition occurs in $MgSiO_3$ at 120 GPa, the perovskite/post-perovskite phase transition in $NaMgF_3$ is driven at much lower pressures. Using X-ray diffraction data collected from $NaMgF_3$ in the diamond anvil cell, we identify the pressure where this material transitions to a post-perovskite structure.

Upon heating post-perovskite $NaMgF_3$, we find crystallization of a new phase(s) in the $NaMgF_3$ system. Through Rietveld structure refinement of perovskite and post-perovskite $NaMgF_3$, we propose a method for predicting the pressure where a post-perovskite structure becomes more stable than a perovskite structure of a given ABX_3 composition.

The material $CaIrO_3$ is isostructural to the post-perovskite structure of $MgSiO_3$ (*Cmcm*). Utilizing X-ray powder diffraction we identify the compressibility and thermal expansion of the $CaIrO_3$ unit cell. Via Rietveld refinement of structure models fit to the X-ray diffraction data, we identify structure changes in $CaIrO_3$ at high temperature. Rietveld refinement of structure models fit to time-of-flight neutron diffraction data reveal structure changes occurring at high pressure. Through a synthesis of the data, we propose a method for predicting the Clapeyron slope between perovskite and post-perovskite ($CaIrO_3$-type) structures.

To the Family who pushes for success and bears its burden

Table of Contents

Abstract iii

Table of Contents vii

List of Figures xiii

List of Tables xxiv

Acknowledgements xxvi

Chapter I

Introduction

1.1. Introduction 1

1.2. Experiments utilizing materials with analogous structure 2

1.3. Properties of perovskite and post-perovskite structures with changing pressure and temperature. 3

1.4. Chapter introduction and highlights 5

1.4.1. Chapter II, Details for performance of novel or non-conventional experiments utilized in this thesis. 5

1.4.2. Chapter III, Local and long range order of (K, Na)MgF_3 as analog for (Mg, Ca)SiO_3 in the lower mantle. 5

1.4.3. Chapter IV, Pair distribution analysis of the local $NaMgF_3$ structure; implications for silicate perovskites in the lower mantle. 6

1.4.4. Chapter V, Structure and ultrasonic elasticity of $NaMgF_3$ at high pressure and temperature. 7

1.4.5. Chapter VI, Understanding the perovskite/post-perovskite phase transition in $MgSiO_3$ via in-situ observation of $NaMgF_3$ analog material. 7

1.4.6. Chapter VII, Understanding structure changes in $MgSiO_3$ post-perovskite at high pressure and temperature via in-situ observation of $CaIrO_3$ analog material. 8

1.4.7. Chapter VIII, Perovskite and Post-Perovskite: Structure Survey and Implications for $MgSiO_3$ in Earth's Lower Mantle. 8
1.4.8. Appendix, Local structure analysis in-situ at high pressures within the diamond anvil cell. 8
References for Chapter I 10

Chapter II

Details for Performance of Novel or Non-conventional Experiments Utilized in this Thesis

2.1. Introduction 20
2.2. Pair-distribution function analysis 20
2.3. Laser-heated diamond anvil cell with X-ray powder diffraction 21
2.3.1. X-ray diffraction from samples quenched from simultaneous high pressure and temperature 22
2.3.2. X-ray diffraction from samples at high pressures quenched from high temperature 22
2.3.3. X-ray diffraction from samples at simultaneous high pressure and temperature 23
References for Chapter II 24

Chapter III

Effect of A-site cation radius on ordering of BX_6 octahedra in $(K,Na)MgF_3$ perovskite

3.1. Abstract 30
3.2. Introduction 30
3.2.1. Structure 32
3.2.2. Previous Work 32

3.3. Experimental methods 36
3.3.1. Sample Synthesis 36
3.3.2. X-ray Diffraction 37
3.3.3. Nuclear Magnetic Resonance (NMR) Spectroscopy 38
3.4. Results and Discussions 39
3.4.1. Synthesis 39
3.4.2. X-ray diffraction 39
3.4.3. Nuclear Magnetic Resonance (NMR) of Type 1 Samples 43
3.4.3.1 ^{23}Na MAS NMR 43
3.4.3.2 ^{19}F MAS NMR 44
3.4.3.3 BABA 2D MQ Investigation of the Local Environments 45
3.4.4. Strain and Broken Periodicity 46
References for Chapter III 50

Chapter IV

Local vs. average structure; a study of Neighborite ($NaMgF_3$) utilizing the pair-distribution function for quantitative structure determination

4.1. Abstract 74
4.2. Introduction 75
4.3. Experimental Methods 77
4.4. Results 78
4.5. Discussion 81
References for Chapter IV 84

Chapter V

Structural distortion, critical behavior, and elasticity of $NaMgF_3$ perovskite at simultaneous high pressure and temperature

5.1. Abstract 100

5.2. Introduction 100

5.3. Experimental Methods 102

5.3.1. Monochromatic X-ray diffraction 102

5.3.2. Ultrasonic elasticity 103

5.4. Results and discussion 104

5.4.1. Monochromatic X-ray diffraction 104

5.4.2. Elastic properties 107

References for Chapter V 110

Chapter VI

Phase transitions, compressibility, and Rietveld structure refinement of $NaMgF_3$ (Neighborite) in perovskite- and post-perovskite-related structures.

6.1. Abstract 130

6.2. Introduction 131

6.3. Experimental Methods 132

6.4. Results 133

6.4.1. Phase transitions 133

6.4.2. Rietveld structure refinement 134

6.5. Discussion 136

References for Chapter VI 139

Chapter VII

Compression, thermal expansion, structure and bonding in $CaIrO_3$ at high pressure and temperature; the structure model of $MgSiO_3$ post-perovskite investigated with monochromatic X-ray and time-of-flight neutron powder diffraction

7.1. Abstract 148

7.2. Introduction 149

7.3. Experimental Methods 150

7.3.1. X-ray diffraction 150

7.3.2. Neutron diffraction 150

7.4. Results 153

7.4.1. X-ray diffraction 153

7.4.2. Neutron diffraction 155

7.5. Discussion 160

References for Chapter VII 164

Chapter VIII

Perovskite and Post-Perovskite: Structure Survey and Implications for $MgSiO_3$ in Earth's Lower Mantle.

8.1. Predicting the post-perovskite phase transition 186

8.1.1. Introduction 186

8.1.2. Results 187

8.1.2.1 Observations in the perovskite structure 187

8.1.2.2 Observations in the post-perovskite ($CaIrO_3$-type) structure 188

8.1.2.3 Resolution of conflicting data on $MgGeO_3$ 189

8.2. Thesis Summary and Conclusion 189

References for Chapter VIII 192

Appendix

Quantitative Pair Distribution Function Analysis of Nanocrystalline Gold at High Pressure

A.1.	Abstract	199
A.2.	Introduction	199
A.3.	Methods	201
A.4.	Results and discussion	202
	References for Appendix	205

List of Figures

FIGURE 1.1. The density of, and seismic velocities within, the mantle are shown as a function of depth according to the Preliminary Reference Earth Model (Dziewonski and Anderson, 1981). Stable phases of Mg_2SiO_4 and $MgSiO_3$ are designated by α (olivine), β (Wadsleyite), γ (Ringwoodite) and pv (perovskite) - ppv (post-perovskite), respectively. 13

FIGURE 1.2. The equilibrium density increase of pyrolite as minerals and chemical species partition between crystalline phases with increasing pressure (Irifune and Isshiki, 1998). 14

FIGURE 1.3. Author's/Artist's rendition of the Earth's interior with emphasis on location and topology of the D" layer. 15

FIGURE 1.4. The main classes of D" shear-wave velocity structures. Schematic shear-wave velocity structures (shown as percent deviations (dVS) relative to a standard reference Earth model which has smoothly varying structure in the lower mantle) for circum-Pacific (left) and central Pacific (right) regions. The circum-Pacific regions under Alaska and the Caribbean are well characterized to have relatively abrupt shear velocity increases near 250 km above the CMB, with mild negative gradients throughout the D" layer. The blue model indicates that these high-velocity regions are relatively cold. These regions also have shearwave splitting consistent with transverse isotropy, which is represented here by thin horizontal lamellae of strongly varying material properties (possibly involving melt), concentrated near the depth of the discontinuity. Any ULVZ in these regions is so thin as to not be detectable in most cases, and it may not be present. The central Pacific region is characterized by strong negative gradients of shear velocity extending over 200–300 km above the CMB, with little evidence for any discontinuity. The red model indicates that these low-velocity regions are relatively hot. This region has a thick, pronounced ULVZ, with shear velocity decreases that are of the order of 5–30 %. There appears to be laterally variable general anisotropy, concentrated towards the base of the D" region (and possibly in the ULVZ as well). The sense of velocity perturbation with respect to increasing or decreasing Fe concentration, temperature (T) or partial melt is indicated by the inset box. Caption and figure taken from (Lay et al., 1998). 16

FIGURE 1.5. Polyhedral representation of the orthorhombic (*Pbnm*) perovskite structure. With stoichiometry ABX_3, A-site cations reside in the dodecahedron composed from eight B-site octahedra. 17

FIGURE 1.6. Tilting schemes of octahedra composing perovskite structures can be classified in terms of rotational components about pseudo-cubic axes. 18

FIGURE 1.7. The orthorhombic (*Cmcm*) $CaIrO_3$-type post-perovskite structure. Octahedra share corners about [0 0 1] and edges about [1 0 0]. 19

FIGURE 2.1. (a) Representative pair distribution function as G(r) with correlations (b) corresponding to the first three atom-atom distances in a material. This specific example shows nanocrystalline gold under high pressure and the usefulness of the technique to define structures lacking long-range order. 25

FIGURE 2.2. (a) Representative pair distribution function as G(r) with correlations (b) corresponding to the first three atom-atom distances in a material. This specific example shows nanocrystalline gold under high pressure and the usefulness of the technique to define structures lacking long-range order. 26

FIGURE 2.3. Exemplary data collected using the RA-PDF technique. Plots (upper tier) shows a background spectra is required to isolate sample scattering (lower tier). 27

FIGURE 2.4. Schematic diagram showing 'perforated (DBP)' and 'partially-perforated (PPA)' diamond anvils which minimize the volume (length shown here) of diamond in the beam path. A miniature anvil (MA) is required in order to introduce a polished diamond surface and optical access to the sample. Figure provided by D'Anvils Ltd. 28

FIGURE 2.5. Schematic diagram of a laser heated diamond anvil cell experiment. 29

FIGURE 3.1. The potassium ion that occupies the perovskite A-site in cubic *Pm*3*m* $KMgF_3$ is large enough to support MgF_6 octahedra that mirror each other in three dimensions. 58

FIGURE 3.2. The smaller sodium ion that occupies the perovskite A-site in orthorhombic *Pbnm* $NaMgF_3$ allows octahedra to collapse or tilt. 59

FIGURE 3.3. In the $NaMgF_3$ structure MgF_6 octahedrons tilt with both in-phase (left) and anti-phase (right) components. 60

FIGURE 3.4. Octahedral tilt may be quantified as a function of rotation about pseudo-cubic axes. Shown here axes φ, θ, and Φ denote rotation about the [001], [110], and [111] directions, respectively. 61

FIGURE 3.5. (a) The steep linear trend of the unit-cell volume changes to a higher-order dependence in the cubic region. (b) Pseudo-cubic lattice parameters follow a similar trend. Uncertainty in placement of the boundary between tetragonal and cubic symmetry results from the poor quality of super-structure reß ections which broaden with potassium substitution. The error bars are small than the marker symbols. 62

FIGURE 3.6. Orthorhombic unit-cell length increase linearly to transition at $(K_{0.37}Na_{0.63})MgF_3$. The error bars are smaller than the markers. 63

FIGURE 3.7. Rotation of MgF_6 octahedra as potassium concentration increases. The variable serves as an order parameter for phase transition. The error bars are otherwise smaller than the marker size. The dashed line is intended to guide the eye. 64

FIGURE 3.8. X-ray diffraction patterns of $(K_{0.15}Na_{0.85})MgF_3$ perovskite samples demonstrate the effect of annealing on unit-cell and tilting of MgF_6 octahedrons. Type 1 indicates a method where samples are synthesized with just two 5 hour fring periods at 1023 K, while type 3 denotes one where the same type 1 samples are further annealed at 1023 K for 30 days. Annealed samples show a 1-0.5% increase in unit-cell and a 2-4 degree reduction in tilting about the pseudo-cubic [111]. 65

FIGURE 3.9. X-ray diffraction patterns of type 1 $(K_xNa_{1-x})MgF_3$ perovskite samples. The phase boundary at x = ~0.37 was chosen upon the extinction of the orthorhombic [212/103/211] triplet. Yet broad and very weak tetragonal refection between x = 0.35-0.6 convolute the distinction between tetragonal and cubic phases. 66

FIGURE 3.10. Rp error of models obtained with Rietveld refnement, demonstrating the difficulty applying Rietveld techniques to diffraction patterns of $(K_xNa_{1-x})MgF_3$ samples. Difficulty comes from ubiquitous peak broadening most pronounced in super-structure reflections and irregular intensities. The error in orthorhombic or cubic models is marked in blue. Errors $\chi 2$, Rp, and Rwp can be found in Table 3.3. 67

FIGURE 3.11. Plot of type 1 $(K_{0.40}Na_{0.60})MgF_3$ perovskite generated by FullProf. Cubic substructure (upper tier markers) and tetragonal *P*4/*mbm* superstructure (lower tier markers) are fit each as a separate phase to allow for large tetragonal FWHM. Misfit of reflections from both sub and superstructure occurs from inconsistent peak shape and intensity. The plot inset shows the intensity contrast between 210 and 211 indices which cannot be calculated by the *P*4/*mbm* model. 68

FIGURE 3.12. The fluorine decoupled ^{23}Na MAS at a spinning speed of 16 kHz. 69

FIGURE 3.13. A diagram showing the local coordination environment of the sodium ion in (a) orthorhombic and (b) cubic space group. 70

FIGURE 3.14. The ^{19}F NMR spectrum under 42 kHz MAS conditions for different K-doping levels. 71

FIGURE 3.15. The calculated probabilities (P), based on random occupation of A sites by Na^+ and K^+ are plotted next to observed intensities of the K0, K1, K2, K3, and K4 local environments via ^{19}F NMR at different concentration levels. It appears from this data that end-member configurations are preferred vs. intermediate. 72

FIGURE 3.16. 2D MQ BABA spectra for (a) x = 0.3 showing broad cross peaks connecting like environments and (b) x = 0.7, where cross peaks connection different fluorine sublattices are now resolved. Projections onto the single and double quantum dimension are shown along with the assignments of some of the cross-peaks. 73

FIGURE 4.1. (a) The reduced pair distribution functions (G(r)) obtained through direct Fourier transformation of the observed structure functions (S(Q)) normalized from data collected at high temperature are plotted and stacked in order of increasing temperature. The function shown as a thin line is data at 731 ˚C. Features occurring at distances < 1 Å are unavoidable error from normalization of the structure function. 88

FIGURE 4.2. (a) The normalized structure functions (S(Q)-1) of $NaMgF_3$ at 59 ˚C (lower tier) and 819 ˚C (upper tier) are plotted adjacent to the corresponding reduced pair distribution functions (G(r)) fit using program PDFFIT. (b) Fits were achieved constraining to the orthorhombic (lower tier) and cubic (upper tier) structure models observed with Rietveld refinement (Zhao *et al.* 1993a), allowing the unit cell parameter(s), scale factor, anisotropic displacement parameters of fluorine, and resolution terms to refine, as 9 parameters. (c) Fits were achieved allowing atomic positions, isotropic displacement parameters, unit cell parameter(s), and resolution terms to refine as 16 parameters. 89

FIGURE 4.3. Radial distribution functions (G(r) + baseline, $[4\pi r\rho_o]$) obtained at minimum and maximum temperature. Peak positions assigned from structural models are marked. Data appear to confirm molecular dynamics simulation data presented in Street *et al.* (1997), where the Mg-F correlation shows significant asymmetry at high temperature. 90

FIGURE 4.4. The isotropic displacement parameter of each ion in $NaMgF_3$ is plotted as a function of temperature. Black symbols are data in the current study, while open symbols and solid black line are data from Zhao *et al.* (1993a). Errors bars are on the order of symbol size and grey lines are intended to guide the eye. Labels include the Wyckoff position of the ion in the crystal structure. 91

FIGURE 4.5. (a) The reduced (pseudo-cubic: $\sqrt{2}$, $\sqrt{2}$, 2^{-1}) unit cell axes and (b) volume are plotted as a function of temperature. Black symbols are data in the current study, while open circles and solid black lines are data from Zhao *et al.* (1993a). Errors bars are on the order of symbol size and grey lines are intended to guide the eye. 92

FIGURE 4.6. A structure model of $NaMgF_3$ perovskite at room temperature illustrates the octahedral coordination environment of the MgF_6 unit normal to the c-axis. Labels include the Wyckoff position of the fluorine ion in the crystal structure. 93

FIGURE 4.7. The specific Mg-F bond lengths are plotted as a function of temperature. Black symbols are data in the current study, grey circles are the average Mg-F bond length value, while open circles are the average Mg-F bond length value from Zhao *et al.* (1993a). Errors bars are on the order of symbol size, though larger near the transition, and grey lines are intended to guide the eye. Labels include the Wyckoff position of the fluorine ion in the crystal structure. 94

FIGURE 4.8. The four unique Mg-Na distances are plotted as a function of temperature. Errors bars are on the order of symbol size and larger near the transition. 95

FIGURE 4.9. The position parameters of the (a) Na, (b) $F_{[4c]}$, and (c) $F_{[8d]}$ ions in the orthorhombic $NaMgF_3$ crystal structure are respectively normalized to the cubic position and plotted as a function of temperature. Black symbols are data in the current study, while open symbols and solid black line are data from Zhao *et al.* (1993a). The solid black line approximates the very close $F_{[8d]}$ x, y, and z values reported in Zhao *et al.* (1993a). Errors bars are on the order of symbol size and larger near the transition. 96

FIGURE 4.10. The Mg-F-Mg and F-Mg-F (inset) bond angles are plotted as a function of temperature. Black symbols are data in the current study, while open symbols and solid black line are data from Zhao *et al.* (1993a). Errors bars are on the order of symbol size and larger near the transition. Labels include the Wyckoff position of the fluorine ion in the crystal structure. 97

FIGURE 4.11. The volume ratio of the sodium polyhedra to the magnesium octahedra (V_A/V_B) in $NaMgF_3$ is plotted as a function of temperature. The volume of the MgF_6 unit is plotted a function of temperature (inset). Black symbols are data in the current study, while open symbols are data from Zhao *et al.* (1993a). Errors bars are on the order of symbol size. 98

FIGURE 4.12. Structure model diagram illustrating orbital thermal motion of the $F_{[4c]}$ and two $F_{[8d]}$ ions in the $NaMgF_3$ structure. The radius of each torus is defined by the distance from the position of the ion in the ideal cubic ($Pm\bar{3}m$) perovskite and the midpoint between two nearest Mg ions, which defines the Mg-F bond length in the average structure (<Mg-F>). 99

FIGURE 5.1. Pressure-temperature experimental pathways taken in the Paris-Edinburgh press. 120

FIGURE 5.2. PVT data set compiled from Zhao et al. (1993a), (Liu et al., 2005), and this study. 121

FIGURE 5.3. Pseudo-cubic unit cell parameters of $NaMgF_3$ at high pressure and temperature. 122

FIGURE 5.4. Projected equation of state isotherms of $NaMgF_3$ in comparison to experimental data. 123

FIGURE 5.5. Average Mg-F bondlengths in $NaMgF_3$ derived from Rietveld refinement. 124

FIGURE 5.6. The tilt angle of Mg-F octahedra are plotted at several isobars with increasing temperature. 125

FIGURE 5.7. The ratio of the Mg-F bond length determined from atomic positions of Rietveld structure models is normalized according to the value determined from the unit cell. 126

FIGURE 5.8. The distortion of MgF_6 octahedra is plotted vs. pressure. Error bars are larger that symbol size and not shown for clarity. 127

FIGURE 5.9. ....The distortion of MgF_6 octahedra is plotted vs. pressure. Error bars are larger that symbol size and not shown for clarity. 128

FIGURE 5.10. .....The distortion of MgF_6 octahedra is plotted vs. pressure. Error bars are larger that symbol size and not shown for clarity. 129

FIGURE 6.1. The orthorhombic post-perovskite structure of $NaMgF_3$ as (**a**) *Cmcm* and (**b**) $Cmc2_1$. 144

FIGURE 6.2. The 2nd order Birch-Murnaghan equations of state (EoS) of $NaMgF_3$ are compiled from three high pressure runs. Each high pressure run contained different materials to preclude reaction with the sample (SS, stainless steel; C, graphite). 145

FIGURE 6.3. X-ray diffraction pattern of N-phase $NaMgF_3$ after laser heating at 37(1) GPa with Pt and MgO internal standards. The N-phase unit cell (Pnnm), Pt, and MgO are fit with a Le Bail model. Arrows pointing down indicate residual $CaIrO_3$-type $NaMgF_3$. Inset: X-ray diffraction patterns of $NaMgF_3$ at 55(2) GPa before and after laser heating. This data series (inset) was obtained by stepping the x-ray beam position away from the position of the heating laser, allowing the collection of x-ray diffraction patterns from sample heated to temperatures consecutively less than the maximum to room temperature. Arrows pointing up show indexed peak positions of the post-perovskite structure, while arrows pointing down highlight peaks of N-phase $NaMgF_3$. Sample also contains NaCl (◊) and graphite (no diffraction). 146

FIGURE 6.4. In-situ high pressure Rietveld structure modeling of (a) $NaMgF_3$ perovskite and (b) post-perovskite $NaMgF_3$. Portions of the raw two-dimensional data are inset in each plot to show sample texture. Difference curves of Rietveld structure models are plotted below the calculated (solid) and observed (dotted) background-subtracted X-ray diffraction patterns; (b) in descending order: (1) *Cmcm* with 4th order spherical harmonic preferred orientation correction (POC), (2) *Cmcm* without POC, (3) $Cmc2_1$ without POC. Weak reflections marked with an arrow are indexed as $NaMgF_3$ post-perovskite. 147

FIGURE 7.1. Structure model of $CaIrO_3$ (*Cmcm*), showing coordination environment of each ion site. Each oxygen site is designated by the Wyckoff position symbol 4c or 8f. The number of each unique bond belonging to each ion environment is listed for clarity. 173

FIGURE 7.2. The unit cell parameters and volume of $CaIrO_3$ are plotted as a function of pressure. Data collected in an alcohol pressure medium (black) are plotted along side data collected from several sample runs (grey, dark grey, and white) in a NaCl pressure media after laser annealing (1500±300 K). All error bars are smaller than symbol size. 174

FIGURE 7.3. Results of a typical Rietveld refinement of $CaIrO_3$ showing the fit to the data collected at 1089 K. Data above 10˚ 2θ are magnified by a factor of 20 for clarity. The arrow pointing down indicates the I_o reflection from the dissociation product Ca_2IrO_4. A picture of the $CaIrO_3$ structural model is inset. 175

FIGURE 7.4. The unit cell parameters and volume of $CaIrO_3$ are plotted as a function of temperature. Error bars are smaller than symbol size. 176

FIGURE 7.5. The change in atom positional parameters, in fractional coordinates, plotted as a function of the change in temperature increasing from 332 K. The asymmetric unit for the $CaIrO_3$ structure model in space group *Cmcm* has 4 independent atomic positional parameters; each is normalized according to their value at 332 K. Error bars are larger than symbol size and are not shown for clarity. Each parameter, with standard deviation, has been fit according to the linear equation displayed within the plot. Equations refer to the real atomic position within the unit cell (Ca: 0, y, 0; Ir: 0, 0, 0; O_{4c}: 0, y, 0.25; O_{8f}: 0, y, z) so the estimated structure may be calculated by the reader at any temperature, where T = 0 at 332 K. Atom labels contain the Wyckoff position of each atom (8f or 4c) in addition to the variable direction (y or z) within the unit cell. 177

FIGURE 7.6. Isotropic displacement parameter for each atom is shown a function of change in temperature increasing from 332 K. Some error bars are larger than symbol size and not shown for clarity. Each parameter, with standard deviation, has been fit according to the second-order polynomial equation displayed within the plot. 178

FIGURE 7.7. The volume of the Ca polyhedra (V_A), IrO_6 octahedra (V_B), and V_A/V_B ratio (inset) calculated from structure models derived from Rietveld refinement, along with the change in each parameter are plotted as a function of change in temperature increasing from 332 K. Error bars are smaller than symbol size and each parameter, with standard deviation, has been fit according to the linear equation displayed within the figure. The Ca polyhedra assumes: $V_A = (V_{UC}/4)-V_B$. 179

FIGURE 7.8. The deformation of IrO_6 octahedra as bias from a perfect octahedra plotted as a function of change in temperature increasing from 332 K. Oxygen labels contain the Wyckoff position of each atom (8f or 4c). Ir-O bias = $[(\text{Ir-O}) - (\text{Ir-O})_m] / (\text{Ir-O})_m$, while O-Ir-O bias = $\tan [(\pi/2) - (\text{O-Ir-O})]$. 180

FIGURE 7.9. Rietveld structure refinement of $CaIrO_3$ showing the fit to the data collected at 9.72(5) GPa. Data below 1.3 Å d-spacing are magnified (counts-scale) by a factor of 4, while the intensities below 0.82 Å are magnified by a factor of 16. Weight fraction of each phase is refined and included in the plot at this pressure. 181

FIGURE 7.10. The change in atom positional parameters, in fractional coordinates, plotted as a function of pressure. The asymmetric unit

of the $CaIrO_3$ structure model in space group *Cmcm* has 4 independent atomic positional parameters and each is normalized according to the 'room pressure' value (70 oil bar). Error bars are larger than symbol size and are not shown for clarity. Each parameter, with standard deviation, has been fitted according to the linear equation displayed within the plot. Quasi-hydrostatic data (850 bar) are shown as symbols with dotted line. Equations refer to the real atomic position within the unit cell (Ca: 0, y, 0; Ir: 0, 0, 0; O_{4c}: 0, y, 0.25; O_{8f}: 0, y, z). 182

FIGURE 7.11. The volume of the Ca polyhedra (V_A), IrO_6 octahedra (V_B), and V_A/V_B ratio (inset) derived from Rietveld refinement are plotted as a function of pressure. Error bars are smaller than symbol size and each parameter, with standard deviation, has been fitted according to the linear equation displayed within the figure. Quasi-hydrostatic data (850 bar) are shown as symbols with dotted line. $V_A/V_B = [(V_{UC}/4)-V_B]/V_B$. 183

FIGURE 7.12. Strain of IrO_6 octahedra as bias from a perfect octahedra is plotted as a function of pressure. Quasi-hydrostatic data (850 bar) are shown as symbols with dotted line. Ir-O bias = $[(\text{Ir-O}) - (\text{Ir-O})_m] / (\text{Ir-O})_m$, while O-Ir-O bias = $\tan [(\pi/2) - (\text{O-Ir-O})]$. 184

FIGURE 7.13. (a) Bond lengths within the $CaIrO_3$ structure plotted as a function of pressure and (b) as a function of temperature. Error bars are of the order of the symbol size and each parameter, with standard deviation, has been fitted according to the linear equation displayed within the figure. 185

FIGURE 8.1. The V_A:V_B ratio of $NaMgF_3$ is plotted as a function of pressure. Data < 20 GPa are taken from Liu et al. (2005) and data > 20 GPa is from Chapter 6. 195

FIGURE 8.2. The ratio between specific extra-octahedral anion-anion distance $[(X\text{-}X)_E]$ and the average intra-octahedral anion-anion $[(X\text{-}X)_I]$ distance is plotted as a function of the V_A:V_B ratio. The average $(X\text{-}X)_E$ distance is used to calculate the data in black, while just the shortest $(X\text{-}X)_E$ distance is used to calculate the data in white. The data show that all perovskite structures in our sample have an average $(X\text{-}X)_I$ distance that is shorter than the $(X\text{-}X)_E$ distance. The three unique $(X\text{-}X)_E$ distances are indicated for the inset orthorhombic (*Pbnm*) perovskite structure. Errors bars are smaller than symbol size unless otherwise indicated or the standard deviations of raw structure parameters are not present in the ICSD. 196

FIGURE 8.3. Raw area-detector image of x-ray diffraction from $MgGeO_3$ post-perovskite at 87 GPa after laser-heating at ~1500K. Data do not

show texturing and the spotty texture may be overcome with integration around 360° chi. 197

FIGURE 8.4. Rietveld refinements of $MgGeO_3$ post-perovskite, where data in grey is observed, data in black is calculated from the structure model, and data below is the difference which corresponds to each of the above diffraction patterns with respect to vertical position. Black ticks mark the position of sample reflections and upper-tier black ticks mark the position of reflections from platinum, which are fit with a Le Bail model. 198

FIGURE A.1. Typical two-dimensional sample exposure illustrating the single crystal diamond spots along side sample powder diffraction. These spots, including the surrounding diffuse scatter, must be carefully masked prior to data integration. To avoid saturation of the detector and obtain optimal counting statistics, the bright spots from the diamond anvils demonstrate the need to average many short exposures. The intensity of parasitic DAC Compton scatter is best observed when comparing the central beamstop shadow with adjacent background intensity. The diamond anvil Compton scatter and sample diffuse scatter cannot be distinguished by eye. 208

FIGURE A.2. Diagrams comparing S(Q) and G(r) for gold in the diamond anvil cell (DAC) at 1 bar, with Gold in the DAC at 8.1 GPa. Full-profile fitting plots of G(r) are represented with observed data (dashed blue), model data (solid black), and difference plot below (solid black). 209

FIGURE A.3. A plot comparing the PDF of gold taken from a 1mm capillary (solid black) vs. that taken in the DAC at 1 bar (dash blue). The difference plot below (solid black) shows no asymmetry about PDF Au-Au correlations and we conclude our DAC background correction is valid. 210

FIGURE A.4. Unit cell and Au-Au distance as determined by Rietveld and HPQ-PDF analysis. The PDF-derived unit cell values were fit from the entire G(r) profile (Program PDFFIT), while a Gaussian was fit to the first Au-Au correlation to independently derive this distance. The discrepancy between the Au-Au distances may be explained as an effect of imperfect Gaussian peak-shape. The data point at the final pressure shown in the Au-Au PDF analysis was not included in the regression, due to an increase in the full-width at half-maximum in the G(r) Au-Au correlation (indicating a deviatoric-stress). 211

List of Tables

TABLE 3.1. Unit-cell volume (Z=1) vs. composition and synthesis method. 55

TABLE 3.2. Lattice parameters and phase transitions vs. composition. 56

TABLE 3.3. Errors associated with Rietveld trials in various space groups. 57

TABLE 4.1. (a) Structure parameters, (b) displacement parameters, and atom distances derived from PDFFIT are listed for $NaMgF_3$ (*Pbnm*) at several temperatures. At temperatures greater than 731 ˚C, the unit cell lengths of our structure models were constrained to a single pseudo-cubic lattice parameter according to the relationship (*Pbnm*) $\sqrt{2}, \sqrt{2}, 2^{-1}$ for the *a*-, *b*-, and *c*-axes, respectively. 87

TABLE 5.1. PVT data set compiled from Zhao et al. (1993a), (Liu et al., 2005), and this study. 113

TABLE 5.2. Derived equation of state parameters from the data set presented in Table 5.1. (a) The bulk modulus is refined in the first trial and held constant in the second. (b) The equation of state of the cube of each unit cell length (i.e., a^3) and (c) the volume of each polyhedron is fit to give a comparative bulk modulus. 114

TABLE 5.3. Various structural parameters derived from Rietveld structure models from (Liu et al., 2005) and this study are listed. 117

TABLE 5.4. Ultrasonic elasticity data for $NaMgF_3$. 118

TABLE 5.5. Equation of state data for $NaMgF_3$ derived from ultrasonic elasticity. 119

TABLE 6.1. Structure parameters derived from Rietveld refinement of data for (**a**) $NaMgF_3$ perovskite at 27(1) GPa, (**b**) post-perovskite structure models of $NaMgF_3$ at 54(2) GPa without correction for preferred orientation as *Cmcm*, (**c**) with correction for preferred orientation as *Cmcm*, and (**d**) without correction for preferred orientation as $Cmc2_1$. V_A/V_B ratio was calculated considering, $V_A = (V_{UC}/Z)-V_B$. 143

TABLE 7.1. (a) Unit cell data from $CaIrO_3$ at high pressure. (b) Bulk modulus constants were obtained using a 2^{nd} order Birch-Murnaghan equation of state. The cube of each unit cell length, i.e. a^3, has been fit to obtain a comparative bulk modulus. (c) The raw unit cell from every ~7^{th} data in the high temperature series. (d) The fitted thermal expansion constants are listed with those obtained by fitting the cube of each unit cell length, i.e. a^3, to obtain a comparative thermal expansion. 169

TABLE 7.2. Refined unit cell parameters, atomic coordinates, isotropic temperature factors (*U*), and refinement statistics are listed for $CaIrO_3$ (*Cmcm*) at several low temperatures in section (a), while the residual bond strain value (*R*1) of the structure, experimental bond valence sums (S_{ij}), and chemical strain (P_i) of each ion are listed at room temperature in section (b). (Ca: 0, y, 0; Ir: 0, 0, 0; O_{4c}: 0, y, 0.25; O_{8f}: 0, y, z) 170

TABLE 7.3. Refined unit cell parameters, atomic coordinates, isotropic temperature factors (*U*), and refinement statistics are listed for $CaIrO_3$ ($Cmc2_1$) structure model trials at room pressure and low temperatures (2.0(1) and 293(2) K) with a trial at high pressure and room temperature (9.72(5) GPa). (Ca: 0, y, z; Ir: 0, y, z; O_{4c}: 0, y, z; O_{8f}: 0, y, z) 171

TABLE 7.4. Refined unit cell parameters, positional parameters, isotropic temperature factors (*U*), and refinement statistics are listed for $CaIrO_3$ (*Cmcm*) at high pressure. 172

TABLE 8.1. (a) The perovskite structure sample from the ICSD includes 51 perovskite structures ordered according to V_A:V_B and listed with (b) all materials known to adopt the $CaIrO_3$-type structure. Unless otherwise noted, the structures represent the atomic configuration at ambient conditions. 194

TABLE A.1. Comparison of cell parameter and Au-Au distance as determined by Rietveld and PDF analysis. Estimated standard deviation (ESD) is listed to the right of their applicable variables. 207

Acknowledgements

I owe this dissertation to many collaborators who contributed their time, talent, resources, and ingenuity towards its completion. Above all, I thank Professor John B. Parise for critical comments, corrections, guidance, and support during this research. His strong dedication to and great enthusiasm for science catalyzed my own commitment to crystal chemistry, and mineral physics. I thank Professor Donald J. Weidner for interesting discussions regarding the structure behavior and physical properties of $NaMgF_3$ and for donation of a diamond anvil cell with a copy of Yusheng Zhao's dissertation for assistance during this research. Peter J. Chupas and Karena Chapman at Sector 11 at the Advanced Photon Source generously donated their time and beamline resources in order to assist work supporting several portions of this dissertation. Wilson A. Crichton's diligence, at beamline ID-27 at the European Synchrotron Radiation Facility, during operation and preparation of diamond anvil cells and the large-volume Paris-Edinburgh press was an indispensable contribution towards the success of the experiments described in Chapters 5 & 6. Comprehensive instructions by Jennifer Kung and Baosheng Li enabled me use the large volume multi-anvil press in order to prepare and synthesize high quality polycrystalline samples as well as high pressure cell assemblies suitable for ultrasonic measurements—techniques vital to work described in Chapters 5 and 7. Haozhe Liu and Yue Meng, at Sector 16 at the Advanced Photon Source, generously offered up portions of their own beamtime during the course of this research to allow collection of data reported in Chapter 6. Enlightening discussions with Yue Meng regarding high pressure techniques have transformed the way I think about and use the diamond anvil cell. Donald H. Lindsley, Distinguished Professor Emeritus of the Geosciences Department at the State University of New York at Stony Brook, donated his free time and petrological expertise towards understanding the pressure-temperature stability of $CaIrO_3$ and the optimum procedure for large-volume synthesis of this material. Finally, I want to acknowledge the integral contributions of Henry P Scott, Elise B. Knittle, Quentin C. Williams, and especially Javier Santillan, during my undergraduate education at the University of California at Santa Cruz. The personal as well as professional interaction I enjoyed while working in the Knittle-Williams Mineral

Physics Laboratory gave me the confidence and technical experience to pursue this graduate-level education at Stony Brook. To these and others whom I have worked with while at Stony Brook: Thank you. I look forward to an opportunity to return favors provided.

Chapter I

Introduction

1.1. Introduction

While the composition, temperature distribution, and convection scheme of Earth's mantle is uncertain (Anderson and Bass, 1984; Angel, 1997; Ito et al., 1984), abrupt increases in bulk density and seismic velocity occur with depth (Fig. 1.1). Attributed to high pressure phase transitions in silicate minerals (Ringwood, 1994) (Fig. 1.2), Earth's upper mantle, transition zone, and lower mantle are marked by strong density contrasts at depths of ~410 and ~660 km, respectively (Dziewonski and Anderson, 1981). Through high pressure experiments, these boundaries are known to correspond to phase transitions in forsterite (Mg_2SiO_4, olivine), and yield a lower mantle dominated by $MgSiO_3$ perovskite and MgO e.g., (Boehler, 2000; da Silva et al., 2000; Hemley et al., 2000; Jeanloz and Thompson, 1983). While seismic anomalies are thought to occur in various regions of the mid-lower mantle e.g., (Vinnik et al., 2001), the discontinuity at ~2750 km marking the D" region is observed almost ubiquitously above the core-mantle boundary (Lay and Helmberger, 1983; Sidorin et al., 1999).

The D" layer lies just above the core/mantle boundary (2891 km) and has significant lateral variation (Fig. 1.3). Tending to correlate with past subduction, the discontinuity is observed at greater depths in regions expected to have higher temperatures. Below the discontinuity, an increase in seismic velocity is generally observed however, many studies report anomalous seismic features in D", including azimuthal anisotropy, transverse isotropy, shear wave splitting, ultra low seismic velocities, and variable Vs/Vp ratio (Garnero et al., 2004; Hernlund et al., 2005; Lay et al., 1998; Sidorin et al., 1999; Thomas et al., 2007) (Fig. 1.4). While the D" discontinuity has long been suspected as resulting from a phase transformation in $MgSiO_3$ perovskite, recent mineral physics experiments and research have made the first step towards understanding the D" layer within a mineral physics context.

A post-perovskite phase of $MgSiO_3$ was discovered from experiments performed in the diamond anvil cell at 120 GPa and ~2500 K and preferred orientation of the post-perovskite phase in D" is expected to account for seismic anisotropy within the layer (Garnero, 2004; Lay et al., 2004; Lay et al., 2006; Murakami et al., 2004; Murakami et al., 2005; Oganov and Ono, 2004). The post-perovskite structure is isostructural to $CaIrO_3$ and very rarely observed in materials at room pressure (Berndt, 1997). Naturally, there has been a recent frenzy of research aimed at characterization of the structure and properties of the post-perovskite phase (Hirose and Fujita, 2005; Hirose et al., 2005; Kubo et al., 2006; Mao et al., 2006; Santillan et al., 2006; Tateno et al., 2006). Because of the extreme pressures required to stabilize $MgSiO_3$ post-perovskite, the volume of knowledge gained from direct experimentation has yet to match that provided by computer simulation. Therefore, research on materials with analogous structure may prove useful for a preliminary understanding of post-perovskite.

1.2. Experiments utilizing materials with analogous structure

Reproduction in the laboratory of the very high pressures and temperatures expected in Earth's lower mantle (~23-130 GPa and ~2000-4800 K) restricts experimental access to the sample. By identifying the structure and properties of analog materials under modest pressures and temperatures, it is possible to show changes which may be expected of the silicate structure under lower mantle conditions. For example, while the structure and elasticity of analog materials at ambient conditions might be different than the silicate under extreme conditions, modes of structure change and pressure and temperature derivatives of thermodynamic parameters are usually quite similar. In addition, it is useful to confirm phase transitions between structures and the pressure and temperature stability of each structure using analog materials.

The mineral neighborite, $NaMgF_3$, is isostructural and isoelectronic to $MgSiO_3$ (Chao et al., 1961; O'Keeffe et al., 1979), making it an ideal analog. $MgSiO_3$ and $NaMgF_3$ contain ions with similar radius ratios (A>B>X) and a 1:2 electronic charge ratio for both anion and cations. Neighborite ($NaMgF_3$) (Chao et al., 1961) is a well studied analog for $MgSiO_3$ perovskite, helpful in demonstrating the effects of pressure and temperature on the perovskite structure (Liu et al., 2005; Martin et al., 2005; Zhao et

al., 1993b). The flexible bonding of fluoride perovskite permits simulation of ultra-high pressure and temperature conditions on silicate perovskites at much lower conditions (O'Keeffe et al., 1979). $NaMgF_3$ perovskite has a bulk modulus less than one third that of $MgSiO_3$ and nearly half that of $MgGeO_3$ perovskite. Thus $NaMgF_3$ may require a lower pressure to stabilize post-perovskite, and thereby assist Rietveld structural modeling. Because the structure of $NaMgF_3$ has previously been studied at high pressure and temperature, the material is even more suited for studies of physical properties, such as elasticity.

As an analog to the post-perovskite structure of $MgSiO_3$, $CaIrO_3$ is the only oxide available for study at room pressure and temperature and only a few sulfides and high Z halides share this rare structure type at ambient conditions. While this may make selection of the post-perovskite analog material an easy task, it highlights problems associated with the utilization of analogs. Because of the rarity of the structure type and obscurity of the composition, initial steps of experimentation, such as preparation and phase stability, are an exploration not applicable to the silicate analog. However, considering the scarcity of alternative analog materials, such exploration of $CaIrO_3$ is sure to assist a future understanding of post-perovskite $MgSiO_3$ if an underlying instability in the $CaIrO_3$-type structure is identified.

1.3. Properties of perovskite and post-perovskite structures with changing pressure and temperature.

Because of its significance to Earth science and many applications in industry, the perovskite structure is one of the most interesting and common structure-types for materials with octahedral coordination and ABX_3 stoichiometry. Well known for exhibiting both continuous and discontinuous phase transitions with changing pressure, and temperature, perovskite structures are often characterized by ferroelastic behavior and typically develop twin states, domain microstructure, and anomalies in spontaneous strain near phase transition (Aleksandrov, 1976; Aleksandrov, 1978; Ali and Yashima, 2005; Angel et al., 2005; Glazer, 1972; Glazer, 1975; Redfern, 1996; Thomas, 1996; Thomas, 1998). As a result, seemingly simple changes in perovskite structure are often

accompanied by a complex response in physical properties (Bonamour et al., 1991; Karen and Woodward, 1998; Salje and Smaston, 1989; Woodward et al., 1994; Woodward, 1997; Zhao et al., 2004) and elasticity of perovskites have been carefully studied and sought to explain anomalous seismic observation in the lower mantle (Liebermann et al., 1977).

The perovskite structure is composed of corner-sharing BX_6 octahedra which define a framework enclosing the AX_{12} dodecahedra site (Fig. 1.5). Upon application of pressure and temperature, the perovskite structure changes by rotating (tilting) the relative orientations of BX_6 octahedra, which typically determine the space group of the structure. Commonly referred to as the aristotype structure, cubic perovskites have no tilted octahedra and lose symmetry elements with octahedra rotation about the pseudo-cubic axes (Fig. 1.6). Driving phase transition to several possible perovskite structure-types, octahedra rotations introduce modes of atomic vibration characteristic of the in- or anti-phase tilts (Glazer, 1972; Glazer, 1975; Zhao et al., 1993a; Zhao et al., 1993b). Because of the corner-sharing nature of the perovskite structure, each tilted octahedra in the structure is correlated to the tilt of neighboring octahedra and ideally the average octahedra tilt environment is the same as each local tilt environment. Usually structure analysis assumes rigid octahedra. However, when a perovskite structure is subject to partial substitution of elements on a given site for example, octahedra surrounding a cation with small ionic radius will prefer a different tilting state than octahedra surrounding a cation with large ionic radius and in this case the average tilt environment of octahedra is not representative of each local tilt environment. Thus, it is important to realize the length-scale by which each experimental technique is sensitive to structure and average structure may not be a satisfactory approximation for local structure.

The post-perovskite structure (*Cmcm*) is very rare and $CaIrO_3$ itself is the only oxide known to crystallize with this structure at room pressure. The structure of $CaIrO_3$ Fig. 1.7), stoichiometry ABX_3, consists of single layers of IrO_6 octahedra normal to the b-axis. The octahedra share edges along the a-axis and corners along the c-axis, while calcium occupies sites between these layers (Rodi and Babel, 1965). Because of significant structural anisotropy, materials adopting this structure are expected to have very different physical properties from those crystallizing with structures related to

perovskite. Experimental observation of structure changes in post-perovskite under variable pressure and temperature is reported in detail within subsequent chapters of this thesis.

1.4. Chapter introduction and highlights

1.4.1. Chapter II, Details for performance of novel or non-conventional experiments utilized in this thesis.

The experiments presented in this thesis were performed almost exclusively using synchrotron-based monochromatic X-ray powder diffraction. Details on synchrotron X-ray facilities and how to perform a powder diffraction experiment are not presented here. Rather, this chapter provides complementary information on experiments performed that may be considered novel or non-conventional.

Pair distribution function analysis is not a new technique. Aimed at local structure determination, studies of the pair distribution function are today very rarely preferred over conventional Bragg diffraction and traditional crystallography. However, with industrial applications for nanostructured and amorphous materials pair distribution function analysis is making resurgence and finding new applications such as studies of mineral structure at extreme conditions. This technique is difficult to perform and an overview of critical details is presented here.

The laser heated diamond anvil cell is a time-tested and very difficult technique for exploratory structure and equation of state characterization of minerals under extreme conditions. This section summarizes three types of experiments where the laser heated diamond anvil cell technique finds common use.

1.4.2. Chapter III, Local and long range order of (K, Na)MgF_3 as analog for (Mg, Ca)SiO_3 in the lower mantle.

As orthorhombic (***P****bmn*) and cubic (***P****m*$\bar{3}$*m*) perovskites, $NaMgF_3$ and $KMgF_3$ are theoretically isostructural to high pressure perovskite phases of $MgSiO_3$ and $CaSiO_3$ present in Earth's lower mantle. We show how defects in the local structure (< 5 Å), driven by mismatch in the Na and K ionic radius, creates a greater bulk volume in

$(K,Na)MgF_3$ perovskites than a proportionate mixture of endmember perovskites. Based on these results we predict $NaMgF_3$ and $KMgF_3$ should not form a solid solution at high pressure and suggest a similar cation radius mismatch may be a reason why Ca and Mg silicate perovskites prefer separate phases at extreme conditions. In detail, a local structure model is presented for $(K,Na)MgF_3$ perovskite using results from high-resolution synchrotron X-ray powder diffraction and nuclear magnetic resonance (NMR) spectroscopy. The average structure of $(K,Na)MgF_3$ perovskite is found to transition from orthorhombic (***P****bnm*) to tetragonal (***P***4/*mbm*) to cubic ($\boldsymbol{Pm\bar{3}m}$) as potassium concentration is increased. These phase transitions are not accompanied by a discontinuity in pseudo-cubic unit-cell volume and occur close to compositions $(K_{.37},Na_{.63})MgF_3$ and $(K_{.47},Na_{.53})MgF_3$, respectively. ^{19}F-NMR spectra indicate that the Na^+ and K^+ cations do not occupy the A cation site at random and endmember environments are favored in all compositions. Based on results from both X-ray diffraction and NMR, we propose that diffuse diffraction is the result of strain between coexisting regions of different octahedra (MgF_6) tilts brought about by the ionic radius mismatch of Na^+ and K^+ cations. We suggest A-site cations group with like-cations as neighbors to reduce excess volume and total strain.

1.4.3. Chapter IV, Pair distribution analysis of the local $NaMgF_3$ structure; implications for silicate perovskites in the lower mantle.

Through quantitative analysis of the pair distribution function, the local structure (< 20 Å) of $NaMgF_3$ is reported at high temperature. Contrary to previous studies of the average structure (> 100 Å), the Mg-F bond length is found to increase with increasing temperature. This study suggests differences between the local and average structure could develop in the analog structure, $MgSiO_3$. In detail, we find that the average Mg-F bond length, corresponding a ~2 Å peak in the PDF, increases between 50 and 850 ˚C. At each temperature, asymmetry in this peak is consistent with an orthorhombic (***P****bnm*) perovskite local structure, allowing 3 unique Mg-F values and deformation of MgF_6 octahedra. Defined by the three orthogonal Mg-Mg distances, the pseudo-cubic unit cell of local structure models becomes metrically tetragonal and cubic at temperatures greater than ~350 and 765 ˚C, respectively. A discontinuity in the temperature dependence of the

fluorine atomic displacement parameters at 765˚C suggests thermal-activation of new vibrational modes in $NaMgF_3$ at high temperature consistent with transverse vibration of the bridging fluorine atoms (Mg-F-Mg).

1.4.4. Chapter V, Structure and ultrasonic elasticity of $NaMgF_3$ at high pressure and temperature.

Using monochromatic x-ray diffraction with Rietveld refinement, the average $NaMgF_3$ structure is found to transition from orthorhombic (***P****bnm*) to cubic (***P****m*$\bar{3}$*m*) at high pressures (7 GPa) and temperatures (1400 K) via second-order transition. Ultrasonic measurements of $NaMgF_3$ yield thermoelastic equation of state and provide evidence for sample-induced elastic attenuation at pressures and temperature near the orthorhombic to cubic phase transition. Data from the average structure modeling suggests rotation and deformation of perovskite octahedra coincide with unit cell distortion as a function of distance from the phase transition in pressure-temperature space. The apparent linear relationship between pressure and temperature induced structural modification suggests the average $NaMgF_3$ structure will not transition to tetragonal (***P***4/*mbm*) symmetry. The strong effect of pressure on the stability of the orthorhombic perovskite suggests $MgSiO_3$ in Earth's lower mantle should not undergo perovskite-perovskite phase transformations.

1.4.5. Chapter VI, Understanding the perovskite/post-perovskite phase transition in $MgSiO_3$ via in-situ observation of $NaMgF_3$ analog material.

As an isostructural analog material to $MgSiO_3$, the structure behavior observed in $NaMgF_3$ at high pressure and temperature may help predict that occurring in the silicate at lower mantle conditions. In this work, we confirm $NaMgF_3$ does transition to a post-perovskite ($CaIrO_3$-type) structure at high pressure and we identify a further transition from post-perovskite $NaMgF_3$ to an unknown structure designated N-phase upon laser heating. Using full-profile Rietveld structure refinement, this work reports the perovskite and post-perovskite $NaMgF_3$ (ABX_3) structures via X-ray diffraction data collected from within the diamond anvil cell *in situ* at pressures close to the phase transition (~30 GPa). This study recognizes that the volume ratio of cation-centered coordination polyhedra (V_A/V_B) in perovskites is distinct from that in post-perovskites and suggests that the

pressure of a post-perovskite phase transition in perovskite structures may be predicted by extrapolating V_A/V_B to a value of ~4.

1.4.6. Chapter VII, Understanding structure changes in $MgSiO_3$ post-perovskite at high pressure and temperature via in-situ observation of $CaIrO_3$ analog material.

This study reports changes in $CaIrO_3$ structure occurring at high pressure and temperature. This study uncovers structure evolution in $CaIrO_3$ is significantly different than that occurring in perovskite structure types. (i) Axial compression and thermal expansion of this structure is significantly anisotropic and (ii) Rietveld structure refinements of $CaIrO_3$ indicate deformation rather than tilting, of IrO_6 octahedra. In addition, (iii) the volume ratio of cation-centered coordination polyhedra (V_A/V_B) is found to increase with temperature and (iv) $CaIrO_3$ dissociates to [IrO_2 + Ca_2IrO_4]. Using the trends in the volume ratio of cation-centered coordination polyhedra (V_A/V_B), a Clapeyron slope for the perovskite/post-perovskite phase transition is calculated for $CaIrO_3$ which is in excellent agreement with previous experimental observation. Based on this result we propose a method for calculating this transition slope in $MgSiO_3$.

1.4.7. Chapter VIII, Structure Science of the ABX_3 Stoichiometry and Implications for Perovskite and Post-Perovskite Structures of $MgSiO_3$ in Earth's Lower Mantle.

Data, research, predictions and conclusions presented in this thesis are drawn together in a final chapter which illustrates the comprehensive contribution and impact to crystal chemistry and mineral physics of perovskite and post-perovskite structures with implications for Earth's lower mantle. We investigate perovskite structures from the International Crystal Structure Database and the post-perovskite structure of $MgGeO_3$, based on results of the investigation was propose a method for predicting the p-T condition were perovskite structure should transition to post-perovskite.

1.4.8. Appendix, Local structure analysis in-situ at high pressures within the diamond anvil cell.

Structural studies at high pressures and temperatures almost exclusively apply crystallographic techniques that make the assumption that the material under study

possesses long range periodic order. An obvious consequence of the application of extreme pressure and temperature on materials is the introduction of disorder (both static and dynamic) into materials. Pair distribution function analysis is a technique allowing direct examination of local structure (<20 Å) in crystalline as well as amorphous materials and is complementary to powder diffraction which allows characterization of the average crystalline structure (>100 Å). In this work we present a technique allowing rapid collection of the pair distribution function of materials in the diamond anvil cell. In detail, we study the total scattering of nanocrystalline gold to 20 $Å^{-1}$ at pressures up to 10 GPa in a hydrostatic alcohol pressure-medium. Through direct Fourier transformation of the structure function (S(Q)), pair distribution functions (PDFs) (G(r)) are calculated without Kaplow-type iterative corrections. Quantitative high-pressure PDF (QHP-PDF) analysis is performed via full-profile least-squares modeling and confirmed through comparison of Rietveld analysis of Bragg diffraction. The quality of the high pressure PDFs obtained demonstrates the integrity of our technique and suggests the feasibility of future QHP-PDF studies of liquids, disordered solids, and materials at phase transition under pressure.

References

Aleksandrov, K.S. (1976) Sequences of Structural Phase-Transitions in Perovskites. Ferroelectrics, 14(3-4), 801-805.

-. (1978) Mechanisms of Ferroelectric and Structural Phase-Transitions, Structural Distortions in Perovskites. Ferroelectrics, 20(1-2), 61-67.

Ali, R., and Yashima, M. (2005) Space group and crystal structure of the Perovskite $CaTiO_3$ from 296 to 1720K. Journal of Solid State Chemistry, 178(9), 2867-2872.

Anderson, D.L., and Bass, J.D. (1984) Mineralogy and Composition of the Upper Mantle. Geophysical Research Letters, 11(7), 637-640.

Angel, R. (1997) Mineralogy-the earth's mantle remodeled. Nature, 385, 490-491.

Angel, R.J., Zhao, J., and Ross, N.L. (2005) General rules for predicting phase transitions in perovskites due to octahedral tilting. Physical Review Letters, 95(2), 025503(1-4).

Berndt, M. (1997) ICSC/RETRIEVE 2.01 Crystal Structure Database., Gmelin Institute/FIZ Karlsruhe, Germany.

Boehler, R. (2000) High-pressure experiments and the phase diagram of lower mantle and core materials. Reviews of Geophysics, 38(2), 221-245.

Bonamour, P., Bouffard, V., Fermon, C., Goldman, M., Jacquinot, J.F., and Saux, G. (1991) Nuclear Ferromagnetism in a Perovskite Structure. Physical Review Letters, 66(21), 2810-2813.

Chao, E.C.T., Evans, H.T., Skinner, B.J., and Milton, C. (1961) Neighborite, $NaMgF_3$, a New Mineral From the Green River Formation, South Ouray, Utah. American Mineralogist, 46(3-4), 379-393.

da Silva, C.R.S., Wentzcovitch, R.M., Patel, A., Price, G.D., and Karato, S.I. (2000) The composition and geotherm of the lower mantle: constraints from the elasticity of silicate perovskite. Physics of the Earth and Planetary Interiors, 118(1-2), 103-109.

Dziewonski, A.M., and Anderson, D.L. (1981) Preliminary Reference Earth Model. Physics of the Earth and Planetary Interiors, 25(4), 297-356.

Garnero, E.J. (2004) A new paradigm for Earth's core-mantle boundary. Science, 304(5672), 834-836. DOI:10.1126/science.1097849.

Garnero, E.J., Maupin, V., Lay, T., and Fouch, M.J. (2004) Variable azimuthal anisotropy in Earth's lowermost mantle. Science, 306(5694), 259-261. DOI:10.1126/science.1103411.

Glazer, A.M. (1972) Classification of Tilted Octahedra in Perovskites. Acta Crystallographica Section B-Structural Science, B 28(V15), 3384-3392.

-. (1975) Simple Ways of Determining Perovskite Structures. Acta Crystallographica Section a, 31(V1), 756-762.

Hemley, R.J., Mao, H.K., and Gramsch, S.A. (2000) Pressure-induced transformations in deep mantle and core minerals. Mineralogical Magazine, 64(2), 157-184.

Hernlund, J.W., Thomas, C., and Tackley, P.J. (2005) A doubling of the post-perovskite phase boundary and structure of the Earth's lowermost mantle. Nature, 434(7035), 882-886. DOI:10.1038/nature03472.

Hirose, K., and Fujita, Y. (2005) Clapeyron slope of the post-perovskite phase transition in $CaIrO_3$. Geophysical Research Letters, 32(13), L13313(1-4). DOI:10.1029/2005GL023219.

Hirose, K., Kawamura, K., Ohishi, Y., Tateno, S., and Sata, N. (2005) Stability and equation of state of $MgGeO_3$ post-perovskite phase. American Mineralogist, 90(1), 262-265.

Irifune, T., and Isshiki, M. (1998) Iron partitioning in a pyrolite mantle and the nature of the 410-km seismic discontinuity. Nature, 392(6677), 702-705.

Ito, E., Takahashi, E., and Matsui, Y. (1984) The Mineralogy and Chemistry of the Lower Mantle - an Implication of the Ultrahigh-Pressure Phase-Relations in the System MgO-FeO-SiO_2. Earth and Planetary Science Letters, 67(2), 238-248.

Jeanloz, R., and Thompson, A.B. (1983) Phase-Transitions and Mantle Discontinuities. Reviews of Geophysics, 21(1), 51-74.

Karen, P., and Woodward, P.M. (1998) Liquid-mix disorder in crystalline solids: $ScMnO_3$. Journal of Solid State Chemistry, 141(1), 78-88.

Kubo, A., Kiefer, B., Shen, G.Y., Prakapenka, V.B., Cava, R.J., and Duffy, T.S. (2006) Stability and equation of state of the post-perovskite phase in $MgGeO_3$ to 2 Mbar. Geophysical Research Letters, 33(12), L12S12(1-4). DOI:10.1029/2006GL025686.

Lay, T., Garnero, E.J., and William, Q. (2004) Partial melting in a thermo-chemical boundary layer at the base of the mantle. Physics of the Earth and Planetary Interiors, 146(3-4), 441-467.

Lay, T., and Helmberger, D.V. (1983) A Lower Mantle S-Wave Triplication and the Shear Velocity Structure of D". Geophysical Journal of the Royal Astronomical Society, 75(3), 799-837.

Lay, T., Hernlund, J., Garnero, E.J., and Thorne, M.S. (2006) A post-perovskite lens and D " heat flux beneath the central Pacific. Science, 314(5803), 1272-1276.

Lay, T., Williams, Q., and Garnero, E.J. (1998) The core-mantle boundary layer and deep Earth dynamics. Nature, 392(6675), 461-468. DOI:10.1038/33083.

Liebermann, R.C., Jones, L.E.A., and Ringwood, A.E. (1977) Elasticity of Aluminate, Titanate, Stannate and Germanate Compounds with Perovskite Structure. Physics of the Earth and Planetary Interiors, 14(2), 165-178.

Liu, H.Z., Chen, J., Hu, J., Martin, C.D., Weidner, D.J., Hausermann, D., and Mao, H.K. (2005) Octahedral tilting evolution and phase transition in orthorhombic $NaMgF_3$ perovskite under pressure. Geophysical Research Letters, 32(4), L04304(1-5). DOI:10.1029/2004GL022068.

Mao, L.W., Mao, H.K., Sturhahn, W., Zhao, J., Prakapenka, V.B., Meng, Y., Shu, J.F., Fei, Y.W., and Hemley, R.J. (2006) Iron-Rich Post-Perovskite and the Origin of Ultralow-Velocity Zones. Science, 312(5773), 564 - 565. DOI:10.1126/science.1123442.

Martin, C.D., Chaudhuri, S., Grey, C.P., and Parise, J.B. (2005) Effect of A-site cation radius on ordering of BX6 octahedra in (K,Na)MgF_3 perovskite. American Mineralogist, 90(10), 1522-1533.

Murakami, M., Hirose, K., Kawamura, K., Sata, N., and Ohishi, Y. (2004) Post-perovskite phase transition in $MgSiO_3$. Science, 304(5672), 855-858. DOI:10.1126/science.1095932.

Murakami, M., Hirose, K., Sata, N., and Ohishi, Y. (2005) Post-perovskite phase transition and mineral chemistry in the pyrolitic lowermost mantle. Geophysical Research Letters, 32(3), L03304. DOI:10.1029/2004GL021956.

O'Keeffe, M., Hyde, B.G., and Bovin, J.O. (1979) Contribution to the Crystal-Chemistry of Orthorhombic Perovskites - $MgSiO_3$ and $NaMgF_3$. Physics and Chemistry of Minerals, 4(4), 299-305.

Oganov, A.R., and Ono, S. (2004) Theoretical and experimental evidence for a post-perovskite phase of $MgSiO_3$ in Earth's D " layer. Nature, 430(6998), 445-448. DOI:10.1038/nature02701.

Redfern, S.A.T. (1996) High-temperature structural phase transitions in perovskite ($CaTiO_3$). Journal of Physics-Condensed Matter, 8(43), 8267-8275.

Ringwood, A.E. (1994) Role of the Transition Zone and 660 Km Discontinuity in Mantle Dynamics. Physics of the Earth and Planetary Interiors, 86(1-3), 5-24.

Rodi, F., and Babel, D. (1965) Ternare Oxide Der Ubergangsmetalle .4. Erdalkaliiridium(4)-Oxide - Kristallstruktur Von $CaIrO_3$. Zeitschrift Fur Anorganische Und Allgemeine Chemie, 336(1-2), 17.

Salje, E., and Smaston, M.F. (1989) Characteristics of Perovskite-Related Materials. Philosophical Transactions of the Royal Society of London Series a-Mathematical Physical and Engineering Sciences, 328(1599), 409-416.

Santillan, J., Shim, S.H., Shen, G.Y., and Prakapenka, V.B. (2006) High-pressure phase transition in Mn_2O_3: Application for the crystal structure and preferred orientation of the $CaIrO_3$ type. Geophysical Research Letters, 33(15), L15307(1-5).

Sidorin, I., Gurnis, M., and Helmberger, D.V. (1999) Evidence for a ubiquitous seismic discontinuity at the base of the mantle. Science, 286(5443), 1326-1331.

Tateno, S., Hirose, K., Sata, N., and Ohishi, Y. (2006) High-pressure behavior of $MnGeO_3$ and $CdGeO_3$ perovskites and the post-perovskite phase transition. Physics and Chemistry of Minerals, 32(10), 721-725. DOI:10.1007/s00269-005-0049-7.

Thomas, C., Wookey, J., and Simpson, M. (2007) D " anisotropy beneath Southeast Asia. Geophysical Research Letters, 34(4), L04301.

Thomas, N.W. (1996) The compositional dependence of octahedral tilting in orthorhombic and tetragonal perovskites. Acta Crystallographica Section B-Structural Science, 52, 16-31.

-. (1998) New global parameterization of perovskite structures. Acta Crystallographica Section B-Structural Science, 54, 585-599.

Vinnik, L., Kato, M., and Kawakatsu, H. (2001) Search for seismic discontinuities in the lower mantle. Geophysical Journal International, 147(1), 41-56.

Woodward, P., Hoffmann, R.D., and Sleight, A.W. (1994) Order-Disorder in $A_2M^{3+}M^{5+}O_6$ Perovskites. Journal of Materials Research, 9(8), 2118-2127.

Woodward, P.M. (1997) Octahedral tilting in perovskites .2. Structure stabilizing forces. Acta Crystallographica Section B-Structural Science, 53, 44-66.

Zhao, J., Ross, N.L., and Angel, R.J. (2004) Polyhedral control of the rhombohedral to cubic phase transition in $LaAlO_3$ perovskite. Journal of Physics-Condensed Matter, 16(47), 8763-8773.

Zhao, Y.S., Weidner, D.J., Parise, J.B., and Cox, D.E. (1993a) Critical Phenomena and Phase-Transition of Perovskite Data For $NaMgF_3$ Perovskite .2. Physics of the Earth and Planetary Interiors, 76(1-2), 17-34.

-. (1993b) Thermal-Expansion and Structural Distortion of Perovskite - Data For $NaMgF_3$ Perovskite .1. Physics of the Earth and Planetary Interiors, 76(1-2), 1-16.

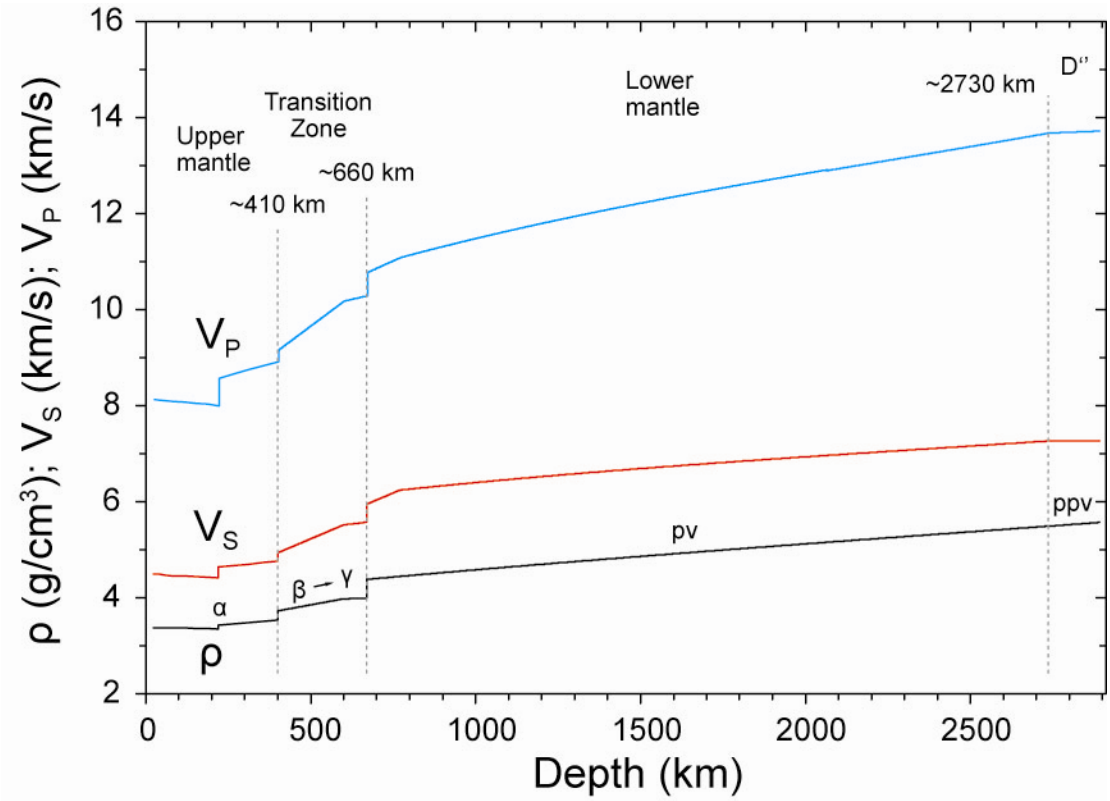

[Fig. 1.1] The density of, and seismic velocities within, the mantle are shown as a function of depth according to the Preliminary Reference Earth Model (Dziewonski and Anderson, 1981). Stable regions for α (olivine), β (Wadsleyite), γ (Ringwoodite), pv (perovskite), and ppv (post-perovskite) are indicated.

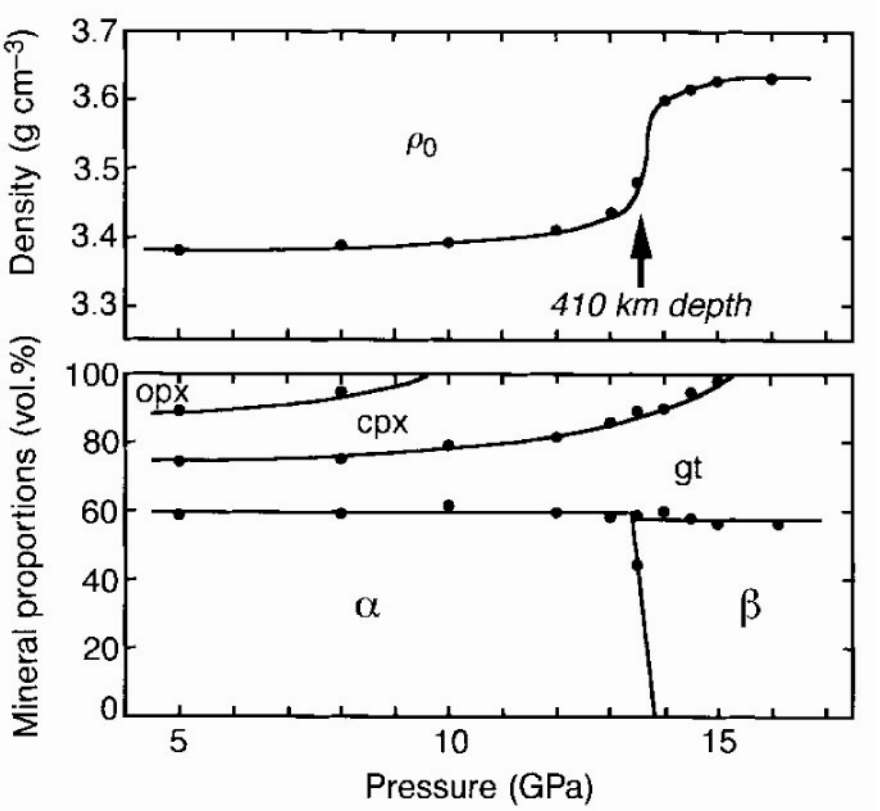

[Fig. 1.2] The equilibrium density increase of pyrolite as minerals and chemical species partition between crystalline phases with increasing pressure (Irifune and Isshiki, 1998).

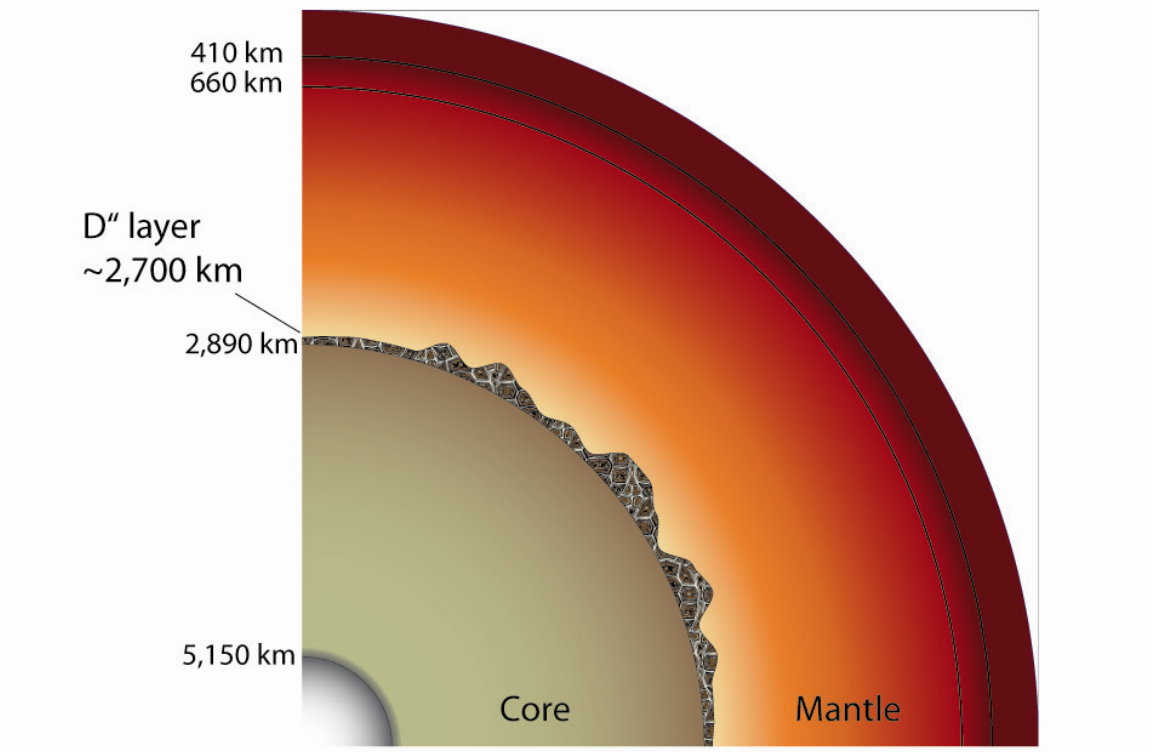

[Fig. 1.3] Author's/Artist's rendition of the Earth's interior with emphasis on location and topology of the D" layer.

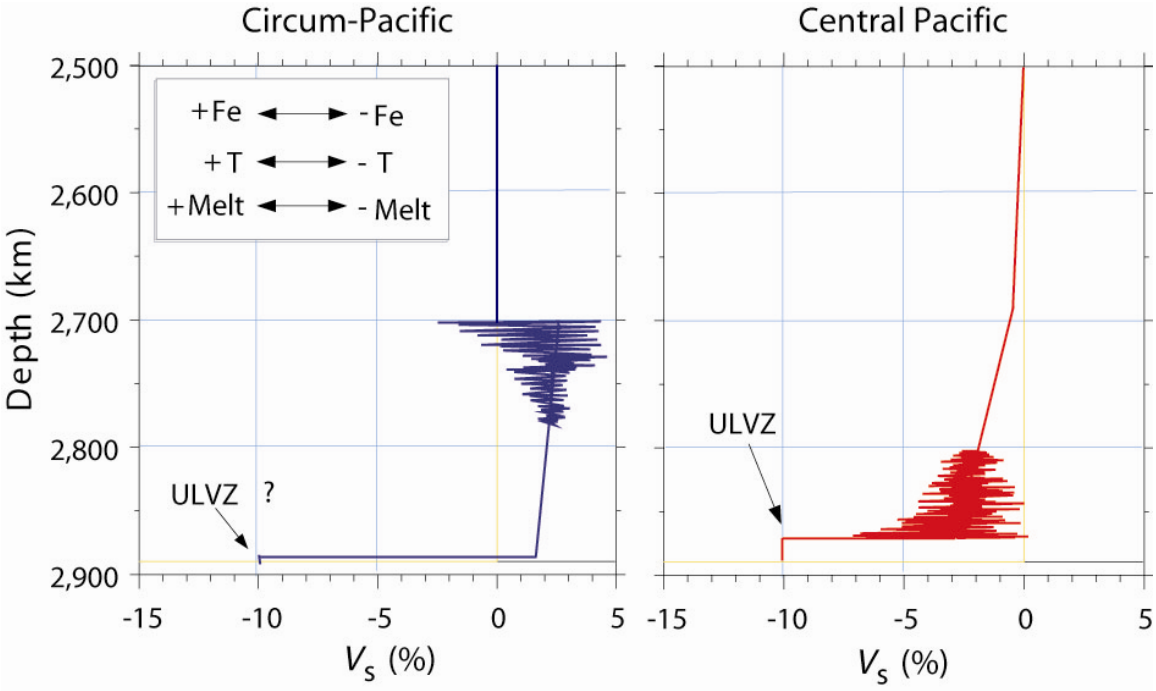

[Fig. 1.4] The main classes of D" shear-wave velocity structures. Schematic shear-wave velocity structures (shown as percent deviations (dVS) relative to a standard reference Earth model which has smoothly varying structure in the lower mantle) for circum-Pacific (left) and central Pacific (right) regions. The circum-Pacific regions under Alaska and the Caribbean are well characterized to have relatively abrupt shear velocity increases near 250 km above the CMB, with mild negative gradients throughout the D" layer. The blue model indicates that these high-velocity regions are relatively cold. These regions also have shearwave splitting consistent with transverse isotropy, which is represented here by thin horizontal lamellae of strongly varying material properties (possibly involving melt), concentrated near the depth of the discontinuity. Any ULVZ in these regions is so thin as to not be detectable in most cases, and it may not be present. The central Pacific region is characterized by strong negative gradients of shear velocity extending over 200–300 km above the CMB, with little evidence for any discontinuity. The red model indicates that these low-velocity regions are relatively hot. This region has a thick, pronounced ULVZ, with shear velocity decreases that are of the order of 5–30 %. There appears to be laterally variable general anisotropy, concentrated towards the base of the D" region (and possibly in the ULVZ as well). The sense of velocity perturbation with respect to increasing or decreasing Fe concentration, temperature (T) or partial melt is indicated by the inset box. Caption and figure taken from (Lay et al., 1998).

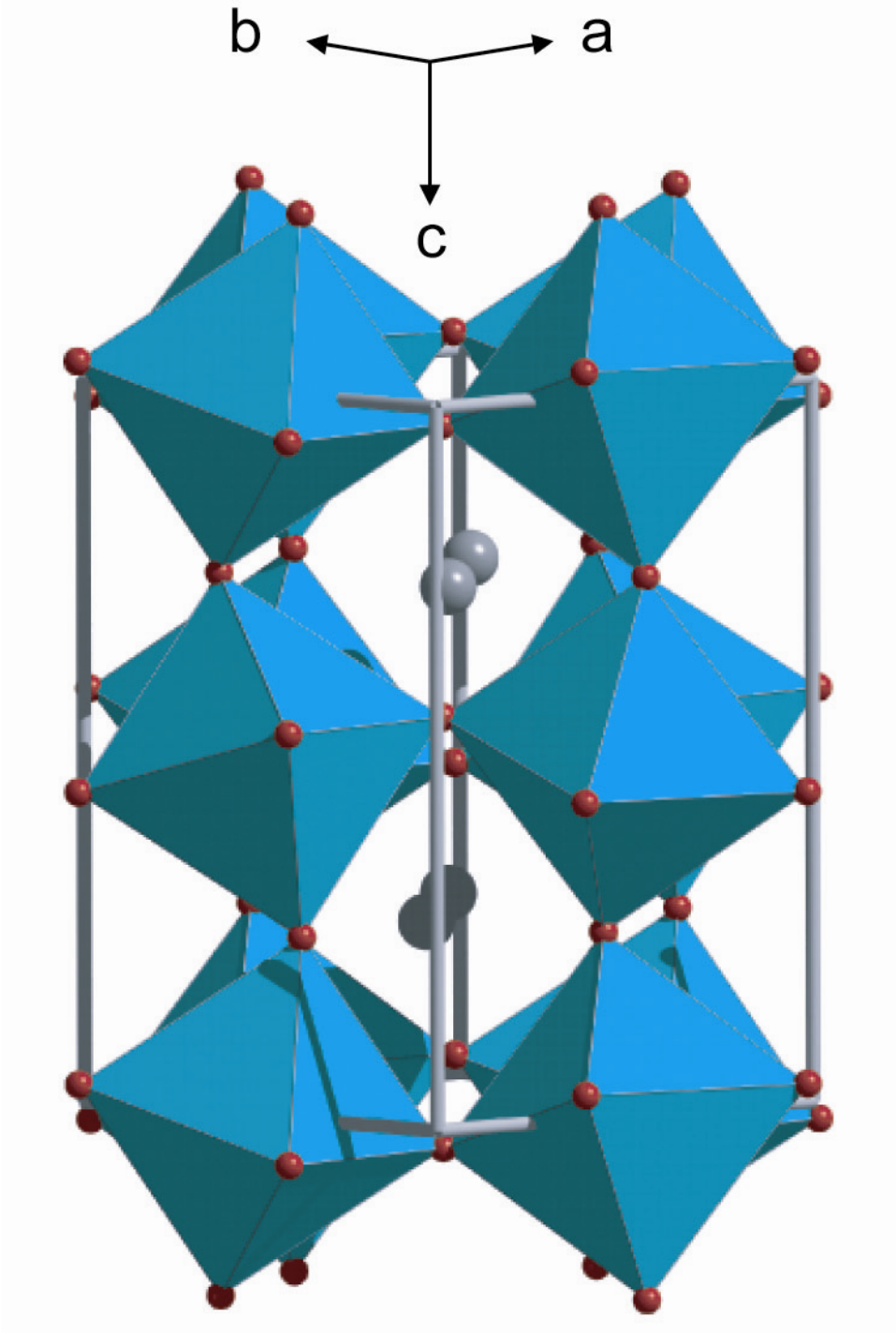

[Fig. 1.5] Polyhedral representation of the orthorhombic (*Pbnm*) perovskite structure. With stoichiometry ABX_3, A-site cations reside in the dodecahedron composed from eight B-site octahedra.

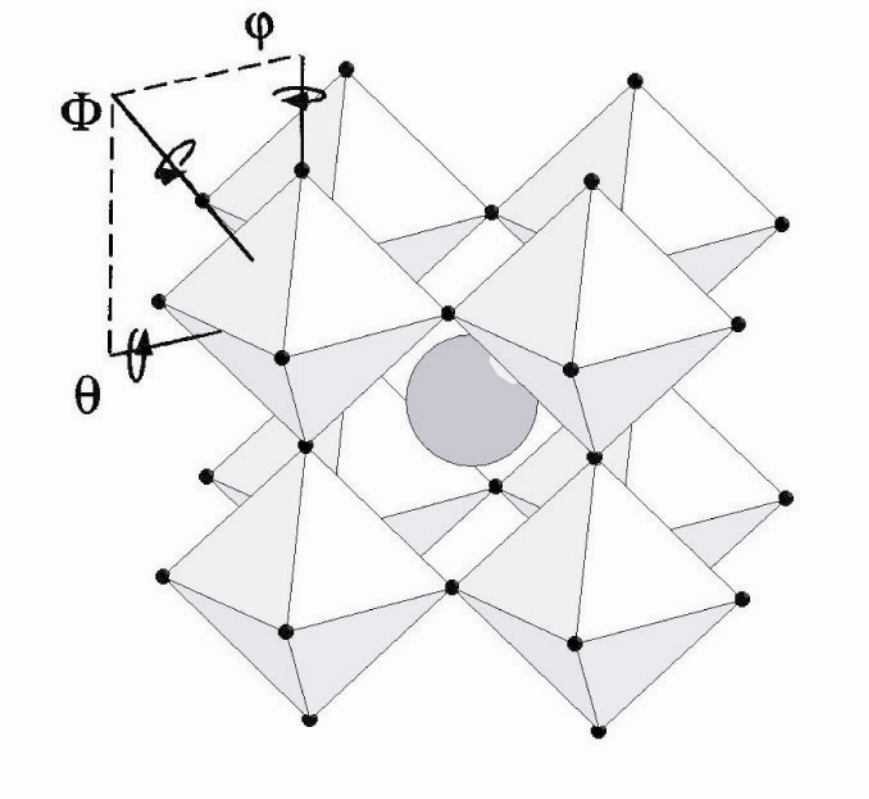

[Fig. 1.6] Tilting schemes of octahedra composing perovskite structures can be classified in terms of rotational components about pseudo-cubic axes. This figure is drawn to resemble that illustrated in Zhao et al. (1993a).

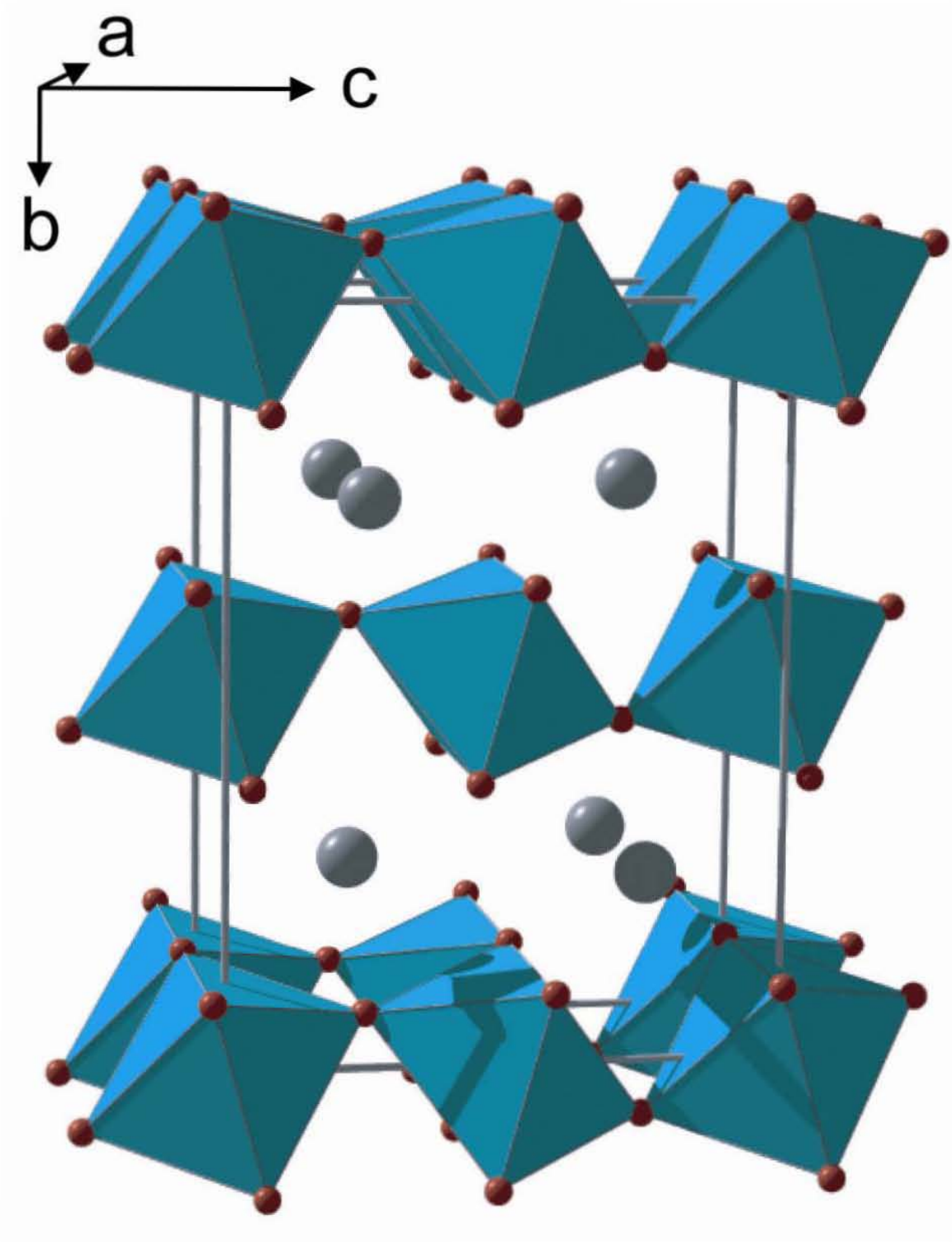

[Fig. 1.7] The orthorhombic (*Cmcm*) $CaIrO_3$-type post-perovskite structure. Octahedra share corners about [0 0 1] and edges about [1 0 0].

Chapter II

Details for Performance of Novel or Non-conventional Experiments Utilized in this Thesis

2.1. Introduction

The experiments presented in this thesis were performed almost exclusively using synchrotron-based monochromatic X-ray powder diffraction. Details on synchrotron X-ray facilities and how to perform a powder diffraction experiment are presented elsewhere. This chapter provides complementary information on performed experiments which may be considered novel or non-conventional. However, a brief definition of X-ray scattering is provided (Fig. 2.1).

2.2. Pair-distribution function analysis

When a material has periodic atomic order (crystallinity) on a scale comparable to the coherence length (~100·λ) of an incident monochromatic neutron or X-ray beam a structural model fit to the diffraction pattern will usually be a satisfactory approximation to the real arrangement of atoms in the crystal structure. However, when perfect periodic order does not occur in a crystal, a structural model fit to the diffraction pattern will usually not yield a satisfactory structure approximation. The latter case describes a typical structure study of a liquid, glass, nanocrystal, or a material which exhibits correlated atomic motion.

The pair distribution function describes the relative probability of finding a given atom distance between any two atoms in a material and is useful for characterizing the short-range structure of materials (Fig. 2.2). The pair distribution function is the Fourier transform of the structure function (see Chapter 4) normalized from the total scattered radiation by subtraction of background contributions, i.e. the sample holder, surrounding atmosphere, and diffractometer.

During a typical RA-PDF experiment (Chupas et al., 2003), the sample is placed within a thin-walled capillary and the background scattering contribution is isolated by duplicating the sample assembly without the sample in place. Because the intensity contribution from the sample holder is usually comparable to that from the sample, the great challenge of these experiments is collecting sufficient statistics in order to properly distinguish the sample contribution from the background (Fig. 2.3).

Using a thin-walled capillary to house the sample during experiments permits temperature manipulation when either a cold finger or resistive coil are used. However, high pressure equipment introduces additional background contributions. Studies of nanocrystalline gold in the diamond anvil cell find that the background contribution was ~5 times larger than that of the sample. Thus, studies of the pair-distribution function of Earth materials at high pressure are much more difficult and require some innovation.

Pair distribution function studies of materials under high pressure in the diamond anvil cell may reduce the Compton scattering contribution to the background by utilization of perforated diamond anvils (Fig. 2.4). While these diamond anvils dramatically reduce the background contribution to the total scattered intensity, this experimental configuration suffers from greatly reduced stability and the maximum pressure possible with any given culet size is reduced by almost a factor of ~6. For example, when the miniature anvil has a 350 μm culet face, it can only reach sample pressures of about 13 GPa before anvil breakage.

2.3. Laser-heated diamond anvil cell with X-ray powder diffraction

Laser heating samples *in situ* at high pressure within the diamond anvil cell with monochromatic X-ray powder diffraction is a very useful technique for studies of materials at extreme conditions. Many high pressure mineral phases were first discovered as a result of this technique (Liu, 1976), which allows collection of X-ray powder diffraction from a sample under simultaneous ultra high pressure and temperature conditions (Fig. 2.5). The synchrotron-based instrumentation used for this technique has been documented previously (Mezouar et al., 2005; Shen et al., 2005; Shen et al., 2001), and a brief introduction to the experiment is written here.

When using a YAG of YLF laser, a sample must be loaded in a diamond anvil cell with an insulating layer in order to heat. This layer must be transparent and is usually NaCl, MgO, or some other material of which the equation of state is well known so the sample pressure may be estimated with diffraction. If the sample is dark, it will absorb power from the infrared heating laser. If the sample is not dark an inert dark material must be mixed with the sample, such as platinum or pyrolytic graphite. It is important to keep in mind that the more materials added to the sample will reduce the signal from the sample and both insulating layer and laser absorber should be introduced very sparingly according to each specific experiment.

One may consider three types of laser heated diamond cell experiments and it is very important to distinguish which variant is required to complete experimental goals.

2.3.1. X-ray diffraction from samples quenched from simultaneous high pressure and temperature

When x-ray powder diffraction is desired from a high pressure phase and it is believed that the phase is pressure-quenchable (recoverable as a metastable phase to room pressure), the high pressure phase may be synthesized in the LDAC and recovered to ambient conditions where a simple Debye-Scherrer camera or synchrotron X-ray diffractometer may be used to collect diffraction from the sample. In this case, the sample must be completely rastered with the laser for a sufficient period to increase kenetics to drive the high pressure phase transition. The initial sample pressure may be estimated from diffraction from sample, absorber, or insulating layer. When *in situ* diffraction is not available, a ruby grain may be inserted on the gasket by the sample (beware ruby-sample chemical reaction) for a rough pressure estimate.

2.3.2. X-ray diffraction from samples at high pressures quenched from high temperature

When *in situ* X-ray diffraction is available, one can use laser annealing to relax differential stress in the sample at high pressure and then use diffraction from the sample at various pressures to determine pressure-based equation of state. In this case, it is important to realize that because of the geometry between x-ray diffraction and axis of

force in the diamond cell, if differential stress is not properly relaxed one will obtain a bulk modulus which is too large. Also, it is important to consider the x-ray beam may not be directly on the spot of the heating laser and this is difficult to identify if diffraction is not possible during laser heating. In this case it is important to move the x-ray beam relative to the sample between x-ray exposures and identify a position in the sample which has the sharpest diffraction features or a 'spotty' diffraction texture.

2.3.3. X-ray diffraction from samples at simultaneous high pressure and temperature

This is the most difficult type of LDAC work for both the technical staff and experimenter and should not be used or specified in a proposal unless it is absolutely required for the project. This is very difficult for the support staff because both the x-ray beam and heating laser must be absolutely stable. The diameter of the X-ray beam must be smaller than the diameter of the laser spot, ~10 and ~50 μm respectively. In addition, sample temperatures must be determined from the black-body radiation from the sample and the errors in this technique are on the order of 300-400 K. Thermal pressure from the sample is significant and the equation of state of the insulating layer cannot strictly be used to determine the pressure of the sample since it remains cold. Pressure must be determined from a material intimately mixed with the sample, such as the laser absorber (usually platinum).

References

Chupas, P.J., Qiu, X.Y., Hanson, J.C., Lee, P.L., Grey, C.P., and Billinge, S.J.L. (2003) Rapid-acquisition pair distribution function (RA-PDF) analysis. Journal of Applied Crystallography, 36, 1342-1347.

Liu, L.G. (1976) Orthorhombic Perovskite Phases Observed in Olivine, Pyroxene and Garnet At High-Pressures and Temperatures. Physics of the Earth and Planetary Interiors, 11(4), 289-298.

Mezouar, M., Crichton, W.A., Bauchau, S., Thurel, F., Witsch, H., Torrecillas, F., Blattmann, G., Marion, P., Dabin, Y., Chavanne, J., Hignette, O., Morawe, C., and Borel, C. (2005) Development of a new state-of-the-art beamline optimized for monochromatic single-crystal and powder X-ray diffraction under extreme conditions at the ESRF. Journal of Synchrotron Radiation, 12, 659-664.

Shen, G.Y., Prakapenka, V.B., Eng, P.J., Rivers, M.L., and Sutton, S.R. (2005) Facilities for high-pressure research with the diamond anvil cell at GSECARS. Journal of Synchrotron Radiation, 12, 642-649. DOI:10.1107/S0909049505022442.

Shen, G.Y., Rivers, M.L., Wang, Y.B., and Sutton, S.R. (2001) Laser heated diamond cell system at the Advanced Photon Source for in situ x-ray measurements at high pressure and temperature. Review of Scientific Instruments, 72(2), 1273-1282. DOI:10.1063/1.1343867.

$\mathbf{x}$ is a general position

$\mathbf{k} \bullet \mathbf{x}$ is 'phase angle'

$\psi(\mathbf{x}) = A \exp(i\mathbf{k} \bullet \mathbf{x})$

$\psi(\mathbf{x}) = A[\cos(\mathbf{k} \bullet \mathbf{x}) + i\sin(\mathbf{k} \bullet \mathbf{x})]$

$|\psi(\mathbf{r})|^2 = A^2$

$|\mathbf{k}| = k = 2\pi\lambda^{-1}$

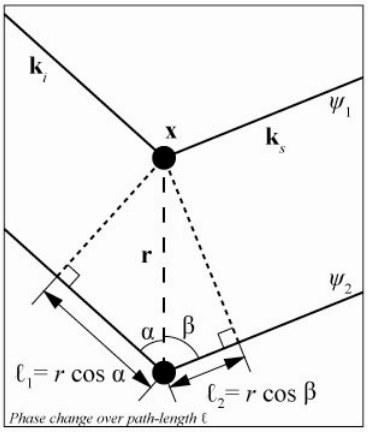

Phase change over path-length ℓ

$\mathbf{k}_i \bullet \mathbf{r} = |\mathbf{k}_i|\,|\mathbf{r}| \cos \alpha = 2\pi r\lambda^{-1} \cos \alpha = 2\pi \ell_1 \lambda^{-1}$

$\mathbf{k}_s \bullet \mathbf{r} = |\mathbf{k}_s|\,|\mathbf{r}| \cos (180 - \beta) = -2\pi r\lambda^{-1} \cos \beta = -2\pi \ell_2 \lambda^{-1}$

Total phase change:

$2\pi \ell_1 \lambda^{-1} + 2\pi \ell_2 \lambda^{-1} = (\mathbf{k}_i \bullet \mathbf{r}) - (\mathbf{k}_s \bullet \mathbf{r}) = (\mathbf{k}_i - \mathbf{k}_s) \bullet \mathbf{r}$

$\mathbf{Q} = \mathbf{k}_i - \mathbf{k}_s$

$\psi_1(\mathbf{x}) = \exp(i\mathbf{k}_s \bullet \mathbf{x})$

$\psi_2(\mathbf{x}) = \exp(i\mathbf{k}_s \bullet \mathbf{x}) \exp(i\mathbf{Q} \bullet \mathbf{r})$

Total scattering:

$\psi_1(\mathbf{x}) + \psi_2(\mathbf{x}) = \exp(i\mathbf{k}_s \bullet \mathbf{x})\,(1 + \exp(i\mathbf{Q} \bullet \mathbf{r}))$

Amplitude modified by:

$1 + \exp(i\mathbf{Q} \bullet \mathbf{r}) = F(\mathbf{Q})$

First atom's component Second atom's component

$|\mathbf{Q}|^2 = |\mathbf{k}_i - \mathbf{k}_i|^2 = k_i^2 + k_s^2 - 2\mathbf{k}_i \bullet \mathbf{k}_s$

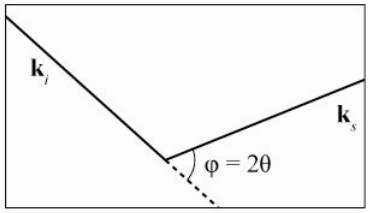

$\mathbf{k}_i \bullet \mathbf{k}_s = (2\pi\lambda^{-1})^2 \cos 2\theta$

$|\mathbf{Q}|^2 = 2(2\pi\lambda^{-1})^2 - 2(2\pi\lambda^{-1})^2 \cos 2\theta$

$= 8\pi^2\lambda^{-2}(1-\cos 2\theta) = 8\pi^2\lambda^{-2}(1 + (-1 + 2\sin^2 \theta))$

$= 16\pi^2\lambda^{-2}\sin^2 \theta$

$|\mathbf{Q}| = 4\pi\lambda^{-1}\sin \theta$

Bragg diffraction, special case where rays have equal glancing angles off lattice plane

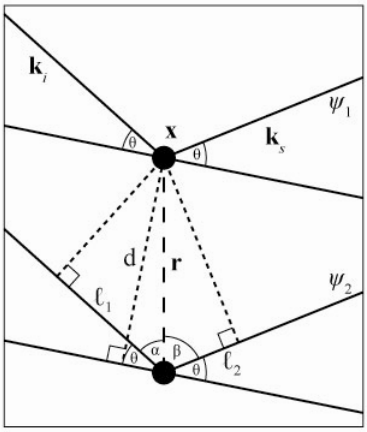

Total phase change = $n\lambda = \ell_1 + \ell_2 = r \cos \alpha + r \cos \beta$

$r = d\sin (\alpha + \theta)$

After much half, double, addition and subtraction angle formulas:

$n\lambda = 2d\sin \theta$

$\mathbf{Q} = 2\pi d^{-1}$

[Fig. 2.1] Derivation of scattering vector ($\mathbf{Q}$) and Bragg's law considering geometric relations.

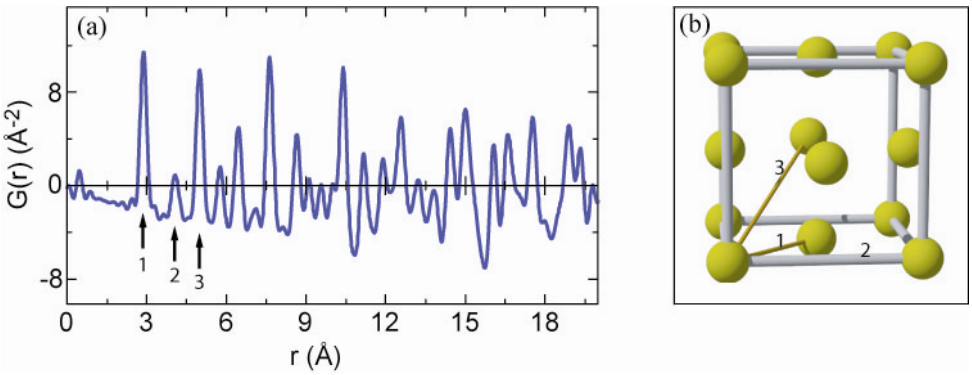

[Fig. 2.2] (a) Representative pair distribution function as G(r) with correlations (b) corresponding to the first three atom-atom distances in a material. This specific example shows nanocrystalline gold under high pressure and the usefulness of the technique to define structures lacking long-range order.

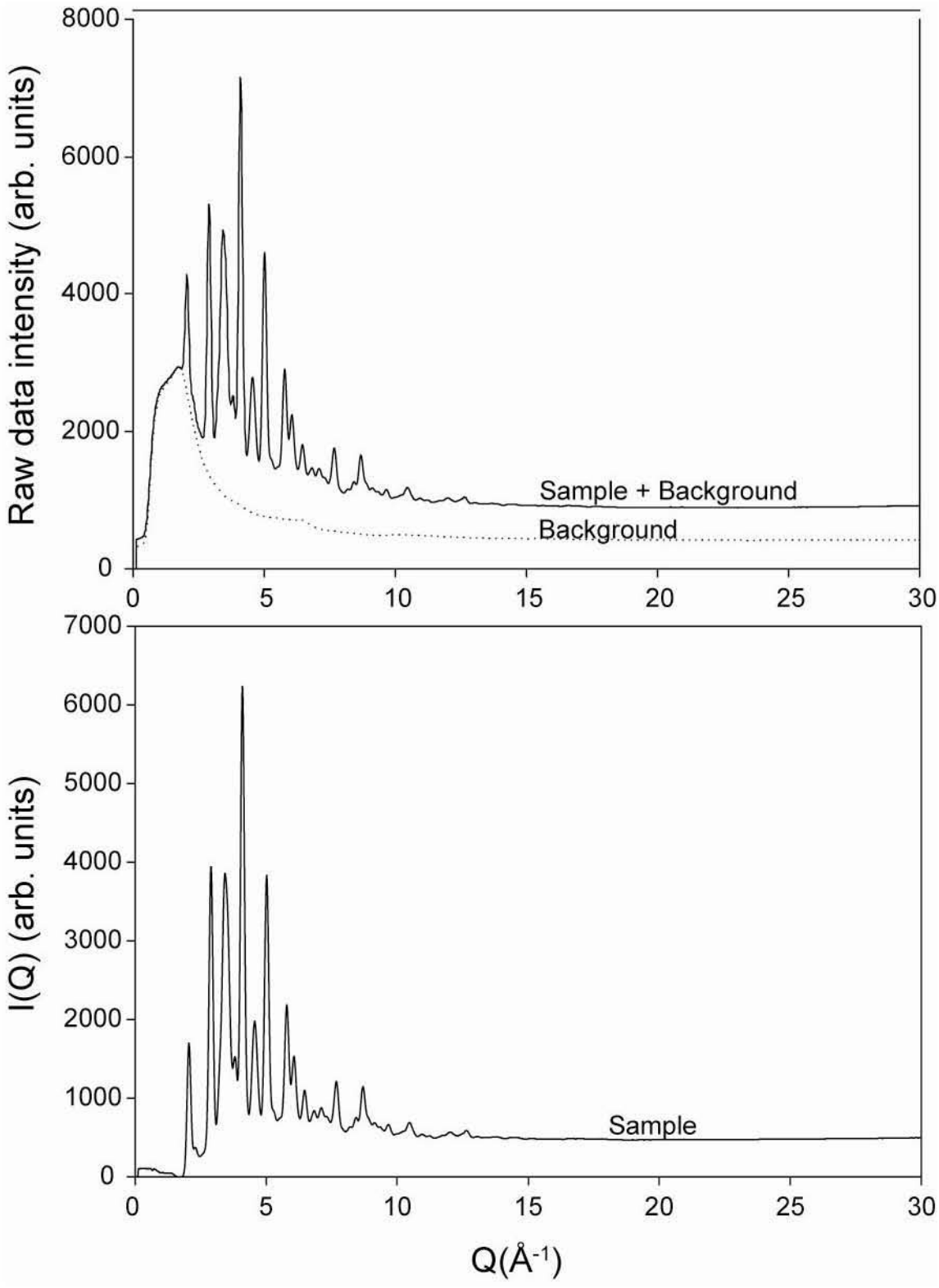

[Fig 2.3] Exemplary data collected using the RA-PDF technique. Plots (upper tier) shows a background spectra is required to isolate sample scattering (lower tier).

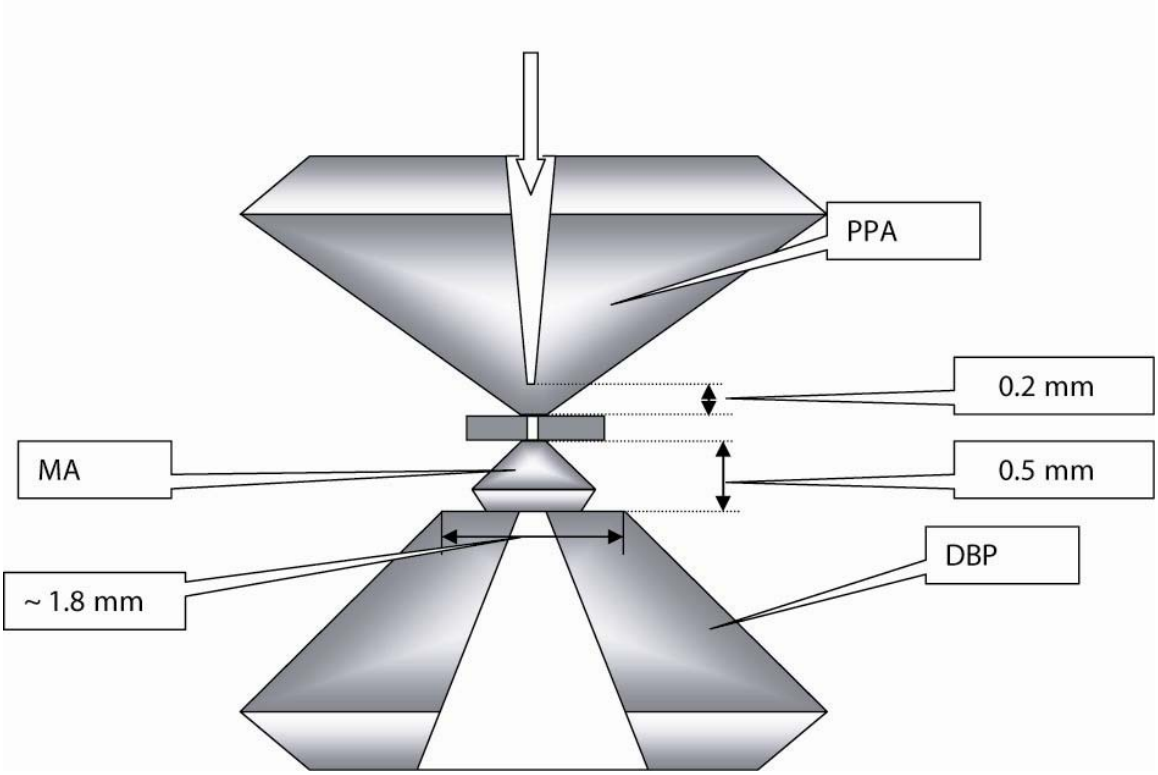

[Fig. 2.4] Schematic diagram showing 'perforated (DBP)' and 'partially-perforated (PPA)' diamond anvils which minimize the volume (length shown here) of diamond in the beam path. A miniature anvil (MA) is required in order to introduce a polished diamond surface and optical access to the sample. Figure provided by D'Anvils Ltd.

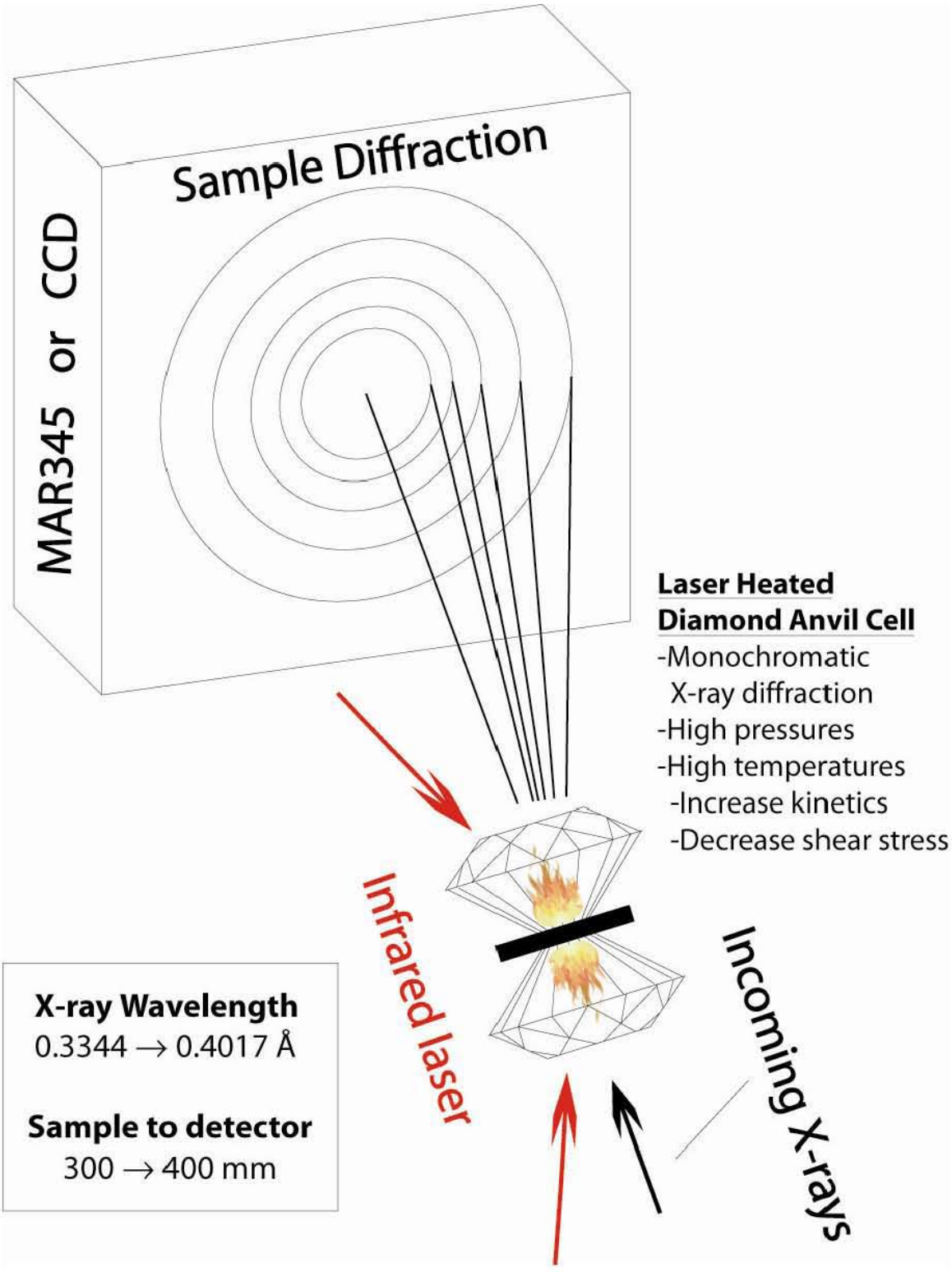

[Fig. 2.5] Schematic diagram of a laser heated diamond anvil cell experiment.

Chapter III

Effect of A-site cation radius on ordering of BX_6 octahedra in (K,Na)MgF_3 perovskite

THIS CHAPTER PUBLISHED AS:

MARTIN, C.D., CHAUDHURI, S., GREY, C.P., AND PARISE, J.B. (2005) EFFECT OF A-SITE CATION RADIUS ON ORDERING OF BX_6 OCTAHEDRA IN (K,NA)MGF_3 PEROVSKITE. AMERICAN MINERALOGIST, 90(10), 1522-1533.

3.1. Abstract

In this chapter we present a structural model for (K,Na)MgF_3 perovskite using results from high-resolution synchrotron X-ray powder diffraction and nuclear magnetic resonance (NMR) spectroscopy. (K,Na)MgF_3 perovskite is found to transition from orthorhombic (***P****bnm*) to tetragonal (***P****4/mbm*) to cubic (***Pm*** $\bar{3}$ *m*) as potassium concentration is increased. These phase transitions are not accompanied by a discontinuity in pseudo-cubic unit-cell volume and occur close to compositions ($K_{0.37}$,$Na_{0.63}$)MgF_3 and ($K_{0.47}$,$Na_{0.53}$)MgF_3, respectively. ^{19}F-NMR spectra indicate that the Na^+ and K^+ cations do not occupy the A cation site at random and endmember environments are favored in all compositions. Based on results from both X-ray diffraction and NMR, we propose that diffuse diffraction is the result of strain between coexisting regions of different octahedra (MgF_6) tilts brought about by the ionic radius mismatch of Na^+ and K^+ cations. We suggest A-site cations group with like-cations as neighbors to reduce excess volume and total strain.

3.2. Introduction

Changes in seismic velocities marking discontinuities in Earth's lower mantle (Dziewonski and Anderson, 1981; Lay et al., 1998; Liu et al., 1998; Sidorin et al.,

1999; Su and Dziewonski, 1997; Vinnik et al., 2001) are only partially understood in a mineralogical context. Alternative to chemical stratification (Kellogg et al., 1999; van der Hilst and Karason, 1999) and magnetic collapse (Cohen et al., 1997; Guo et al., 2002), these discontinuities may result from structural phase transitions in lower mantle minerals. With the transition of upper mantle garnet and spinel below 660 km (~ 22 GPa, 1700 °C), the Earth's lower mantle is expected to be dominated by (Mg,Fe)O and $(Mg,Ca,Fe,Al)(Al,Si)O_3$ perovskite (Brodholt, 2000; Liu, 1976; Liu and Ringwood, 1975; Zhang and Weidner, 1999). Since Liu and Ringwood (1975), many studies have applied extreme conditions and/or molecular dynamics simulations to investigate the structure of silicate perovskite under lower mantle conditions (Hemley et al., 2000; Ito et al., 1984; Knittle and Jeanloz, 1991; Knittle et al., 1986; Matsui and Price, 1991; Shim et al., 2001; Shim and Jeanloz, 2002; Wolf and Bukowinski, 1987; Zhou et al., 1998). Yet, literature remains divided upon the stability and existence of structural phase transitions in silicate perovskite (Dubrovinsky et al., 1999; Hemley et al., 2000; Meade et al., 1995; Saxena et al., 1998; Serghiou et al., 1998; Shim et al., 2001) and recently a post-perovskite phase has been proposed (Murakami et al., 2004).

The controversy results from the great difficulty and large errors in pressure and temperautre (Dubrovinsky et al., 1999) introduced when generating lower mantle conditions within the laboratory. One way to circumvent this difficulty, and those caused by the metastability of silicate perovskite (Knittle et al., 1986; Wang et al., 1990), is the study of materials with analogous structure and higher compressibility. Thus, analogs work as a proxy, providing an opportunity to examine structural modifications that are difficult to attain with $(Mg,Ca,Fe)SiO_3 + Al_2O_3$ perovskite (Redfern, 1996; Ringwood and Major, 1967; Wang et al., 1992; Zhao et al., 1993b), or post-perovskite.

Neighborite ($NaMgF_3$) is isostructural and isoelectronic to $MgSiO_3$ (Chao et al., 1961; O'Keeffe and Bovin, 1979), making it an ideal analog. $MgSiO_3$ and $NaMgF_3$ contain ions with similar radius ratios (A>B>X) and a 1:2 electronic charge ratio for both anion and cations. The flexible bonding of fluoride perovskite permits simulation of ultra-high pressure and temperature conditions on silicate perovskites at much lower conditions (O'Keeffe et al., 1979).

In the perovskite structure, variables such as pressure, temperature and partial ion substitution commonly drive structural changes (Brodholt, 2000; Salje, 1992; Woodward et al., 2000; Woodward et al., 1999; Woodward et al., 1998; Zhang and Weidner, 1999). Understanding how structural phase transitions affect acoustic waves and elastic moduli is of particular interest in understanding observations in the deep Earth. While the study of $(K,Na)MgF_3$ provides an understanding of perovskite structure, the effects of substitution must be very well characterized prior to measurement of elastic properties.

3.2.1. Structure

Simple stoichiometric compounds crystallizing with the perovskite structure have the composition ABX_3, where BX_6 octahedra form a framework by corner-sharing each X ion. The A-site cations sit in an often distorted dodecahedron formed by eight octahedra. Cubic perovskite structures commonly exist in space group $\boldsymbol{P}m\bar{3}m$, where octahedrons do not tilt (Fig. 3.1). This is the aristotype perovskite structure. However in many instances the A-site cation is not large enough to completely fill the 12-fold site. In this case, octahedra collapse into the 12-fold site, producing a measure of distortion between neighboring octahedra that breaks symmetry elements of cubic phase (Fig. 3.2). In the case of Neighborite, the structure is orthorhombic (***P****bnm*) and sodium has 4 bonds to fluorine atoms.

Phase transitions in perovskites often result from tilting of BX_6 octahedra and are commonly second-order with respect to free-energy. When octahedra tilt (B-X-B < 180˚), a superstructure is created, and additional X-ray reflections appear. Commonly, the appearances of superstructure reflections are observed well in advance of splitting of cubic substructure reflections (Woodward et al., 1994). These phase transitions are typically driven by pressure and temperature, however in the case of $(K,Na)MgF_3$, the ionic radii difference between sodium and potassium drives the transition.

3.2.2. Previous Work

Previous work has developed multiple systems of nomenclature to classify tilting in perovskite octahedra. Among these, that developed by Glazer (Glazer, 1972;

Glazer, 1975) is best known. Glazer (1975) notation adopts a pseudo-cubic multiple cell ($2a_p$ x $2b_p$ x $2c_p$) to universally classify tilting of BX_6 octahedra in each perovskite. Three letters a, b, or c indicate tilt magnitude about axes, while a superscript after each letter indicates in-phase (+), anti-phase (-) (Fig. 3.3), or absence of tilting octahedra (0) along the particular axis. For example, aristotype perovskite $KMgF_3$ ($\boldsymbol{Pm\bar{3}m}$) has notation $a^0a^0a^0$, while perovskite $NaMgF_3$ (***Pbnm***) is noted $a^-a^-c^+$ (octahedra are tilted anti-phase equally about the pseudo-cubic [100] and [010] directions while in-phase about the [001] axis).

Another system (O'Keeffe and Hyde, 1977; Zhao et al., 1993a) quantifies tilt of octahedra as a function of rotation about the pseudo-cubic axes, where tilt may be expressed in terms of two rotations—one 'φ' about [001] and another 'θ' about [110], or just one rotation about [111], 'Φ' (Fig. 3.4). Previous work by Aleksandrov (Aleksandrov, 1976; Aleksandrov, 1978) uses a similar approach to discuss mode-softening with progressive perovskite phase transitions and organizes a phonon-pathway map detailing typical phase transition routes.

The perovskites $KMgF_3$, $NaMgF_3$, and $(K,Na)MgF_3$ have been studied in detail and several points of disagreement emerge (Bonamour et al., 1991; Chadwick et al., 1983; Chakhmouradian et al., 2001; Chao et al., 1961; Kaliaperumal and Sears, 1988; O'Keeffe and Bovin, 1979; Smith et al., 2000; Wood et al., 2002; Yoshiasa et al., 2003; Zhao, 1998; Zhao et al., 1994a; Zhao et al., 1994b; Zhao et al., 1993a; Zhao et al., 1993b). Early X-ray diffraction reports of $NaMgF_3$ and $(K,Na)MgF_3$ conflict. One controversy centered on whether $NaMgF_3$ transforms to a tetragonal phase before changing to a cubic phase at high temperature. Similarly, another controversy involves several conflicting reports of the occurrence of a tetragonal phase in $(K,Na)MgF_3$ at room temperature.

$NaMgF_3$, as first characterized by Chao et al. (Chao et al., 1961), is orthorhombic (***Pbnm***). Using in-house high temperature X-ray diffraction, Chao reported that $NaMgF_3$ transforms to a "pseudo-tetragonal phase" at 760˚C, then to Cubic ($\boldsymbol{Pm\bar{3}m}$) at 900˚C. More recent structural studies of $NaMgF_3$ at room and elevated pressure and temperature (Zhao et al., 1994a; Zhao et al., 1994b; Zhao et al.,

1993a; Zhao et al., 1993b), show $NaMgF_3$ transforms directly from orthorhombic to cubic symmetry at all pressure and temperature conditions via a second-order phase transition (765˚C at zero pressure). As temperature increases, rotation of octahedra is found to diminish (Zhao et al., 1993b). Cubic ($\boldsymbol{Pm}\,\bar{3}\,m$) perovskite $KMgF_3$ demonstrates stability with high compressibility and has not been found to undergo any phase transitions at any temperature or pressure, suggesting it may be used as an internal X-ray calibrant (Wood et al., 2002).

Initial work on the $(K,Na)MgF_3$ system (Zhao, 1998), using monochromatic synchrotron X-ray powder diffraction with Rietveld refinement, reports an orthorhombic (***P****bnm*) and tetragonal (***P***4/*mbm*) phase coexistence between $(K_{0.5},Na_{0.95})MgF_3$ and $(K_{0.30},Na_{0.70})MgF_3$, which aids in explanation of "diffuse" X-ray diffraction from sodium-rich $(K,Na)MgF_3$ samples. The tetragonal phase fraction is found to increase with potassium content—ending with pure tetragonal at $(K_{0.35},Na_{0.65})MgF_3$. In addition, Zhao reports a high temperature region of pure tetragonal phase in these compositions before a transition to cubic symmetry. Meanwhile, $(K,Na)MgF_3$ samples are cubic at room temperature when potassium content is greater than $(K_{.35},Na_{.65})MgF_3$ and no volume discontinuity is reported anywhere in T-X space.

A later study by Smith et al. (2000) reports molecular dynamics simulations, differential thermal analysis (DTA), and differential scanning calorimetry (DSC) on $(K,Na)MgF_3$ samples. Smith et al. (2000) calculates the presence of a tetragonal phase in $(K,Na)MgF_3$ samples and verifies a similar phase diagram to that found experimentally by Zhao (1998). Yet no DTA signal is observed to correspond with the orthorhombic to tetragonal phase transition in samples with a potassium concentration greater than $(K_{0.04},Na_{0.96})MgF_3$, while the tetragonal to cubic phase transition is clearly observed with DTA in this composition range. The authors attribute this discrepancy to the potassium substitution reducing the latent heat required for the phase transition. The DTA signal marking the tetragonal to cubic phase transition is found to decrease in intensity with increasing potassium content, and is not observed in samples with a potassium concentration greater than $(K_{0.28},Na_{0.72})MgF_3$. X-ray diffraction in Smith et al. (2000) does not address the possibility of coexisting phases in $(K,Na)MgF_3$ samples,

although a coexistence of orthorhombic and tetragonal, or tetragonal and cubic, phases would likely explain the observed reduction in latent heat required to drive a complete orthorhombic to tetragonal, or tetragonal to cubic, phase transition.

A third study, utilizing room temperature X-ray and neutron powder diffraction with Rietveld refinement, finds no evidence for the coexistence of tetragonal and orthorhombic phases (Chakhmouradian et al., 2001). The authors, with reference to fitting both tetragonal and orthorhombic phases in a single Rietveld refinement, suggest that "'fitting' of composite two-phase peaks into the observed diffraction lines may not be a valid procedure for two topologically and dimensionally similar structures, although such an approach does produce statistically 'improved' results". Thus, the authors conclude that the solid solution is pure orthorhombic when the potassium concentration is less than $(K_{0.37},Na_{0.63})MgF_3$ and find that a pure tetragonal region exists between $(K_{0.37},Na_{0.63})MgF_3$ and $(K_{0.48},Na_{0.65})MgF_3$, while samples with greater potassium concentration are cubic. This study reports that samples at intermediate compositions exhibit random occupancy of A-site cations.

The fourth and most recent study using in-house high temperature X-ray powder diffraction with Rietveld refinement, finds no evidence for a tetragonal phase anywhere in T-X space (Yoshiasa et al., 2003). This work finds that all samples transform directly from orthorhombic to cubic with decreasing critical temperatures as potassium content increases. The critical composition is found to be $(K_{0.22},Na_{0.88})MgF_3$ at room temperature. Yoshiasa et al (2003) does not cite previous work on the solid solution so perhaps $(K,Na)MgF_3$ samples with weak superstructure reflections were missed with an in-house X-ray source, where peak-to-background discrimination may be insufficient to distinguish reflections indicative of subtle changes in perovskite symmetry.

The controversy between these four recent studies illustrates the necessity for a new approach to study $(K,Na)MgF_3$ perovskite. While X-ray diffraction is an excellent probe for long-range order, Nuclear Magnetic Resonance (NMR) is ideal for examining local structure. The utilization of both methods together should provide a more complete structural understanding of order-disorder in both A-site cations and MgF_6 octahedra. NMR has previously been applied to perovskite solid solutions (Choy et al., 2001; Hoatson et al., 2002) and quenched samples of $MgSiO_3$ (George and Stebbins,

1998; Kirkpatrick et al., 1991; Stebbins and Kanzaki, 1991; Stebbins et al., 2003; Stebbins et al., 2001). Individually, the endmember perovskites have been examined for characterization of fluorine chemical shielding environment (Aleksandrova and Beznosikov, 1968; Kaliaperumal and Sears, 1988), ferroelectricity at very low temperatures (Bonamour et al., 1991), and to demonstrate a lack of fluoride ion motion at close to ambient temperatures (Chadwick et al., 1983).

In this study we apply high-resolution synchrotron X-ray diffraction and Nuclear Magnetic Resonance (NMR) spectroscopy on (K,Na)MgF_3 samples to probe short and long-range order. Also, we introduce the topic of structure alterations caused by sample annealing and offer possible explanations for contradictions between previous studies.

3.3. Experimental methods

3.3.1. Sample Synthesis

Three different synthesis regimes were employed on identical compositions in order to examine possible structural changes caused by synthesis technique alone. Two of these methods model procedures described previously, while a 3rd is unique. All three methods include the following:

In a procedure modeled after Zhao (1998), Smith et al. (2000), and Chakhmouradian et al. (2001), later referred to as "type 1", $(K_x,Na_{1-x})MgF_3$ samples x/100 = {0, 8, 15, 22, 30, 35, 40, 45, 50, 55, 60, 70, 80, 90} were mixed from Puratronic NaF, MgF_2, and KF reactants, weighed to stoichiometric proportion and ground in a Diamondite mortar and pestle. To eliminate errors in stoichiometry originating from the hygroscopic nature of reactant KF, all weighing, grinding, and subsequent regrinding were completed in a dry nitrogen atmosphere. Samples were prepared in large 5 gram batches to minimize small errors caused by loss of reactants to mortar and crucible walls. Mixtures were synthesized in air for two 5 hour periods at 1023 K. Samples were thoroughly ground for 45 minutes before and after the first firing. Each firing was performed in a platinum crucible and samples were quenched to room temperature. A small amount of MgO and NaF is occasionally produced in each sample, the amount determined by Rietveld analysis is less than 1 mole percent. It is

useful to note Chakhmouradian et al. (2001) finds no significant difference between samples fired in air and samples fired in N_2 flow.

The following procedure is modeled after techniques used by Yoshiasa et al. (2003) and will be referred to as "type 2". A single type 1 sample of composition $(K_x,Na_{1-x})MgF_3$, x= .22 (the composition at which a direct orthorhombic to cubic phase transition was previously reported) was pressed into a pellet and fired for 24 hours under pure nitrogen atmosphere before being quenched to room temperature and ground in open air. This procedure was repeated 4 times.

Samples that will be referred to as "type 3" were synthesized by loading type 1 samples of composition $(K_x,Na_{1-x})MgF_3$, x/100= {15, 22, 30, 35, 40} into gold tubes (3 cm long / 0.5 cm in diameter) and sealed. Gold tubes were then placed in evacuated silica tubes before being annealed at 1023 K for 30 days. Samples were removed from the oven and allowed to cool to room temperature in air; this was estimated to take 20 minutes within the gold and glass tubes.

3.3.2. X-ray Diffraction

High-resolution monochromatic X-ray powder diffraction data were collected at the National Synchrotron Light Source at Brookhaven National Laboratory, Upton, NY. Room temperature data were collected at beamline X3B1 using a wavelength of 1.15072(5) Å and a Ge 111 analyzer crystal. Sample powders of type 1 were mounted on flat quartz plates and data were collected at compositions where x/100 = (0, 8, 15, 22, 30, 35, 40, 45, 50, 55, 60, 70, 80, 90). Scans were collected between 16° and 70° 2θ, in steps of 0.007° in 2θ with a 1 second count time.

Room- and variable temperature X-ray powder diffraction patterns were collected at Beamline X7A. A wavelength of 0.70470(2) Å was used with a linear position-sensitive detector that has a spatial resolution of less than 50 microns (Cox et al., 1988). Samples of 'type 1, 2, and 3' were loaded in 0.2 mm diameter quartz capillaries, which were either rocked by 10° or rotated completely to ensure powder averaging. Scans were collected between 10° and 40° 2θ, in steps of 0.025° 2θ with a 30 second count time while data were averaged over a 3° 2θ detector-window.

X-ray diffraction patterns were modeled with full-profile Rietveld refinement using programs EXPGUI for GSAS (Larson and Von Dreele, 2000; Toby, 2001) and FullProf (Rodriguez-Carvajal, 1990). X-ray peak-shapes were fitted using a Pseudo-Voigt profile function (Thompson et al., 1987) and background was fit using a 3^{rd}-6^{th} order polynomial in GSAS, while an interpolation between 10-20 selected points was used to fit background in FullProf.

3.3.3. Nuclear Magnetic Resonance (NMR) Spectroscopy

(NMR performed by Santanu Chadhuri)

A wide range of samples were investigated by NMR to probe the local structure in the region of the phase diagram where the largest structural changes are occurring. ^{23}Na and ^{19}F NMR spectra of type 1 samples were acquired using a 8.45T magnet, a CMX360 and a 3.2mm double resonance Magic Angle Spinning (MAS) Chemagnetics pencil probe spinning at 16 - 22 kHz under MAS conditions. This probe is equipped with zirconia rotors. Additional ^{19}F spectra were collected at 42 kHz in a probe built by A. Samoson and coworkers which uses 2 mm sapphire rotors. A $\pi/2$ pulse length of 3.8μs and 20s pulse delays were used for the experiments, while a shorter pulse length of 1μs was used for ^{23}Na. Liquid $CFCl_3$ (δ= 0 ppm) was used as the external chemical shift standard. One-pulse and Hahn-echo experiments were performed. The two NMR active nuclei, spin-1/2 ^{19}F and spin-3/2 (quadrupolar) ^{23}Na, are both close to 100% natural abundance and resonate at 338 and 94 MHz, respectively at the field strengths used in the experiments.

Two-dimensional ^{19}F exchange spectroscopy was performed on type 1 samples of composition x= {0.3, 0.7} to explore the proximity between different fluorine local environments. A modified "back-to-back" BABA sequence (Feike et al., 1996) was used to generate double quantum (DQ) coherences. The experiment was carried out using a Bruker™ Avance 600 MHz system with a MAS probe fitted with 2.5 mm diameter zirconia rotors spinning at 25 kHz. The pulse sequence comprises a composite sequence of $90^o_x90^o_y$ pulses repeated N-rotor periods in the excitation period. The DQ coherences are allowed to evolve in the evolution period before reconversion to zero coherence with the same composite sequence of $90^o_x90^o_y$ pulses, where a phase shift is

applied to the pulses used in the reconversion period to select for DQ coherences in the evolution period. A time delay period was used to remove unwanted coherences, before the final $\pi/2$ detection pulse was applied. Excitation (and reconversion) times of either four (0.16 ms) or 16 rotor periods (0.64 ms) were used. A sweep width of 50 kHz (96 data points) was collected in the DQ dimension by incrementing the evolution period in steps of one-rotor period (40μs), for each 1D experiment. Data was collected over a period ranging from 1-2 days per sample.

3.4. Results and discussion

3.4.1. Synthesis

To assist future studies of (K,Na)MgF_3 perovskite, it is important to note that when samples (including end-members) are fired for extended periods (over ~24 hours), even in pure N_2 atmosphere, a decomposition reaction occurs on the sample surface. In an open atmosphere, this reaction includes the production of MgO powder. A similar decomposition occurs when samples are prepared in a pure N_2 atmosphere and corrodes the SiO_2 chamber walls containing the inert gas. The process is assisted if synthesis temperatures exceed 1073 K, but may be eliminated by welding samples in an inert container, such as a small gold tube.

3.4.2. X-ray diffraction

X-ray diffraction of type 1 (Na,K)MgF_3 samples at room temperature confirm the solubility of potassium in Neighborite. The larger ionic radius of potassium increases the pseudo-cubic unit cell volume of $NaMgF_3$ by 12% at complete substitution (Table 3.1). This increase is not entirely uniform and is associated with different trends on either side of the solid solution: the increase is linear in the sodium-rich region and curved in the potassium-rich (Fig. 3.5a). Pseudo-cubic lattice parameters increase uniformly until $(K_{0.22},Na_{0.78})MgF_3$, where the lattice parameter *a* increases abruptly to values closer to *c* and *b* (Fig. 3.5b). The separation of linear and curved trend in the (Na,K)MgF_3 system is a direct result of the freedom of tilt in MgF_6 octahedra allowed by space group symmetry. Thus, orthorhombic and tetragonal compositions appear more sensitive to potassium concentration by increasing pseudo-

cubic unit-cell parameters more rapidly. In addition, all compositions exhibit an excess unit cell volume when juxtaposed on a straight line between endmember volumes (Vegard's Rule). Although deviations from Vegard's Rule are not uncommon (i.e. olivine, magnetite-ulvospinel, and feldspars), it is important to note here. The reason for this volume excess is discussed later.

Consistent with the work of Zhao (1998), Chakhmouradian (2001), and Smith (2000), potassium substitution is found to increase orthorhombic (***P****bnm*) unit cell lengths in (K,Na)MgF_3 samples (Fig. 3.6) and reduce rotation of octahedra about the pseudo-cubic [111] axis (Fig. 3.7). This tilt, calculated from unit cell lengths, has been corrected for distortion in octahedra using methods described elsewhere (Zhao et al., 1993b).

Annealed (K,Na)MgF_3 compositions show an increase in unit cell volume (Table 3.2) and decrease in MgF_6 tilting. The most dramatic instance is found in composition ($K_{0.15}$,$Na_{0.85}$)MgF_3 comparing type 1 and type 3 preparations (Fig. 3.8).

X-ray diffraction patterns of (K,Na)MgF_3 samples at intermediate compositions do not exhibit reflections characteristic of unit-cell-doubling, indicating occupancies of A-site cations are not ordered over a long enough range to give rise to diffraction features. In addition, the peak full-width at half-maximum (FWHM) for all X-ray reflections broaden between endmembers. This observation is also reported by Zhao (1998) and Chakhmouradian et al. (2001). The increase in FWHM is most pronounced in reflections from superstructure, suggesting that octahedra exist in multiple tilting states within the sample. Due to the very broad and weak nature of diffraction from perovskite superstructure, features might be missed without data exhibiting an excellent peak-to-background ratio. This possibility may explain the result of Yoshiasa et al. (2003), where laboratory X-ray diffraction indicates a direct orthorhombic to cubic phase transition at ($K_{0.22}$,$Na_{0.78}$)MgF_3.

With respect to observations of weak superstructure reflections indicative of tetragonal symmetry, we observe a tetragonal (***P***4/*mbm*) phase in the X-ray diffraction patterns between ($K_{0.37}$,$Na_{0.63}$)MgF_3 and ($K_{0.47}$,$Na_{0.53}$)MgF_3, confirming the previous boundary assignment of (Chakhmouradian et al., 2001). The best indication of the phase boundary is the disappearance of superstructure reflections, rather than

convergence of otherwise near-identical unit cell lengths. The disappearance of the orthorhombic superstructure triplet, (121/103/211) marks the orthorhombic/tetragonal (O/T) boundary, while the tetragonal (210) and (211) reflections are forbidden in the cubic region—a more detailed discussion of critical criteria can be found elsewhere (Zhao et al., 1993a). It is again important to note that tetragonal superstructure peaks are broad and weak and although much reduced, these peaks are still faintly detected as far into the cubic field as $(K_{0.6},Na_{0.4})MgF_3$ (Fig. 3.9). This creates significant uncertainty (~15 mole percent) in phase boundary assignment and raises the issue of whether the T/C boundary should instead be determined by an apparent convergence of lattice parameters.

If lattice parameters are used as the sole indicator of phase transition, the T/C boundary exists in more sodium rich space, $(K_{0.4},Na_{0.6})MgF_3$, and confirms the previous boundary assignment of Zhao (1998). In this case, we find the stability region of the pure tetragonal phase to be smaller than 5 mole percent potassium at room temperature, which defeats the resolution of this study. Since we do not find a Rietveld trial which prefers the tetragonal over cubic model, within our doping increment, this approach to boundary assignment may shed doubt to the existence of the pure tetragonal phase at room temperature.

Regardless of which Rietveld refinement program is used, large errors accompany refinements of samples near the composition $(K_{0.37},Na_{0.63})MgF_3$ (Fig. 3.10). However, previous studies also record difficulties. Zhao (1998) characterizes X-ray diffraction from $(K,Na)MgF_3$ samples as 'diffuse' and reports just one Rietveld model, while Chakhmouradian et. al. (2001) report physically impossible negative displacement parameters for magnesium ions in both cubic and tetragonal trials of neutron diffraction data from $(K_{0.4},Na_{0.6})MgF_3$. In addition to observing diffuse diffraction, we too obtain negative displacement parameters for magnesium when refining either tetragonal or cubic models to X-ray diffraction data from samples in this region. These negative values are found to closely correlate with small displacement parameter values for fluorine, such as those reported for $NaMgF_3$ at room temperature, ~0.7 $Å^2$. However, when fluorine displacement parameters are assigned and fixed at high values ~3 to 4 $Å^2$, the magnesium values refine to reasonable numbers between

0.6 and 0.4 $Å^2$. Large fluorine displacement values are reported previously in Zhao (1998) and are also found, as a result of thermal vibration, in the orthorhombic/cubic transition region of pure $NaMgF_3$ (500 - 600˚C) (Zhao et al., 1993b). Furthermore, values for fluorine as high as 8 $Å^2$ are found just before the $NaMgF_3$ O/C phase transition (765˚C). Thus, in our room temperature case, large fluorine displacements likely indicate disorder of MgF_6 octahedra.

In the Rietveld models Zhao (1998) and Chakhmouradian (2001), a single function was utilized to determine peak half-width for all hkl. However, since reflections from the superstructure are often twice as wide as those from the substructure, separate functions must be used. We have chosen implementations of the Rietveld approach (Rodriguez-Carvajal, 1990) that allow the refinement of a single structure model with substructure and superstructure reflections each having different half-widths (Woodward et al., 1994) (Fig. 3.11). When this refinement approach is applied to X-ray diffraction data from $(K_{0.4},Na_{0.6})MgF_3$, a better overall fit is observed. However, considerable misfit remains as the result of 2 features: (i) Intensity of substructure reflections become inconsistent with the structural model. (ii) The refinements of the tetragonal (P4/mbm) structure model of $(K,Na)MgF_3$ always partition slightly more intensity to the (211) reflection than it does to the (210). Upon examination of powder diffraction patterns, the (210) is found always to be twice as intense as the (211) reflection. This duplicates observations present in figures from Chakhmouradian et al. (2001). Despite accounting for most of the tetragonal superstructure, Rietveld refinement does not strongly prefer the tetragonal over cubic model when applied to X-ray diffraction data from compostion $(K_{0.4},Na_{0.6})MgF_3$ (Table 3.3).

We observe some direct evidence for a coexistence of orthorhombic and tetragonal symmetry in $(K_{0.15},Na_{0.85})MgF_3$, which supports the work of Zhao (1998). However, it appears that when the synthesis method is changed to type 3, a coexistence of phases can not be directly observed as a result of annealed samples having an increased unit cell where orthorhombic and tetragonal superstructure reflections overlap (Fig. 3.8).

The diffuse diffraction, indistinct phase boundaries, and evidence for phase coexistence together indicate that considerable disorder exists within the $(K,Na)MgF_3$ system at room temperature. Thus, X-ray diffraction in conjunction with Rietveld refinement, a probe of average or global structure, appear incapable of completely characterizing the structure of $(K,Na)MgF_3$ perovskites using a conventional unit cell model. The broad reflections observed in all regions of this solid solution indicate broken atomic periodicity and long-range structure. Thus, fine details obtained with Rietveld refinement, such as atomic parameters, do not represent the entire structure (Egami and Billinge, 1994) and are not reported here as a result. In this case, information about the local ion environment becomes useful and shall aid in understanding the short-range structure. In this study we employ Nuclear Magnetic Resonance of ^{23}Na and ^{19}F active nuclei.

3.4.3. Nuclear Magnetic Resonance (NMR) of Type 1 Samples

3.4.3.1 ^{23}Na MAS NMR

The ^{23}Na MAS NMR spectrum of pure $NaMgF_3$ shows a characteristic second-order quadrupolar broadened resonance (Fig. 3.12) consistent with distortion of the sodium site from cubic symmetry (Fig. 3.13a). The MAS line shape can be fit with a quadrupolar coupling constant (QCC) (550(±20) kHz) and asymmetry parameter, η of 550(±20) kHz and 0.25(±.02), respectively. The perovskites $NaMgF_3$, $(K_{0.45}Na_{0.55})MgF_3$, and $(K_{0.8}Na_{0.2})MgF_3$ have resonances with discontinuities at -11, -24, and -26 ppm respectively. Resonances shift noticeably to lower frequencies on occupation of the perovskite A-site by potassium. For compositions between $NaMgF_3$ and $(K_{0.5}Na_{0.65})MgF_3$, the resonance signals are broad and asymmetric, and the characteristic discontinuities due to second-order quadrupolar broadening are not observed. This is indicative of a distribution of QCCs, and is ascribed to a distribution of changes in the electric field gradients at the Na^+ site due to K^+ ion doping.

The linewidths decrease noticeably between $(K_{0.35}Na_{0.65})MgF_3$ and $(K_{0.80}Na_{0.2})MgF_3$ due to an increase in the symmetry of the sodium environment from a 4- to 12-fold coordination environment (Fig. 3.13b). Although the QCC is too small to result in substantial broadening of the isotropic resonances of the cubic samples

($(K_{0.5}Na_{0.5})MgF_3$ - $(K_{0.8}Na_{0.2})MgF_3$), the ^{23}Na satellite transitions persist indicating a non-zero QCC. An estimate of the residual QCC of 80-100 kHz was estimated by simulating the full spectrum of $(K_{0.7},Na_{0.3})MgF_3$.

3.4.3.2 ^{19}F MAS NMR

^{19}F NMR of $(K,Na)MgF_3$ samples reveal five different environments for fluorine that depend on the number and type of cations in the 1st coordination shell, $F(Na_y,K_{4-y})$ (abbreviated as $F(K_{4-y})$). The most abundant fluorine environment shifts from –201 ppm ($F(Na)_4$; y = 4) for $NaMgF_3$ to –183 ppm ($F(K)_4$; y = 0) for $KMgF_3$. The different resonances were not well resolved in spectra acquired at a relatively fast MAS frequency of 22 kHz, as a result of residual ^{19}F homonuclear dipolar coupling. Spectra were therefore collected with very fast MAS (42 kHz), and showed much better spectral resolution (Fig. 3.14). These spectra are readily deconvoluted, yielding values for the concentrations of the different local environments. Since the chemical shift positions for the different local environments remain fairly similar for different compositions, the ^{19}F chemical shift is clearly dominated by the 1st cation coordination sphere, and the second and third coordination spheres may be ignored to first approximation. Based on this model, the intermediate local environments $F(K_1)$, $F(K_2)$, and $F(K_3)$ have chemical shifts of around -185(±2), -190(±2), and -196(±2) ppm respectively. Small deviations from these shifts are seen in some samples, (x = 0.3 and 0.5) and are most pronounced for the K_4 and K_3 environments. These deviations are seen in samples that display the largest range of tilting states (as determined by the broadening of the XRD reflections). The deviations are ascribed to contributions from more distant coordination spheres and the effect of octahedral tilting on the shift. A K_3 and K_4 local environment in a potassium-rich sample will be nearby other local environments with very small or no MgF_6 tilts. In lower potassium-content samples, the K_0 and K_1 domains with their larger tilt angles will impose strain, as discussed below, and presumably increase the tilt angles in potassium-rich regions. Hence small variations in the chemical shifts of the same local environment across the series are not too surprising.

At low potassium concentrations (i.e. $(K_{0.15},Na_{0.85})MgF_3$), new resonances due to the environments $F(K_4)$ and $F(K_3)$ are clearly observed (in addition to the $F(K_0)$ and $F(K_1)$ resonances), while all five possible fluorine coordination environments are found at intermediate substitution levels. Chakhmouradian et al. (2001) suggest that the Na^+ and K^+ ions may be occupying A-sites at random based on the absence of extra reflections indicative of A-site ordering in diffraction patterns. Such a hypothesis can be tested by normalizing intensities of ^{19}F NMR resonances from each fluoride environment to unity. We find the population of each fluorine environment is found to differ noticeably from that expected by random A-site occupancy (Fig. 3.15) in all compositions. This analysis finds a larger population of each endmember fluorine environment and a decrease in $F(K_2)$ population. Thus there is a tendency for the environments to cluster into potassium-rich and potassium-poor local environments.

3.4.3.3 BABA 2D MQ Investigation of the Local Environments

2D ^{19}F MAS spectra were acquired from type 1 $(K_{0.3},Na_{0.7})MgF_3$ and $(K_{0.7},Na_{0.3})MgF_3$ to investigate the proximity between different ^{19}F local environments. This experiment makes use of the dipolar coupling that occurs between two or more nuclear spins, which depends inversely upon the distance between the spins to the third power. The 1st string of (back-to-back or BABA) pulses used here selects pairs of nuclei that are close together spatially (typically 2 – 5 Å, the exact distance depending on how long the pulses are applied). Spins that are isolated in the solid will not be excited. Two nearby local environments with associated frequencies ν_A and ν_B, will then evolve in the first dimension with a frequency that represents the sum of the two individual frequencies (i.e., at $\nu_A + \nu_B$). This first evolution serves to "label" the spins with the correct chemical shift frequency (in the so-called double quantum, DQ dimension). A second string of pulses reconverts these pairs into their individual resonances (i.e., the spins are now uncoupled). The spins now evolve separately with their own individual frequencies (i.e., ν_A and ν_B), again "labeling" the spins in the single quantum dimension. The signals are then Fourier transformed in both the single and double quantum dimension to yield a 2D DQ NMR spectrum. These spectra contain characteristic cross-peaks, which may be used to explore spatial proximity.

Two nearby pins with associated frequencies ν_A and ν_B give rise to cross-peaks connecting the peaks at frequencies ν_A and ν_B in the single quantum dimension with a peak at a frequency of ($\nu_A + \nu_B$) in the DQ dimension. Two local environments with the same frequency ν_A give rise to a single peak on the so-called diagonal, with frequencies ν_A and $2\nu_A$ (i.e., $\nu_A + \nu_A$) in the 2nd and 1st dimensions, respectively.

Both the one and two dimensional spectra (Fig. 3.16a) of $(K_{0.3},Na_{0.7})MgF_3$ perovskite contain broad resonances. Most of the intensity in the 2D spectrum is located close to the diagonal and corresponds to cross-peaks connecting identical local environments. Weak off- diagonal intensity is, however, observed. For example, broad peaks around -200 ppm in the single quantum dimension are connected to $F(K_0)$ and some $F(K_1)$ local environments. The results indicate that most local environments are nearby environments of the same type, suggesting segregation into clusters with similar K/Na concentrations. The DQ coherences are lost, and no spectral intensity is observed, when the data are collected for sixteen rotor periods (0.64 ms) as opposed to four (0.16 ms).

The BABA 2D MQ ^{19}F MAS spectrum of $(K_{0.7},Na_{0.3})MgF_3$ (Fig. 3.16b) is very well resolved. As expected from 1D ^{19}F MAS NMR spectrum, the strongest peaks arise from the potassium-rich environments $F(K_3)$ and $F(K_4)$. However, unlike the composition $(K_{0.3},Na_{0.7})MgF_3$, cross-peaks between a wide range of environments are seen, indicating a greater mixing of the Na^+ and K^+ cations. The strongest cross-peaks are seen for $F(K_3)$ - $F(K_4)$, $F(K_3)$ - $F(K_3)$ and $F(K_3)$ - $F(K_2)$, but even some of the $F(K_4)$ environments are nearby $F(K_1)$ and $F(K_2)$. Note that any fluorine local environment $F(K_n)$ will always share two A cations with its 10 nearest $F(K_{n'})$ environments. Thus, the strongest cross-peaks will be observed for neighboring between $F(K_n)$ - $F(K_{n'})$ where $|n - n'| < 3$. The weaker $F(K_4)$ - $F(K_1)$ peak must therefore arise between a central F and a more distance F ion in the second anion coordination shell.

3.4.4. Strain and Broken Periodicity

The cause for diffuse diffraction and related structural anomalies observed in $(K,Na)MgF_3$ perovskites has not previously been identified. The NMR spectra together

with X-ray diffraction provide a novel view supporting the conclusion that long-range periodicity is strained as a result of short-range cation clustering. ^{23}Na NMR resonances shift, broaden, and a distribution of QCCs are observed as potassium substitution increases to 50 mole-percent. The QCC drops significantly in potassium-rich compositions, reflecting an increase in the symmetry of the average sodium environment, but the QCC remains non-zero. This indicates some tilting of octahedra (Mg-F-Mg < 180˚) occurs in sodium-rich clusters. ^{19}F NMR spectra of (K,Na)MgF_3 samples show endmember cation environments are favored as opposed to a random or ordered cation arrangement. Thus, clustering of both sodium and potassium occur locally. While the NMR spectra confirm sodium and potassium prefer to neighbor with like cations, the data alone do not offer an explanation for why this occurs. However, a probable mechanism is suggested when considering how tilting of MgF_6 octahedra must accommodate two cations of very different radii.

The impetus for cation clustering in (K,Na)MgF_3 perovskites is derived from the difference in ionic radii—potassium is about 20% larger than sodium. The sodium cation is small and allows adjacent octahedra to tilt and reduce A-site volume, while the larger potassium cation occupies a cubic arrangement of octahedra. Despite the small size of the sodium cation, when sodium neighbors potassium the octahedra about sodium are forced into a cubic configuration to maintain a perovskite structure, enlarging the volume of such sodium sites. When this enlarged sodium site neighbors other sodium sites not adjacent to potassium, octahedra about these sodium sites will prefer to tilt from a cubic configuration, producing a measure of strain. Such strain is likely accommodated over several sodium sites, resulting in diffuse diffraction. Furthermore, potassium substitution should favor a cluster arrangement and sites neighboring potassium since less work is required to further un-tilt these octahedra to a cubic environment. Ultimately, cations cluster in (K,Na)MgF_3 perovskites to reduce the strain and excess volume created when sodium neighbors potassium.

The abovementioned strain and increased A-site volume created in (K,Na)MgF_3 perovskites go far to explain observed structural anomalies. First, the excess unit cell volume of intermediate compositions is likely caused by the enlarged sodium sites. Second, the diffuse X-ray diffraction and broad reflections observed from the

$(K,Na)MgF_3$ perovskite sub- and superstructure result from the strain occurring between clusters of tilted and un-tilted octahedra, including the weak tetragonal diffraction between $(K_{0.15},Na_{0.85})MgF_3$ and $(K_{0.70},Na_{0.30})MgF_3$. While the tetragonal phase never manifests sharp diffraction features at room temperature it does at high temperature (Zhao, 1998). This result is consistent with high temperature enlarging the A-sites of sodium-rich clusters to match the volume of the sodium A-sites strained by potassium neighbors, reducing strain. Because strain occurs between two different octahedra arrangements in $(K,Na)MgF_3$ structures, DTA (Smith et al., 2000) may not observe phase transitions from intermediate compositions—since upon heating, octahedra will un-tilt locally according to individual proximity to potassium. As a result, the phase transition will occur across a temperature range perhaps too wide to be resolved with DTA.

When samples are annealed for 30 days, X-ray diffraction indicates a small increase in the unit cell volumes of $(K,Na)MgF_3$ perovskites and a small reduction in FWHM for diffraction peaks—although signs of strain do not vanish. For example, when $(K_{0.15},Na_{0.85})MgF_3$ is annealed, the average octahedra tilt angle decreases and the diffraction pattern indicates an orthorhombic phase with the [211/103/121] triplet still observed. Subsequently, the evidence for tetragonal diffraction is no longer distinct, but may still over-lie orthorhombic (Fig. 3.8). ^{19}F NMR spectra of this sample do not show a large change before and after annealing. However, annealing may distribute potassium more evenly, reducing local variations in octahedral tilt and the tendency of cations to group with like-neighbors. Since all compositions are synthesized in the cubic field, other variables such as synthesis temperature and cooling-rate may alter the final ordering of A-site cations. More research is needed to completely quantify this effect.

Generally, when pressure is applied to a material, the system will always find the state of minimum volume. Because $(K,Na)MgF_3$ perovskites require a greater unit cell volume than a proportionate mixture of endmember perovskites, $NaMgF_3$ and $KMgF_3$ may not form a solid solution at high pressure. It is likely that perovskites $CaSiO_3$ (cubic) and $MgSiO_3$ (orthorhombic), present in Earth's lower mantle, would

give rise to excess unit cell volume in solid solution. This may be a reason each perovskite prefers a separate phase at high pressure (Kesson et al., 1998).

Because silicate perovskites are believed to dominate Earth's lower mantle, it is necessary to understand how structural phase transitions in perovskites affect acoustic velocity and elastic moduli, since such transitions may occur in the deep earth. The (K,Na)MgF_3 system provides an opportunity to study the elasticity of perovskite phase transitions at room pressure and temperature with ultrasonic interferometry. However, because of the difference in ionic radii between the two A-site cations, a complex structure results. The knowledge gained in this work will aid in evaluating ultrasonic studies of (K,Na)MgF_3 perovskite and understanding other perovskite systems with A-site substitution.

Recently, an ultrasonic study of (Ca, Sr)TiO_3 reveals elastic anomalies associated with phase transitions occurring with changing percent substitution of Sr for Ca (Carpenter et al., 2007) and interpretation of the data assumes phase regions based on the average structure. Upon inspection of the (Ca, Sr)TiO_3 phase diagram and raw diffraction patterns from individual samples, many similarities between (Ca, Sr)TiO_3 and (Na, K)MgF_3 become apparent. As is the case for (Na, K)MgF_3, the (Ca, Sr)TiO_3 solid solution does not follow Vergard's rule and excess unit cell volume occurs, suggesting disorder of cations, octahedra tilt environments, and instability of the solid solution at high pressure. Because the contrast between the ionic radii of A-site ions gives rise to different phases in both (Ca, Sr)TiO_3 and (Na, K)MgF_3 solid solutions, we should expect clustering of A-site cations in (Ca, Sr)TiO_3. The dominant cluster environment in (Na, K)MgF_3 changes with composition and the state of cation order in (Ca, Sr)TiO_3 is not discussed. As was recently shown with Mg_2FeO_4 spinel, the effect of cation order on structure elasticity should not be ignored (Antao, PhD Thesis).

References

Aleksandrov, K.S. (1976) Sequences of Structural Phase-Transitions in Perovskites. Ferroelectrics, 14(3-4), 801-805.

-. (1978) Mechanisms of Ferroelectric and Structural Phase-Transitions, Structural Distortions in Perovskites. Ferroelectrics, 20(1-2), 61-67.

Aleksandrova, I.P., and Beznosikov, B.V. (1968) Magnetic screening of fluorine-19 nuclei in MgF_2, $KMgF_3$, and $NaMgF_3$ single crystals. Zhurnal Strukturnoi Khimii, 9(3), 418-22.

Bonamour, P., Bouffard, V., Fermon, C., Goldman, M., Jacquinot, J.F., and Saux, G. (1991) Nuclear Ferromagnetism in a Perovskite Structure. Physical Review Letters, 66(21), 2810-2813.

Brodholt, J.P. (2000) Pressure-induced changes in the compression mechanism of aluminous perovskite in the Earth's mantle. Nature, 407(6804), 620-622.

Carpenter, M.A., Li, B.S., and Liebermann, R.C. (2007) Elastic anomalies accompanying phase transitions in $(Ca,Sr)TiO_3$ perovskites: Part III. Experimental investigation of polycrystalline samples. American Mineralogist, 92(2-3), 344-355.

Chadwick, A.V., Strange, J.H., Ranieri, G.A., and Terenzi, M. (1983) Studies of Ionic Motion in Perovskite Fluorides. Solid State Ionics, 9-10(DEC), 555-558.

Chakhmouradian, A.R., Ross, K., Mitchell, R.H., and Swainson, I. (2001) The crystal chemistry of synthetic potassium-bearing neighborite, $(Na_{1-x}K_x)MgF_3$. Physics and Chemistry of Minerals, 28(4), 277-284.

Chao, E.C.T., Evans, H.T., Skinner, B.J., and Milton, C. (1961) Neighborite, $NaMgF_3$, a New Mineral From the Green River Formation, South Ouray, Utah. American Mineralogist, 46(3-4), 379-393.

Choy, J.H., Kim, J.Y., Kim, S.J., Sohn, J.S., and Han, O.H. (2001) New Dion-Jacobson-type layered perovskite oxyfluorides, $ASrNb_2O_6F$ (A = Li, Na, and Rb). Chemistry of Materials, 13(3), 906-912.

Cohen, R.E., Mazin, II, and Isaak, D.G. (1997) Magnetic collapse in transition metal oxides at high pressure: Implications for the Earth. Science, 275(5300), 654-657.

Cox, D.E., Toby, B.H., and Eddy, M.M. (1988) Acquisition of Powder Diffraction Data with Synchrotron Radiation. Australian Journal of Physics, 41(2), 117-131.

Dubrovinsky, L.S., Saxena, S.K., Rekhi;, S., Serghiou, G., Zerr, A., and Boehler;, R. (1999) $(Mg,Fe)SiO_3$-Perovskite Stability and Lower Mantle Conditions. Science, 285(5430), 983a.

Dziewonski, A.M., and Anderson, D.L. (1981) Preliminary Reference Earth Model. Physics of the Earth and Planetary Interiors, 25(4), 297-356.

Egami, T., and Billinge, S.J.L. (1994) Underneath the Bragg Peaks: Structural analysis of complex materials. Pergamon Press, Oxford.

Feike, M., Demco, D.E., Graf, R., Gottwald, J., Hafner, S., and Spiess, H.W. (1996) Broadband multiple-quantum NMR spectroscopy. Journal of Magnetic Resonance Series A, 122(2), 214-221.

George, A.M., and Stebbins, J.F. (1998) Structure and dynamics of magnesium in silicate melts: A high-temperature ^{25}Mg NMR study. American Mineralogist, 83(9-10), 1022-1029.

Glazer, A.M. (1972) Classification of Tilted Octahedra in Perovskites. Acta Crystallographica Section B-Structural Science, B 28(V15), 3384-3392.

-. (1975) Simple Ways of Determining Perovskite Structures. Acta Crystallographica Section a, 31(V1), 756-762.

Guo, Q.Z., Mao, H.K., Hu, J.Z., Shu, J.F., and Hemley, R.J. (2002) The phase transitions of CoO under static pressure to 104 GPa. Journal of Physics-Condensed Matter, 14(44), 11369-11374.

Hemley, R.J., Mao, H.K., and Gramsch, S.A. (2000) Pressure-induced transformations in deep mantle and core minerals. Mineralogical Magazine, 64(2), 157-184.

Hoatson, G.L., Zhou, D.H.H., Fayon, F., Massiot, D., and Vold, R.L. (2002) ^{93}Nb magic angle spinning NMR study of perovskite relaxor ferroelectrics $(1-x)Pb(Mg_{1/3}Nb_{1/6})O_3 - xPb(Sc_{1/2}Nb_{1/2})O_3$. Physical Review B, 66(22).

Ito, E., Takahashi, E., and Matsui, Y. (1984) The Mineralogy and Chemistry of the Lower Mantle - an Implication of the Ultrahigh-Pressure Phase-Relations in the System MgO-FeO-SiO_2. Earth and Planetary Science Letters, 67(2), 238-248.

Kaliaperumal, R., and Sears, R.E.J. (1988) F-19 Shielding Anisotropy in $KMgF_3$. Journal of Chemical Physics, 88(2), 1468-1469.

Kellogg, L.H., Hager, B.H., and van der Hilst, R.D. (1999) Compositional stratification in the deep mantle. Science, 283(5409), 1881-1884.

Kesson, S.E., Fitz Gerald, J.D., and Shelley, J.M. (1998) Mineralogy and dynamics of a pyrolite lower mantle. Nature, 393(6682), 252-255.

Kirkpatrick, R.J., Howell, D., Phillips, B.L., Cong, X.D., Ito, E., and Navrotsky, A. (1991) Mas NMR Spectroscopic Study of $^{29}MgSiO_3$ with the Perovskite Structure. American Mineralogist, 76(3-4), 673-676.

Knittle, E., and Jeanloz, R. (1991) Earths Core-Mantle Boundary - Results of Experiments at High- Pressures and Temperatures. Science, 251(5000), 1438-1443.

Knittle, E., Jeanloz, R., and Smith, G.L. (1986) Thermal-Expansion of Silicate Perovskite and Stratification of the Earths Mantle. Nature, 319(6050), 214-216.

Larson, A.C., and Von Dreele, R.B. (2000) General Structure Analysis System (GSAS). Los Alamos National Laboratory Report, 86-748.

Lay, T., Williams, Q., and Garnero, E.J. (1998) The core-mantle boundary layer and deep Earth dynamics. Nature, 392(6675), 461-468. DOI:10.1038/33083.

Liu, L.G. (1976) Orthorhombic Perovskite Phases Observed in Olivine, Pyroxene and Garnet At High-Pressures and Temperatures. Physics of the Earth and Planetary Interiors, 11(4), 289-298.

Liu, L.G., and Ringwood, A.E. (1975) Synthesis of a Perovskite-Type Polymorph of $CaSiO_3$. Earth and Planetary Science Letters, 28(2), 209-211.

Liu, X.F., Tromp, J., and Dziewonski, A.M. (1998) Is there a first-order discontinuity in the lowermost mantle? Earth and Planetary Science Letters, 160(3-4), 343-351.

Matsui, M., and Price, G.D. (1991) Simulation of the Pre-Melting Behavior of $MgSiO_3$ Perovskite At High-Pressures and Temperatures. Nature, 351(6329), 735-737.

Meade, C., Mao, H.K., and Hu, J.Z. (1995) High-Temperature Phase-Transition and Dissociation of $(Mg,Fe)SiO_3$ Perovskite at Lower Mantle Pressures. Science, 268(5218), 1743-1745.

Murakami, M., Hirose, K., Kawamura, K., Sata, N., and Ohishi, Y. (2004) Post-perovskite phase transition in $MgSiO_3$. Science, 304(5672), 855-858. DOI:10.1126/science.1095932.

O'Keeffe, M., and Bovin, J.O. (1979) Solid Electrolyte Behavior of $NaMgF_3$ - Geophysical Implications. Science, 206(4418), 599-600.

O'Keeffe, M., and Hyde, B.G. (1977) Some Structures Topologically Related to Cubic Perovskite ($E2_1$), ReO_3 $(D)O_9$) and Cu_3Au ($L1_2$). Acta Crystallographica Section B-Structural Science, 33(12), 3802-3813.

Redfern, S.A.T. (1996) High-temperature structural phase transitions in perovskite ($CaTiO_3$). Journal of Physics-Condensed Matter, 8(43), 8267-8275.

Ringwood, A.E., and Major, A. (1967) Some High-Pressure Transformations of Geophysical Significance. Earth and Planetary Science Letters, 2(2), 106-110.

Rodriguez-Carvajal, J. (1990) FULLPROF: A Program for Rietveld Refinement and Pattern Matching Analysis. Abstracts of the Satellite Meeting on Powder Diffraction of the XV Congress of the IUCr, Toulouse, France, 127.

Salje, E.K.H. (1992) Application of Landau Theory for the Analysis of Phase-Transitions in Minerals. Physics Reports-Review Section of Physics Letters, 215(2), 49-99.

Saxena, S.K., Dubrovinsky, L.S., Lazor, P., and Hu, J.Z. (1998) In situ X-ray study of perovskite ($MgSiO_3$): Phase transition and dissociation at mantle conditions. European Journal of Mineralogy, 10(6), 1275-1281.

Serghiou, G., Zerr, A., and Boehler, R. (1998) $(Mg,Fe)SiO_3$-perovskite stability under lower mantle conditions. Science, 280(5372), 2093-2095.

Shim, S.H., Duffy, T.S., and Shen, G.Y. (2001) Stability and structure of $MgSiO_3$ perovskite to 2300-kilometer depth in Earth's mantle. Science, 293(5539), 2437-2440.

Shim, S.H., and Jeanloz, R. (2002) P-V-T equation of state of $MgSiO_3$ perovskite and the chemical composition of the lower mantle. Geochimica Et Cosmochimica Acta, 66(15A), A708-A708.

Sidorin, I., Gurnis, M., and Helmberger, D.V. (1999) Evidence for a ubiquitous seismic discontinuity at the base of the mantle. Science, 286(5443), 1326-1331.

Smith, R.W., Mei, W.N., Flocken, J.W., Dudik, M.J., and Hardy, J.R. (2000) Polymorphic phase transitions in mixed alkali magnesium fluoride solid solutions. Materials Research Bulletin, 35(3), 341-349.

Stebbins, J.F., and Kanzaki, M. (1991) Local-Structure and Chemical-Shifts for 6-Coordinated Silicon in High-Pressure Mantle Phases. Science, 251(4991), 294-298.

Stebbins, J.F., Kojitani, H., Akaogi, M., and Navrotsky, A. (2003) Aluminum substitution in $MgSiO_3$ perovskite: Investigation of multiple mechanisms by Al-27 NMR. American Mineralogist, 88(7), 1161-1164.

Stebbins, J.F., Kroeker, S., and Andrault, D. (2001) The mechanism of solution of aluminum oxide in $MgSiO_3$ perovskite. Geophysical Research Letters, 28(4), 615-618.

Su, W.J., and Dziewonski, A.M. (1997) Simultaneous inversion for 3-D variations in shear and bulk velocity in the mantle. Physics of the Earth and Planetary Interiors, 100(1-4), 135-156.

Thompson, P., Cox, D.E., and Hastings, J.B. (1987) Rietveld Refinement of Debye-Scherrer Synchrotron X-Ray Data from Al_2O_3. Journal of Applied Crystallography, 20, 79-83.

Toby, B.H. (2001) EXPGUI, a graphical user interface for GSAS. Journal of Applied Crystallography, 34, 210-213.

van der Hilst, R.D., and Karason, H. (1999) Compositional heterogeneity in the bottom 1000 kilometers of Earth's mantle: Toward a hybrid convection model. Science, 283(5409), 1885-1888.

Vinnik, L., Kato, M., and Kawakatsu, H. (2001) Search for seismic discontinuities in the lower mantle. Geophysical Journal International, 147(1), 41-56.

Wang, Y.B., Guyot, F., and Liebermann, R.C. (1992) Electron-Microscopy of (Mg, Fe)SiO_3 Perovskite - Evidence For Structural Phase-Transitions and Implications For the Lower Mantle. Journal of Geophysical Research-Solid Earth, 97(B9), 12327-12347.

Wang, Y.B., Guyot, F., Yeganehhaeri, A., and Liebermann, R.C. (1990) Twinning in $MgSiO_3$ Perovskite. Science, 248(4954), 468-471.

Wolf, G.H., and Bukowinski, M.S.T. (1987) Theoretical study of the structural and thermoelatic properties of $MgSiO_3$ and $CaSiO_3$ perovskites: Implications for lower mantle composition. 313-331 p. Terra Science, Tokyo.

Wood, I.G., Knight, K.S., Price, G.D., and Stuart, J.A. (2002) Thermal expansion and atomic displacement parameters of cubic $KMgF_3$ perovskite determined by high-resolution neutron powder diffraction. Journal of Applied Crystallography, 35, 291-295.

Woodward, P., Hoffmann, R.D., and Sleight, A.W. (1994) Order-Disorder in $A_2M^{3+}M^{5+}O_6$ Perovskites. Journal of Materials Research, 9(8), 2118-2127.

Woodward, P.M., Cox, D.E., Moshopoulou, E., Sleight, A.W., and Morimoto, S. (2000) Structural studies of charge disproportionation and magnetic order in $CaFeO_3$. Physical Review B, 62(2), 844-855.

Woodward, P.M., Cox, D.E., Vogt, T., Rao, C.N.R., and Cheetham, A.K. (1999) Effect of compositional fluctuations on the phase transitions in $(Nd_{.5}Sr_{.5})MnO_3$. Chemistry of Materials, 11(12), 3528-3538.

Woodward, P.M., Vogt, T., Cox, D.E., Arulraj, A., Rao, C.N.R., Karen, P., and Cheetham, A.K. (1998) Influence of cation size on the structural features of

($Ln_{.5}A_{.5}$)MnO_3 perovskites at room temperature. Chemistry of Materials, 10(11), 3652-3665.

Yoshiasa, A., Sakamoto, D., Okudera, H., Ohkawa, M., and Ota, K.i. (2003) Phase relation of ($Na_{1-x}K_x$)MgF_3 (0 x <= 1) perovskite-type solid-solutions. Materials Research Bulletin, 38(3), 421-427.

Zhang, J.Z., and Weidner, D.J. (1999) Thermal equation of state of aluminum-enriched silicate perovskite. Science, 284(5415), 782-784.

Zhao, Y.S. (1998) Crystal chemistry and phase transitions of perovskite in P-T-X space: Data for (K_xNa_{1-x})MgF_3 perovskites. Journal of Solid State Chemistry, 141(1), 121-132.

Zhao, Y.S., Parise, J.B., Wang, Y.B., Kusaba, K., Vaughan, M.T., Weidner, D.J., Kikegawa, T., Chen, J., and Shimomura, O. (1994a) High-Pressure Crystal-Chemistry of Neighborite, $NaMgF_3$ - an Angle-Dispersive Diffraction Study Using Monochromatic Synchrotron X-Radiation. American Mineralogist, 79(7-8), 615-621.

Zhao, Y.S., Weidner, D.J., Ko, J.D., Leinenweber, K., Liu, X., Li, B.S., Meng, Y., Pacalo, R.E.G., Vaughan, M.T., Wang, Y.B., and Yeganehhaeri, A. (1994b) Perovskite At High P-T Conditions - an in-Situ Synchrotron X- Ray-Diffraction Study of $NaMgF_3$ Perovskite. Journal of Geophysical Research-Solid Earth, 99(B2), 2871-2885.

Zhao, Y.S., Weidner, D.J., Parise, J.B., and Cox, D.E. (1993a) Critical Phenomena and Phase-Transition of Perovskite Data For $NaMgF_3$ Perovskite .2. Physics of the Earth and Planetary Interiors, 76(1-2), 17-34.

-. (1993b) Thermal-Expansion and Structural Distortion of Perovskite - Data For $NaMgF_3$ Perovskite .1. Physics of the Earth and Planetary Interiors, 76(1-2), 1-16.

Zhou, L.X., Hardy, J.R., and Xu, X. (1998) Molecular dynamics simulation of $MgSiO_3$ perovskite. Chinese Physics Letters, 15(6), 444-446.

Composition (x)	Type 1 (Å^3)	Type 2' (Å^3)	Type 3 (Å^3)
0	56.381(7)		
0.08	57.093(8)		
0.15	57.943(5)		58.486(5)
0.22	59.188(4)	58.853(8)	59.135(6)
0.3	59.585(7)		59.865(5)
0.35	59.887(5)		60.124(7)
0.4	60.362(10)		60.614(8)
0.45	60.742(8)		
0.5	61.168(8)		
0.55	61.514(7)		
0.6	61.830(6)		
0.7	62.398(6)		
0.8	62.739(5)		
0.9	63.218(5)		
1	63.226(1)		

[Table 3.1] Unit-cell volume (Z=1) vs. composition and synthesis method.

$(K_x,Na_{1-x})MgF_3$

Composition (x)	a (Å)	b	c	Volume ($Å^3$)	Unit Cell Z
0	5.3606(1)	5.4873(1)	7.6668(2)	225.52(1)	4
0.08	5.398(2)	5.494(2)	7.701(3)	228.3(1)	4
0.15	5.4372(2)	5.5060(2)	7.7419(3)	231.77(2)	4
0.22	5.491(1)	5.5126(7)	7.782(1)	235.59(6)	4
0.3	5.518(1)	5.523(1)	7.818(2)	238.34(9)	4
0.35	5.530(2)	5.532(1)	7.827(2)	239.5(1)	4
0.4	5.546(1)	5.546(1)	3.924(2)	120.72(7)	2
0.45	5.558(1)	5.558(1)	3.931(2)	121.48(6)	2
0.5	3.9401(1)	3.9401(1)	3.9401(1)	61.168(3)	1
0.55	3.9475(1)	3.9475(1)	3.9475(1)	61.514(3)	1
0.6	3.9542(2)	3.9542(2)	3.9542(2)	61.830(6)	1
0.7	3.9663(2)	3.9663(2)	3.9663(2)	62.398(5)	1
0.8	3.9735(3)	3.9735(3)	3.9735(3)	62.739(7)	1
0.9	3.9836(1)	3.9836(1)	3.9836(1)	63.218(4)	1
1	3.9838(1)	3.9838(1)	3.9838(1)	63.226(2)	1

[Table 3.2] Lattice parameters and phase transitions vs. composition.

$(K_x,Na_{1-x})MgF_3$

	as Cubic / Orthorhombic			as Tetragonal		
Composition (x)	Rwp	Rp	χ^2	Rwp	Rp	χ^2
0	8.3	6.57	4.6			
0.08	10.8	7.21	30			
0.15	19.24	14.84	31.69			
0.22	8.04	5.62	12.15			
0.3	21.15	16.48	26.27			
0.35	18.79	13.58	23.87			
0.4	20.5	30.6	10.41	19.2	27.7	9.233
0.45	17	22.1	5.643	16.4	19.6	5.442
0.5	10.56	7.15	5.306			
0.55	9.47	7.29	5.38			
0.6	8.883	7.11	3.714			
0.7	9.25	7.22	3.02			
0.8	8.885	7.51	2.464			
0.9	7.92	6.22	3.14			
1	4.32	3.45	2.711			

[Table 3.3] Errors associated with Rietveld trials in various space groups.

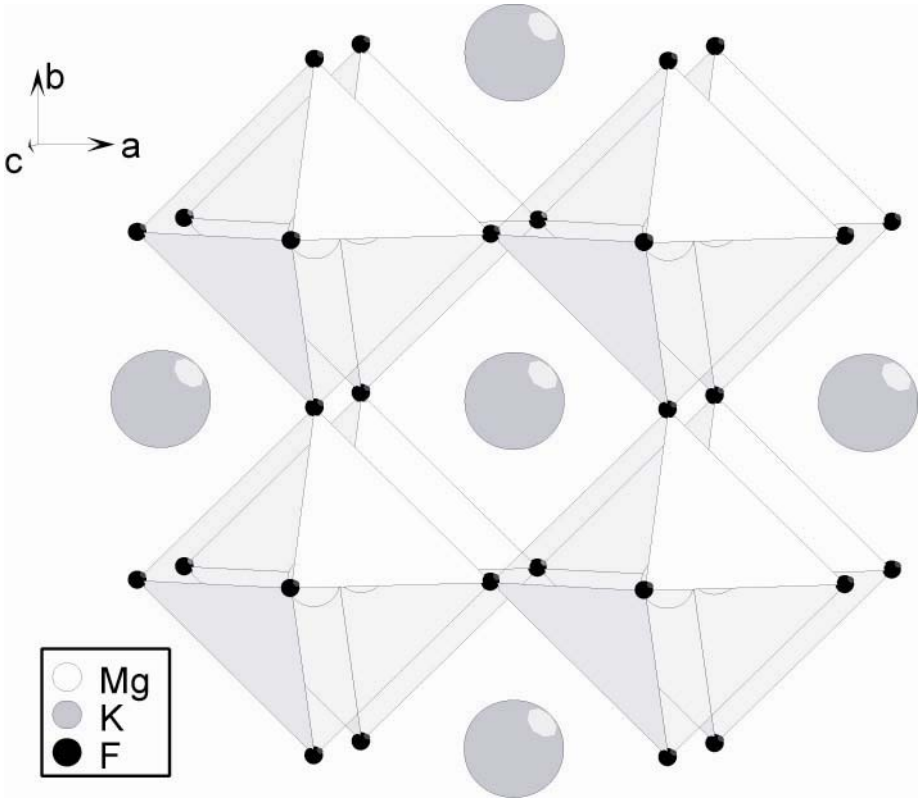

[Fig. 3.1] The potassium ion that occupies the perovskite A-site in cubic *Pm*3*m* $KMgF_3$ is large enough to support MgF_6 octahedra that mirror each other in three dimensions.

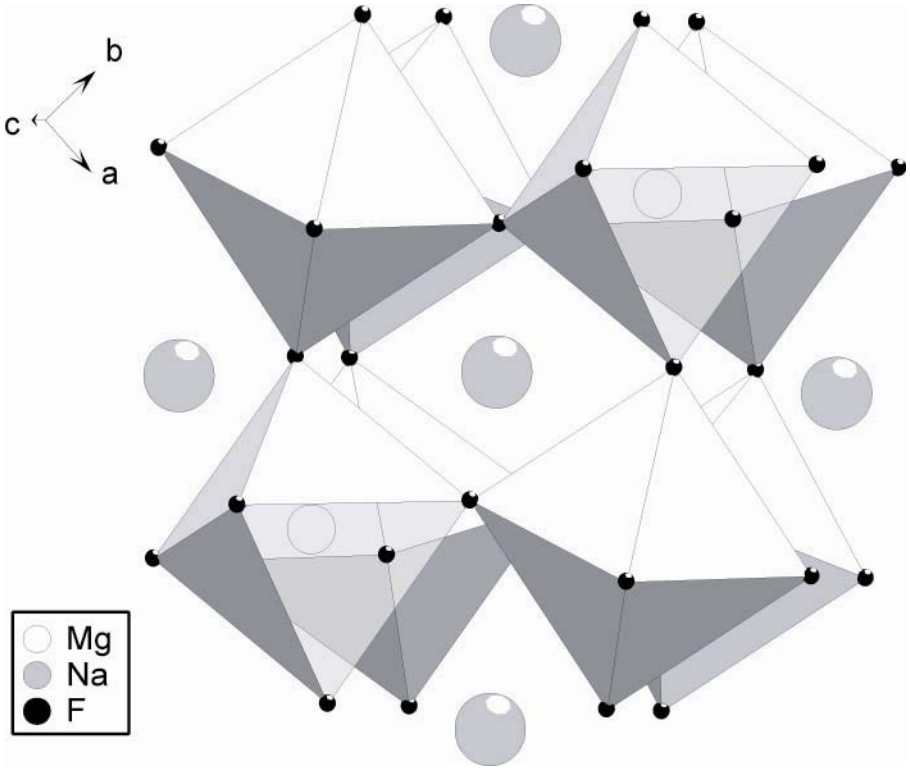

[Fig. 3.2] The smaller sodium ion that occupies the perovskite A-site in orthorhombic *Pbnm* $NaMgF_3$ allows octahedra to collapse or tilt.

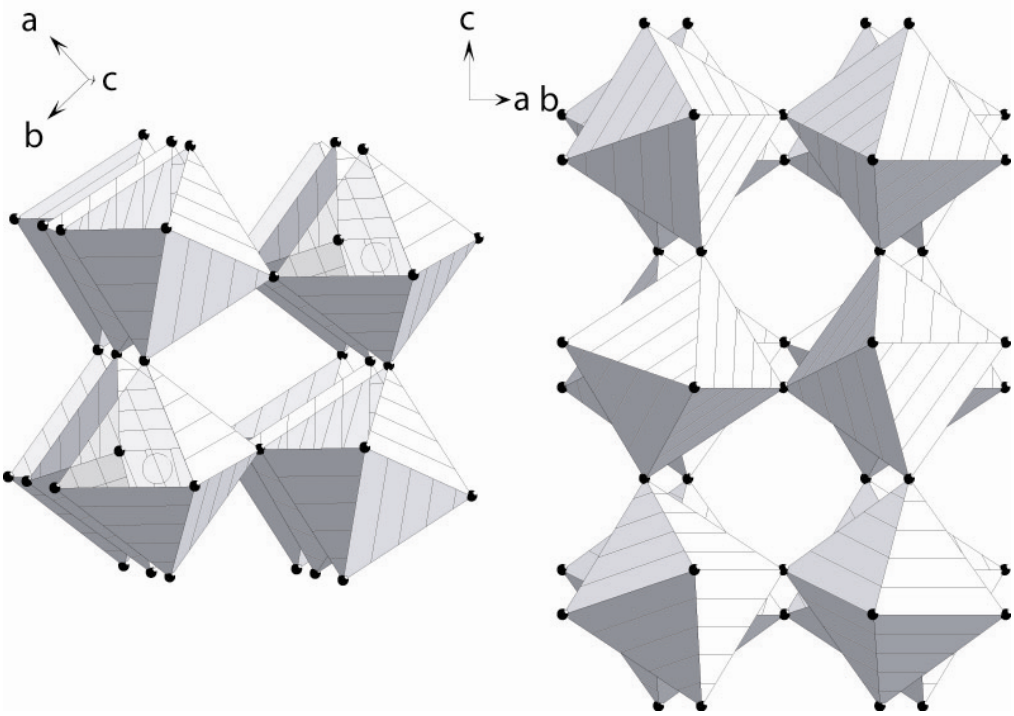

[Fig. 3.3] In the $NaMgF_3$ structure MgF_6 octahedrons tilt with both in-phase (left) and anti-phase (right) components.

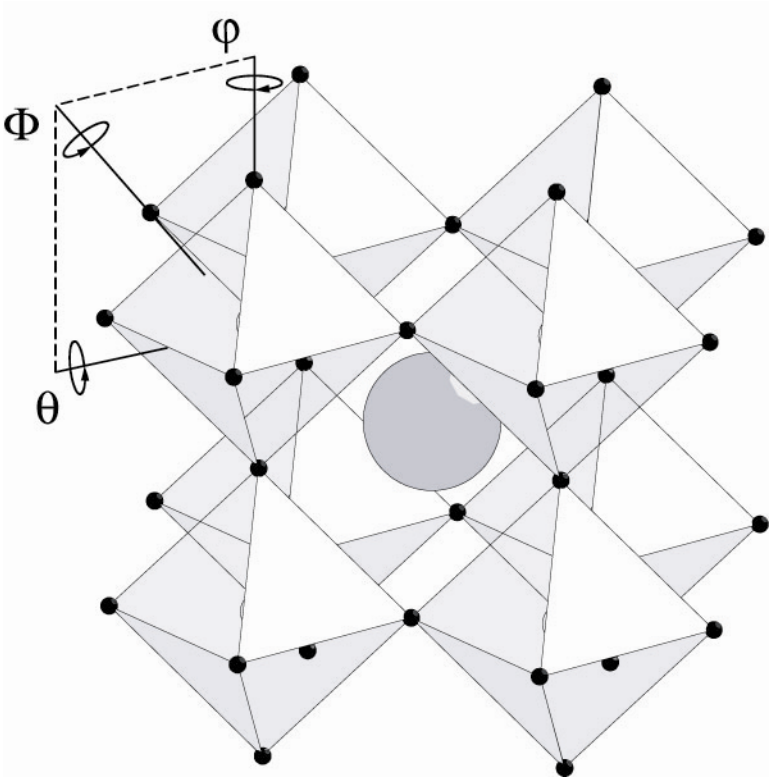

[Fig. 3.4] Octahedral tilt may be quantified as a function of rotation about pseudo-cubic axes. Shown here axes φ, θ, and Φ denote rotation about the [001], [110], and [111] directions, respectively.

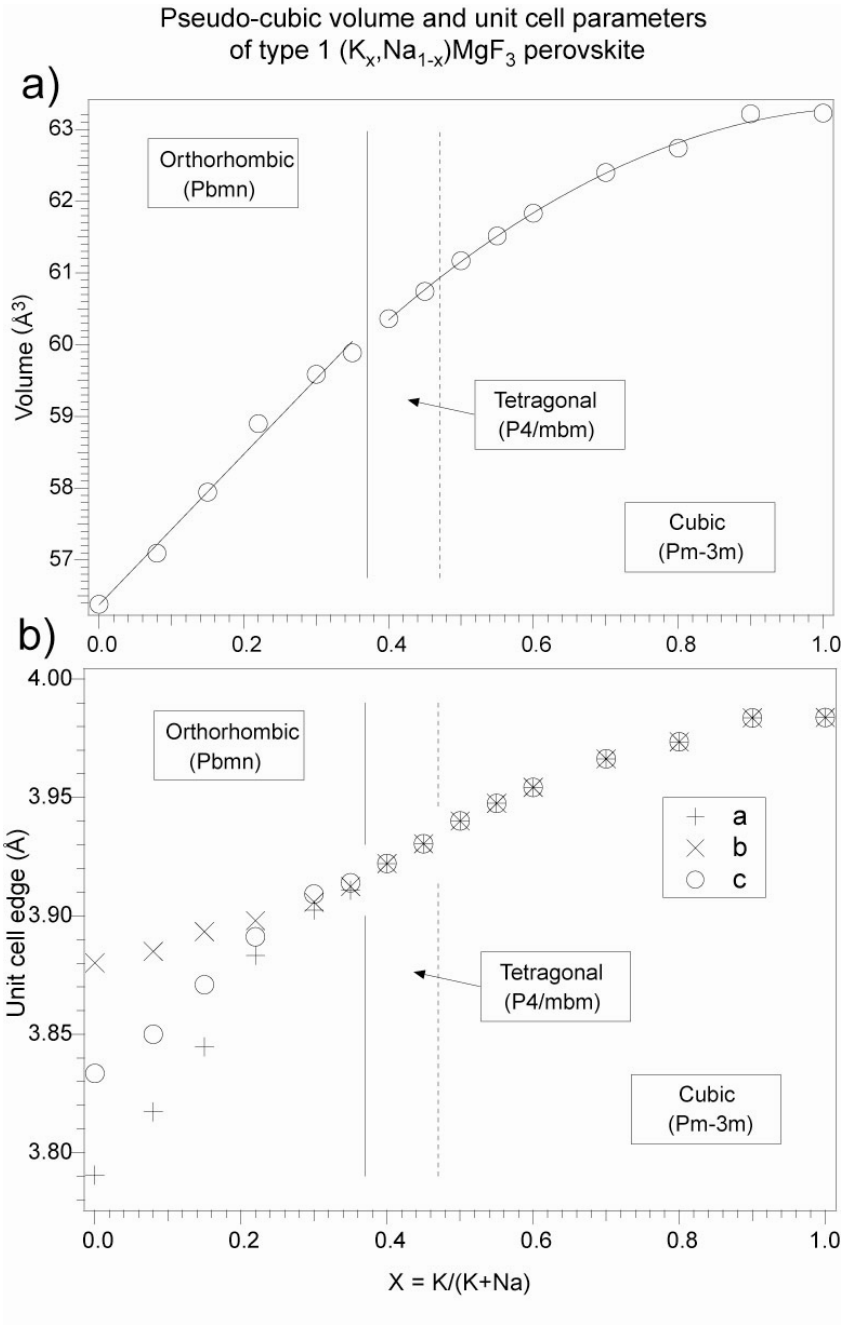

[Fig. 3.5] (a) The steep linear trend of the unit-cell volume changes to a higher-order dependence in the cubic region. (b) Pseudo-cubic lattice parameters follow a similar trend. Uncertainty in placement of the boundary between tetragonal and cubic symmetry results from the poor quality of super-structure reß ections which broaden with potassium substitution. The error bars are small than the marker symbols.

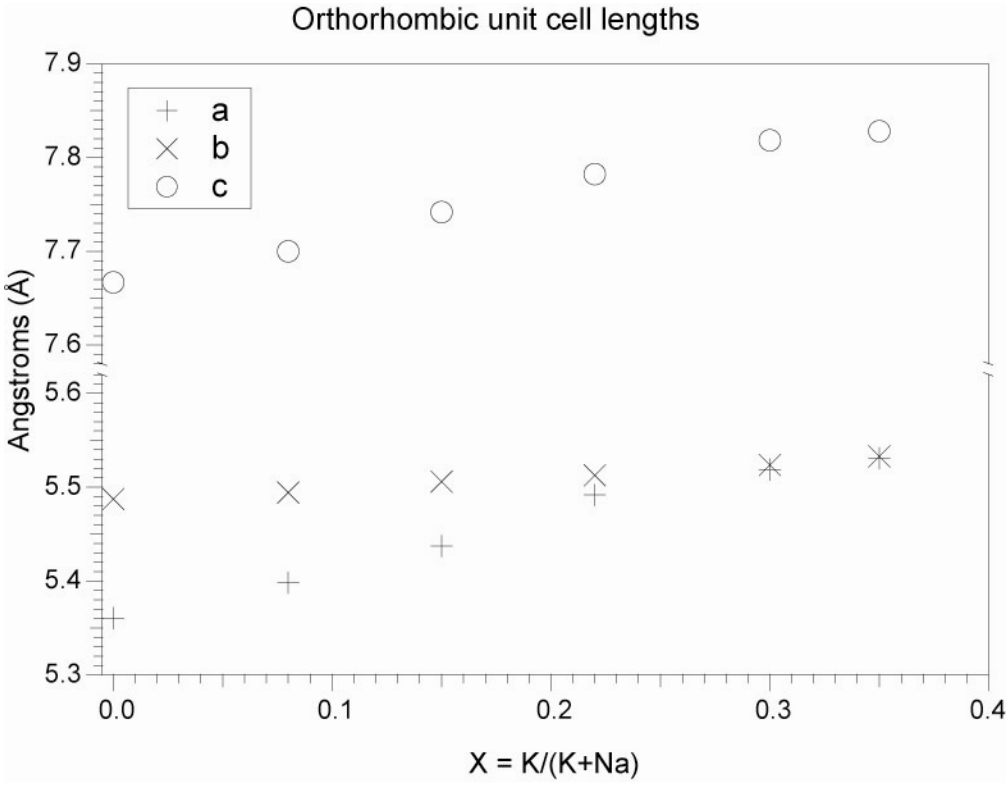

[Fig. 3.6] Orthorhombic unit-cell length increase linearly to transition at $(K_{0.37}Na_{0.63})MgF_3$. The error bars are smaller than the markers.

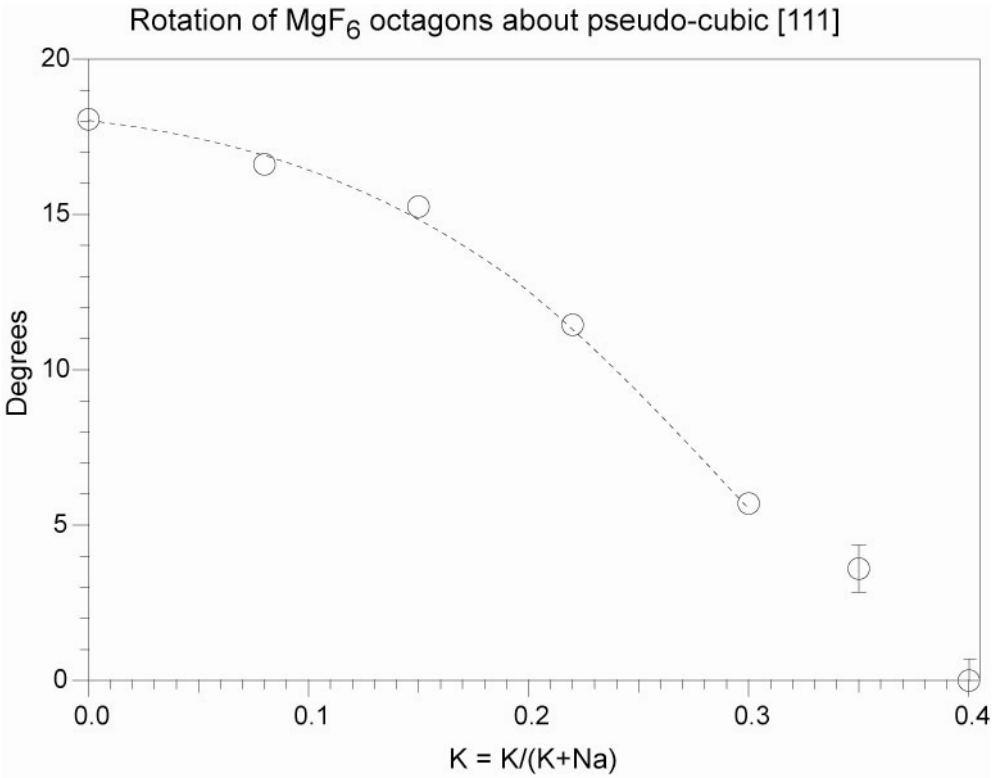

[Fig. 3.7] Rotation of MgF_6 octahedra as potassium concentration increases. The variable serves as an order parameter for phase transition. The error bars are otherwise smaller than the marker size. The dashed line is intended to guide the eye.

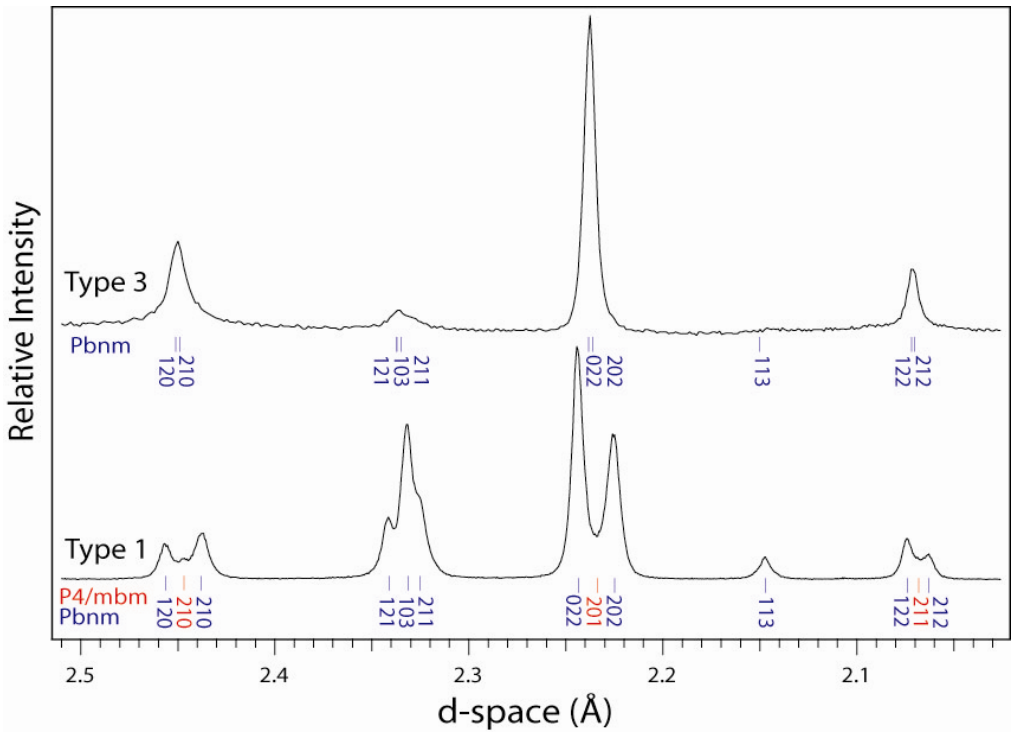

[Fig. 3.8] X-ray diffraction patterns of $(K_{0.15}Na_{0.85})MgF_3$ perovskite samples demonstrate the effect of annealing on unit-cell and tilting of MgF_6 octahedrons. Type 1 indicates a method where samples are synthesized with just two 5 hour fring periods at 1023 K, while type 3 denotes one where the same type 1 samples are further annealed at 1023 K for 30 days. Annealed samples show a 1-0.5% increase in unit-cell and a 2-4 degree reduction in tilting about the pseudo-cubic [111].

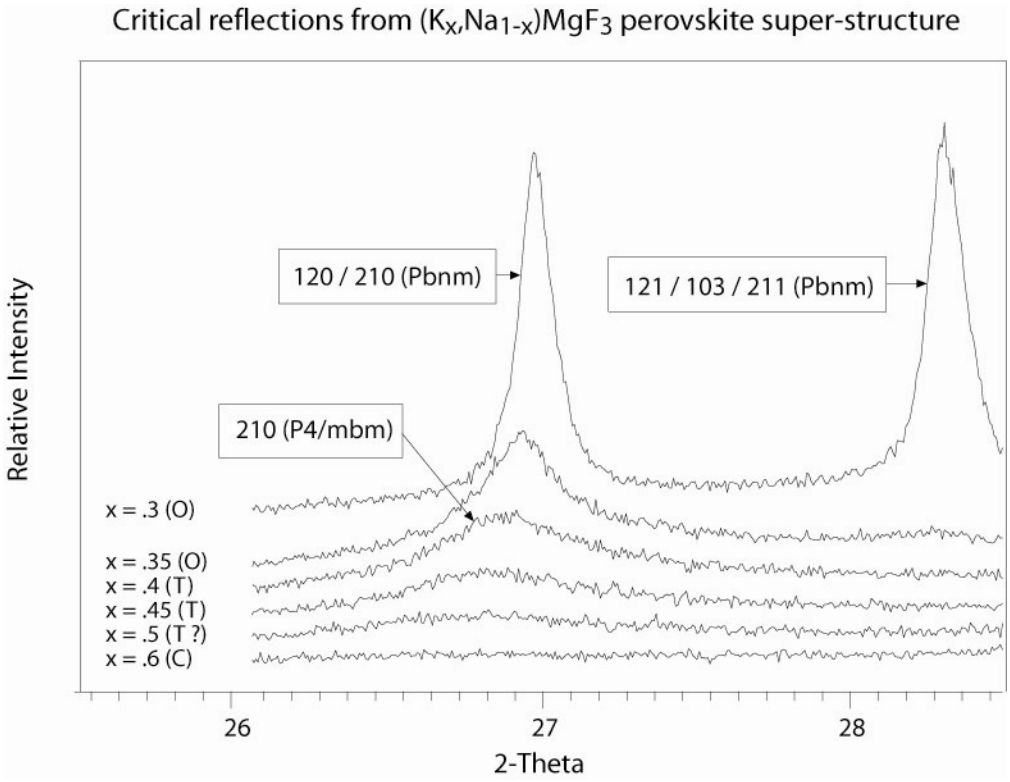

[Fig. 3.9] X-ray diffraction patterns of type 1 $(K_xNa_{1-x})MgF_3$ perovskite samples. The phase boundary at x = ~0.37 was chosen upon the extinction of the orthorhombic [212/103/211] triplet. Yet broad and very weak tetragonal refection between x = 0.35-0.6 convolute the distinction between tetragonal and cubic phases.

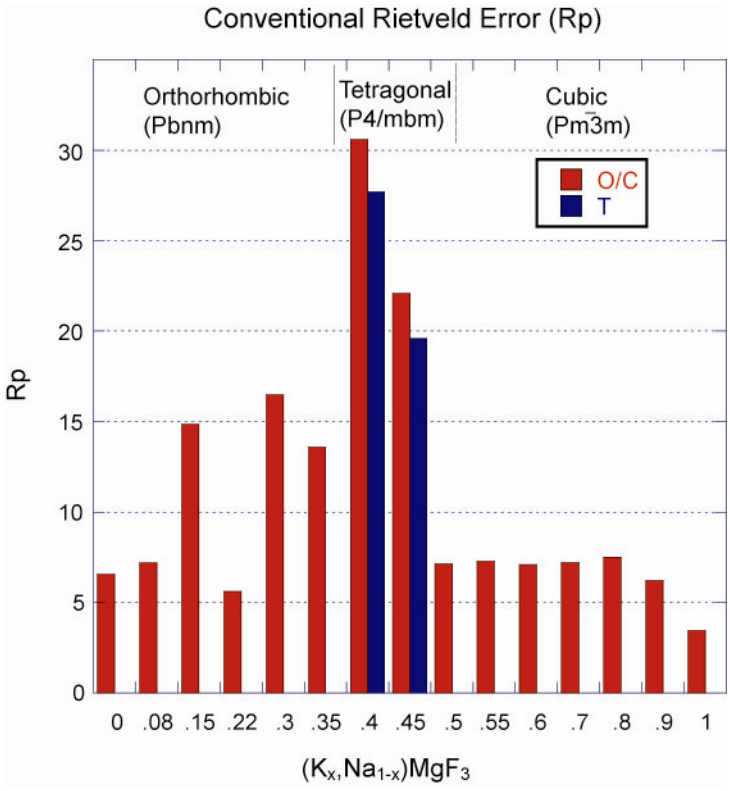

[Fig. 3.10] Rp error of models obtained with Rietveld refnement, demonstrating the difficulty applying Rietveld techniques to diffraction patterns of $(K_xNa_{1-x})MgF_3$ samples. Difficulty comes from ubiquitous peak broadening most pronounced in super-structure reflections and irregular intensities. The error in orthorhombic or cubic models is marked in blue. Errors $\chi 2$, Rp, and Rwp can be found in Table 3.3.

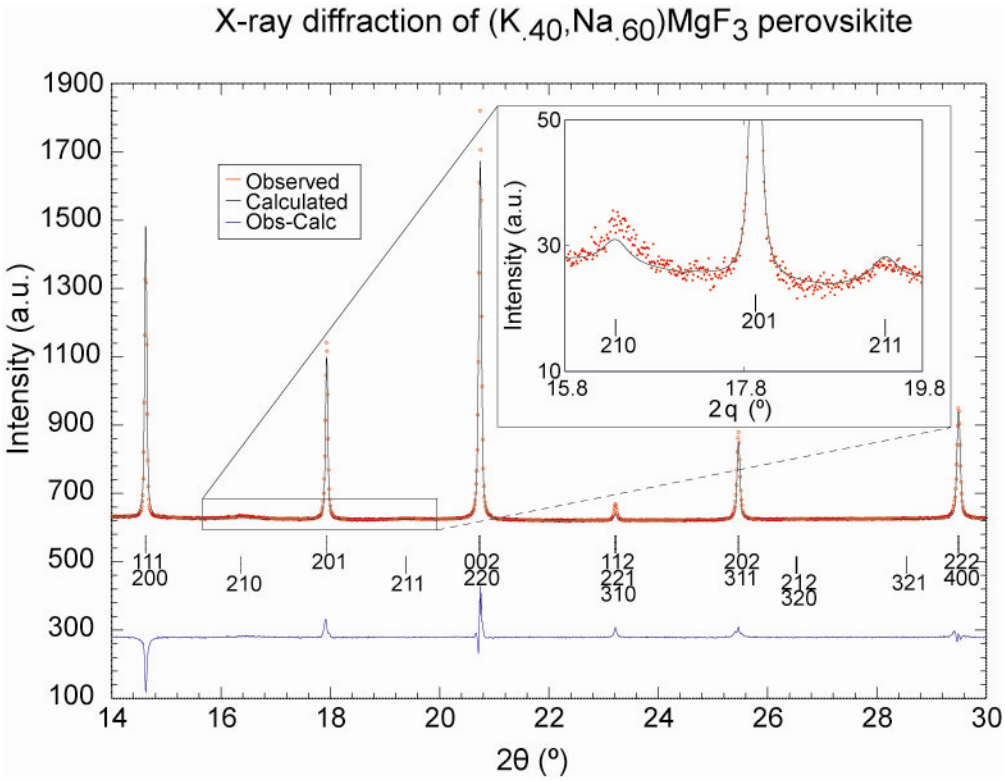

[Fig. 3.11] Plot of type 1 $(K_{0.40}Na_{0.60})MgF_3$ perovskite generated by FullProf. Cubic substructure (upper tier markers) and tetragonal *P*4/*mbm* superstructure (lower tier markers) are fit each as a separate phase to allow for large tetragonal FWHM. Misfit of reflections from both sub and superstructure occurs from inconsistent peak shape and intensity. The plot inset shows the intensity contrast between 210 and 211 indices which cannot be calculated by the *P*4/*mbm* model.

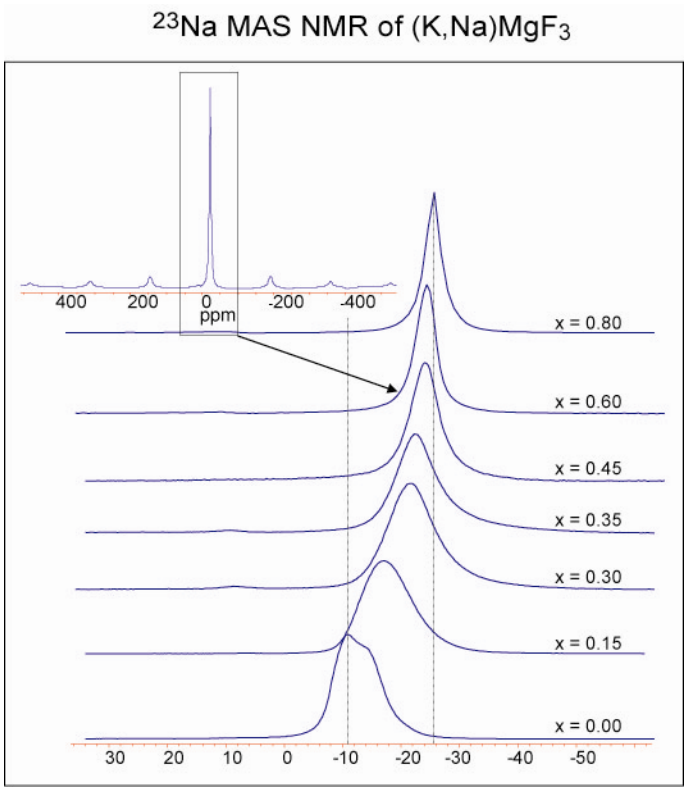

[Fig. 3.12] The fluorine decoupled ^{23}Na MAS at a spinning speed of 16 kHz.

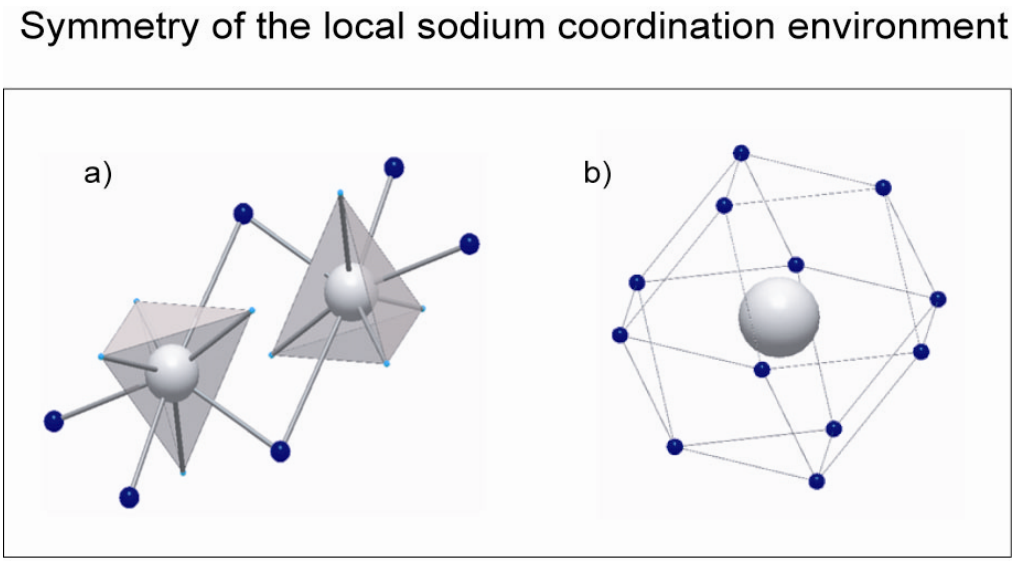

[Fig. 3.13] A diagram showing the local coordination environment of the sodium ion in (a) orthorhombic and (b) cubic space group.

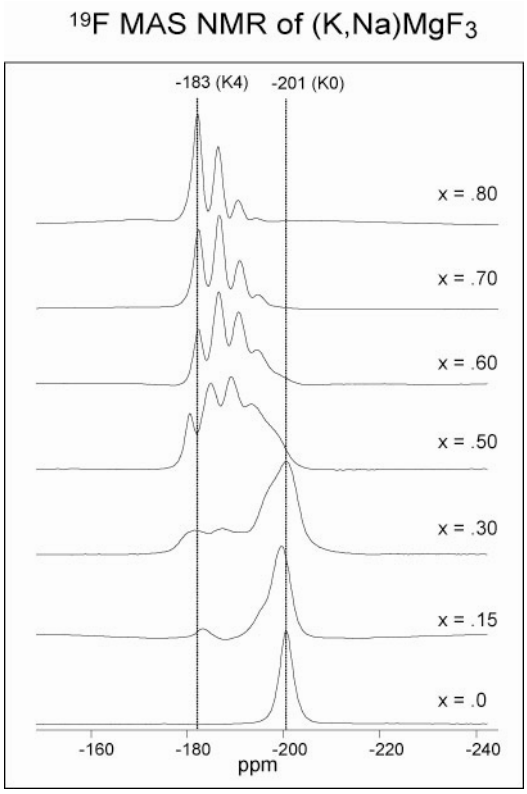

[Fig. 3.14] The ^{19}F NMR spectrum under 42 kHz MAS conditions for different K-doping levels.

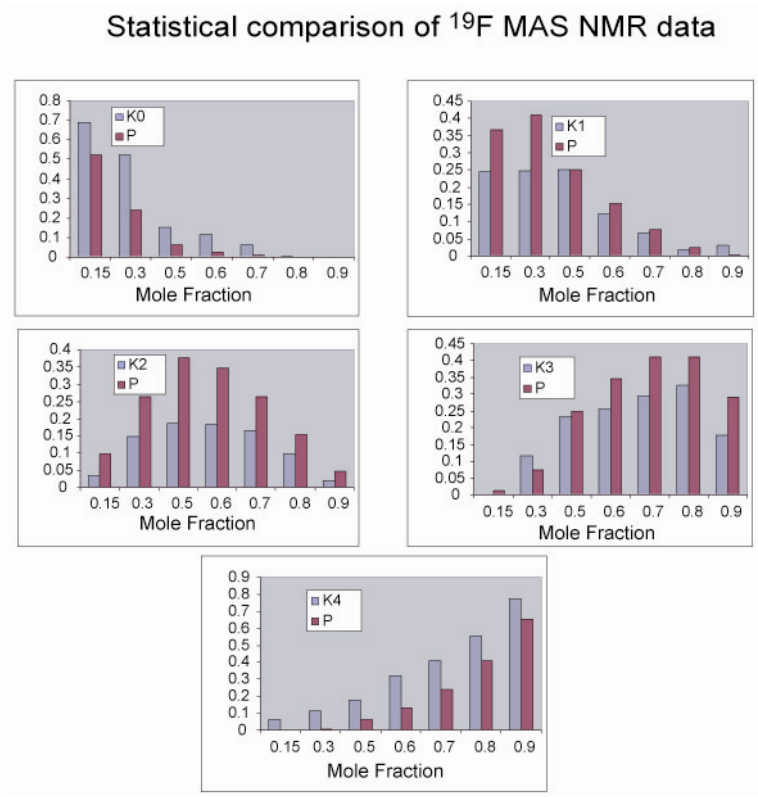

[Fig. 3.15] The calculated probabilities (P), based on random occupation of A sites by Na+ and K+ are plotted next to observed intensities of the K0, K1, K2, K3, and K4 local environments via ^{19}F NMR at different concentration levels. It appears from this data that end-member configurations are preferred vs. intermediate.

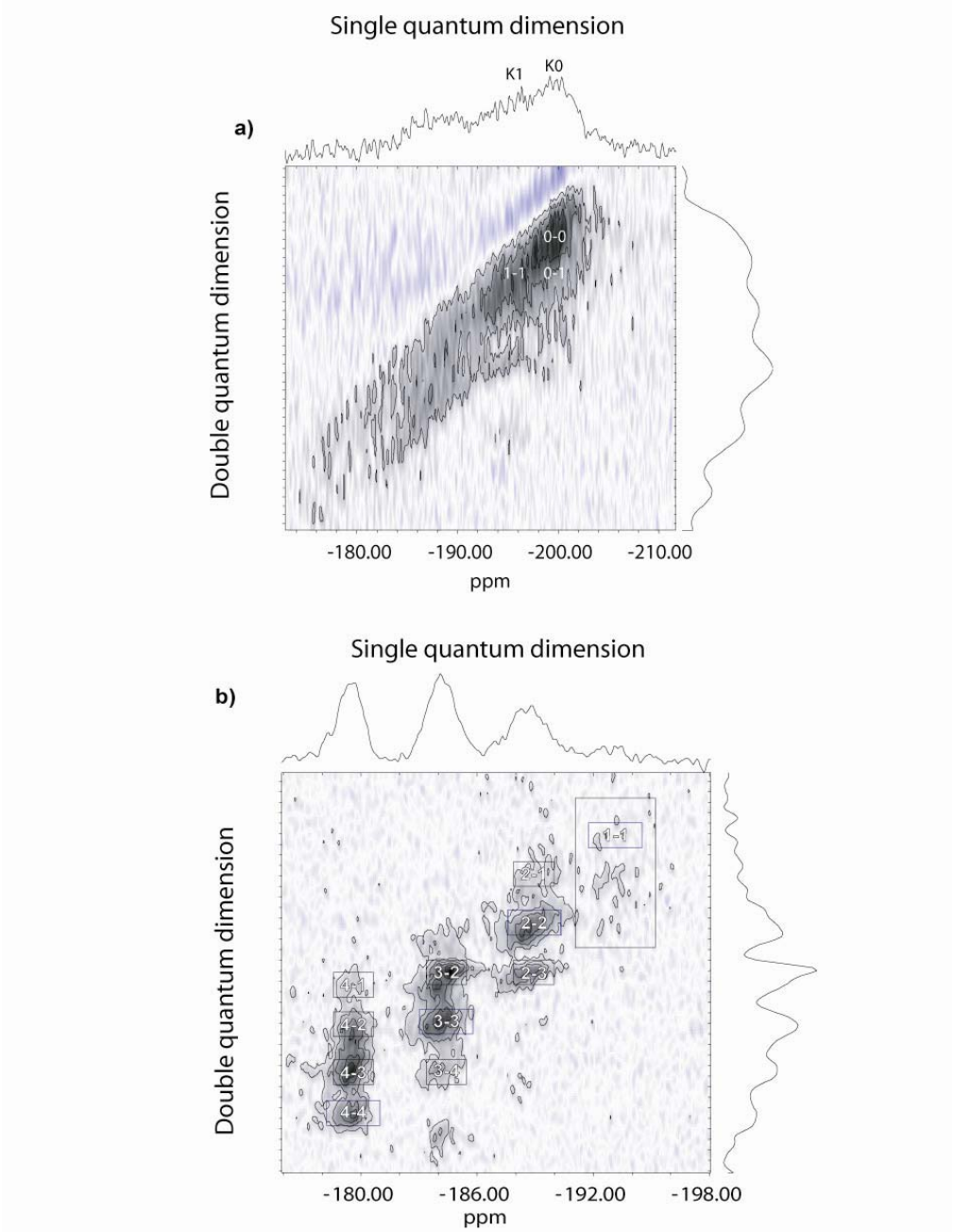

[Fig. 3.16] 2D MQ BABA spectra for (a) x = 0.3 showing broad cross peaks connecting like environments and (b) x = 0.7, where cross peaks connection different fluorine sublattices are now resolved. Projections onto the single and double quantum dimension are shown along with the assignments of some of the cross-peaks.

Chapter IV

Local vs. average structure; a study of Neighborite ($NaMgF_3$) utilizing the pair-distribution function for quantitative structure determination

THIS CHAPTER PUBLISHED AS:

MARTIN, C.D., CHUPAS, P.J., CHAPMAN, K.W., AND PARISE, J.B. (2007) LOCAL VS. AVERAGE STRUCTURE; A STUDY OF NEIGHBORITE ($NaMgF_3$) UTILIZING THE PAIR-DISTRIBUTION FUNCTION FOR QUANTITATIVE STRUCTURE DETERMINATION. JOURNAL OF APPLIED CRYSTALLOGRAPHY, IN PRESS.

4.1. Abstract

In this chapter we examine the temperature dependent local structure (< 2 nm) of Neighborite ($NaMgF_3$) probed through least-squares refinement of structure models fit to the pair-distribution function (G(r)) derived from the total x-ray scattering of sample powders. In contrast to previous structure models obtained through powder diffraction and Rietveld refinement, we find the average Mg-F bond length increases between 50 and 850 ˚C. At high temperature, asymmetry evident in the low-r peak at ~2 Å is consistent with an orthorhombic (***P****bnm*) perovskite structure, allowing 3 unique Mg-F values and deformation of MgF_6 octahedra. While data prefer structure models with ***P****bnm* internal symmetry the unit cell becomes metrically tetragonal and cubic at temperatures greater than 350 and 765 ˚C, respectively. Thermal ellipsoids describing fluorine ions do not prefer asymmetry when isotropic constraints are relaxed during local structure refinement and temperature trends suggest a transition between modes of atomic vibration in $NaMgF_3$ at 765 ˚C. Data are consistent with temperature activation of transverse atomic vibration of fluorine atoms (Mg-F-Mg) at high temperature.

4.2. Introduction

Crystal structure determination typically relies on x-ray or neutron diffraction, where average atomic positions are observed and assumed to represent both short- (< 20 Å) and long-range (>100 Å) order. While this assumption is appropriate in general, exceptions occur when minerals exhibit correlated atomic motion (Jeong *et al.*, 2003, Tucker *et al.*, 2001) or defects (Viani *et al.*, 2002, Chrosch *et al.*, 1998, Martin *et al.*, 2005, Dodony *et al.*, 2006) and techniques utilizing Bragg diffraction with structure refinement fail to approximate the local structure. In these special cases, studies considering the diffuse scattering with the Bragg reflections, i.e. the total scattering, may sample the local structure (Egami & Billinge, 1994).

Structure models fitted to the Bragg peaks represent the time-averaged crystal structure and a Debye-Waller factor, accounting for relative atomic motion in the crystal and the shape of the scattering factor (Warren, 1969), is required to calculate atomic displacement parameters, defining probability ellipsoids (Rietveld, 1969). However, when the Debye-Waller factor is applied to an aperiodic crystal (Guinier, 1994) or one with correlated atomic motion, displacement parameters compensate for differences between the sample and structure model (Young, 1993). Structure models calculated from the total scattering represent the local structure (Egami & Billinge, 1994). However, distinguishing the total scatting, i.e. structure function (S(Q(Å^{-1}))), of the sample from the rest of the scattered intensity in the complete intensity spectrum (I(Q)) is non-trivial. Normalization of S(Q) from I(Q) usually requires a background spectra be collected, scaled and subtracted from I(Q) (Chupas *et al.*, 2003, Proffen *et al.*, 1999).

Because the structure function operates in terms of reciprocal space, a function defined in terms of real-space may be obtained by Fourier transform,

$$\frac{2}{\pi}\int_0^\infty Q[S(Q)-1]\sin(Qr)dQ = 4\pi r\rho_0(g(r)-1) \qquad (4.1)$$

where ρ_0 is the average number density of the scatterers. As a Fourier transform of S(Q) (a frequency spectrum, Å^{-1}), the pair distribution function (PDF, g(r(Å))) describes the probability of finding a given distance between any two atoms in the structure (Egami & Billinge, 1994).

Analysis of the structure function S(Q) and g(r) have traditionally been reserved for studies of glasses and amorphous materials where no long range order exists (Ansell *et al.*, 1997, Billinge, 2004, Guthrie *et al.*, 2004, Okabe *et al.*, 1996). However, relatively recently with development of technological applications for nanocrystalline and complex crystalline materials software packages have been developed to aid quantitative analysis of the pair distribution function (Egami & Billinge, 1994, Proffen & Billinge, 1999, Qiu *et al.*, 2004). Mineralogists concerned with defects, disorder, phase transitions, glasses, and melts are likely to find advantage in quantitative analysis of the structure function and may consider total scattering a complementary tool in the crystallography suite.

Program PDFFIT (Proffen & Billinge, 1999) uses least-squares fitting to perform quantitative structure refinement in real-space. By fitting to the density weighted radial distribution function,

$$4\pi r\rho_0(g(r)-1) = G(r) \tag{4.2}$$

or 'reduced pair distribution function' (G(r)) rather than g(r), PDFFIT does not assume the average number density and all parameters describing the instantaneous local structure model may be refined.

The PDF provides a vantage point from which novel views of crystal structures are possible and in the case of mineral Neighborite ($NaMgF_3$) (Chao et al., 1961) a new view is warranted. Perovskite-structured $NaMgF_3$ (neighborite) has been extensively studied as a proxy for $MgSiO_3$ perovskite (Chen *et al.*, 2005, Liu *et al.*, 2005, Martin *et al.*, 2006a, O'Keeffe *et al.*, 1979) which dominates the mineralogy of Earth's lower mantle (Liu, 1976, Ringwood, 1994, Stixrude & Karki, 2005). At high temperature, $NaMgF_3$ exhibits an anomalous structural phase transition and becomes a solid electrolyte (O'Keeffe & Bovin, 1979) before melting. Contrary to behavior expected for pairs of bonded atoms, Rietveld structure refinement reveals a rapid increase in fluorine displacement parameters and a decrease in the Mg-F bond lengths during the final 150 K preceding phase transition from orthorhombic (***P****bnm*) to cubic ($\boldsymbol{P}m\bar{3}m$) at 765 ˚C (Zhao *et al.*, 1993a, 1993b). Zhao *et al.* (1993a) conclude that the instantaneous bond length would be underestimated with Rietveld analysis due to thermal vibration of fluorine ions and dynamic tilting of the MgF_6 octahedra in the cubic phase.

Analysis of the pair distribution function (PDF) of crystalline materials (Billinge & Kanatzidis, 2004, Egami & Billinge, 1994, Petkov *et al.*, 2006) is advantageous for structure and bond length determination when structures exhibit correlated atomic motion and average atomic positions derived from Rietveld refinement are believed to poorly approximate the true local (< 20 Å) order. Many such examples involve three dimensional frameworks consisting of corner-sharing or bridged coordination polyhedra (Chapman *et al.*, 2005, Chupas *et al.*, 2004, Tucker *et al.*, 2001, Qiu *et al.*, 2005), where correlated atomic motion is often thermally-populated and manifests as transverse atomic vibration of the shared anion bridging two polyhedra units.

The local structure of $NaMgF_3$ has been investigated previously by molecular dynamics simulation. Street et al. (1997) generate a statistical distribution of Mg-F bond lengths in $NaMgF_3$ at various temperatures and consider the asymmetric peak shape of the simulated correlation. The statistical mode value of the Mg-F bond length distribution shifts to lower distances while the statistical average value increases with temperature. Considering this result, Street et al. (1997) conclude the cell parameter of the high temperature $NaMgF_3$ phase is approximately 2% less than twice the average Mg-F bond length.

In this study, the local $NaMgF_3$ structure (< 2 nm) is probed directly through least-squares refinement of structure models fit to the pair-distribution function (G(r)) derived from the total x-ray scattering of sample powders *in situ* at high temperature. Based on refined structure models, we examine Mg-F distances and the local three dimensional $NaMgF_3$ structure as a function of temperature. Considering previous studies utilizing diffraction and molecular dynamics simulation, we discuss how differences between local and average $NaMgF_3$ structure develop at high temperature.

4.3. Experimental Methods

Polycrystalline $NaMgF_3$ was synthesized according to methods described in Zhao *et al.* (1993a). X-ray scattering was performed using the RA-PDF technique (Chupas *et al.*, 2003), utilizing a monochromatic high energy (0.13724(2) Å, 90.43(1) keV) x-ray beam selected from a Si 111 monochromator at beamline 11-ID-B at the Advanced Photon Source, Argonne National Laboratory, Argonne IL. Sample powder was loaded

into a 0.8 mm polyimide capillary, which provided an inert barrier between the sample and an outer 1 mm quartz capillary under vacuum. The sample assembly was heated using a resistive heater (Chupas *et al.*, 2001) and temperature was ramped from 50 to 850 ˚C over 4 hours. Scattering data were collected every ~4 minutes, while temperature was increased in 16 ˚C steps, on a MAR345 imaging plate detector positioned 238.55(2) mm from the sample. The parasitic scattering from the atmosphere and capillary were collected using the same temperature ramp, duplicating the assembly without sample in place. To enhance signal-to-noise discrimination at high Q values, every 6 exposures of raw data were averaged below 731 ˚C (a ±48 ˚C temperature range) and every 4 images were averaged above 731 ˚C (a ±32 ˚C temperature range) apart from 843 ˚C where 2 frames were averaged (a ±16 ˚C temperature range). Raw images were integrated to plots of intensity vs. 2theta using program Fit2D (Hammersley *et al.*, 1996). Program PDFgetX2 (Qiu *et al.*, 2004) was used for normalization of S(Q) from I(Q) and Fourier transformation to the reduced pair distribution function (G(r)). Program PDFFIT (Proffen & Billinge, 1999) was used for quantitative structural refinement from the reduced pair distribution function.

During structure refinement with program PDFFIT, the room temperature $NaMgF_3$ structure (Zhao *et al.*, 1993a) was constrained according to the space group ***P****bnm*. Each refined structure model served as the initial starting model for each successive structure refinement. Structure models were confirmed by conducting refinements in each temperature direction. Within PDFFIT, the scale factor and 3 resolution terms, delta, sigma, and srat (rcut = 3 Å) were refined along with cell parameters, atomic positions and isotropic temperature factors. Based on our preliminary structure refinements, the unit cell lengths for structure models at temperatures ≥779 ˚C were constrained to a single pseudo-cubic lattice parameter according to the relationship (***P****bnm*) $\sqrt{2}, \sqrt{2}, 2^{-1}$ for the *a*, *b*, and *c*-axes, respectively. Reasons for imposing these constraints are outlined in the results section.

4.4. Results

Through qualitative observation, the PDFs of $NaMgF_3$ (Fig. 4.1) show no evidence to support a decrease in average Mg-F distance with increasing temperature, as

observed with Rietveld refinement (Zhao *et al.*, 1993a). The first feature in G(r), three overlapping Mg-F distances (***P****bnm*) at 2 Å, broadens asymmetrically with increasing temperature. This asymmetry and close proximity of Na-F distances at 2.3 Å complicate a Gaussian extraction (Chapman *et al.*, 2005, Chupas *et al.*, 2004) of the average Mg-F distance. Because fitting a structure model to a full G(r) profile is not without experimenter bias, studies compare residuals from several structure models (Billinge & Kanatzidis, 2004, Michel *et al.*, 2006, Petkov *et al.*, 2002, Paglia *et al.*, 2006). It is important to realize that models obtained through direct fitting of a constrained structure to the PDF may not be a unique solution to the data and other interpretations may exist. In this study, the possibility of falling into false minima during refinement with PDFFIT was minimized by testing various starting structure configurations at each temperature and obtaining the same, hopefully global, minimum in the structure refinement.

Normalized structure functions (S(Q)-1) of $NaMgF_3$ at 59 ˚C and 819 ˚C are shown in (Fig. 4.2a) beside the corresponding G(r) profile fit with the published (Fig. 4.2b) and refined (Fig. 4.2c) structure models. PDFFIT finds structure models in the orthorhombic (***P****bnm*) space group provide a better fit to the G(r) profiles (Paglia *et al.*, 2006) at each temperature and local structure models refined here have subtle differences from the published long-range model of $NaMgF_3$ (Zhao *et al.*, 1993a).

The full data set of fitted parameters including bond lengths, displacement factors, unit cell, and atomic positions between 50 and 850 ˚C are listed in Table 4.1. Examination of structure models shows that asymmetry of the Mg-F feature at high temperature results from divergence of Mg-$F_{[4c]}$ and Mg-$F_{[8d]}$ distances and increasing displacement parameters (Fig. 4.3). Asymmetry of the Mg-F feature resembles that calculated previously by molecular dynamics simulation (Street *et al.*, 1997).

While structure models in space group ***P****bnm* better fit the data at all temperatures within our range, isotropic displacement parameters of fluorine ions in $NaMgF_3$ have very different trends before and after 765 ˚C (Fig. 4.4), suggesting a transition (Zhao *et al.*, 1993a) between high and low temperature structure. Displacement parameters of the two fluorine sites are inconsistent with values reported by Zhao *et al.* (1993a). Zhao *et al.* (1993a) find both fluorine sites in NaMgF3 (***P****bnm*) have very similar displacement parameters, which increase rapidly preceding 765 ˚C, whereas analysis of the PDF shows

each fluorine site has unique isotropic displacement parameters. Also contrary to previous studies utilizing powder diffraction and Rietveld refinement (Street *et al.*, 1997, Zhao *et al.*, 1993a), when the isotropic constraint to the displacement parameter is relaxed during structure refinement, models with anisotropic displacement parameters do not improve fit to the data.

A transition in $NaMgF_3$ near 765 ˚C is suggested by the lattice parameters derived from refinement of local structure models. Because the magnesium ion occupies the special position (Wyckoff 4a, ***P****bnm*; 0, 0.5, 0), by transforming the orthorhombic lattice parameters of $NaMgF_3$ to pseudo-cubic (PC) lattice parameters, the unit cell is defined in terms of the Mg-Mg distances concordant with the pseudo-cubic axes (Fig. 4.5a). Structure models indicate convergence of the two Mg-Mg distances along $(0\ 1\ 0)_{PC}$ and $(0\ 0\ 1)_{PC}$ before convergence of all three Mg-Mg distances. Thus, the unit cell describing the local structure of $NaMgF_3$ appears metrically tetragonal above 350 ˚C and metrically cubic above 765 ˚C. Local structure models show an increase in the Mg-Mg distances at the transition (765 ˚C) and this is reflected in the unit cell volume (Fig. 4.5b), which shows an otherwise linear relationship with temperature.

The three unique Mg-F bond lengths (Fig. 4.6) are plotted as a function of temperature in Figure 4.7 alongside the average Mg-F distance and the average Mg-F distance reported by Zhao *et al.* (1993a). As temperature increases, structure models show a continuous monotonic increase in the $Mg\text{-}F_{[4c]}$ bond length, while the two $Mg\text{-}F_{[8d]}$ bond lengths converge at the transition. The average Mg-F bond length in local structure models increases linearly without discontinuity. Because all Mg-F bond lengths must be equal in a cubic perovskite (***P****m*$\bar{3}$*m*) structure, data indicate $NaMgF_3$ maintains orthorhombic internal symmetry and MgF_6 octahedra have local distortion.

In $NaMgF_3$ perovskite, the sodium ion occupies the cage created by 8 corner-sharing MgF_6 octahedra, thus 4 unique Mg-Na distances (***P****bnm*, mirror plane perpendicular to $[0\ 0\ 1]_{Pbnm}$) show how the sodium ion changes position in the structure. We find Mg-Na distances converge as temperature increases and at 765 ˚C, sodium appears equal distant to the surrounding 8 magnesium ions, occupying a position consistent with that in cubic (***P****m*$\bar{3}$*m*) perovskite (Fig. 4.8). Above the transition, sodium is displaced from the this position by equal values in x and y such only two unique Mg-

Na distances occur as Na sits equidistant to each 4 neighboring magnesium ions in the [1 1 0]$_{Pbnm}$ plane.

Program PDFFIT returns atom positions based on interatomic distances and space group symmetry within the unit cell. Local structure models of $NaMgF_3$ at temperatures below transition reveal Na and $F_{[4c]}$, have one position parameter ($Na_{[y]}$; $F_{[x]}$) in close agreement with Zhao *et al.* (1993), while the other position parameter ($Na_{[x]}$; $F_{[y]}$) deviates (Fig. 4.9). Fractional coordinates of the fluorine ion in the general Wycoff position 8d (x, y, z) deviate to a lesser extent from values reported by Zhao *et al.* (1993).

Using structure data we are able to construct F-Mg-F and Mg-F-Mg bond angles, addressing the deformation (bias) of the MgF_6 unit from a perfect octahedron as well as tilt angle (Glazer, 1972, , 1975) of MgF_6 octahedra. In the ideal cubic ($\boldsymbol{Pm\bar{3}m}$) $NaMgF_3$ structure, the MgF_6 unit is a perfect octahedron and tilt is forbidden, thus all F-Mg-F angles are 90˚ and all Mg-F-Mg angles are 180˚. While previous structure models (Zhao *et al.*, 1993a) find the $F_{[4c]}$-Mg-$F_{[8d]}$ and $F_{[8d]}$-Mg-$F_{[8d]}$ angles very similar, local structure models show more deformation of the MgF_6 unit as a result of two unique $F_{[4c]}$-Mg-$F_{[8d]}$ angles (Fig. 4.10). Because calculation of the tilt angle assumes perfect MgF_6 octahedra (Zhao *et al.*, 1993a), tilt angle measures are not reported for local structure models showing significant deformation of the MgF_6 unit.

The ratio between A- (Na, dodecahedra) and B-site (Mg, octahedra) volume (V_A/V_B) is useful for predicting phase transitions in perovskites (Zhao *et al.*, 2004, Thomas, 1998) as well as in other ABX_3 structures (Martin *et al.*, 2007, in press, Martin *et al.*, 2006b). Geometry dictates that V_A/V_B equal 5 in cubic perovskites and < 5 in all other perovskites where V_A is reduced due to tilting of the MgF_6 V_B unit. Local structure models show that the V_A/V_B ratio follows values from Zhao *et al.* (1993a) until the transition where the ratio adopts a more gentle increase with temperature (Fig. 4.11). A decrease in V_B precedes the transition due to the divergence of the $F_{[8d]}$-Mg-$F_{[8d]}$ and $F_{[4c]}$-Mg-$F_{[8d]}$ angles which increase deformation of the MgF_6 unit.

4.5. Discussion

Local structure models fitted to the pair distribution function indicate the average Mg-F distance in $NaMgF_3$ increases linearly and neighborite maintains orthorhombic

(***P****bnm*) structure between 50 and 850 ˚C. However, it is important to realize previous Rietveld structure models (Street *et al.*, 1997, Zhao *et al.*, 1993a), finding a reduced Mg-F distance and a cubic structure at high temperature, are both consistent and correctly report the average long-range $NaMgF_3$ structure. Zhao *et al.* (1993a) and Street *et al.* (1997) conclude the Mg-F distance must be underestimated at high temperature as the result of thermal-motion of fluorine ions.

Evident in Rietveld structure models and molecular dynamics simulations as large discus-shaped probability-density ellipsoids, thermal-motion of fluorine could account for a reduction in Mg-F distance if the motion were not random, but correlated. If fluorine were to orbit about its average position in the cubic structure, we may understand the apparent reduction in the Mg-F distance as the structure model forcing fluorine to the average position within the probability-density ellipsoid. This phenomenon is well known (Chapman *et al.*, 2005, Chupas *et al.*, 2004, Tucker *et al.*, 2001, Qiu *et al.*, 2005). However, Street *et al.* (1997) find the probability-density ellipsoid describing fluorine in 'cubic' $NaMgF_3$ is shaped as a discus not a torus. Assuming one unique fluorine site in the structure (***Pm*** $\bar{3}$ *m*), the orbital thermal motion model is discounted.

Local structure models presented here have two unique fluorine sites (***P****bnm*) and in this case the orbital thermal motion of fluorine model (Fig. 4.12) is in agreement with the average $NaMgF_3$ structure. Using fluorine positions and unit cell dimensions for local structure models, we can calculate the radius of each fluorine ion torus. The radius of $F_{[4c]}$ is always larger than $F_{[8d]}$ and a 2:1 radius-ratio is reached by 600 ˚C. At 843 ˚C, $F_{[4c]}$ and $F_{[8d]}$ are displaced from the average cubic position by 0.517(7) Å and 0.238(6) Å, respectively. Considering the $NaMgF_3$ structure has two $F_{[8d]}$ per $F_{[4c]}$, these numbers confirm the F^- ion density reported in the Fourier maps of Street *et al.* (1997). Local structure models find the pseudo-cubic cell parameter is 1.73(23) % less than twice the average Mg-F bond distance at 843 ˚C, whereas "approximately 2 %" is reported in Street *et al.* (1997).

The exact nature of the apparent phase transition in $NaMgF_3$ at 765 ˚C is not clear. However, it is very likely the transition partitions modes of fluorine ion vibration. Raman spectra (Ocafrain *et al.*, 1996) show the vibrational modes associated with anti- and in-phase (Zhao *et al.*, 1993a) tilting vibrations of octahedra (250-50 cm^{-1}) decrease in

intensity before the transition at 765 ˚C. Yet, it appears the overall mode intensity is instead transferred to the background. The volume discontinuity at 765 ˚C corresponds to an increase in the average Mg-Mg distance. In order for this to take place some positional coordinates of each fluorine site may reach coordinates consistent with the cubic ($\boldsymbol{P}m\bar{3}m$) phase and $NaMgF_3$ may transition from the low temperature ***P****bnm* structure to the high temperature ***P****bnm* structure through a bridging phase with increased internal symmetry. However, a detailed investigation of the local $NaMgF_3$ structure in the critical region (600 ˚C – 765 ˚C) requires data with improved temperature resolution.

Reports of reflection splitting in the cubic $CaSiO_3$ perovskite sublattice at high pressure without the appearance of superlattice reflections (Hirose *et al.*, 2005, Kurashina *et al.*, 2004, Shim *et al.*, 2002) imply distortion of the unit cell to a tetragonal structure without tilting of SiO_6 octahedra. Because this type of structure distortion has not previously been reported in analogous perovskites, correlated atomic motion similar to that described here for $NaMgF_3$ may be responsible for this observation in $CaSiO_3$ (Li *et al.*, 2006a, 2006b).

References

Ansell, S., Krishnan, S., Weber, J. K. R., Felten, J. J., Nordine, P. C., Beno, M. A., Price, D. L. & Saboungi, M. L. (1997). *Physical Review Letters* **78**, 464-466.

Billinge, S. J. L. (2004). *Zeitschrift Fur Kristallographie* **219**, 117-121.

Billinge, S. J. L. & Kanatzidis, M. G. (2004). *Chemical Communications* 749-760.

Chao, E. C. T., Evans, H. T., Skinner, B. J. & Milton, C. (1961). *Am. Miner.* **46**, 379-393.

Chapman, K. W., Chupas, P. J. & Kepert, C. J. (2005). *Journal of the American Chemical Society* **127** 15630-15636

Chen, J. H., Liu, H. Z., Martin, C. D., Parise, J. B. & Weidner, D. J. (2005). *Am. Miner.* **90**, 1534-1539.

Chrosch, J., Colombo, M., Malcherek, T., Salje, E. K. H., Groat, L. A. & Bismayer, U. (1998). *Am. Miner.* **83**, 1083-1091.

Chupas, P. J., Chaudhuri, S., Hanson, J. C., Qiu, X. Y., Lee, P. L., Shastri, S. D., Billinge, S. J. L. & Grey, C. P. (2004). *Journal of the American Chemical Society* **126**, 4756-4757.

Chupas, P. J., Ciraolo, M. F., Hanson, J. C. & Grey, C. P. (2001). *Journal of the American Chemical Society* **123**, 1694-1702.

Chupas, P. J., Qiu, X. Y., Hanson, J. C., Lee, P. L., Grey, C. P. & Billinge, S. J. L. (2003). *Journal of Applied Crystallography* **36**, 1342-1347.

Dodony, I., Posfai, M. & Buseck, P. R. (2006). *Am. Miner.* **91**, 1831-1838.

Egami, T. & Billinge, S. J. L. (1994). *Underneath the Bragg Peaks: Structural analysis of complex materials.* Oxford: Pergamon Press.

Glazer, A. M. (1972). *Acta Crystallogr. Sect. B-Struct. Commun.* **B 28**, 3384-3392.

Glazer, A. M. (1975). *Acta Crystallogr. Sect. A* **31**, 756-762.

Guinier, A. (1994). *X-Ray Diffraction: In Crystals, Imperfect Crystals, and Amorphous Bodies*. New York Dover Publication.

Guthrie, M., Tulk, C. A., Benmore, C. J., Xu, J., Yarger, J. L., Klug, D. D., Tse, J. S., Mao, H. K. & Hemley, R. J. (2004). *Physical Review Letters* **93**.

Hammersley, A. P., Svensson, S. O., Hanfland, M., Fitch, A. N. & Hausermann, D. (1996). *High Pressure Research* **14**, 235-248.

Hirose, K., Takafuji, N., Sata, N. & Ohishi, Y. (2005). *Earth Planet. Sci. Lett.* **237**, 239-251.

Jeong, I. K., Heffner, R. H., Graf, M. J. & Billinge, S. J. L. (2003). *Phys Rev B* **67**.

Kurashina, T., Hirose, K., Ono, S., Sata, N. & Ohishi, Y. (2004). *Physics of the Earth and Planetary Interiors* **145**, 67-74.

Li, L., Weidner, D. J., Brodholt, J., Alfe, D., Price, G. D., Caracas, R. & Wentzcovitch, R. (2006a). *Physics of the Earth and Planetary Interiors* **155**, 249-259.

Li, L., Weidner, D. J., Brodholt, J., Alfe, D., Price, G. D., Caracas, R. & Wentzcovitch, R. (2006b). *Physics of the Earth and Planetary Interiors* **155**, 260-268.

Liu, H. Z., Chen, J., Hu, J., Martin, C. D., Weidner, D. J., Hausermann, D. & Mao, H. K. (2005). *Geophys. Res. Lett.* **32**, L04304(1-5).

Liu, L. G. (1976). *Physics of the Earth and Planetary Interiors* **11**, 289-298.

Martin, C. D., Chapman, K. W., Chupas, P. J., Prakapenka, V. B., Lee, P. L., Shastri, S. D. & Parise, J. B. (2007, in press). *Am. Miner.*

Martin, C. D., Chaudhuri, S., Grey, C. P. & Parise, J. B. (2005). *Am. Miner.* **90**, 1522-1533.

Martin, C. D., Crichton, W. A., Liu, H. Z., Prakapenka, V., Chen, J. H. & Parise, J. B. (2006a). *Geophys. Res. Lett.* **33**, L11305.
Martin, C. D., Crichton, W. A., Liu, H. Z., Prakapenka, V. B., Chen, J. & Parise, J. B. (2006b). *Am. Miner.* **91**, 1703-1706.
Michel, F. M., Schoonen, M. A. A., Zhang, X. V., Martin, S. T. & Parise, J. B. (2006). *Chem Mater* **18**, 1726-1736.
O'Keeffe, M. & Bovin, J. O. (1979). *Science* **206**, 599-600.
O'Keeffe, M., Hyde, B. G. & Bovin, J. O. (1979). *Phys. Chem. Miner.* **4**, 299-305.
Ocafrain, A., Chaminade, J. P., Viraphong, O., Cavagnat, R., Couzi, M. & Pouchard, M. (1996). *Journal of Crystal Growth* **166**, 414-418.
Okabe, I., Tanaka, H. & Nakanishi, K. (1996). *Physical Review E* **53**, 2638-2647.
Paglia, G., Bozin, E. S., Vengust, D., Mihailovic, D. & Billinge, S. J. L. (2006). *Chem Mater* **18**, 100-106.
Petkov, V., Gateshki, M., Niederberger, M. & Ren, Y. (2006). *Chem. Mater.* **18**, 814-821.
Petkov, V., Trikalitis, P. N., Bozin, E. S., Billinge, S. J. L., Vogt, T. & Kanatzidis, M. G. (2002). *Journal of the American Chemical Society* **124**, 10157-10162.
Proffen, T. & Billinge, S. J. L. (1999). *Journal of Applied Crystallography* **32**, 572-575.
Proffen, T., DiFrancesco, R. G., Billinge, S. J. L., Brosha, E. L. & Kwei, G. H. (1999). *Physical Review B* **60**, 9973-9977.
Qiu, X., Thompson, J. W. & Billinge, S. J. L. (2004). *Journal of Applied Crystallography* **37**, 678.
Qiu, X. Y., Proffen, T., Mitchell, J. F. & Billinge, S. J. L. (2005). *Physical Review Letters* **94**, 177203.
Rietveld, H. M. (1969). *Journal of Applied Crystallography* **2**, 65.
Ringwood, A. E. (1994). *Physics of the Earth and Planetary Interiors* **86**, 5-24.
Shim, S. H., Jeanloz, R. & Duffy, T. S. (2002). *Geophys. Res. Lett.* **29**.
Stixrude, L. & Karki, B. (2005). *Science* **310**, 297-299.
Street, J. N., Wood, I. G., Knight, K. S. & Price, G. D. (1997). *J. Phys.-Condes. Matter* **9**, L647-L655.
Thomas, N. W. (1998). *Acta Crystallogr. Sect. B-Struct. Commun.* **54**, 585-599.
Tucker, M. G., Keen, D. A. & Dove, M. T. (2001). *Mineral. Mag.* **65**, 489-507.
Viani, A., Gaultieri, A. F. & Artioli, G. (2002). *Am. Miner.* **87**, 966-975.
Warren, B. E. (1969). *X-ray Diffraction*. Reading-MA: Addison-Wesley.
Young, R. A. (1993). Editor. The Rietveld Method, 1st ed. Oxford: Oxford University Press.
Zhao, J., Ross, N. L. & Angel, R. J. (2004). *Acta Crystallogr. Sect. B-Struct. Commun.* **60**, 263-271.
Zhao, Y. S., Weidner, D. J., Parise, J. B. & Cox, D. E. (1993a). *Physics of the Earth and Planetary Interiors* **76**, 1-16.
Zhao, Y. S., Weidner, D. J., Parise, J. B. & Cox, D. E. (1993b). *Physics of the Earth and Planetary Interiors* **76**, 17-34.

a)

T(°C)	*R_W (%)	a (Å)	b (Å)	c (Å)	V (Å^3)	$Na_{[4c, x]}$	$Na_{[4c, y]}$	$F_{[4c, x]}$	$F_{[4c, y]}$	$F_{[8d, x]}$	$F_{[8d, y]}$	$F_{[8d, z]}$
59	11.9	5.34955(64)	5.48590(71)	7.68550(75)	225.547(45)	0.98910(35)	0.04266(19)	0.08940(53)	0.45395(60)	0.71250(28)	0.29195(21)	0.05069(12)
107	11.6	5.36280(68)	5.49100(68)	7.69590(82)	226.622(51)	0.98880(39)	0.04217(20)	0.08805(53)	0.45420(60)	0.71230(32)	0.29140(21)	0.04962(13)
155	12.0	5.37645(94)	5.4928(11)	7.7103(12)	227.700(69)	0.98800(50)	0.03975(29)	0.08705(64)	0.45470(75)	0.71265(39)	0.29105(25)	0.04897(18)
203	12.2	5.39050(96)	5.5012(11)	7.7176(12)	228.862(70)	0.98645(53)	0.03815(32)	0.08545(67)	0.45485(74)	0.71400(40)	0.29000(28)	0.04846(16)
251	13.1	5.4002(10)	5.5060(12)	7.7324(13)	229.912(76)	0.98610(57)	0.03575(36)	0.08350(68)	0.45275(78)	0.71450(46)	0.28970(28)	0.04749(19)
299	13.4	5.4010(16)	5.5095(16)	7.7622(16)	230.98(11)	0.98675(72)	0.03345(45)	0.08085(72)	0.45170(87)	0.71595(51)	0.28830(36)	0.04705(18)
347	14.4	5.4147(15)	5.5082(19)	7.7805(21)	232.05(12)	0.98615(88)	0.03105(53)	0.07990(84)	0.45040(96)	0.71395(67)	0.28750(39)	0.04500(21)
395	14.1	5.4329(16)	5.5141(17)	7.7882(21)	233.31(12)	0.9878(10)	0.02850(51)	0.07765(79)	0.45060(97)	0.71435(65)	0.28755(36)	0.04321(24)
443	15.5	5.4505(25)	5.5205(25)	7.7980(32)	234.63(18)	0.9863(14)	0.02670(74)	0.0777(11)	0.4459(12)	0.71565(92)	0.28550(53)	0.04145(32)
491	15.8	5.4625(21)	5.5190(21)	7.8190(28)	235.72(15)	0.9846(13)	0.02490(78)	0.0746(11)	0.4457(12)	0.71440(92)	0.28420(57)	0.04030(32)
534	15.0	5.4760(29)	5.5270(29)	7.8160(36)	236.55(21)	0.9873(18)	0.02425(85)	0.0736(11)	0.4475(13)	0.7158(10)	0.28460(60)	0.03895(35)
587	16.8	5.4935(28)	5.5370(32)	7.8150(46)	237.71(23)	0.9855(21)	0.02320(99)	0.0726(13)	0.4454(14)	0.7160(13)	0.28405(78)	0.03635(46)
635	16.8	5.5040(32)	5.5455(32)	7.8300(42)	238.99(23)	0.9865(21)	0.0179(11)	0.0671(13)	0.4405(13)	0.7171(12)	0.28265(78)	0.03415(46)
683	17.6	5.5210(46)	5.5585(46)	7.8370(64)	240.50(34)	0.9900(42)	0.0123(13)	0.0618(19)	0.4333(18)	0.7185(17)	0.28130(99)	0.02940(64)
731	22.1	5.5510(51)	5.5755(45)	7.8625(61)	243.34(35)	0.995(11)	0.0027(18)	0.0520(19)	0.4269(17)	0.7240(21)	0.2778(13)	0.02355(92)
779	19.9	3.92940(50)			242.682(53)	0.9910(52)	0.0032(12)	0.0561(13)	0.4290(11)	0.7205(11)	0.27830(80)	0.02105(68)
787	20.3	3.93140(53)			243.053(57)	0.9955(49)	0.0098(13)	0.0591(14)	0.4294(12)	0.7194(12)	0.27905(88)	0.01945(69)
803	18.9	3.93320(57)			243.387(61)	0.9895(40)	0.0088(13)	0.0587(15)	0.4298(13)	0.7197(14)	0.2784(10)	0.01915(74)
819	18.9	3.93370(50)			243.480(54)	0.9895(29)	0.0094(12)	0.0580(13)	0.4287(11)	0.7196(11)	0.27835(83)	0.01925(67)
827	19.2	3.93430(50)			243.591(54)	0.9894(23)	0.0094(11)	0.0580(11)	0.42870(96)	0.7196(10)	0.27835(73)	0.01925(60)
835	19.7	3.93805(64)			244.288(68)	0.9890(49)	0.0104(16)	0.0590(21)	0.4281(17)	0.7208(20)	0.2785(12)	0.01895(96)
843	21.4	3.93560(80)			243.833(86)	0.9890(40)	0.0111(18)	0.0583(14)	0.4275(12)	0.7212(13)	0.27850(92)	0.01900(71)

!! Continued on next page !!

!! Continued from last page !!

b)

T(°C)	U-Na (Å^2)	U-Mg (Å^2)	U-$F_{[4c]}$ (Å^2)	U-$F_{[8d]}$ (Å^2)	Mg-$F_{[4c]}$ (Å)	Mg-$F_{[8d]}$ (Å)	Mg-$F_{[8d]}$ (Å)	Mg-Na (Å)	Mg-Na (Å)	Mg-Na (Å)	Mg-Na (Å)
59	0.015595(57	0.007318(2(	0.04125(32)	0.013100(3:	1.9961(8)	1.9544(14)	2.0023(13)	3.1607(9)	3.2546(15)	3.3491(16)	3.5437(9)
107	0.018215(71	0.008400(2:	0.04450(32)	0.014905(3(	1.9970(8)	1.9592(15)	2.0006(14)	3.1663(9)	3.2599(17)	3.3572(17)	3.5452(10)
155	0.02232(10)	0.009810(3:	0.04755(43)	0.017370(5(	1.9991(10)	1.9613(19)	2.0014(17)	3.1797(13)	3.2630(22)	3.3676(22)	3.5369(14)
203	0.02542(12)	0.010715(3:	0.05175(46)	0.019270(57	1.9991(10)	1.9625(20)	2.0039(18)	3.1911(15)	3.2623(23)	3.3808(24)	3.5344(16)
251	0.02943(14)	0.011690(3(	0.05305(53)	0.021540(6(	2.002(1)	1.9628(22)	2.0052(19)	3.2057(17)	3.2660(25)	3.3878(26)	3.5276(18)
299	0.03245(17)	0.012550(4(	0.05365(58)	0.023700(9(	2.0068(11)	1.9615(25)	2.0042(23)	3.2215(21)	3.2728(32)	3.3888(33)	3.5226(22)
347	0.03700(21)	0.013690(4(	0.05535(67)	0.02558(11)	2.0113(13)	1.9727(32)	1.9931(28)	3.2344(25)	3.2775(39)	3.3991(40)	3.5136(26)
395	0.04241(23)	0.015120(5(	0.05925(72)	0.02768(12)	2.0108(13)	1.9733(31)	1.9959(27)	3.2488(24)	3.2923(44)	3.3999(45)	3.5054(25)
443	0.04595(32)	0.016630(7(	0.06140(96)	0.03083(19)	2.0172(18)	1.9770(44)	1.9925(38)	3.2608(34)	3.2936(62)	3.4149(64)	3.5015(36)
491	0.04880(28)	0.017635(71	0.06205(92)	0.03275(21)	2.0191(17)	1.9879(44)	1.9827(39)	3.2716(36)	3.2935(58)	3.4302(59)	3.4958(37)
534	0.05215(32)	0.018355(7(	0.06395(99)	0.03555(25)	2.0161(18)	1.9829(48)	1.9908(43)	3.2767(40)	3.3101(80)	3.4232(82)	3.4955(41)
587	0.05575(42)	0.019170(8(	0.0638(11)	0.03875(32)	2.0168(21)	1.9861(62)	1.9906(55)	3.2853(46)	3.3086(94)	3.4383(96)	3.4951(48)
635	0.06145(42)	0.020455(9:	0.0641(11)	0.04210(28)	2.0192(20)	1.9872(59)	1.9890(53)	3.3143(51)	3.3184(94)	3.4394(96)	3.4765(53)
683	0.06690(67)	0.02170(11)	0.0632(13)	0.04465(46)	2.023(3)	1.9865(82)	1.9883(73)	3.3452(62)	3.3409(189)	3.4310(191)	3.4570(63)
731	0.07285(83)	0.02323(15)	0.0561(14)	0.05085(65)	2.0281(28)	1.9790(102)	1.9948(93)	3.3989(84)	3.3785(497)	3.4238(500)	3.4235(85)
779	0.07210(49)	0.02359(11)	0.00579(92)	0.04995(34)	2.0280(16)	1.9894(55)	1.9800(52)	3.3888(55)	3.3623(235)	3.4440(237)	3.4179(55)
787	0.07435(50)	0.02386(12)	0.05900(99)	0.04960(32)	2.0313(18)	1.9916(61)	1.9795(56)	3.3604(59)	3.3847(222)	3.4256(223)	3.4494(60)
803	0.07445(61)	0.02406(12)	0.0592(11)	0.05060(39)	2.0314(19)	1.9932(70)	1.9784(65)	3.3669(59)	3.3591(180)	3.4544(183)	3.4468(60)
819	0.07505(56)	0.02429(12)	0.05910(90)	0.05075(34)	2.0322(17)	1.9941(56)	1.9782(52)	3.3646(54)	3.3596(131)	3.4549(133)	3.4500(55)
827	0.07505(45)	0.02429(11)	0.05910(83)	0.05075(29)	2.0325(14)	1.9945(50)	1.9785(47)	3.3652(50)	3.3596(104)	3.4559(105)	3.4505(50)
835	0.07580(92)	0.02465(15)	0.0595(13)	0.05095(57)	2.0360(27)	1.9904(97)	1.9850(87)	3.3639(73)	3.3611(221)	3.4611(224)	3.4584(74)
843	0.07560(80)	0.02462(18)	0.0597(15)	0.05080(50)	2.0348(19)	1.9875(65)	1.9851(60)	3.3586(81)	3.3591(180)	3.4590(183)	3.4595(83)

* $R_w = 100\%[\Sigma w(r_i)(G_{obs}(r_i)-G_{calc}(r_i))^2 / \Sigma w(r_i)(G^2_{obs}(r_i))]^{1/2}$

$G_{obs}(r_i)$ is the observed PDF value, $G_{calc}(r_i)$ is the calculated PDF value and $w(r_i)$ is the weight associated with each data point.

[Table 4.1] (a) Structure parameters, (b) displacement parameters, and atom distances derived from PDFFIT are listed for $NaMgF_3$ (*Pbnm*) at several temperatures. At temperatures greater than 731 ˚C, the unit cell lengths of our structure models were constrained to a single pseudo-cubic lattice parameter according to the relationship (*Pbnm*) $\sqrt{2}, \sqrt{2}, 2^{-1}$ for the *a*-, *b*-, and *c*-axes, respectively.

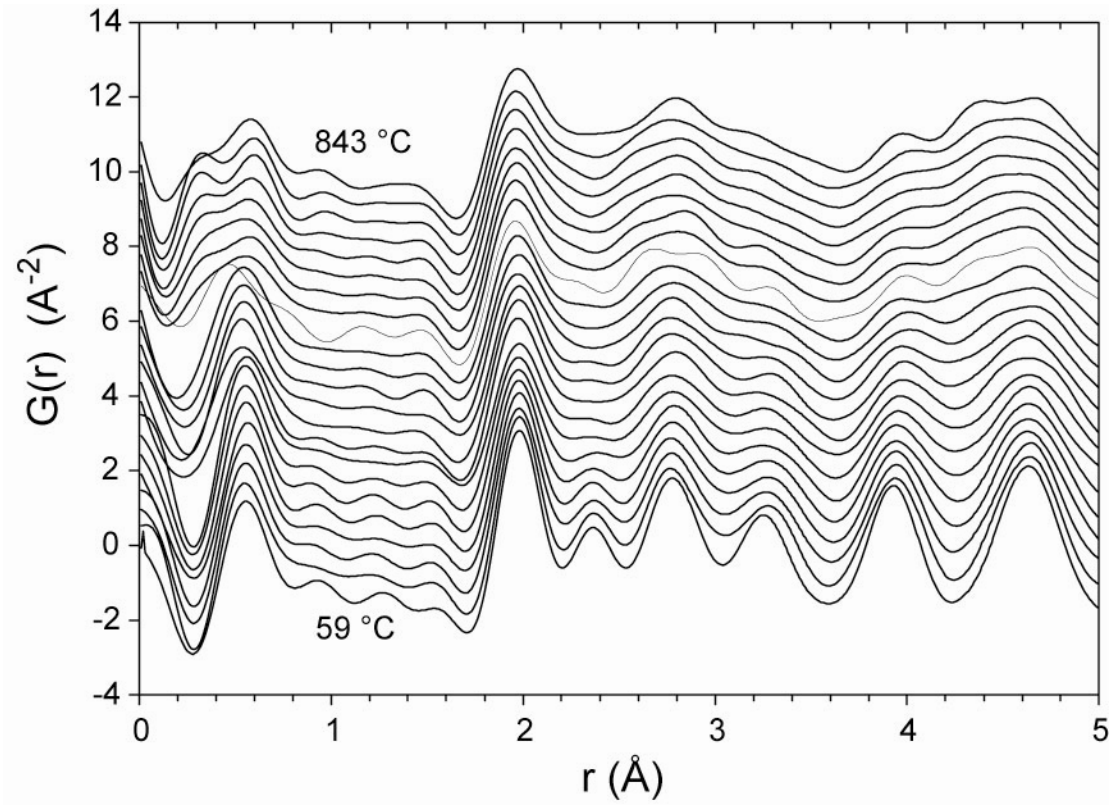

[Fig. 4.1] (a) The reduced pair distribution functions (G(r)) obtained through direct Fourier transformation of the observed structure functions (S(Q)) normalized from data collected at high temperature are plotted and stacked in order of increasing temperature. The function shown as a thin line is data at 731 ˚C. Features occurring at distances < 1 Å are residual error from normalization of the structure function.

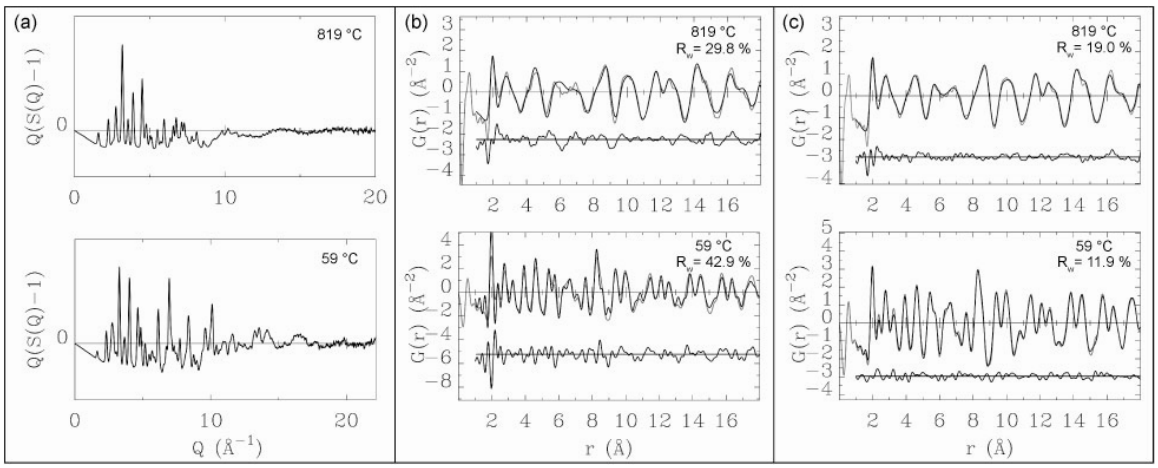

[Fig. 4.2] (a) The normalized structure functions (S(Q)-1) of $NaMgF_3$ at 59 ˚C (lower tier) and 819 ˚C (upper tier) are plotted adjacent to the corresponding reduced pair distribution functions (G(r)) fit using program PDFFIT. (b) Fits were achieved constraining to the orthorhombic (lower tier) and cubic (upper tier) structure models observed with Rietveld refinement (Zhao *et al.* 1993a), allowing the unit cell parameter(s), scale factor, anisotropic displacement parameters of fluorine, and resolution terms to refine, as 9 parameters. (c) Fits were achieved allowing atomic positions, isotropic displacement parameters, unit cell parameter(s), and resolution terms to refine as 16 parameters.

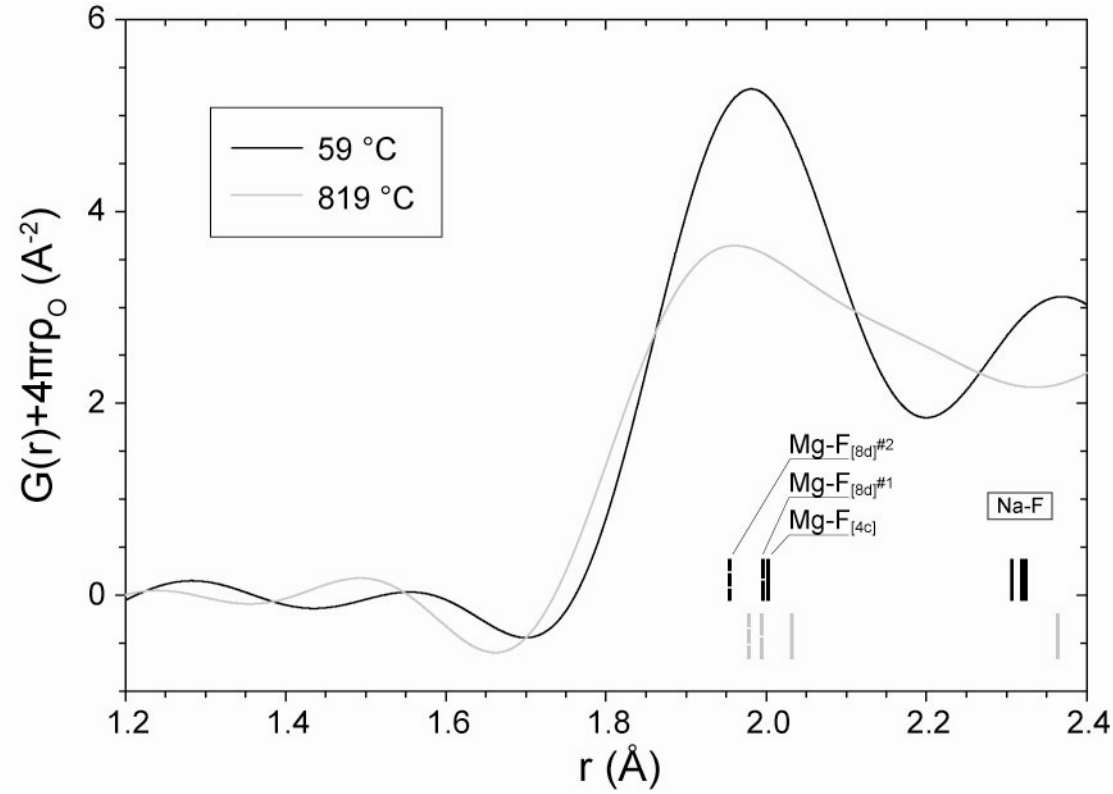

[Fig. 4.3] Radial distribution functions (G(r) + baseline, [$4\pi r\rho_o$]) obtained at minimum and maximum temperature. Peak positions assigned from structural models are marked. Data appear to confirm molecular dynamics simulation data presented in Street *et al.* (1997), where the Mg-F correlation shows significant asymmetry at high temperature.

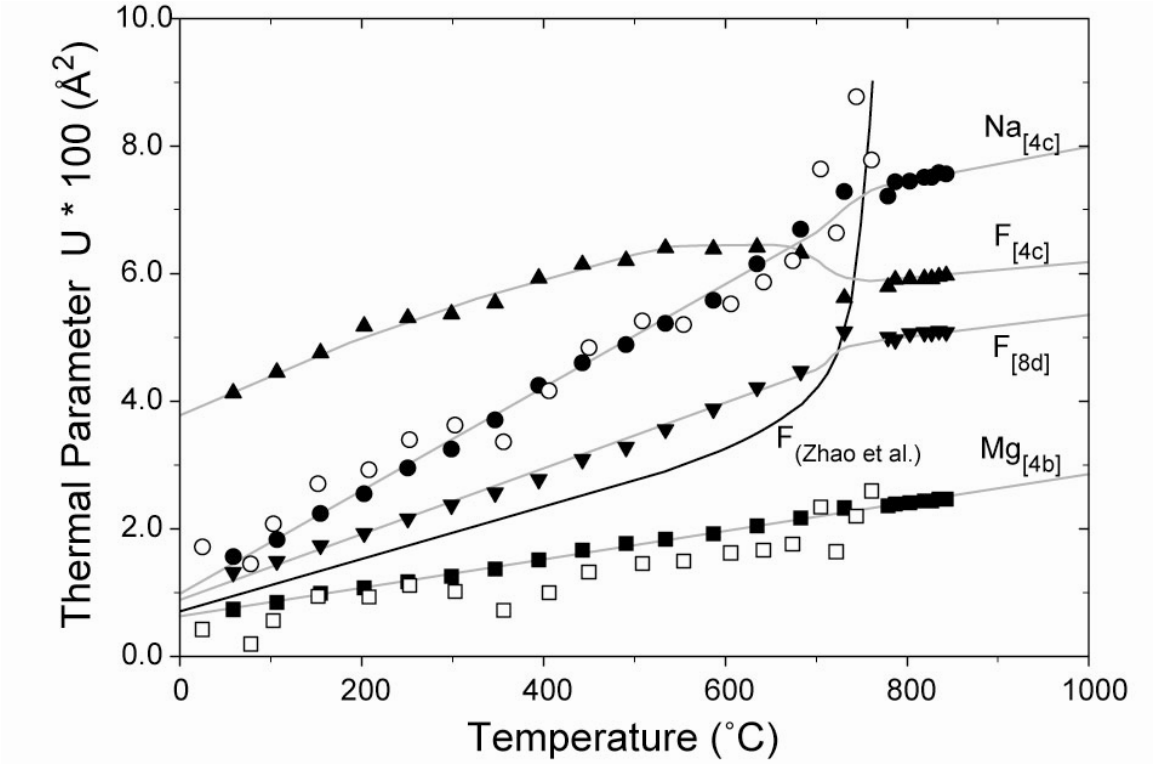

[Fig. 4.4] The isotropic displacement parameter of each ion in $NaMgF_3$ is plotted as a function of temperature. Black symbols are data in the current study, while open symbols and solid black line are data from Zhao *et al.* (1993a). Errors bars are on the order of symbol size and grey lines are intended to guide the eye. Labels include the Wyckoff position of the ion in the crystal structure.

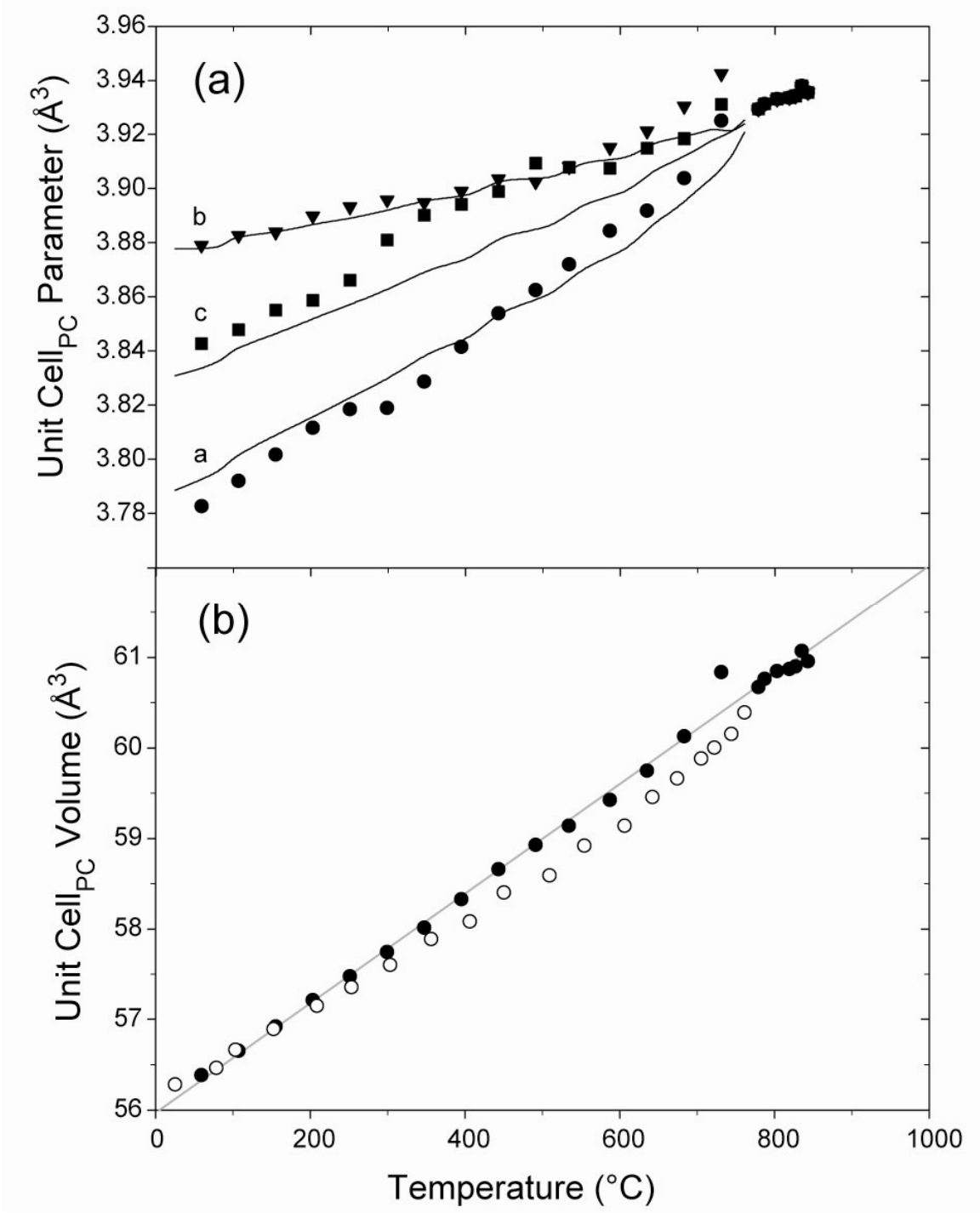

[Fig. 4.5] (a) The reduced (pseudo-cubic, $\sqrt{2}, \sqrt{2}, 2^{-1}$) unit cell axes and (b) volume are plotted as a function of temperature. Black symbols are data in the current study, while open circles and solid black lines are data from Zhao *et al.* (1993a). Errors bars are on the order of symbol size and grey lines are intended to guide the eye.

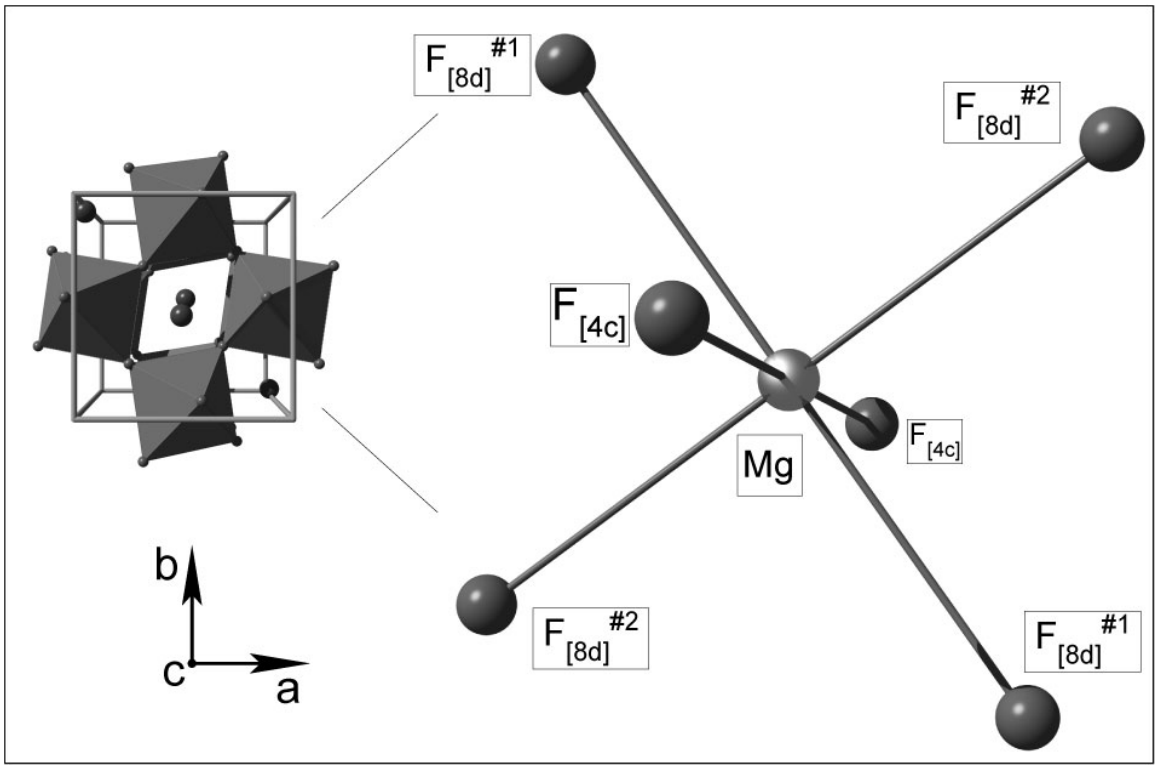

[Fig. 4.6] A structure model of $NaMgF_3$ perovskite at room temperature illustrates the octahedral coordination environment of the MgF_6 unit normal to the c-axis. Labels include the Wyckoff position of the fluorine ion in the crystal structure.

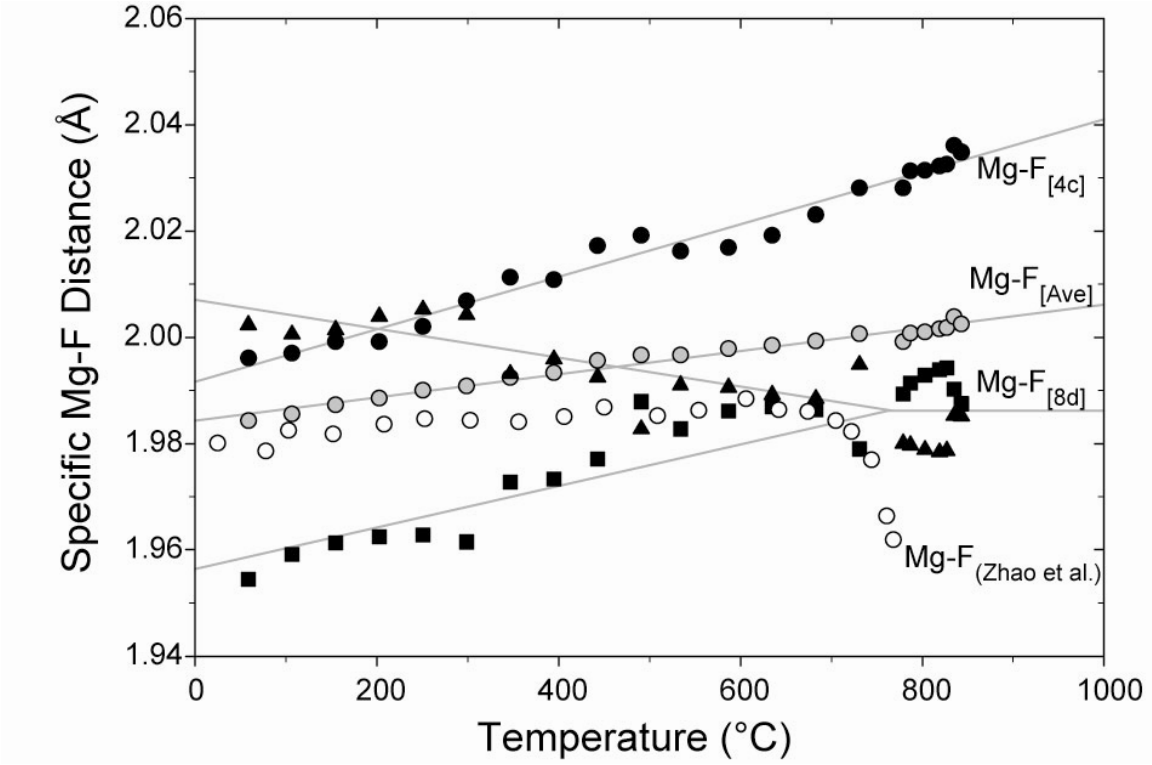

[Fig. 4.7] The specific Mg-F bond lengths are plotted as a function of temperature. Black symbols are data in the current study, grey circles are the average Mg-F bond length value, while open circles are the average Mg-F bond length value from Zhao *et al.* (1993a). Errors bars are on the order of symbol size, though larger near the transition, and grey lines are intended to guide the eye. Labels include the Wyckoff position of the fluorine ion in the crystal structure.

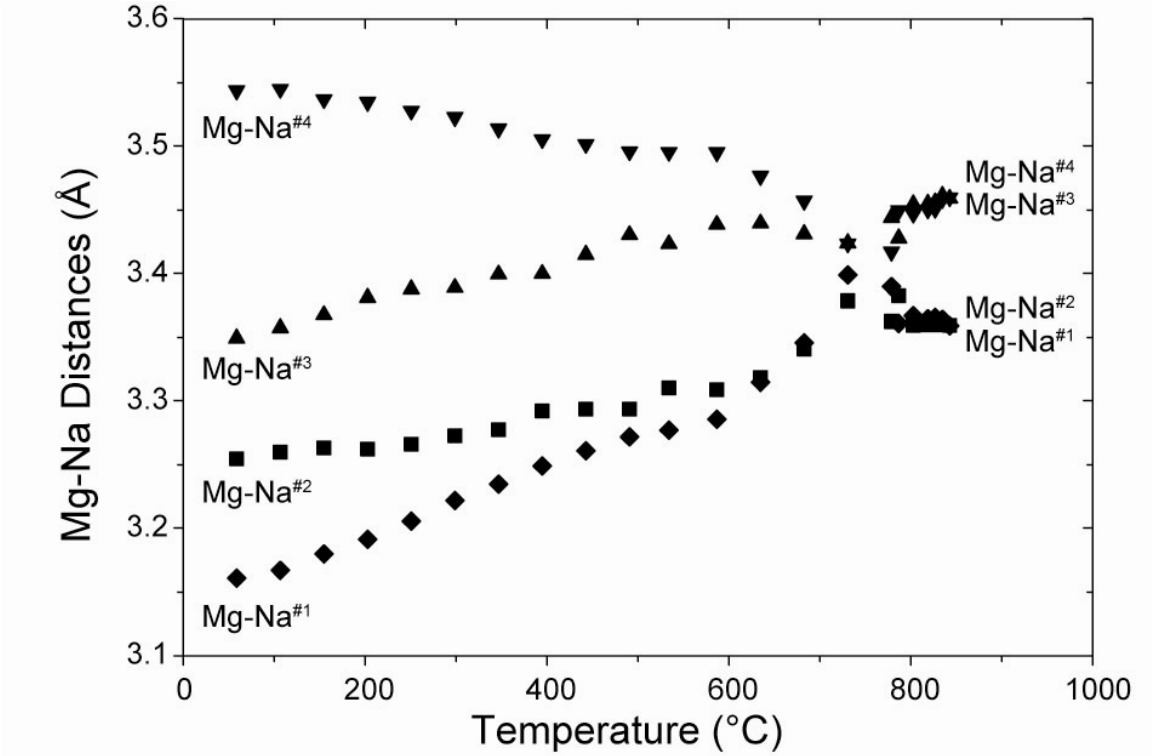

[Fig. 4.8] The four unique Mg-Na distances are plotted as a function of temperature. Errors bars are on the order of symbol size and larger near the transition.

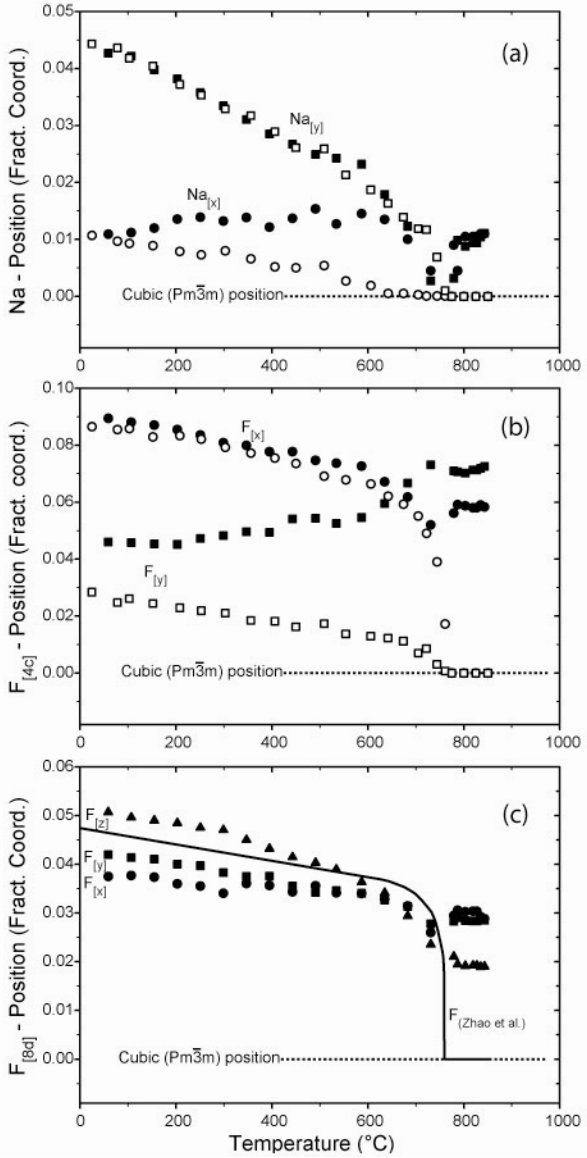

[Fig. 4.9] The position parameters of the (a) Na, (b) $F_{[4c]}$, and (c) $F_{[8d]}$ ions in the orthorhombic $NaMgF_3$ crystal structure are respectively normalized to the cubic position and plotted as a function of temperature. Black symbols are data in the current study, while open symbols and solid black line are data from Zhao *et al.* (1993a). The solid black line approximates the very close $F_{[8d]}$ x, y, and z values reported in Zhao *et al.* (1993a). Errors bars are on the order of symbol size and larger near the transition.

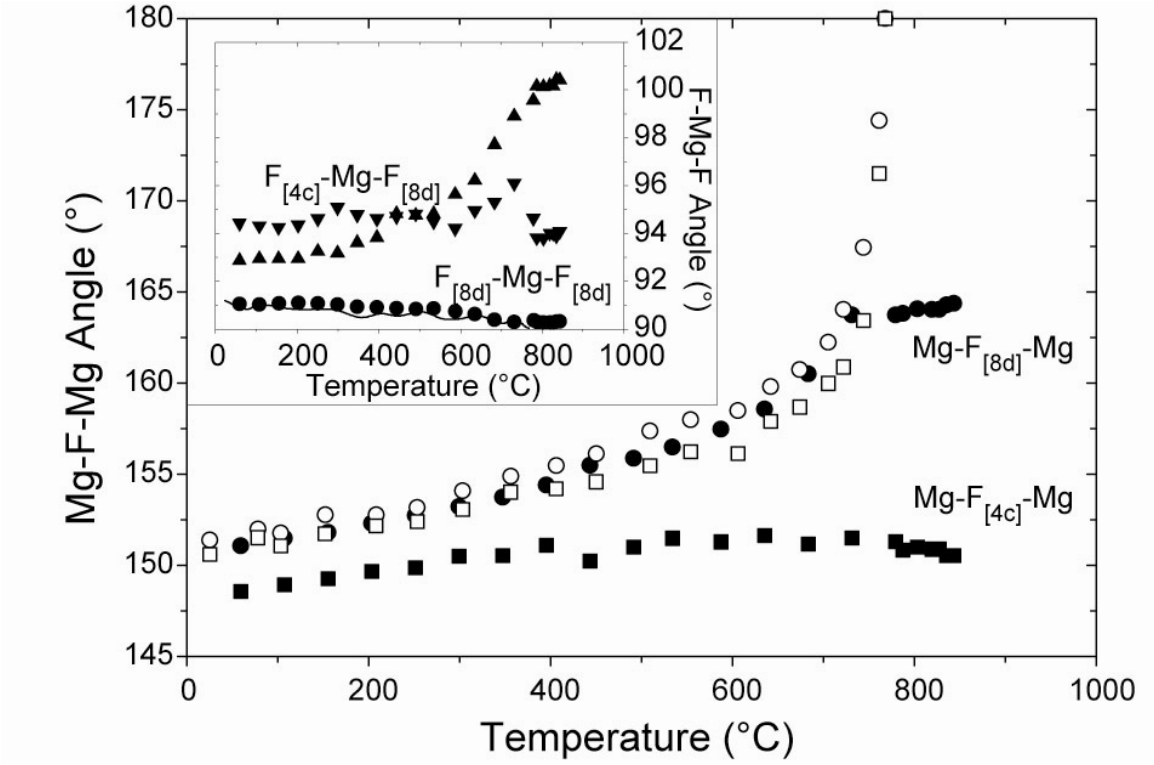

[Fig. 4.10] The Mg-F-Mg and F-Mg-F (inset) bond angles are plotted as a function of temperature. Black symbols are data in the current study, while open symbols and solid black line are data from Zhao *et al.* (1993a). Errors bars are on the order of symbol size and larger near the transition. Labels include the Wyckoff position of the fluorine ion in the crystal structure.

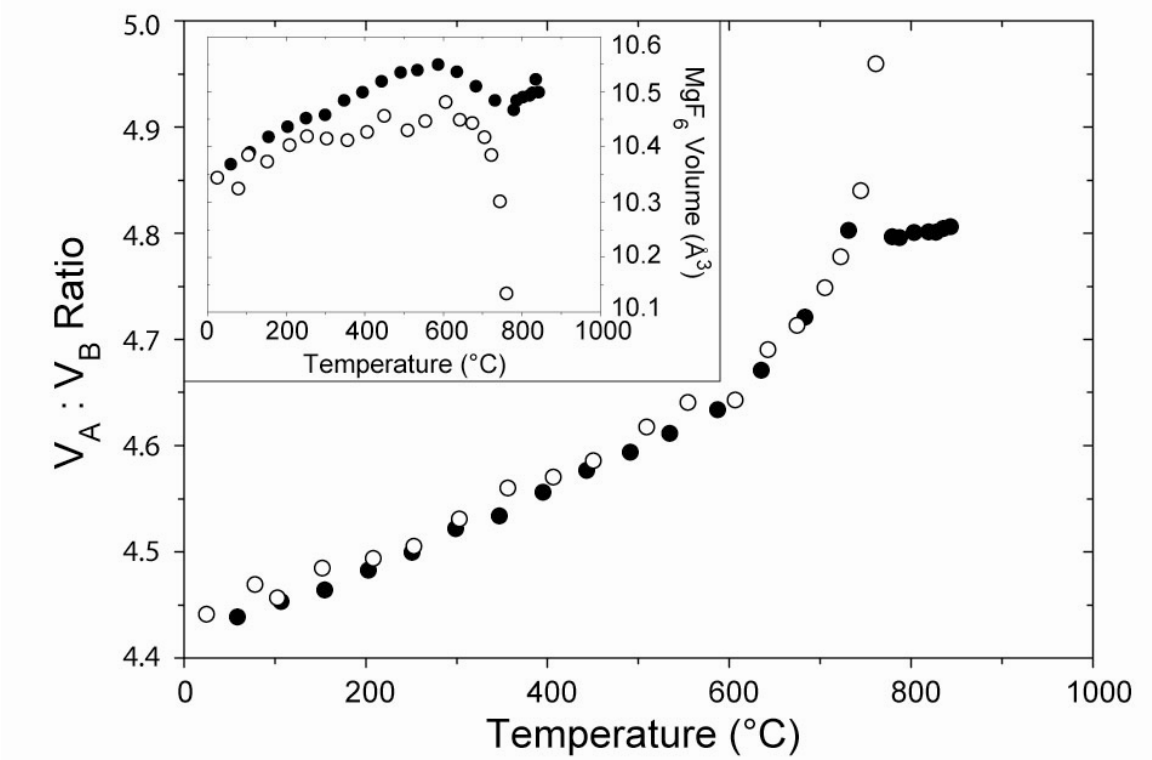

[Fig. 4.11] The volume ratio of the sodium polyhedra to the magnesium octahedra (V_A/V_B) in $NaMgF_3$ is plotted as a function of temperature. The volume of the MgF_6 unit is plotted a function of temperature (inset). Black symbols are data in the current study, while open symbols are data from Zhao *et al.* (1993a). Errors bars are on the order of symbol size.

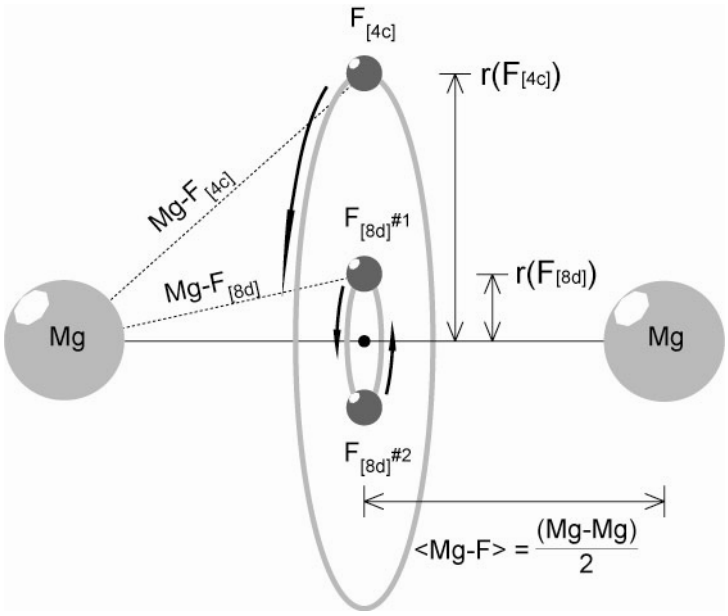

[Fig. 4.12] Structure model diagram illustrating orbital thermal motion of the $F_{[4c]}$ and two $F_{[8d]}$ ions in the $NaMgF_3$ structure. The radius of each torus is defined by the distance from the position of the ion in the ideal cubic ($Pm\bar{3}m$) perovskite and the midpoint between two nearest Mg ions, which defines the Mg-F bond length in the average structure (<Mg-F>).

Chapter V

Structural distortion, critical behavior, and elasticity of $NaMgF_3$ perovskite at simultaneous high pressure and temperature

THIS CHAPTER IN PREPARATION FOR PUBLICATION.:

MARTIN, C.D., KUNG, J., CRICHTON, W.A., LI, B., WEIDNER, D.J., AND PARISE, J.B. STRUCTURAL DISTORTION, CRITICAL BEHAVIOR, AND ELASTICITY OF $NaMgF_3$ PEROVSKITE AT SIMULTANEOUS HIGH PRESSURE AND TEMPERATURE.

5.1. Abstract

In this chapter, using monochromatic x-ray diffraction with Rietveld refinement, the long-range structure of $NaMgF_3$ is found to transition from orthorhombic (***P****bnm*) to cubic (***P****m*$\bar{3}$*m*) at high pressures (7 GPa) and temperatures (1400 K) via second-order phase transition. Ultrasonic measurements of $NaMgF_3$ yield thermoelastic equation of state and provide evidence for sample-induced elastic attenuation at pressures and temperature near the orthorhombic to cubic phase transition. Data from the average structure modeling suggests rotation and deformation of perovskite octahedra coincide with unit cell distortion as a function of distance from the phase transition in pressure-temperature space. The apparent linear relationship between the pressure and temperature induced structural modification suggests the average $NaMgF_3$ structure will not transition to tetragonal (i.e., ***P***4/*mbm*) symmetry as both pressure and temperature increase and the strong stabilization effect of pressure on the orthorhombic perovskite suggests $MgSiO_3$ in Earth's lower mantle should not undergo perovskite-perovskite phase transformations.

5.2. Introduction

Perovskite-structured $MgSiO_3$ dominates the mineralogy of Earth's lower mantle; thus the structure and properties of this material under changing pressures and

temperatures must be known in order to interpret seismic observations e.g., (Lay et al., 1998; van der Hilst and Karason, 1999). Because of the extreme conditions required to stabilize $MgSiO_3$ perovskite (Liu, 1976), techniques required to determine the structure and elasticity of this phase are either impossible to implement or subject to unsatisfactorily low precision. However, changes in the structure and properties of other perovskite structures at more modest pressures and temperatures (*p-T*) are readily measurable and may act as a proxy for $MgSiO_3$ in Earth's lower mantle.

The mineral neighborite ($NaMgF_3$) (Chao et al., 1961) is isostructural and a well-suited analog material for $MgSiO_3$ perovskite (Umemoto et al., 2006; Zhao et al., 1993a). The more flexible bonding of fluorine relative to oxygen leads to more structure change per unit pressure and may simulate structures and properties of $MgSiO_3$ perovskite under much higher pressures.

Through analysis of monochromatic X-ray diffraction and Rietveld structure refinement of $NaMgF_3$ at room pressure, the tilt angle of MgF_6 octahedra is found to decrease at high temperature (Zhao et al., 1993a; Zhao et al., 1993b). At 765 ˚C the perovskite appears to undergo a phase transition directly from orthorhombic (***P****bnm*) to cubic (***P****m*$\bar{3}$*m*) and Mg-F bond distances decrease with increasing temperature. However, the pair distribution function of $NaMgF_3$ (local structure), examined in a follow up experiment, indicates the average Mg-F bond length increases linearly with temperature and 765 ˚C may correspond to a change in atomic vibration of fluorine atoms in the ***P****bnm* perovskite (Chapter 3). Thus it is important to consider X-ray diffraction as a probe of the average $NaMgF_3$ structure and susceptible to error when structures exhibit correlated atomic motion (Chapman et al., 2005; Chupas et al., 2004; Qiu et al., 2005; Tucker et al., 2001). At high pressures, the rotation angle of MgF_6 octahedra in $NaMgF_3$ increase (Chen et al., 2005; Liu et al., 2005; Zhao et al., 1994a) and at simultaneous high *p-T*, previous work claims the compressibility of the $NaMgF_3$ unit cell is independent of temperature (Zhao et al., 1994b). Zhao et al. (1994b) argue that if this characteristic were true for $MgSiO_3$, some anomalous seismic observations in the lower mantle may be rationalized.

The elasticity of $NaMgF_3$ has not previously been the subject of study, however elastic discontinuities are known to follow structural phase transitions driven by pressure,

temperature, and partial ion substitution e.g., (Carpenter, 2000; Carpenter et al., 2006a; Carpenter and Salje, 1998; Carpenter et al., 2006b). Thus, characterizing the elasticity of $NaMgF_3$ at the orthorhombic-cubic phase transition may yield clues to seismic anomalies in the lower mantle, avoiding difficulty posed by the extreme conditions required to stabilize $MgSiO_3$ perovskite.

Experiments examining the travel-times of ultrasonic waves through polycrystalline aggregates at extreme conditions are useful for direct measurements of sample elasticity under changing *p-T* (Kung et al., 2006; Li and Kung, 2005; Li et al., 2005) and newer instrumentation has become available, increasing the capacity to collect very high quality monochromatic X-ray diffraction at in situ high *p-T*. Characterizing both structure and elasticity of $NaMgF_3$ in a common *p-T* region demonstrates how perovskite elasticity changes with structure and may assist a future understanding of $MgSiO_3$ and anomalous seismic observations in regions of Earth's lower mantle.

5.3. Experimental Methods

5.3.1. Monochromatic X-ray diffraction

Polycrystalline Neighborite ($NaMgF_3$) was prepared according to standard solid state methods described previously (Chapter 3). In-situ high pressure and temperature monochromatic x-ray diffraction was performed at beamline ID-30 at the European Synchrotron Radiation Facility (ESRF), Grenoble. Pressure was generated using a Paris-Edinburgh press with a boron-epoxy sample assembly capable of resistive heating through a graphite sleeve (Crichton and Mezouar, 2002). The incident x-ray beam was tuned to a wavelength of 0.5339(4) Å selected from a Si (111) channel-cut monochromator. X-ray diffraction was collected to 26˚ 2θ using a MAR345 imaging plate detector calibrated for sample-to-detector distance and position asymmetry with NBS660a LaB_6 powder (a = 4.1569 Å) and Fit2D (Hammersley et al., 1996). Details of the press, sample assembly, and slit system are available elsewhere (Mezouar et al., 2002).

Data were collected in four separate runs: RUN-0, RUN-1, RUN-3, RUN-7 (run numbers not mentioned were blowouts occurring upon pressure increase). During the initial high pressure run (RUN-0), dramatic grain growth was noticed throughout the

sample after just 2-3 hours at high temperature and data collection was halted. Grain growth is a result of the solid electrolytic properties of $NaMgF_3$ (O'Keeffe and Bovin, 1979). Subsequent runs were performed with a 4:1 mixture of $NaMgF_3$:B_4C (by wt.). However, the mixture was ground in an alumina mortar and pestle and a minor amount of Al_2O_3, estimated at 2-5 wt% to $NaMgF_3$, was incorporated in the mixture. The mixture eliminated grain growth of $NaMgF_3$ powders and no reaction with the sample was observed. We included B_4C and Al_2O_3 phases during Rietveld refinement via Le-Bail models in EXP-GUI (Toby, 2001) user-interface for GSAS (Larson and Von Dreele, 2000). Some evidence supporting preferred orientation of $NaMgF_3$ powder was observed during the experiment; however a correction was not applied during Rietveld refinement.

The pressure and temperature was determined using the equations of state of hexagonal-boron nitride (Le Godec Y, 2000) and gold (Anderson et al., 1989) in RUN-0 and RUN-1, while the equations of state of hexagonal-boron nitride and platinum (Holmes et al., 1989) were used in RUN-3 and RUN-4. These standard materials were each placed adjacent to the sample and the cell parameter of each standard was determined from separate X-ray exposures. The boron nitride sample used in this study was identical to the one from which the equation of state was determined. This dual equation of state approach (Crichton and Mezouar, 2002) negates the need for a thermocouple, which may introduce more severe thermal gradients in the cell assembly. When compared to calibration plots of wattage vs. oil bars for the press, the contrast between the p-V-T equations of state of h-BN and Au and/or Pt are found to constrain sample pressure and temperature to ±0.1 GPa and ±20K.

5.3.2. Ultrasonic elasticity

Polycrystalline Neighborite ($NaMgF_3$) was prepared (Zhao et al., 1993b) and hot-pressed (Gwanmesia et al., 1993) at 4 GPa and 1000 °C. This sintered $NaMgF_3$ pellet (diameter = 2.2 mm, length = 0.8 mm) was used for the high *p-T* ultrasonic experiments conducted in the SAM-85 press (Weidner et al., 1992) at X17B2 at the National Synchrotron Light Source at Brookhaven Laboratory. The techniques used during the elasticity experiment were developed previously (Li et al., 2002) for ultrasonic interferometry with dual-mode transducers and a new transfer function method coupled

with X-ray measurements of specimen volume and length at high pressures and temperatures. Acoustic travel times of longitudinal (P) and transverse (S) waves, the length of specimen, and the unit cell parameters of both NaCl and $NaMgF_3$ were collected. Thin gold foil (thickness = 1 μm) was used to improve elastic wave propagation from the alumina buffer-rod to the sample. Sample pressure at variable temperature was determined from the unit cell volumes of NaCl (Decker, 1971) and density of the pellet was determined from the measured unit cell of $NaMgF_3$. From the measured travel time, pellet length, and sample density, the acoustic wave velocities and bulk elastic moduli were calculated. Data from two experiments are reported as NaMgF_11 and NaMgF_12 in tables.

5.4. Results and discussion

5.4.1 Monochromatic X-ray diffraction

Figure 5.1 shows the run numbers and p-T paths where monochromatic x-ray diffraction data were collected. We found sample temperatures in excess of 500˚C eliminate pressure-induced strain broadening of diffraction peak-widths and plots of the Rietveld refinements can be found in Figure 5.2.

We find that the average $NaMgF_3$ structure transitions directly from orthorhombic (***P****bnm*) to cubic (***P****m*$\bar{3}$*m*) and the reflections $\{120, 210\}_{Pbnm}$, $\{121, 103, 211\}_{Pbnm}$, and $\{122, 212\}_{Pbnm}$ become extinct in unison (Zhao et al., 1993a) at the phase boundary, which varies by 105 K/GPa (9.5 MPa/˚C) in p/T space. This experimentally determined slope is significantly different than 45 K/GPa (22.2 MPa/˚C) reported previously (Chen et al., 2005; Zhao et al., 1994b) and sample recrystallization, driven by the solid electrolyte behavior (O'Keeffe and Bovin, 1979) of $NaMgF_3$, may have lead to error in previous works. This conclusion is supported by examination of the $NaMgF_3$ powder pattern at 1000˚C plotted in Chen et al. (2005), showing discrepancies in peak intensities and significant misrepresentation of I_o $(002)_{Pm\text{-}3m}$.

Consistent with Zhao et al. (1993a), pseudo-cubic unit cell lattice parameters converge more rapidly in the last 100-200 K before transition, becoming metrically cubic ~50 K before transition (Fig. 5.3).

We find good consistency between our $NaMgF_3$ p-V-T data and previous T-V (Zhao et al., 1993a; Zhao et al., 1993b) and p-V (Liu et al., 2005) studies. Thus we include this published data to strengthen and support our plots as well as our p-V-T equation of state (EoS). For EoS calculations, data were incorporated to a single set by normalizing volume by the ambient reported value and that found before each high pressure run in the current study. The entire set consists of 62 p-V-T points (Table 5.1), where 19 and 6 points are used from Zhao et al. (1993a) and Liu et al. (2005) respectively. Fit to the data is obtained by weighting according to individual errors in p, V, and T. The EoS constants and data are found in Table 5.2 for both unit cell volume (Table 5.2a) and the unit cell axis lengths (Table 5.2b). Because our data set does not extend far in pressure space, our EoS cannot constrain higher order terms such as dK'/dT which become significant during p-V-T extrapolation. A high temperature modification in compressibility is clear from examination of Figure 5.4, and contrary to Zhao et al. (1994) which find "$dK/dT \approx 0$".

Table 5.3 displays structural parameters derived from in-situ Rietveld refinement of $NaMgF_3$ at high pressure and temperature. The most notable feature of the high temperature behavior of $NaMgF_3$ is that which happens to the Mg-F bond 150-200 K below the orthorhombic-cubic critical region Figure 5.5. Mg-F bond lengths in $NaMgF_3$ appear to contract with increasing temperature to match ½ the cubic unit cell length. Zhao et al. (1993b) report that because this phenomena corresponds to a large increase in displacement parameters, the phase transition of the $NaMgF_3$ perovskite is a dynamic process driven by coupling of soft vibrational modes. Investigating only the time-averaged Bragg scattering is not sufficient and only modeling contributions of the diffuse scatter will truly sense the true Mg-F distance (Chupas et al., 2004; Egami and Billinge, 1994). Our previous study detailed in Chapter 4 finds that this behavior occurs as the result of correlated atomic motion in $NaMgF_3$ and the Mg-F distance increases linearly through the phase transition.

Octahedral rotation in orthorhombic $NaMgF_3$ serves as an order parameter to the structural transition and no rotation is allowed in the cubic phase. Zhao et al. (1993ab) reports octahedral rotation follows temperature as:

$$\Phi(T) = \Phi_0\left(1 - \frac{T}{T_C}\right)^{\beta} \tag{5.1}$$

Where Φ is the vector sum of the rotation vectors of perovskite octahedra, $\boldsymbol{T_C}$ the transition temperature, and β an exponent which governs the shape the curve in the critical temperature region. From fitting our data to this equation, we find β independent of pressure at 0.17. Using our knowledge of how Φ and $\boldsymbol{T_C}$ vary with pressure we can now express rotation as a function of pressure and temperature:

$$\Phi(p,T) = \left(\Phi_{0,T_0} + \frac{d\Phi_{0,T_0}}{dp}\,p\right)\left(1 - (T - T_0)\Big/\left(\left(T_C + \frac{dT_C}{dp}\,p\right) - T_0\right)\right)^{0.17} \tag{5.2}$$

Variable $\boldsymbol{T_0}$ is the reference (floor) temperature, while Φ_{0,T_0} is the vector sum of the rotation vectors of perovskite octahedra at room pressure and reference temperature. From room temperature diamond anvil cell data (Liu et al., 2005) within our pressure range, from the data published in Liu et al., we find that $\frac{d\Phi_{0,T_0}}{dp}$ is equal to 0.241 (˚/GPa). The parameter Φ is plotted as a function of temperature at several pressures in Figure 5.6.

If perovskite octahedra are without deformation, octahdera tilt angle and Mg-F bond length can be determined directly from the unit cell lengths (Zhao et al., 1993b). Zhao et al (1993) find both rotation of MgF_6 octahedra and length of Mg-F bond are underestimated when calculated from the lattice parameter as the result of deformation in octahedra. Subsequently, Chen et al. (2005) find that the difference between the Mg-F bond length determined by structural refinement ($(Mg\text{-}F)_{xyz}$) and the Mg-F bond length calculated from the lattice parameters ($(Mg\text{-}F)_{abc}$) increases at high pressure. This study uses this result to justify pressure increases deformation in perovskite octahedra. However, data collected subsequently in Liu et al. (2005) find that the difference between $(Mg\text{-}F)_{xyz}$ and $(Mg\text{-}F)_{abc}$ actually decreases at high pressure. This result is in agreement with data reported here Figure 5.7. Thus, it seems $(Mg\text{-}F)_{xyz}$ and $(Mg\text{-}F)_{abc}$ each have independent relations with pressure and the difference between these parameters may not be used to quantify deformation in octahedra. However, when the structure data are

examined using the strain matrix introduced by Zhao et al. (1993a), it is clear that the MgF_6 octahedra increase deformation at high pressure (Figure 5.8).

Because pressure increases deformation in octahedra, calculation of the tilt angle of octahedra becomes less valid in high pressure $NaMgF_3$ structure. Recently a new parameterization of the perovskite structure utilizes the A and B site polyhedral volume, as a new means for understanding lattice distortion and critical behavior (Thomas, 1998) in perovskites as an independent variable. Examination of the relative volumes of perovskite polyhedra and how each changes provides an equivalent means of understanding structural distortion and predicting phase transitions with pressure and temperature. The V_A/V_B ratio is 5 in cubic perovskites and less than 5 in perovskites where octahedral tilt occurs. Our data shows the V_A/V_B ratio as a function of pressure and temperature Figure 5.9. Our previous study of the pair distribution function (Chapter 4) of $NaMgF_3$ finds that the V_A/V_B ratio in the average structure (***P**bnm*) is the same as that in the local structure. Previous work suggests that hardening of the A-site polyhedra relative to the B-site in $MgSiO_3$ will reverse the pressure effect on rotation of octahedra and decrease lattice distortion (Magyari-Kope et al., 2002). As one would expect from the observed trend in rotation of $NaMgF_3$ octahedra, we find the A-site is ~25% more compressible than the B-site. The B-site hardens at higher pressures, while the A-site appears to soften with pressure.

5.4.2 Elastic properties

The pressure and temperature path of the $NaMgF_3$ ultrasonic experiment is plotted in Figure 5.10. Conditions are plotted where both successful and unsuccessful ultrasonic measurements were performed and these values are listed in Table 5.4, respectively. By fitting the elastic moduli, G, L, and K,

$$G = \rho V_S^2 \tag{5.3}$$

$$L = \rho V_P^2 \tag{5.4}$$

$$K = \rho\left(V_P^2 - \frac{4}{3}V_S^2\right) \tag{5.5}$$

to the equation,

$$M = M_O + \frac{\partial M}{\partial P}\Delta P + \frac{\partial M}{\partial T}\Delta T\,, \tag{5.6}$$

we obtain the pressure and temperature dependence of each parameter (Table 5.5) and only data from the temperature-annealed sample are included in this fit. There is evidence to support a second-order temperature-dependence of the shear modulus near the phase transition, however additional data is required to constrain this relationship and the longitudinal and bulk moduli are well-represented by a linear relationship with pressure and temperature.

The adiabatic bulk modulus of $NaMgF_3$ determined here (K_S) is consistent with the isothermal bulk modulus (K_T) calculated from the p-V-T equation of state. However, the temperature dependence of the bulk modulus determined in the two experiments is significantly different. This discrepancy may have to do with the assumption of the Birch-Murnaghan equation of state, or the difference could originate from errors in the equations of state of BN and Au used in the monochromatic X-ray diffraction experiment. In this case, we believe the ultrasonic data represents the most accurate equation of state data for $NaMgF_3$, though sample porosity may be responsible for the slightly lower K value.

When conditions are within 200 K of the orthorhombic to cubic phase transition, attenuation of the ultrasonic signal is observed and the travel time of the ultrasonic wave through the sample cannot be resolved. Several phenomena may explain the attenuation of the signal and in each case we must consider the relatively high frequencies of the deconvoluted ultrasonic wave (30-60 MHz). While the ultrasonic wavelength is ~100 microns, because the phase transition in $NaMgF_3$ is at high temperature and within 300 K of the melting point of gold, some attenuation could be due to anelasticity in the gold foil (1 μm) used to couple the sample to the buffer-rod. Alternatively, the attenuation of the ultrasonic signal may relate to a stress-strain hysteresis loop in the sample or the attenuation may be frequency-dependent and it is possible that no attenuation would occur in waves with frequencies characteristic of seismic waves (~0.1 Hz). Some attenuation in shear waves may be expected based on mobility of transition twin walls (Carpenter et al., 2007), but because attenuation is also observed in the compressional

waves, the observed attenuation may at least be partially derived from another effect (Harrison and Redfern, 2002; Harrison et al., 2004a; Harrison et al., 2004b).

The results of our study have implications for $MgSiO_3$ perovskite in the lower mantle, if the behavior of $NaMgF_3$ is considered as a proxy. The very steep transition slope and softening in the A-site suggests little possibility for transition to cubic at extreme pressures. The similarity of the temperature-dependence of the tilt angle of MgF_6 octahedra between pressures suggests a tetragonal phase should not stabilize between orthorhombic and 'cubic' $NaMgF_3$. While the ultrasonic data suggest attenuation may occur in $NaMgF_3$ near phase transition, the data are inconclusive and currently cannot be directly compared to $MgSiO_3$. However, considering the very steep transition slope, laterally variable seismic anomalies in the mid-lower mantle (Vinnik et al., 2001) may be chemical heterogeneities, or perhaps phase transition in $CaSiO_3$ (Kurashina et al., 2004; Shim et al., 2002) as opposed to $MgSiO_3$ perovskite.

References

Anderson, O.L., Isaak, D.G., and Yamamoto, S. (1989) Anharmonicity and the Equation of State for Gold. Journal of Applied Physics, 65(4), 1534-1543.

Carpenter, M.A. (2000) Strain and elasticity at structural phase transitions in minerals. Transformation Processes in Minerals, 39, p. 35-64.

Carpenter, M.A., Howard, C.J., Knight, K.S., and Zhang, Z. (2006a) Structural relationships and a phase diagram for (Ca, Sr) TiO_3 perovskites. Journal of Physics-Condensed Matter, 18(48), 10725-10749.

Carpenter, M.A., Li, B.S., and Liebermann, R.C. (2007) Elastic anomalies accompanying phase transitions in (Ca,Sr)TiO_3 perovskites: Part III. Experimental investigation of polycrystalline samples. American Mineralogist, 92(2-3), 344-355.

Carpenter, M.A., and Salje, E.K.H. (1998) Elastic anomalies in minerals due to structural phase transitions. European Journal of Mineralogy, 10(4), 693-812.

Carpenter, M.A., Sondergeld, P., Li, B.S., Liebermann, R.C., Walsh, J.W., Schreuer, J., and Darling, T.W. (2006b) Structural evolution, strain and elasticity of perovskites at high pressures and temperatures. Journal of Mineralogical and Petrological Sciences, 101(3), 95-109.

Chao, E.C.T., Evans, H.T., Skinner, B.J., and Milton, C. (1961) Neighborite, $NaMgF_3$, a New Mineral From the Green River Formation, South Ouray, Utah. American Mineralogist, 46(3-4), 379-393.

Chapman, K.W., Chupas, P.J., and Kepert, C.J. (2005) Direct observation of a transverse vibrational mechanism for negative thermal expansion in $Zn(CN)_2$: An atomic pair distribution function analysis. Journal of the American Chemical Society, 127 (44), 15630-15636

Chen, J.H., Liu, H.Z., Martin, C.D., Parise, J.B., and Weidner, D.J. (2005) Crystal chemistry of $NaMgF_3$ perovskite at high pressure and temperature. American Mineralogist, 90(10), 1534-1539.

Chupas, P.J., Chaudhuri, S., Hanson, J.C., Qiu, X.Y., Lee, P.L., Shastri, S.D., Billinge, S.J.L., and Grey, C.P. (2004) Probing local and long-range structure simultaneously: An in situ study of the high-temperature phase transition of alpha-AlF_3. Journal of the American Chemical Society, 126(15), 4756-4757.

Crichton, W.A., and Mezouar, M. (2002) Noninvasive pressure and temperature estimation in large-volume apparatus by equation-of-state cross-calibration. High Temperatures-High Pressures, 34(2), 235-242.

Decker, D.L. (1971) High-Pressure Equation of State for NaCl, KCl, and CsCl. Journal of Applied Physics, 42(8), 3239.

Egami, T., and Billinge, S.J.L. (1994) Underneath the Bragg Peaks: Structural analysis of complex materials. Pergamon Press, Oxford.

Gwanmesia, G.D., Li, B.S., and Liebermann, R.C. (1993) Hot-Pressing of Polycrystals of High-Pressure Phases of Mantle Minerals in Multi-Anvil Apparatus. Pure and Applied Geophysics, 141(2-4), 467-484.

Hammersley, A.P., Svensson, S.O., Hanfland, M., Fitch, A.N., and Hausermann, D. (1996) Two-dimensional detector software: From real detector to idealized image or two-theta scan. High Pressure Research, 14(4-6), 235-248.

Harrison, R.J., and Redfern, S.A. (2002) The influence of transformation twins on the seismic-frequency elastic and anelastic properties of perovskite: dynamical

mechanical analysis of single crystal $LaAlO_3$. Physics of the Earth and Planetary Interiors, 134(3-4), 253-272.

Harrison, R.J., Redfern, S.A.T., Buckley, A., and Salje, E.K.H. (2004a) Application of real-time, stroboscopic x-ray diffraction with dynamical mechanical analysis to characterize the motion of ferroelastic domain walls. Journal of Applied Physics, 95(4), 1706-1717.

Harrison, R.J., Redfern, S.A.T., and Salje, E.K.H. (2004b) Dynamical excitation and anelastic relaxation of ferroelastic domain walls in $LaAlO_3$. Physical Review B, 69(14).

Holmes, N.C., Moriarty, J.A., Gathers, G.R., and Nellis, W.J. (1989) The Equation of State of Platinum to 660GPa (6.6Mbar). Journal of Applied Physics, 66(7), 2962-2967.

Kung, J., Li, B.S., and Liebermann, R.C. (2006) Ultrasonic observations of elasticity changes across phase transformations in $MgSiO_3$ pyroxenes. Journal of Physics and Chemistry of Solids, 67(9-10), 2051-2055.

Kurashina, T., Hirose, K., Ono, S., Sata, N., and Ohishi, Y. (2004) Phase transition in Al-bearing $CaSiO_3$ perovskite: implications for seismic discontinuities in the lower mantle. Physics of the Earth and Planetary Interiors, 145(1-4), 67-74.

Larson, A.C., and Von Dreele, R.B. (2000) General Structure Analysis System (GSAS). Los Alamos National Laboratory Report, 86-748.

Lay, T., Williams, Q., and Garnero, E.J. (1998) The core-mantle boundary layer and deep Earth dynamics. Nature, 392(6675), 461-468. DOI:10.1038/33083.

Le Godec Y, M.-G.D., Mezouar M, Syfosse G, Itie JP and Besson, J-M. (2000) Equation of State and Order Parameter in Graphite-Like h-BN under High Pressure and Temperature. 925-928.

Li, B.S., Chen, K., Kung, J., Liebermann, R.C., and Weidner, D.J. (2002) Sound velocity measurement using transfer function method. JOURNAL OF PHYSICS: CONDENSED MATTER, 14, 11337-11342.

Li, B.S., and Kung, J. (2005) Composition of the Earth's lower mantle: Results from forward and inverse mineral physics modeling. Geochimica Et Cosmochimica Acta, 69(10), A252-A252.

Li, B.S., Kung, J., Uchida, T., and Wang, Y.B. (2005) Pressure calibration to 20 GPa by simultaneous use of ultrasonic and x-ray techniques. Journal of Applied Physics, 98(1).

Liu, H.Z., Chen, J., Hu, J., Martin, C.D., Weidner, D.J., Hausermann, D., and Mao, H.K. (2005) Octahedral tilting evolution and phase transition in orthorhombic $NaMgF_3$ perovskite under pressure. Geophysical Research Letters, 32(4), L04304(1-5). DOI:10.1029/2004GL022068.

Liu, L.G. (1976) Orthorhombic Perovskite Phases Observed in Olivine, Pyroxene and Garnet At High-Pressures and Temperatures. Physics of the Earth and Planetary Interiors, 11(4), 289-298.

Magyari-Kope, B., Vitos, L., Johansson, B., and Kollar, J. (2002) Origin of octahedral tilting in orthorhombic perovskites. Physical Review B, 66(9).

Mezouar, M., Faure, P., Crichton, W., Rambert, N., Sitaud, B., Bauchau, S., and Blattmann, G. (2002) Multichannel collimator for structural investigation of

liquids and amorphous materials at high pressures and temperatures. Review of Scientific Instruments, 73(10), 3570-3574.
O'Keeffe, M., and Bovin, J.O. (1979) Solid Electrolyte Behavior of $NaMgF_3$ - Geophysical Implications. Science, 206(4418), 599-600.
Qiu, X.Y., Proffen, T., Mitchell, J.F., and Billinge, S.J.L. (2005) Orbital correlations in the pseudocubic O and rhombohedral R phases of $LaMnO_3$. Physical Review Letters, 94(17), 177203.
Shim, S.H., Jeanloz, R., and Duffy, T.S. (2002) Tetragonal structure of $CaSiO_3$ perovskite above 20 GPa. Geophysical Research Letters, 29(24), 2166.
Thomas, N.W. (1998) New global parameterization of perovskite structures. Acta Crystallographica Section B-Structural Science, 54, 585-599.
Toby, B.H. (2001) EXPGUI, a graphical user interface for GSAS. Journal of Applied Crystallography, 34, 210-213.
Tucker, M.G., Keen, D.A., and Dove, M.T. (2001) A detailed structural characterization of quartz on heating through the alpha-beta phase transition. Mineralogical Magazine, 65(4), 489-507.
Umemoto, K., Wentzcovitch, R.M., Weidner, D.J., and Parise, J.B. (2006) $NaMgF_3$: A low-pressure analog of $MgSiO_3$. Geophysical Research Letters, 33(15).
van der Hilst, R.D., and Karason, H. (1999) Compositional heterogeneity in the bottom 1000 kilometers of Earth's mantle: Toward a hybrid convection model. Science, 283(5409), 1885-1888.
Vinnik, L., Kato, M., and Kawakatsu, H. (2001) Search for seismic discontinuities in the lower mantle. Geophysical Journal International, 147(1), 41-56.
Weidner, D.J., Vaughan, M.T., Ko, J., Wang, Y., Liu, X., Yeganeh-Haeri, A., Pacalo, R.E., and Zhao, Y.S. (1992) Characterization of stress, pressure, and temperature in SAM 85,
a DIA type high pressure apparatus. In Y. Syono, Manghnani,, and M., Eds. High Pressure Research: Application to Earth and
Planetary Sciences., p. 13–17. American Geophysical Union, Washington, DC.
Zhao, Y.S., Parise, J.B., Wang, Y.B., Kusaba, K., Vaughan, M.T., Weidner, D.J., Kikegawa, T., Chen, J., and Shimomura, O. (1994a) High-Pressure Crystal-Chemistry of Neighborite, $NaMgF_3$ - an Angle-Dispersive Diffraction Study Using Monochromatic Synchrotron X-Radiation. American Mineralogist, 79(7-8), 615-621.
Zhao, Y.S., Weidner, D.J., Ko, J.D., Leinenweber, K., Liu, X., Li, B.S., Meng, Y., Pacalo, R.E.G., Vaughan, M.T., Wang, Y.B., and Yeganehhaeri, A. (1994b) Perovskite At High P-T Conditions - an in-Situ Synchrotron X- Ray-Diffraction Study of $NaMgF_3$ Perovskite. Journal of Geophysical Research-Solid Earth, 99(B2), 2871-2885.
Zhao, Y.S., Weidner, D.J., Parise, J.B., and Cox, D.E. (1993a) Critical Phenomena and Phase-Transition of Perovskite Data For $NaMgF_3$ Perovskite .2. Physics of the Earth and Planetary Interiors, 76(1-2), 17-34.
-. (1993b) Thermal-Expansion and Structural Distortion of Perovskite - Data For $NaMgF_3$ Perovskite .1. Physics of the Earth and Planetary Interiors, 76(1-2), 1-16.

	P, (GPa)	σP	T, (K)	σT	V, (A^3)	σV
RUN-0	7.04	0.1	830	10	0.94605	0.00025
RUN-0	7.04	0.1	875	10	0.94815	0.00025
RUN-0	6.95	0.1	970	10	0.95266	0.00025
RUN-0	6.87	0.1	1070	10	0.95789	0.00023
RUN-0	6.79	0.1	1170	10	0.96435	0.00048
RUN-1	1.978	0.1	780	10	1.01088	0.00028
RUN-1	1.937	0.1	870	10	1.01671	0.00027
RUN-1	1.889	0.1	980	10	1.02602	0.00027
RUN-1	1.7	0.1	1085	10	1.03765	0.00032
RUN-1	1.68	0.1	1175	10	1.04949	0.00099
RUN-3	3.971	0.1	785	10	0.98341	0.00031
RUN-3	3.983	0.1	860	10	0.98656	0.00028
RUN-3	3.992	0.1	920	10	0.9898	0.00024
RUN-3	3.995	0.1	960	10	0.99182	0.00023
RUN-3	4.003	0.1	1005	10	0.99405	0.00022
RUN-3	4.009	0.1	1030	10	0.9957	0.00021
RUN-3	3.963	0.1	1060	10	0.99758	0.00022
RUN-3	3.951	0.1	1090	10	0.99953	0.00024
RUN-3	3.896	0.1	1115	10	1.0011	0.00026
RUN-3	3.894	0.1	1145	10	1.00282	0.00031
RUN-3	3.856	0.1	1175	10	1.0052	0.00038
RUN-3	3.839	0.1	1190	10	1.0063	0.00035
RUN-3	3.823	0.1	1210	10	1.00861	0.00034
RUN-3	3.813	0.1	1240	10	1.01062	0.00037
RUN-3	3.796	0.1	1270	10	1.01215	0.00042
RUN-3	3.787	0.1	1300	10	1.01446	0.00047
RUN-3	3.786	0.1	1315	10	1.01594	0.00028
RUN-3	3.778	0.1	1345	10	1.01757	0.0004
RUN-3	3.795	0.1	1370	10	1.01977	0.00083
RUN-3	3.785	0.1	1410	10	1.01999	0.00098
RUN-7	5.457	0.1	825	40	0.96127	0.00043
RUN-7	5.461	0.1	930	40	0.96487	0.00038
RUN-7	5.46	0.1	1025	40	0.96912	0.00032
RUN-7	5.391	0.1	1115	40	0.97459	0.00034
RUN-7	5.361	0.1	1205	40	0.98083	0.00034
RUN-7	5.321	0.1	1300	40	0.98577	0.00033
RUN-7	5.217	0.1	1380	40	0.99157	0.00032

	P, (GPa)	σP	T, (K)	σT	V, (A^3)	σV
Zhao et al.	0	1.00E-06	298	1	1	0.00009
Zhao et al.	0	1.00E-06	351	1	1.00321	0.00009
Zhao et al.	0	1.00E-06	376	1	1.00678	0.00009
Zhao et al.	0	1.00E-06	425	1	1.01083	0.0001
Zhao et al.	0	1.00E-06	481	1	1.01542	0.00009
Zhao et al.	0	1.00E-06	526	1	1.01908	0.0001
Zhao et al.	0	1.00E-06	576	1	1.02342	0.0001
Zhao et al.	0	1.00E-06	629	1	1.02856	0.0001
Zhao et al.	0	1.00E-06	679	1	1.03198	0.0001
Zhao et al.	0	1.00E-06	723	1	1.03766	0.0001
Zhao et al.	0	1.00E-06	782	1	1.04098	0.0001
Zhao et al.	0	1.00E-06	827	1	1.04685	0.0001
Zhao et al.	0	1.00E-06	879	1	1.05079	0.0001
Zhao et al.	0	1.00E-06	915	2	1.05638	0.0001
Zhao et al.	0	1.00E-06	947	2	1.06005	0.0001
Zhao et al.	0	1.00E-06	978	2	1.06397	0.0001
Zhao et al.	0	1.00E-06	995	2	1.06611	0.0001
Zhao et al.	0	1.00E-06	1017	2	1.0688	0.00011
Zhao et al.	0	1.00E-06	1034	2	1.07302	0.00011
Liu et al.	0.89	0.01	298	1	0.99083	0.00009
Liu et al.	1.79	0.02	298	1	0.97921	0.00015
Liu et al.	2.89	0.04	298	1	0.9658	0.00015
Liu et al.	4.29	0.06	298	1	0.94988	0.00015
Liu et al.	6.79	0.08	298	1	0.92451	0.00016
Liu et al.	8.29	0.1	298	1	0.91158	0.00016

[Table 5.1] PVT data set compiled from Zhao et al. (1993a), (Liu et al., 2005), and this study.

$NaMgF_3$		K (GPa)	σK	K'	σK'	dK/dT (GPa/K)	σdK/dT	a0	σa0	a1	σa1
(a)	Vol.	76.49715	2.97755	4.02083	1.05106	-0.03845	0.00217	6.29415	0.2687	4.3292	0.46867
	Vol. Brillioun	75.64	0.12	4.29554	0.58261	-0.03807	0.0017	6.29163	0.26908	4.33419	0.46929
(b)	a	70.27623	2.50835	1.59604	0.81101	-0.03147	0.00202	11.05302	0.33015	1.87399	0.61077
	b	91.5304	3.01173	4.41943	1.16519	-0.0448	0.00197	2.05038	0.3027	4.39157	0.54471
	c	79.65409	2.30932	2.38301	0.78288	-0.03598	0.00165	8.40134	0.27687	1.53903	0.50252
(c)	VA	72.82799	3.72409	3.02508	1.11687	-0.03667	0.0035	6.95213	1.40315	5.68166	2.50115
	VB	104.82009	10.35393	2.96445	3.03123	-0.01506	0.00971	3.91226	0.92526	-3.71799	1.55726

[Table 5.2] Derived equation of state parameters from the data set presented in Table 5.1. (a) The bulk modulus is refined in the first trial and held constant in the second. (b) The equation of state of the cube of each unit cell length (i.e., a^3) and (c) the volume of each polyhedron is fit to give a comparative bulk modulus.

File	P	T	wRp	Rp	X^2	a	σa	b	σb	c	σc	a_{PC}	σa_{PC}	b_{PC}
RUN-0	7.04	830	0.081	0.0626	2.09	5.266945	0.0016	5.378965	0.0012	7.5377	0.002	3.724293	0.001131	3.803503
RUN-0	7.04	875	0.082	0.0619	2	5.273094	0.0016	5.380085	0.0012	7.54405	0.0021	3.728641	0.001131	3.804295
RUN-0	6.95	970	0.083	0.0627	2.04	5.286774	0.0016	5.382044	0.0012	7.55759	0.002	3.738314	0.001131	3.80568
RUN-0	6.87	1070	0.084	0.0622	1.74	5.3021	0.0015	5.384899	0.0011	7.57306	0.0017	3.749151	0.001061	3.807699
RUN-0	6.79	1170	0.103	0.0782	2.01	5.318861	0.0034	5.390749	0.0028	7.59185	0.0038	3.761003	0.002404	3.811835
RUN-1	1.98	780	0.055	0.0398	3.26	5.40687	0.0012	5.484559	0.0014	7.71174	0.0023	3.823234	0.000849	3.878169
RUN-1	1.94	870	0.057	0.0426	3.13	5.423619	0.0011	5.488783	0.0013	7.72633	0.0021	3.835078	0.000778	3.881156
RUN-1	1.89	980	0.062	0.0479	3.45	5.447915	0.0011	5.496956	0.0013	7.75078	0.0021	3.852258	0.000778	3.886935
RUN-1	1.70	1085	0.073	0.0557	4.78	5.476621	0.0016	5.509086	0.0016	7.78035	0.0027	3.872556	0.001131	3.895512
RUN-1	1.68	1175	0.093	0.0653	7.09	5.516102	0.005	5.516161	0.007	7.80277	0.008	3.900473	0.003536	3.900515
RUN-3	3.97	785	0.056	0.043	2.62	5.346729	0.0017	5.444307	0.0017	7.63852	0.0028	3.780708	0.001202	3.849706
RUN-3	3.98	860	0.051	0.0402	1.88	5.357468	0.0017	5.443958	0.0014	7.64811	0.0022	3.788302	0.001202	3.84946
RUN-3	3.99	920	0.055	0.042	2.12	5.36761	0.0013	5.445506	0.0012	7.65661	0.002	3.795473	0.000919	3.850554
RUN-3	3.99	960	0.048	0.0366	1.6	5.373911	0.0013	5.446132	0.0011	7.66229	0.0017	3.799929	0.000919	3.850997
RUN-3	4.00	1005	0.051	0.039	1.62	5.380108	0.0013	5.44754	0.001	7.6687	0.0017	3.804311	0.000919	3.851992
RUN-3	4.01	1030	0.048	0.0372	1.46	5.384459	0.0013	5.448685	0.0009	7.67363	0.0015	3.807387	0.000919	3.852802
RUN-3	3.96	1060	0.052	0.0403	1.59	5.389158	0.0014	5.450372	0.0009	7.67905	0.0016	3.81071	0.00099	3.853995
RUN-3	3.95	1090	0.056	0.0431	1.83	5.394172	0.0016	5.452083	0.001	7.68448	0.0016	3.814256	0.001131	3.855205
RUN-3	3.90	1115	0.052	0.0388	2.3	5.398729	0.0018	5.453145	0.001	7.68858	0.0018	3.817478	0.001273	3.855956
RUN-3	3.89	1145	0.079	0.0573	4.78	5.402581	0.0023	5.455248	0.0013	7.69329	0.0022	3.820202	0.001626	3.857443
RUN-3	3.86	1175	0.077	0.0564	4.71	5.408437	0.003	5.457739	0.0017	7.69971	0.0025	3.824342	0.002121	3.859204
RUN-3	3.84	1190	0.07	0.0513	3.58	5.411146	0.0028	5.458951	0.0015	7.7026	0.0021	3.826258	0.00198	3.860061
RUN-3	3.82	1210	0.076	0.0556	4.13	5.417998	0.0027	5.460669	0.0014	7.70804	0.0021	3.831103	0.001909	3.861276
RUN-3	3.81	1240	0.084	0.0599	4.6	5.42363	0.003	5.462535	0.0016	7.71276	0.0023	3.835086	0.002121	3.862596
RUN-3	3.80	1270	0.09	0.0661	4.98	5.428378	0.0034	5.463515	0.0019	7.71633	0.0026	3.838443	0.002404	3.863289
RUN-3	3.79	1300	0.09	0.0647	4.87	5.434867	0.004	5.465293	0.0018	7.72218	0.0028	3.843031	0.002828	3.864546
RUN-3	3.79	1315	0.085	0.0632	4.06	5.439556	0.0021	5.465708	0.0013	7.72616	0.0016	3.846347	0.001485	3.864839
RUN-3	3.78	1345	0.082	0.0612	3.77	5.445198	0.0029	5.465615	0.002	7.73069	0.0028	3.850336	0.002051	3.864773
RUN-3	3.80	1370	0.128	0.1027	7.84	5.457737	0.006	5.464628	0.006	7.73102	0.003	3.859203	0.004243	3.864076
RUN-3	3.79	1410	0.093	0.0702	0.3	5.459537	0.0075	5.461193	0.007	7.73494	0.0025	3.860476	0.005303	3.861647
RUN-7	5.46	825	0.058	0.0438	2.16	5.297687	0.0025	5.412815	0.0018	7.58516	0.0029	3.74603	0.001768	3.827438
RUN-7	5.46	930	0.055	0.0416	1.89	5.31144	0.0019	5.412329	0.0014	7.59455	0.0023	3.755755	0.001344	3.827095
RUN-7	5.46	1025	0.053	0.0396	1.73	5.326053	0.0013	5.412975	0.001	7.60615	0.0014	3.766088	0.000919	3.827551
RUN-7	5.39	1115	0.064	0.0491	0.53	5.343226	0.0015	5.415087	0.0012	7.6215	0.0016	3.778231	0.001061	3.829045
RUN-7	5.36	1205	0.073	0.0537	4.31	5.359676	0.0015	5.420579	0.0011	7.63906	0.0015	3.789863	0.001061	3.832928
RUN-7	5.32	1300	0.071	0.0519	4.8	5.373462	0.0014	5.424582	0.001	7.65214	0.0014	3.799611	0.00099	3.835759
RUN-7	5.22	1380	0.061	0.0438	2.98	5.388421	0.0012	5.430161	0.0009	7.66789	0.0012	3.810189	0.000849	3.839704
Liu et al.	0.89	298				5.3378		5.4718		7.6374		3.774395		3.869147
Liu et al.	1.79	298				5.3167		5.45		7.6081		3.759475		3.853732
Liu et al.	2.89	298				5.2868		5.4301		7.574		3.738332		3.839661
Liu et al.	4.29	298				5.2532		5.4046		7.5322		3.714573		3.821629
Liu et al.	6.79	298				5.1965		5.366		7.4643		3.67448		3.794335
Liu et al.	8.29	298				5.1657		5.3485		7.428		3.652701		3.781961

!! Continued on next page !!

!! Continued from last page !!

σb_{PC}	c_{PC}	σc_{PC}	U-Na	σU-Na	V-Na	σV-Na	U-F1	σU-F1	V-F1	σV-F1	U-F2	σU-F2
0.00085	3.76885	0.001	0.0457592	0.0025	0.211689	0.002878	0.44368	0.003007	0.1075	0.0035	0.26008	0.002107
0.00085	3.77202	0.0011	0.0454383	0.0028	0.203356	0.003029	0.44292	0.003153	0.1098	0.0036	0.2617	0.002199
0.00085	3.77879	0.001	0.0376947	0.0031	0.186725	0.003283	0.43344	0.003347	0.0968	0.0039	0.26259	0.002326
0.00078	3.78653	0.0009	0.0363141	0.0033	0.168283	0.003543	0.43783	0.003733	0.0933	0.0042	0.26311	0.002397
0.00198	3.79592	0.0019	0.0445348	0.0041	0.161356	0.004534	0.42716	0.003984	0.1022	0.0052	0.21322	0.005659
0.00099	3.85587	0.0012	0.0365613	0.002	0.158537	0.002452	0.39909	0.002152	0.1076	0.0027	0.21248	0.001265
0.00092	3.86316	0.0011	0.0368915	0.0022	0.134585	0.002854	0.36409	0.002028	0.0982	0.0029	0.21875	0.001394
0.00092	3.87539	0.0011	0.0207675	0.0028	0.112979	0.003502	0.37	0.003154	0.0695	0.0037	0.21106	0.001553
0.00113	3.89018	0.0014	0.0091241	0.0042	0.082581	0.005608	0.33364	0.00483	0.0658	0.0062	0.1909	0.002404
0.00495	3.90139	0.004	0.0030173	0.0026	0.040781	0.003597	0.06068	0.002968	0.0027	0.0047	0.05675	0.001467
0.0012	3.81926	0.0014	0.0470833	0.0027	0.222863	0.002227	0.4365	0.002673	0.0938	0.0027	0.23639	0.001535
0.00099	3.82405	0.0011	0.0121186	0.0027	0.202047	0.001818	0.41486	0.002256	0.0949	0.0023	0.23618	0.001366
0.00085	3.8283	0.001	5.368E-06	0.0024	0.178672	0.002009	0.42032	0.002013	0.1022	0.0024	0.23014	0.001181
0.00078	3.83115	0.0009	0.0005374	0.0024	0.164931	0.002189	0.43889	0.00208	0.0936	0.0024	0.23557	0.001258
0.00071	3.83435	0.0009	5.38E-05	0.0024	0.151175	0.002375	0.44583	0.002362	0.0925	0.0026	0.24152	0.001372
0.00064	3.83682	0.0008	5.384E-06	0.0024	0.14154	0.002288	0.4281	0.00231	0.0921	0.0024	0.23555	0.001195
0.00064	3.83953	0.0008	5.389E-06	0.0024	0.128062	0.002474	0.42329	0.002156	0.0925	0.0026	0.23665	0.001342
0.00071	3.84224	0.0008	5.394E-06	0.0024	0.123048	0.002966	0.39204	0.003922	0.0949	0.0034	0.23349	0.002255
0.00071	3.84429	0.0009	5.399E-06	0.0024	0.106238	0.002667	0.35348	0.003752	0.1175	0.0031	0.22153	0.002467
0.00092	3.84665	0.0011	5.403E-06	0.0024	0.104801	0.004953	0.35894	0.006235	0.0966	0.0053	0.22869	0.003495
0.0012	3.84986	0.0013	5.408E-06	0.0024	0.087488	0.005158	0.31099	0.006517	0.1066	0.0058	0.18973	0.004765
0.00106	3.8513	0.0011	5.411E-06	0.0024	0.082419	0.004695	0.31253	0.006639	0.1058	0.0051	0.21779	0.004075
0.00099	3.85402	0.0011	5.418E-06	0.0024	0.063295	0.006018	0.2789	0.005445	0.092	0.0058	0.2295	0.003386
0.00113	3.85638	0.0012	5.424E-06	0.0024	0.051408	0.00596	0.27435	0.00096	0.0835	0.0056	0.2439	0.000635
0.00134	3.85816	0.0013	5.428E-06	0.0024	0.05522	0.006398	0.25527	0.001183	0.0892	0.0067	0.24576	0.000673
0.00127	3.86109	0.0014	5.435E-06	0.0024	0.06137	0.006711	0.23988	0.005109	0.0663	0.0075	0.22419	0.004321
0.00092	3.86308	0.0008	5.44E-06	0.0024	0.037063	0.007428	0.21936	0.001501	0.0717	0.0079	0.206	0.000865
0.00141	3.86534	0.0014	5.445E-06	0.0024	0.019796	0.008903	0.22831	0.003126	0.016	0.0088	0.21428	0.003278
0.00424	3.86551	0.0015	5.458E-06	0.0025	5.46E-06	0.016749	0.20366	0.007324	0.0216	0.0183	0.19677	0.005774
0.00495	3.86747	0.0013	0.0054595	0.0025	5.46E-06	0.016739	0.12909	0.006016	5E-06	0.0183	0.16512	0.003936
0.00127	3.79258	0.0015	0.0553184	0.0033	0.23549	0.002577	0.45369	0.003083	0.0992	0.0031	0.2639	0.002278
0.00099	3.79727	0.0012	0.0513669	0.0029	0.211525	0.002381	0.43409	0.002916	0.1001	0.0029	0.25644	0.002034
0.00071	3.80308	0.0007	0.0467308	0.0026	0.19431	0.00197	0.41109	0.001507	0.0934	0.0024	0.2504	0.00123
0.00085	3.81075	0.0008	0.0383056	0.0036	0.176564	0.002583	0.3744	0.002014	0.09	0.0031	0.23731	0.001608
0.00078	3.81953	0.0008	0.0209671	0.004	0.130609	0.003144	0.36259	0.002246	0.1107	0.0034	0.23379	0.001801
0.00071	3.82607	0.0007	5.373E-06	0.0041	0.127152	0.003417	0.35921	0.002477	0.0797	0.0038	0.2284	0.001886
0.00064	3.83395	0.0006	5.388E-06	0.0041	0.108408	0.003361	0.39591	0.002872	0.0602	0.0037	0.21975	0.002269
	3.8187		0.0827359		0.254439		0.47933		0.145		0.25888	
	3.80405		0.104739		0.261055		0.48595		0.1303		0.2653	
	3.787		0.1078507		0.269876		0.51018		0.1276		0.27809	
	3.7661		0.1187223		0.274554		0.51009		0.1708		0.28105	
	3.73215		0.1117248		0.279569		0.51705		0.2023		0.28113	
	3.714		0.1074466		0.313957		0.51605		0.207		0.28876	

!! Continued on next page !!

!! Continued from last page !!

V-F2	σV-F2	W-F2	σW-F2	M-Fave	σM-F	K	σK	Vb	σVb	Va	σVa	Va/b	σVa/b
0.239122	0.00203	0.3487	0.002201	1.94393	0.0038	1.0101	0.002	9.792	0.05741	43.595	0.255607	4.45212	0.0369162
0.245951	0.00213	0.3481	0.002369	1.94587	0.00382	1.0112	0.002	9.821	0.0578	43.685	0.257088	4.44808	0.0370204
0.241939	0.00223	0.3375	0.002486	1.94627	0.0039	1.0119	0.0021	9.829	0.05907	43.931	0.264005	4.46955	0.0379855
0.240727	0.00228	0.3255	0.002666	1.94847	0.0039	1.0133	0.0021	9.862	0.0593	44.193	0.265713	4.48116	0.0381033
0.234551	0.00565	0.3313	0.00287	1.94797	0.00602	1.0127	0.0033	9.865	0.09142	44.555	0.412911	4.51643	0.0591936
0.234723	0.00159	0.3079	0.00172	1.97413	0.00163	1.0095	0.0009	10.253	0.02541	46.919	0.116264	4.57608	0.0160364
0.227049	0.00159	0.2945	0.001615	1.97383	0.00183	1.0097	0.001	10.248	0.02853	47.253	0.131553	4.61099	0.0181542
0.21846	0.00185	0.253	0.002403	1.97447	0.00222	1.0099	0.0012	10.263	0.03462	47.765	0.161132	4.6541	0.0222035
0.206167	0.00268	0.2068	0.00326	1.97357	0.00303	1.0087	0.0016	10.246	0.04719	48.44	0.223082	4.72766	0.0307911
0.039479	0.00293	0.0393	0.010128	1.9517	0.00456	1.0005	0.003	9.912	0.06955	49.443	0.346913	4.98821	0.0494965
0.228846	0.00155	0.3057	0.001994	1.96023	0.0018	1.0081	0.0011	10.042	0.02766	45.546	0.125449	4.53554	0.017667
0.22839	0.00131	0.2795	0.001446	1.95803	0.00155	1.0078	0.0009	10.007	0.02372	45.759	0.108462	4.57268	0.0153281
0.224801	0.00111	0.2754	0.001248	1.9596	0.00174	1.0091	0.001	10.03	0.02676	45.919	0.122497	4.57821	0.0172719
0.229375	0.00121	0.2728	0.001609	1.9624	0.00132	1.0109	0.0008	10.071	0.02034	45.992	0.092882	4.56679	0.0130429
0.226569	0.00126	0.2656	0.001641	1.9639	0.00148	1.0117	0.0009	10.091	0.02279	46.098	0.104104	4.56825	0.0145897
0.226033	0.00118	0.269	0.001397	1.9634	0.00133	1.0114	0.0008	10.087	0.02052	46.196	0.093981	4.57973	0.0131763
0.225433	0.00127	0.2686	0.001497	1.96423	0.00157	1.0117	0.0009	10.1	0.02421	46.289	0.110952	4.58307	0.0155357
0.227919	0.00155	0.2715	0.002083	1.96357	0.00182	1.0112	0.001	10.092	0.02802	46.407	0.128835	4.5984	0.0180539
0.231055	0.00165	0.2933	0.001961	1.96387	0.00152	1.0115	0.0009	10.091	0.02339	46.497	0.107772	4.60777	0.0151038
0.222334	0.00226	0.258	0.003093	1.9615	0.00339	1.01	0.0018	10.06	0.05218	46.625	0.241852	4.63469	0.0339991
0.223784	0.00327	0.2732	0.003141	1.95893	0.00327	1.0085	0.0018	10.012	0.05019	46.808	0.234647	4.67516	0.0331444
0.231285	0.00242	0.2559	0.002927	1.96083	0.0027	1.0094	0.0015	10.046	0.0416	46.836	0.193938	4.66216	0.0273014
0.23097	0.0025	0.2711	0.002921	1.9626	0.00319	1.0105	0.0018	10.066	0.04909	46.946	0.228927	4.66385	0.0321629
0.231491	0.00229	0.2708	0.001103	1.96303	0.00376	1.0108	0.0021	10.067	0.05803	47.059	0.271263	4.67459	0.0381071
0.215279	0.00245	0.2664	0.001188	1.96277	0.00448	1.0109	0.0024	10.062	0.06906	47.151	0.323618	4.68602	0.0454845
0.217038	0.00273	0.2481	0.002572	1.96073	0.00439	1.01	0.0024	10.035	0.06746	47.308	0.318015	4.71432	0.0448172
0.22434	0.00238	0.2329	0.00129	1.95879	0.00405	1.0093	0.0021	10.004	0.06213	47.423	0.2945	4.74037	0.041632
0.224161	0.00259	0.2092	0.002358	1.95877	0.00376	1.0097	0.0021	10.014	0.05776	47.505	0.27402	4.74385	0.0386982
0.156223	0.00392	0.1838	0.004005	1.95153	0.00983	1.0084	0.0053	9.904	0.14972	47.739	0.721708	4.82022	0.1030542
0.176812	0.00581	0.1714	0.003581	1.94661	0.00491	1.0064	0.0032	9.807	0.07438	47.848	0.36288	4.87901	0.0523289
0.240778	0.00188	0.3103	0.002389	1.95187	0.00189	1.0074	0.0012	9.913	0.02883	44.464	0.129336	4.48541	0.0184514
0.239831	0.00161	0.3116	0.001967	1.95207	0.00172	1.009	0.001	9.918	0.02625	44.663	0.118212	4.50319	0.016856
0.235118	0.00135	0.3094	0.001301	1.95184	0.00158	1.01	0.0009	9.914	0.02403	44.907	0.108859	4.52965	0.0155285
0.237506	0.00172	0.2883	0.0017	1.94977	0.00236	1.0097	0.0013	9.881	0.03584	45.249	0.164119	4.57941	0.0234894
0.222309	0.00186	0.2792	0.001841	1.9509	0.00293	1.0101	0.0016	9.897	0.04464	45.587	0.205603	4.6061	0.0293793
0.224198	0.00188	0.2575	0.00189	1.95107	0.00276	1.0103	0.0015	9.902	0.04208	45.861	0.194898	4.63145	0.0278356
0.216577	0.0017	0.2191	0.001764	1.9525	0.002	1.0107	0.0011	9.914	0.03046	46.177	0.141858	4.65772	0.0202358
0.250061		0.3582		1.97621		1.0097		10.286		45.481		4.42165	
0.24961		0.3583		1.96311		1.0069		10.187		44.926		4.41014	
0.2525		0.3575		1.96459		1.0102		10.108		44.25		4.37775	
0.254557		0.3533		1.95557		1.0094		9.964		43.499		4.36557	
0.259178		0.3441		1.94029		1.0069		9.724		42.31		4.35113	
0.266355		0.3551		1.93473		1.0063		9.642		41.665		4.32116	

[Table 5.3] Various structural parameters derived from Rietveld structure models from this study are listed.

File #	GPa	Kelvin	Commen	L (GPa)	G (GPa	K (GPa)
NaMgF_11	0	301		128.301	43.87	69.807
NaMgF_11	0.975	301	cold			
NaMgF_11	1.971	301	cold			
NaMgF_11	3.013	301	cold			
NaMgF_11	4.053	301	cold			
NaMgF_11	5.106	301	cold			
NaMgF_11	7.488	301	cold			
NaMgF_11	7	873		148.956	44.32	89.861
NaMgF_11	8.281	1071		146.537	42.64	89.679
NaMgF_11	7.982	1283		138.528	40.22	84.899
NaMgF_11	6.932	870		148.103	44.48	88.791
NaMgF_11	6.451	671		147.764	44.80	88.025
NaMgF_11	6.08	469		150.718	46.11	89.243
NaMgF_11	5.932	311		154.081	47.45	90.812
NaMgF_11	5.188	309		150.438	46.88	87.927
NaMgF_11	6.295	1273		130.775	38.83	79.006
NaMgF_11	5.985	1074		135.586	41.00	80.913
NaMgF_11	5.65	874		139.246	42.69	82.325
NaMgF_11	5.235	671		143.056	44.31	83.971
NaMgF_11	4.854	471		145.192	45.31	84.775
NaMgF_11	4.573	313		147.269	46.28	85.566
NaMgF_11	5.177	1183		127.095	38.76	75.416
NaMgF_11	5.193	1220		126.041	38.35	74.903
NaMgF_11	4.703	1284		123.347	37.45	73.408
NaMgF_11	4.484	1074		126.432	39.32	74.008
NaMgF_11	4.374	872		131.578	41.38	76.398
NaMgF_11	3.769	670		136.027	43.23	78.384
NaMgF_11	3.52	467		139.178	44.60	79.709
NaMgF_11	3.186	314		141.651	45.59	80.863
NaMgF_11	1.645	312		133.248	44.15	74.382
NaMgF_11	1.924	675		125.371	41.23	70.397
NaMgF_11	1.624	1085		114.15	40.09	60.698
NaMgF_11	1.464	1144	attenuated			

File #	GPa	Kelvin	Comment	L (GPa)	G (GPa)	K (GPa)
NaMgF_12	1.4175	297	cold			
NaMgF_12	2.7072	297	cold			
NaMgF_12	3.8615	297	cold			
NaMgF_12	5.011	297	cold			
NaMgF_12	4.8617	767		138.63	43.00	81.29608
NaMgF_12	4.3986	1269		118.73	36.12	70.5668
NaMgF_12	3.9218	1058		123.26	38.56	71.84542
NaMgF_12	3.1942	671		130.78	42.03	74.74099
NaMgF_12	2.4276	302		138.61	45.20	78.34409
NaMgF_12	2.1202	301		136.63	44.81	76.88546
NaMgF_12	3.206	783		127.71	40.95	73.11287
NaMgF_12	3.7809	1076		121.2	38.14	70.34675
NaMgF_12	4.0025	1180	attenuated			
NaMgF_12	3.903	1264	attenuated			
NaMgF_12	3.8163	1377	attenuated			
NaMgF_12	3.2265	1476	attenuated			
NaMgF_12	2.6585	1371	attenuated			
NaMgF_12	2.6336	1321	attenuated			
NaMgF_12	2.6467	1276	attenuated			
NaMgF_12	2.6147	1234	attenuated			
NaMgF_12	2.737	1177	attenuated			
NaMgF_12	2.2991	1073	attenuated			
NaMgF_12	2.6407	1244	attenuated			
NaMgF_12	2.9437	1325	attenuated			
NaMgF_12	3.0545	1380	attenuated			
NaMgF_12	3.2379	1473	attenuated			

[Table 5.4] Ultrasonic elasticity data for $NaMgF_3$.

	Value	σ
G (GPa)	45.6258	0.2607
δG/δP (no units)	0.8934	0.0537
δG/δT (GPa/K)	-0.0095	0.0003
L (GPa)	134.0309	0.7797
δL/δP (no units)	5.0432	0.1528
δL/δT (GPa/K)	-0.0273	0.0009
K (GPa)	72.5944	0.4914
δK/δP (no units)	4.0898	0.0963
δK/δT (GPa/K)	-0.0156	0.0006

[Table 5.5] Equation of state data for $NaMgF_3$ derived from ultrasonic elasticity.

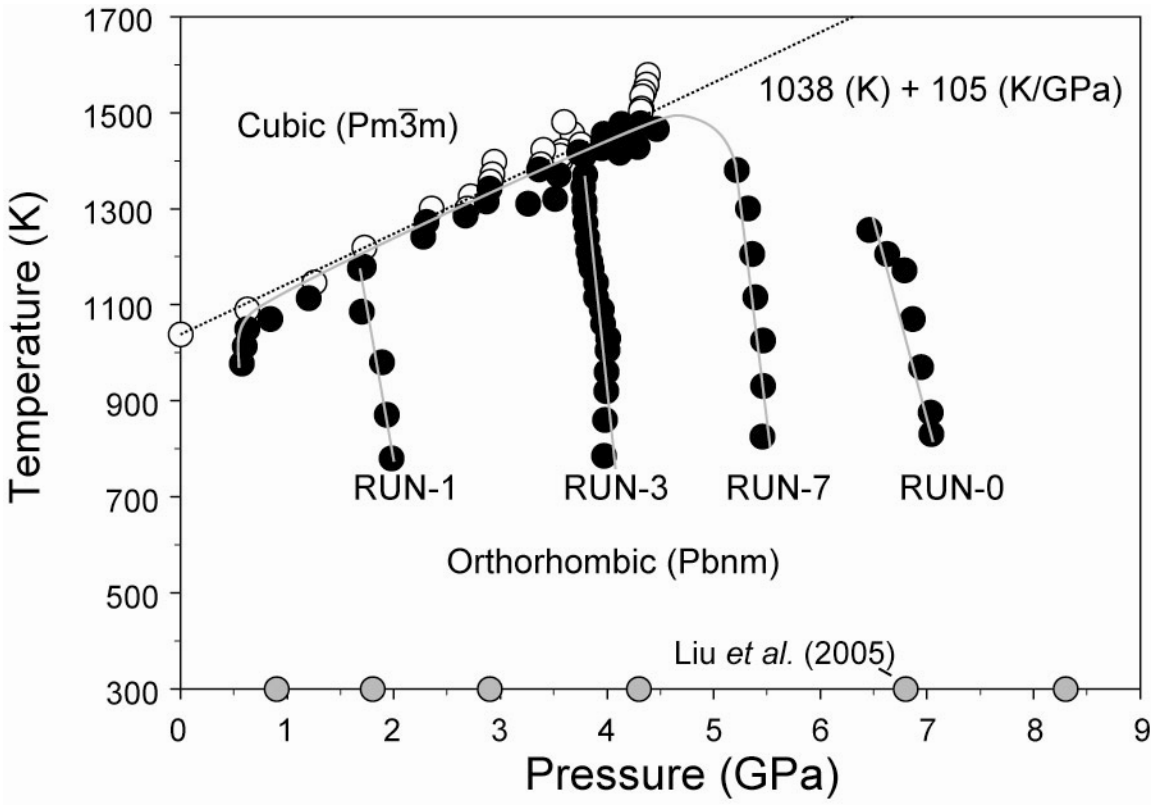

[Fig. 5.1] Orthorhombic (black) and cubic (white) structures of NaMgF3 are plotted in the pressure-temperature experimental pathway taken in the Paris-Edinburgh press. Data (grey) in the orthorhombic field reported in Liu et al. (2005) are included.

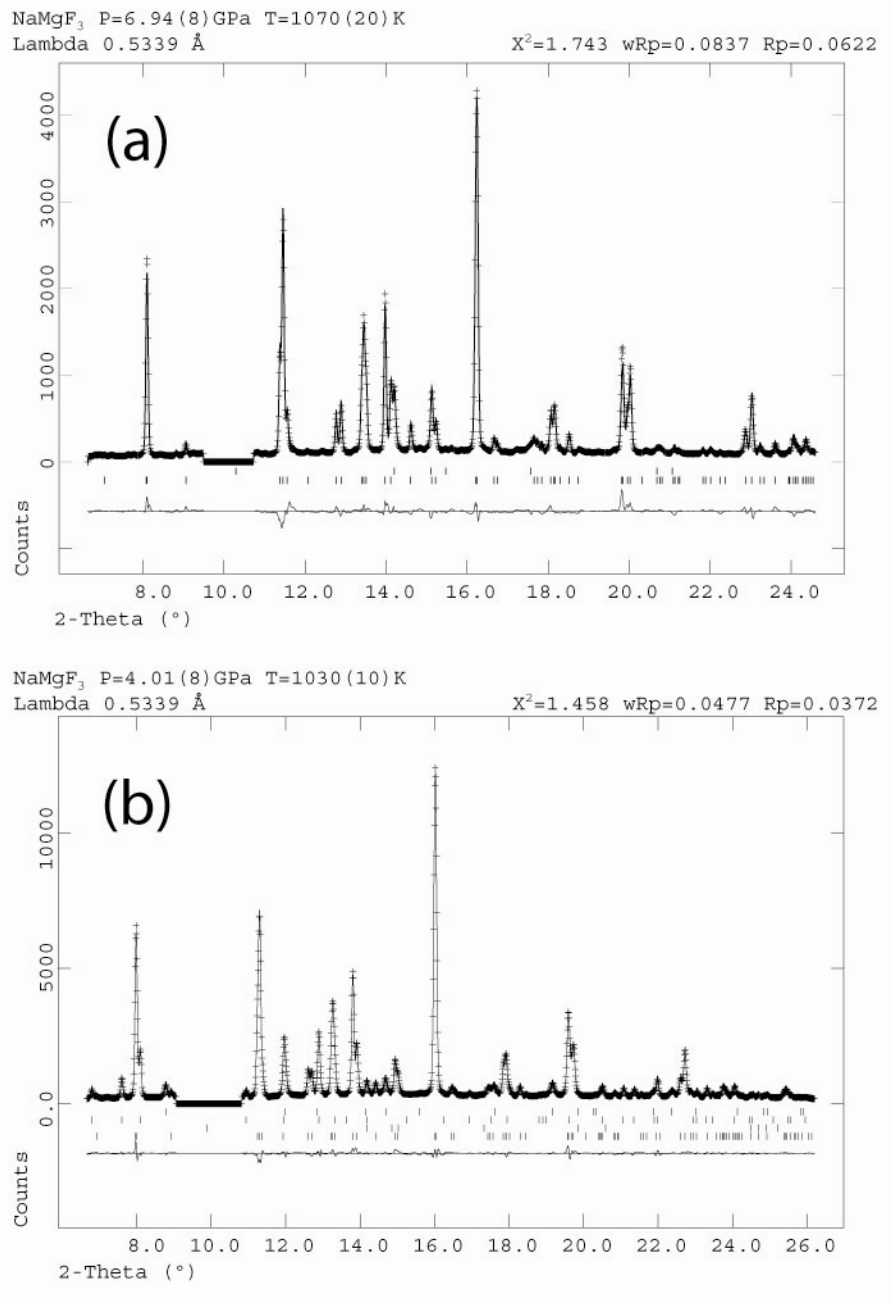

[Fig. 5.2] X-ray diffraction patterns of $NaMgF_3$ within the Paris-Edinburgh press.

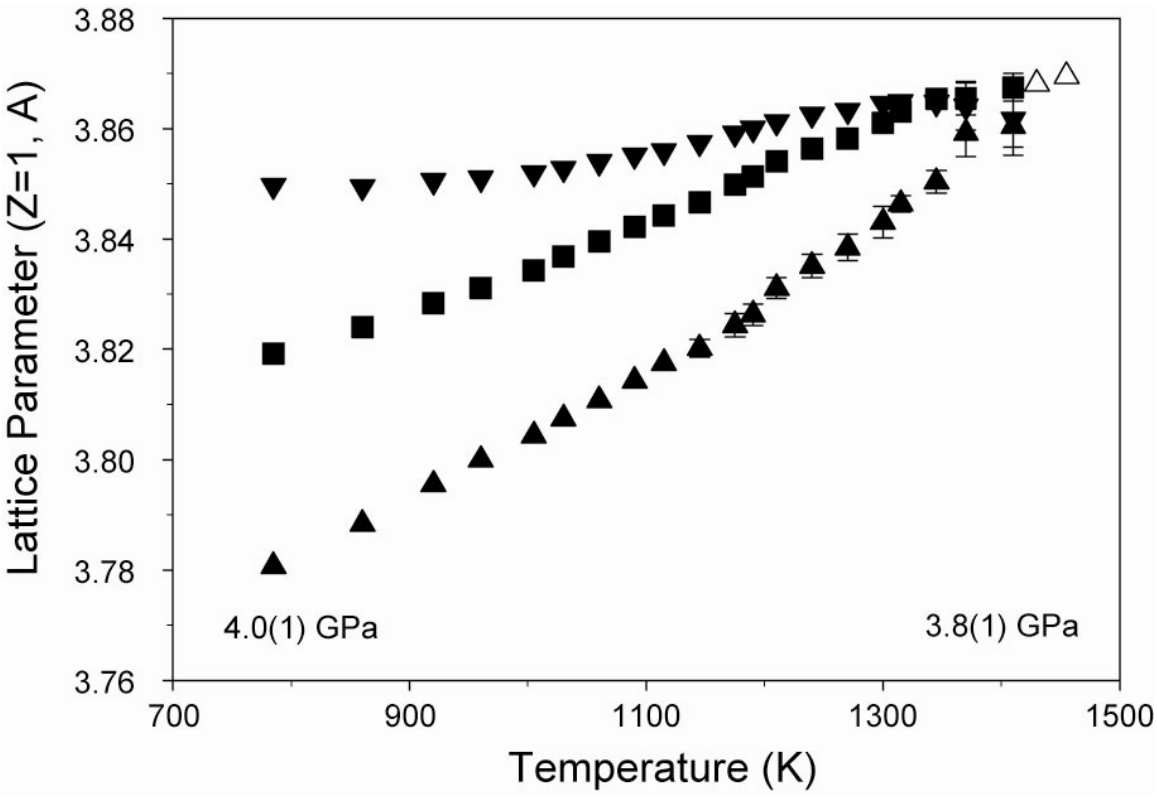

[Fig. 5.3] Pseudo-cubic unit cell parameters of $NaMgF_3$ at high pressure and temperature.

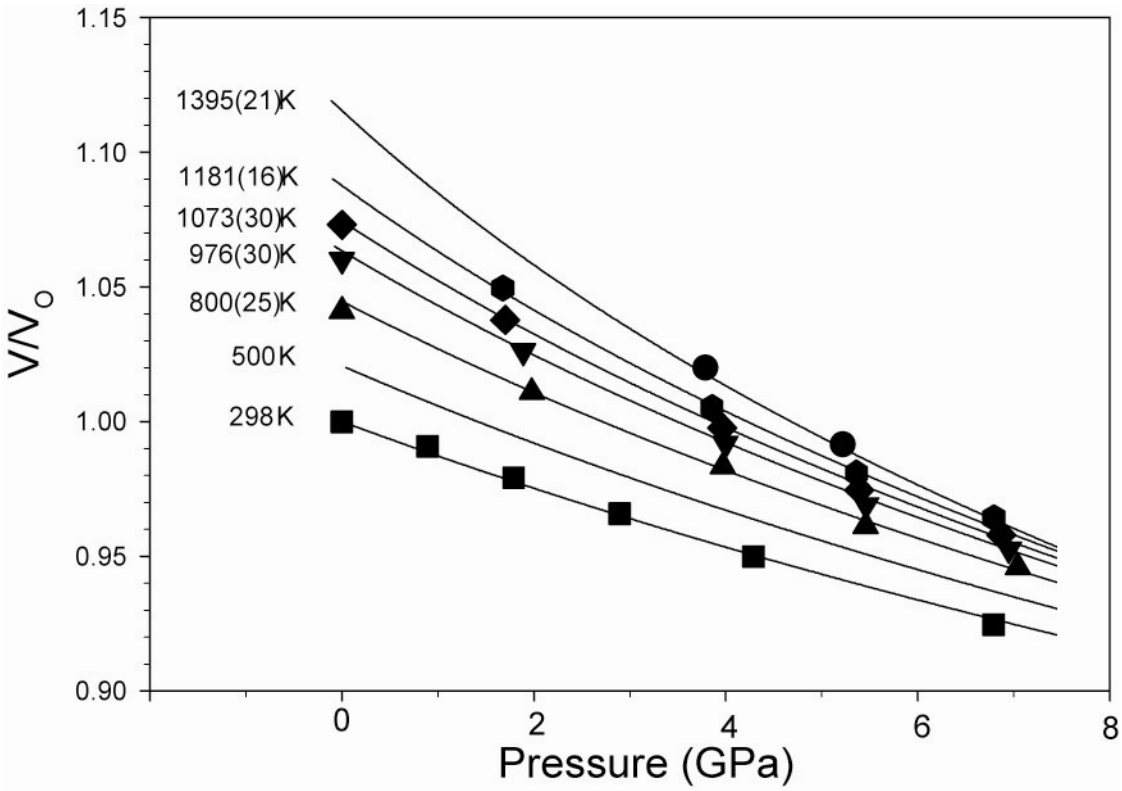

[Fig. 5.4] Projected equation of state isotherms of $NaMgF_3$ in comparison to experimental data.

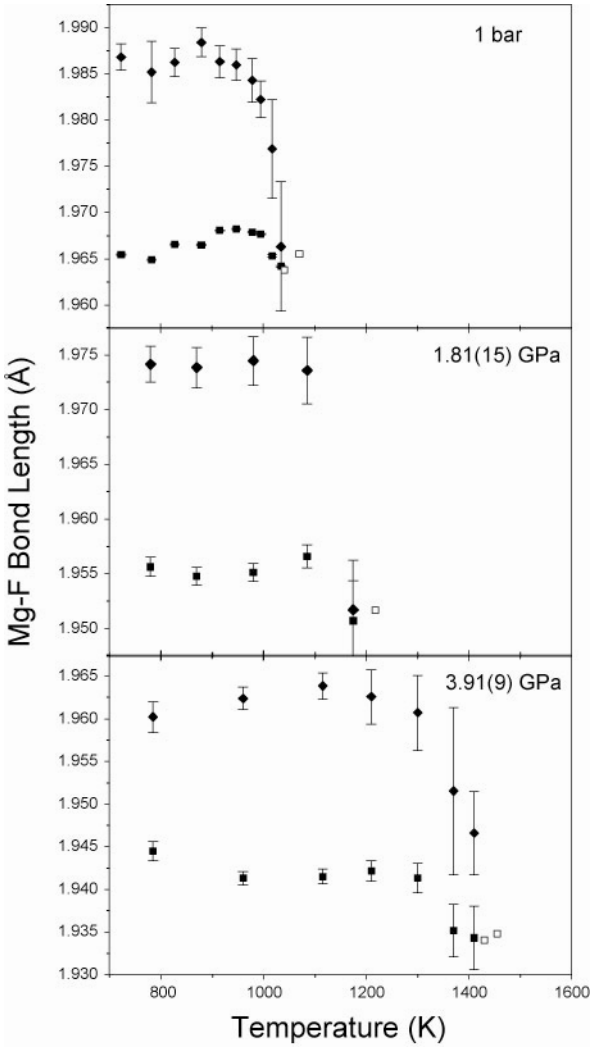

[Fig. 5.5] Average Mg-F bondlengths in $NaMgF_3$ derived from Rietveld refinement.

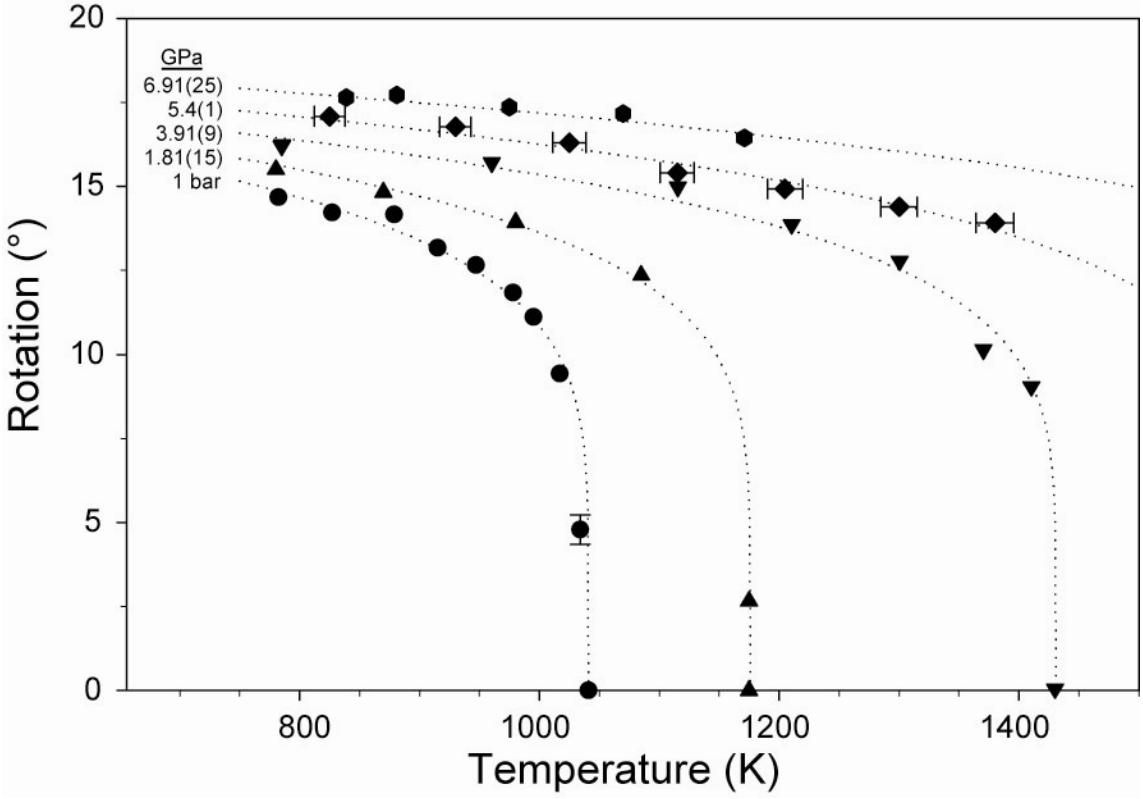

[Fig. 5.6] The tilt angle of Mg-F octahedra are plotted at several isobars with increasing temperature. Dotted lines are intended to guide the eye.

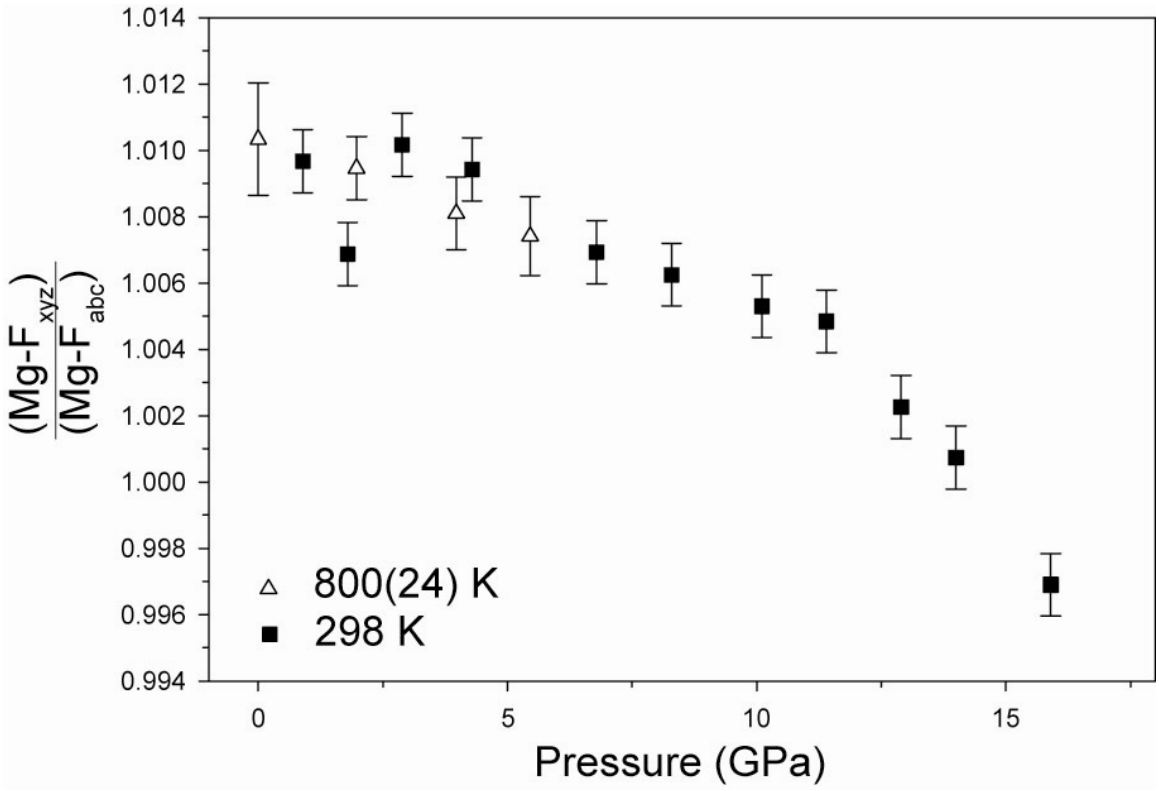

[Fig. 5.7] The ratio of the Mg-F bond length determined from atomic positions of Rietveld structure models is normalized according to the value determined from the unit cell.

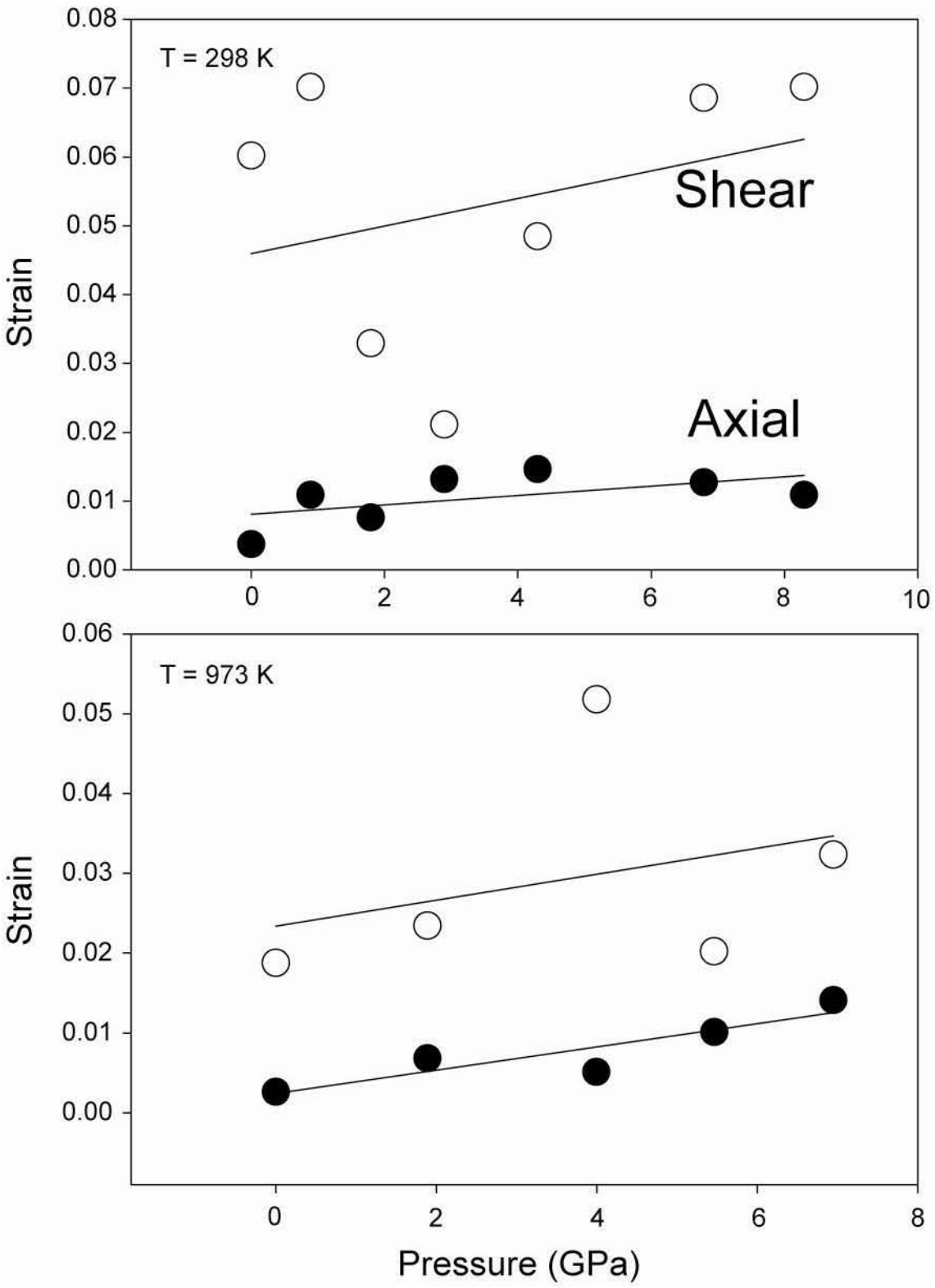

[Fig. 5.8] The distortion of MgF_6 octahedra is plotted vs. pressure. Error bars are larger that symbol size and not shown for clarity.

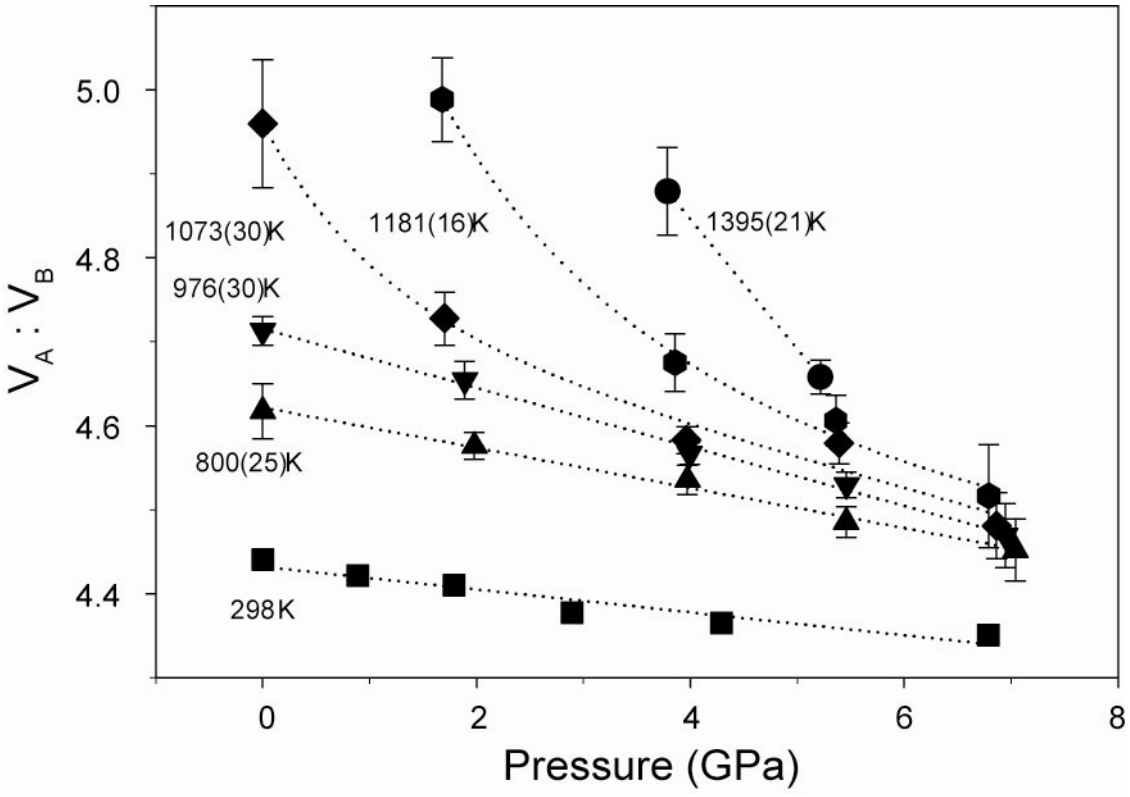

[Fig. 5.9] The V_A/V_B ratio of $NaMgF_3$ is plotted vs. pressure at several temperatures. Dotted lines are intended to guide the eye.

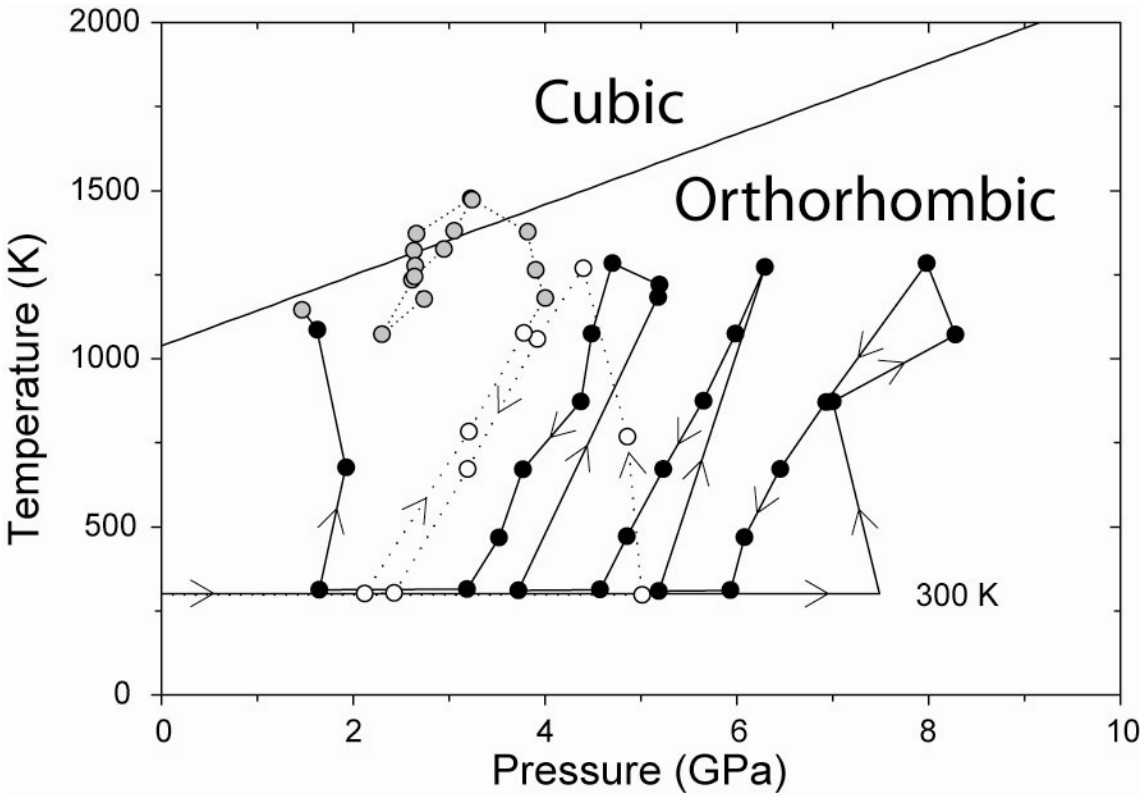

[Fig. 5.10] The experimental path and p-T conditions of NaMgF_11 and NaMgF_12 ultrasonic datasets. Black symbols are p-T conditions of ultrasonic measurements within the NaMgF_11 dataset while, white symbols are those within the NaMgF_12 dataset. Grey symbols are p-T conditions where the ultrasonic signal from the sample was not observed with the signal from the buffer rod. The orthorhombic to cubic phase transition slope from Figure 5.1 is shown and consistent with the energy dispersive X-ray diffraction observed at each p-T condition during the ultrasonic experiments.

Chapter VI

Phase transitions, compressibility, and Rietveld structure refinement of $NaMgF_3$ (Neighborite) in perovskite- and post-perovskite-related structures.

THIS CHAPTER PUBLISHED AS:

MARTIN, C.D., CRICHTON, W.A., LIU, H.Z., PRAKAPENKA, V., CHEN, J.H., AND PARISE, J.B. (2006) PHASE TRANSITIONS AND COMPRESSIBILITY OF $NaMgF_3$ (NEIGHBORITE) IN PEROVSKITE- AND POST-PEROVSKITE-RELATED STRUCTURES. GEOPHYSICAL RESEARCH LETTERS, 33(11), L11305. DOI:10.1029/2006GL026150.

MARTIN, C.D., CRICHTON, W.A., LIU, H.Z., PRAKAPENKA, V.B., CHEN, J., AND PARISE, J.B. (2006) IN-SITU RIETVELD STRUCTURE REFINEMENT OF PEROVSKITE AND POST-PEROVSKITE PHASES OF $NaMgF_3$ (NEIGHBORITE) AT HIGH PRESSURES. AMERICAN MINERALOGIST, 91(10), 1703-1706.

6.1. Abstract

In this chapter, Neighborite ($NaMgF_3$) is found to transform to a post-perovskite (ppv) phase between 27 and 30 GPa. The ppv phase is observed to the highest pressures achieved (56 GPa) at room temperature and transforms to an as yet unknown phase upon heating. Rietveld structure refinement using monochromatic synchrotron X-ray diffraction data provide models for the perovskite and post-perovskite structures at high pressure. The refined models at 27(1) GPa indicate some inter-octahedral F-F distances rival the average intra-octahedral distance, which may cause instability in the perovskite structure and drive the transformation to the post-perovskite phase. The ratio of A-site to B-site volume (V_A/V_B) in perovskite structured $NaMgF_3$ (ABX_3), spans from 5 in the zero-pressure high temperature cubic perovskite phase to 4 in this high pressure perovskite phase at 27(1) GPa, matching the V_A/V_B value in post-perovskite $NaMgF_3$. Using Rietveld refinement on post-perovskite structure models, we observe discrepancies

in pattern fitting, which may be described in terms of development of sample texture in the DAC, recrystallization, or a change of space group to ***C****mc*2_1, a non-isomorphic subgroup of ***C****mcm*—the space group describing the structure of $CaIrO_3$.

6.2. Introduction

At the lowermost region of Earth's mantle, the D" layer (Dziewonski and Anderson, 1981) is the medium through which heat and chemistry from the core may contact the mantle above. As a result, D" is a complex boundary region (Lay et al., 2004), laterally variable and marked by seismic anomalies. Researchers have long sought to understand the origin and dynamics of this distinct layer (Karato and Karki, 2001; Lay et al., 1998). Many high pressure experiments have investigated $MgSiO_3$ perovskite for explanations to anomalous seismic phenomena observed in D" and recent experiments have uncovered a post-perovskite structure of $MgSiO_3$ at pressures and temperatures thought to exist at D" (Murakami et al., 2004; Oganov and Ono, 2004).

A perovskite (pv) to post-perovskite (ppv) transformation is reported to occur in several ABX_3 materials: $MgGeO_3$ (Hirose et al., 2005), $CaIrO_3$ (Hirose and Fujita, 2005), and others (Tateno et al., 2006). In addition, the ppv structure is reportedly adopted by other materials with A_2X_3 stoichiometry, such as Fe_2O_3 (Ono and Ohishi, 2005), and Mn_2O_3 (Santillan et al., 2006). The ppv structure is based on the $CaIrO_3$ model, which is orthorhombic (***C****mcm,* $Z = 4$), and rarely adopted among oxides and sulfides at room pressure. The $CaIrO_3$ structure (Rodi and Babel, 1965) may be summarized as alternating layers of IrO_6 octahedra and Ca^{2+} normal to the b-axis within the *C*-centered lattice (Fig. 6.1a). Octahedra share edges along the a-axis and corners along the c-axis. The significant anisotropy of a $CaIrO_3$-type $MgSiO_3$ structure may explain the zones of strong seismic anisotropy observed within the D" layer (Garnero, 2004; Murakami et al., 2004; Tsuchiya et al., 2004).

The post-perovskite structure is now under intense study (Caracas and Cohen, 2005a; Mao et al., 2006; Murakami et al., 2005; Shieh et al., 2006) and debate. However, Rietveld structure refinement of ppv-$MgSiO_3$ has not yet documented. Powder statistics of X-ray diffraction data collected from samples in excess of 120 GPa are often compromised due to small scattering volumes present during experiments. Rietveld

refinement of ppv structure will confirm the accuracy of the $CaIrO_3$ (***C**mcm*) model and the study of analog materials at extreme conditions is an alternative route to this goal. Analogs, such as $MgGeO_3$ (Duffy et al., 2005; Hirose and Fujita, 2005), transform at lower pressures, increasing sample size, peak-to-background discrimination, and overall data quality.

The structure of neighborite ($NaMgF_3$) (Chao et al., 1961) was recently studied as an analog material for pv $MgSiO_3$ (O'Keeffe et al., 1979) using Rietveld structure modeling (Martin et al., 2005; Zhao et al., 1993). Previous work (Liu et al., 2005) finds a pv-ppv phase transition in $NaMgF_3$ between 28 and 30 GPa.

In the current study, we report results of x-ray diffraction as we observe high pressure structural phase transformation of $NaMgF_3$ perovskite to post-perovskite. Utilizing laser heating within the diamond anvil cell we overcome kinetic transition barriers and observe the formation of an unknown low symmetry phase of $NaMgF_3$ (designated N-phase). We report results of Rietveld refinement, detailing the high pressure perovskite and post-perovskite structures of $NaMgF_3$. From our analysis we reveal a high pressure instability in the pv-$NaMgF_3$ structure and test the $CaIrO_3$ (***C**mcm*) structure model of ppv-$NaMgF_3$.

6.3. Experimental Methods

Synthetic $NaMgF_3$ was prepared according to methods described in Chapter 3. Fine grains of $NaMgF_3$ were isolated from an aqueous suspension and dried at 60 ˚C. The fine powder was loaded into diamond anvil cells with 350 μm anvil culets. Tungsten was used to gasket the sample between the diamond anvils and graphite (1 wt.%) was used to absorb the heating laser radiation. The sample was insulated from the anvils during heating using thin layers of NaCl, which also served as an internal pressure standard (Decker, 1971; Sata et al., 2002).

Synchrotron X-ray diffraction experiments were conducted at the Advanced Photon Source (APS) at GeoSoilEnviroCARS (GSECARS) 13-ID-D, with $\lambda = 0.3344(2)$ Å, and at the High Pressure Collaborative Access Team (HPCAT) 16-ID-B, where $\lambda = 0.4018(2)$ Å. At the European Synchrotron Radiation Facility (ESRF) data were collected at ID-27 with $\lambda = 0.3738(2)$ Å. Beamline details are described previously for both

GSECARS (Shen et al., 2005) and ID-27 (Mezouar et al., 2005). Data at HPCAT and ESRF were collected by a MAR345 imaging plate, while that at GSECARS was collected by a MAR CCD (2048x2048). Data were reduced using the program FIT2D (Hammersley et al., 1996) and any saturated pixels were excluded from the 360 ˚ (chi) intensity integration. The program EXPGUI (Toby, 2001) for GSAS (Larson and Von Dreele, 2000) was used for Rietveld structure modeling. The background, scale factor and peak profile function type 3 (GW and LY only) amounted to 7 variables.

The data presented in this paper were collected during separate runs and after double-sided infrared laser heating (Schultz et al., 2005). Data from pv-$NaMgF_3$ were collected after heating to temperatures of 2000 K ± 200 K (Benedetti and Loubeyre, 2004). To avoid high temperature phase transition in ppv-$NaMgF_3$, this phase was not heated beyond 500 ± 200 ˚C. Because the Debye-Sherrer rings are not elliptical, we believe the variation in intensity around the rings result primarily from preferred orientation of sample powder, rather than from differential stress.

6.4. Results

6.4.1. Phase transitions

High pressure x-ray diffraction data show a complete transformation of $NaMgF_3$ perovskite (***P****bnm*) to a phase resembling $CaIrO_3$-type post-perovskite (***C****mcm*) at room temperature between 28 and 30 GPa (Fig 6.2); pressures much higher than that found previously (Liu et al., 2005). Heating is not required to drive the transition, which is accompanied by a 4% increase in density. This result is in contrast with the ~1% change reported for $CaIrO_3$ (Hirose and Fujita, 2005), $MgSiO_3$ (Murakami et al., 2004), $MgGeO_3$ (Hirose et al., 2005), and Fe_2O_3 (Ono and Ohishi, 2005). The larger change in density may reduce kinetic barriers to transform $NaMgF_3$ perovskite, while significant heating is required in the case of the oxides (Duffy et al., 2005; Murakami et al., 2004).

Our pressure-volume data for $NaMgF_3$ perovskite are consistent with previous estimates of zero pressure bulk modulus (Liu et al., 2005; Zhao et al., 1994), where K_T = 76.5 GPa. Fitting pressure-volume data of the post-perovskite phase to a Birch-Murnaghan equation of state, constrained so that $K_o' \equiv 4$, yields a zero pressure bulk

modulus of 137(18) GPa. The significant error in this value stems from uncertainty in the volume of the unit cell at 1 bar, 200(3) $Å^3$.

Contributing to error in unit cell axis measurements of post-perovskite is the presence of an unknown phase (N-phase) which appears upon laser heating in the region where ppv-$BaMgF_3$ is stable (Fig 6.3). This phase transition is reproducible and observed in 3 different sample loadings with different pressure markers, laser absorber, and gasket from data collected at both GSECARS and ESRF. The new peaks are not those expected of both MgF_2 (cotunnite) (Haines et al., 2001) and NaF (B2) as dissociation of $NaMgF_3$ would imply (Umemoto et al., 2006b). Solutions derived from indexing the new reflections favor an orthorhombic unit cell with 6 formula units (Z). The Inorganic Crystal Structure Database (ICSD) contains no orthorhombic ABX_3 structures with Z=6, and few with Z=12. Considering monoclinic and triclinic structure entries with these criteria are scarce in the ICSD, in addition to the quality of our Le Bail refinement (***P****nnm*, Fig. 6.3), we believe the structure of N-phase $NaMgF_3$ (a=8.353(3) Å, b=5.265(2), c=5.857(3), V=257.58(3) $Å^3$ at 37(1) GPa) may be new and need not belong space group ***P****nnm* necessarily. The density difference between N-phase and $CaIrO_3$-type $NaMgF_3$ is smaller than that between perovskite and post-perovskite, by about 1%, yet a value is difficult to derive since relaxing stress in post-perovskite requires heating, driving the phase transition to N-phase. Upon decompression to the perovskite field, diffraction peaks broaden suggesting the onset of amorphization of N-phase at low pressure.

6.4.2. Rietveld structure refinement

Rietveld structure refinement of pv-$NaMgF_3$ from monochromatic X-ray diffraction data indicate the atomic parameters, MgF_6 tilting angles (Zhao et al., 1993), and relative volumes of the A- and B-site polyhedra (V_A/V_B ratio) (Thomas, 1998) at 27(1) GPa just before the pv to ppv transition (Fig. 6.4a and Table 6.1a). The NaCl pressure media is present as both the B1 and B2 phases (Sata et al., 2002). In addition, we observe very weak reflections (downward pointing arrows, Fig. 6.4a) in diffraction patterns above 14 GPa. The first 3 of these peaks at low angle may be indexed as the 022, 023, and 130 of ppv-$NaMgF_3$, which would confirm the phase requires a lower pressure

to stabilize under shear stress (Liu et al., 2005). The final 2 reflections at high angle result from N-phase $NaMgF_3$ rather than from graphite or unknown contamination. X-ray diffraction data show a complete transformation of pv-$NaMgF_3$ (***P**bnm*) to ppv-$NaMgF_3$ above 27(1) GPa.

The X-ray diffraction data from ppv-$NaMgF_3$ show some evidence for non-uniform texture of the Debye-Scherrer rings and while portions show smooth intensity variation about changing angles of chi, there is evidence of sample recrystallization and/or reorientation close to 111_{Cmcm}. Our Rietveld refinements of ppv-$NaMgF_3$ using the $CaIrO_3$-type (***C**mcm*) structural model assigns too much intensity to the 020_{Cmcm} and 200_{Cmcm}, while assigning too little to the 002_{Cmcm}, and 111_{Cmcm}. Texture due to preferred orientation of sample powder within the diamond anvil cell may be modeled using a spherical-harmonic correction implemented in GSAS (VonDreele, 1997). However, the validity of this correction to in-situ high pressure X-ray diffraction data of orthorhombic materials is debatable and in practice, when carried out to more than 4 orders in this case, we find the spherical-harmonic correction will over-fit the data to the detriment of the structural model. While justification of the correction is difficult in this case, the correction may be checked by the texture index, a value summing the magnitude of each texture constant (VonDreele, 1997). Based on previous studies (Sitepu et al., 2005; VonDreele, 1997) and our own trials, we find the ***C**mcm* structural model requires a cylindrical 4^{th} order spherical harmonic preferred orientation correction (cylindrical, 5 parameters) with a texture index of 2.14 (Fig. 6.4b and Table 6.1c) to achieve a satisfactory fit to the data.

Because it is not clear whether the intensity integration alone is sufficient to overcome effects of preferred orientation in the data, we have investigated six non-isomorphic subgroups (I) of ***C**mcm* (Hahn, 1995) and observe a slightly better fit to diffraction patterns using an alternative structure model of ppv described by lower symmetry space group #36 (***C**mc*2_1, Fig. 6.1b) without a spherical harmonic texture correction. This model was investigated previously to describe a layered sulfide at room pressure (Wada and Onoda, 1990), but was later refuted (Kim et al., 1997). This structure model allows extra degrees of freedom, amounting to displacement of B-site cations within further asymmetric BX_6 octahedra. Residuals from Rietveld refinement of ***C**mc*2_1

models are improved (Fig. 6.4b and Table 6.1d) and better fits to both 002_{Cmc21} and $(200)_{Cmc21}$ are achieved, however some intensity of the 111_{Cmc21} as well as 200_{Cmc21} remain partially misfit. Rietveld structure models in the other subgroups, $\boldsymbol{C}222_1$ for example, improve the fit to 111, but are problematic with data at higher angle. Monoclinic models do not significantly improve the fit to the data nor suggest deviation from orthorhombic symmetry. While the data do not provide irrefutable evidence of a symmetry lower than the $\boldsymbol{C}mcm$ ($CaIrO_3$) structural model for ppv-$NaMgF_3$, the distortion and asymmetry found in the $\boldsymbol{C}mc2_1$ structure model could perhaps stabilize at extreme conditions. High pressure studies on other compositions with the ppv structure, may help differentiate effects from preferred orientation.

6.5. Discussion

Because of a strong resemblance in the diffraction patterns of orthorhombic post-perovskite, it is possible the topology of N-phase $NaMgF_3$ is also layered, containing cations in coordination schemes other than that existing in the orthorhombic structure. While more work is necessary to completely identify a unit cell and structure for N-phase $NaMgF_3$, we can gain insight into possible high pressure structures through comparative analysis of other high pressure fluoride phases. While sodium in post-perovskite $NaMgF_3$ is contained within a tri-capped trigonal prism, at 38 GPa MgF_2 (Sellaite) is reported to form a structure based on mineral cotunnite. (Haines et al., 2001), where magnesium also resides in a tri-capped trigonal prism. Thus, N-phase $NaMgF_3$, or further high pressure forms of $NaMgF_3$, should contain both sodium and magnesium in these 9-fold coordination units, and perhaps adopt structures (Caracas and Cohen, 2005b) expected for A_2X_3 compounds as opposed to simple dissociation (Parise et al., 2004; Umemoto et al., 2006a).

A transformation in "$CaIrO_3$-type" $NaMgF_3$ to N-phase has possible implications for $MgSiO_3$ and the lower mantle. A post-post-perovskite phase such as N-phase may account for previous observations of extra x-ray reflections during studies of $MgSiO_3$ and $MgGeO_3$ post-perovskite (Duffy et al., 2005; Guignot et al., 2007) and several recent studies of lower mantle tomography (Flores and Lay, 2005; Hernlund et al., 2005) suggest a seismic discontinuity below the D". Recent rationale invokes a double-crossing

of the post-perovskite phase boundary by the geotherm at two different depths. $NaMgF_3$ has proven to be a satisfactory analogue material for $MgSiO_3$ thus, solid-solid transformation in silicate post-perovskite via N-phase distortion may be possible within the lower mantle considering geotherms (Lay et al., 2004; Zerr et al., 1998) above the core-mantle boundary as well as within rocky interiors of extraterrestrial bodies.

The MgF_6 tilting angles and V_A/V_B ratio in the structure of pv-$NaMgF_3$ (***P****bnm*) at 27(1) GPa reveal an instability, which may drive structure transformation to ppv. The V_A/V_B ratio, an order parameter for perovskite-perovskite phase transitions, is 5 in cubic (***Pm*** $\bar{3}$ *m*) perovskite structures and less than 5, though greater than 4, in perovskite structures where octahedra are tilted (Thomas, 1998). At 27(1) GPa, the V_A/V_B value in pv-$NaMgF_3$ is 4.07(2), matching the V_A/V_B value observed in our Rietveld models of ppv-$NaMgF_3$ (***C****mcm*), 3.95(5). This ratio is also equal or close to 4 in the ppv-oxides $MgSiO_3$, 4.01, (Murakami et al., 2004), $MgGeO_3$, 4.28, (Hirose et al., 2005), $CaIrO_3$, 4.19, (Rodi and Babel, 1965), and Fe_2O_3, 3.89, (Ono and Ohishi, 2005). This realization is significant because it suggests minimal relative reconstruction of each site is required to transform between pv and ppv. In addition, it may be possible to predict the pressure of a pv-ppv phase transition in other perovskite (or A_2X_3) structured materials by extrapolating the change in V_A/V_B at high pressure to a value close to 4. Combining previous data (Liu et al., 2005) with our current results, we find that V_A/V_B for pv-$NaMgF_3$ decreases linearly with pressure at a rate of $1.40(2)\times10^{-2}$ GPa^{-1} between 1 bar and 27(1) GPa.

Examination of the Rietveld structure model of pv-$NaMgF_3$ at 27(1) GPa reveals that tilting of the perovskite octahedra (Glazer, 1972; Liu et al., 2005; Thomas, 1998) forces some extra-octahedral F-F distances to rival the average intra-octahedral F-F distance. At which point electrostatic repulsion between select pairs of extra-octahedral fluorine atoms may strain the pv octahedral unit enough to drive the transition to ppv structure. The most notable difference between MgF_6 octahedra in pv and ppv is the amount of strain. Octahedra in ppv-$NaMgF_3$, as well as the published $CaIrO_3$-type oxides, demonstrate twice the average value of shear strain (via strain matrix see: (Zhao et al., 1993) as that observed for pv-$NaMgF_3$. This significant strain observed of octahedra in $CaIrO_3$-type structures (Rodi and Babel, 1965) is likely not favored by the B-site cation

and may help explain why so few $CaIrO_3$-type structures are stable at room pressure. Similarly, shear strain of octahedra in ppv-$NaMgF_3$ likely contributes to instability in the structure, which transforms to an unknown orthorhombic phase upon laser heating.

Subsequent studies of $CaIrO_3$ should reveal structure changes which we expect of materials adopting the post-perovskite structure. With this structure knowledge we can further investigate the role of the V_A/V_B parameter on the pv-ppv phase transition and explore the relationship with the Clapeyron slope.

References

Benedetti, L.R., and Loubeyre, P. (2004) Temperature gradients, wavelength-dependent emissivity, and accuracy of high and very-high temperatures measured in the laser-heated diamond cell. High Pressure Research, 24(4), 423-445.

Caracas, R., and Cohen, R.E. (2005a) Effect of chemistry on the stability and elasticity of the perovskite and post-perovskite phases in the $MgSiO_3$-$FeSiO_3$-Al_2O_3 system and implications for the lowermost mantle. Geophysical Research Letters, 32(16).

-. (2005b) Prediction of a new phase transition in Al_2O_3 at high pressures. Geophysical Research Letters, 32(6), L06303.

Chao, E.C.T., Evans, H.T., Skinner, B.J., and Milton, C. (1961) Neighborite, $NaMgF_3$, a New Mineral From the Green River Formation, South Ouray, Utah. American Mineralogist, 46(3-4), 379-393.

Decker, D.L. (1971) High-Pressure Equation of State for NaCl, KCl, and CsCl. Journal of Applied Physics, 42(8), 3239.

Duffy, T.S., Kubo, A., Shieh, S.R., Shen, G.Y., Prakapenka, V.B., Kiefer, B., and Shim, S.H. (2005) Compressibility and Structural Evolution of Germanate and Silicate Post-Perovskite Phases. AGU Fall Meeting 2005 #MR22A-07.

Dziewonski, A.M., and Anderson, D.L. (1981) Preliminary Reference Earth Model. Physics of the Earth and Planetary Interiors, 25(4), 297-356.

Flores, C., and Lay, T. (2005) The trouble with seeing double. Geophysical Research Letters, 32(24), L24305. DOI:10.1029/2005GL024366.

Garnero, E.J. (2004) A new paradigm for Earth's core-mantle boundary. Science, 304(5672), 834-836. DOI:10.1126/science.1097849.

Glazer, A.M. (1972) Classification of Tilted Octahedra in Perovskites. Acta Crystallographica Section B-Structural Science, B 28(V15), 3384-3392.

Guignot, N., Andrault, D., Morard, G., Bolfan-Casanova, N., and Mezouar, M. (2007) Thermoelastic properties of post-perovskite phase $MgSiO_3$ determined experimentally at core-mantle boundary P-T conditions. Earth and Planetary Science Letters, 256(1-2), 162-168.

Hahn, T. (1995) International Tables for Crystallography, Vol. A, SpaceGroup Symmetry. Kluver Academic Publishers.

Haines, J., Leger, J.M., Gorelli, F., Klug, D.D., Tse, J.S., and Li, Z.Q. (2001) X-ray diffraction and theoretical studies of the high-pressure structures and phase transitions in magnesium fluoride. Physical Review B, 6413(13).

Hammersley, A.P., Svensson, S.O., Hanfland, M., Fitch, A.N., and Hausermann, D. (1996) Two-dimensional detector software: From real detector to idealized image or two-theta scan. High Pressure Research, 14(4-6), 235-248.

Hernlund, J.W., Thomas, C., and Tackley, P.J. (2005) A doubling of the post-perovskite phase boundary and structure of the Earth's lowermost mantle. Nature, 434(7035), 882-886. DOI:10.1038/nature03472.

Hirose, K., and Fujita, Y. (2005) Clapeyron slope of the post-perovskite phase transition in $CaIrO_3$. Geophysical Research Letters, 32(13), L13313(1-4). DOI:10.1029/2005GL023219.

Hirose, K., Kawamura, K., Ohishi, Y., Tateno, S., and Sata, N. (2005) Stability and equation of state of $MgGeO_3$ post-perovskite phase. American Mineralogist, 90(1), 262-265.

Karato, S., and Karki, B.B. (2001) Origin of lateral variation of seismic wave velocities and density in the deep mantle. Journal of Geophysical Research-Solid Earth, 106(B10), 21771-21783.

Kim, C., Yun, H.S., Lee, Y., Shin, H., and Liou, K. (1997) Structure and electrical conductivity of $AgTaS_3$. Journal of Solid State Chemistry, 132(2), 389-393.

Larson, A.C., and Von Dreele, R.B. (2000) General Structure Analysis System (GSAS). Los Alamos National Laboratory Report, 86-748.

Lay, T., Garnero, E.J., and William, Q. (2004) Partial melting in a thermo-chemical boundary layer at the base of the mantle. Physics of the Earth and Planetary Interiors, 146(3-4), 441-467.

Lay, T., Williams, Q., and Garnero, E.J. (1998) The core-mantle boundary layer and deep Earth dynamics. Nature, 392(6675), 461-468. DOI:10.1038/33083.

Liu, H.Z., Chen, J., Hu, J., Martin, C.D., Weidner, D.J., Hausermann, D., and Mao, H.K. (2005) Octahedral tilting evolution and phase transition in orthorhombic $NaMgF_3$ perovskite under pressure. Geophysical Research Letters, 32(4), L04304(1-5). DOI:10.1029/2004GL022068.

Mao, L.W., Mao, H.K., Sturhahn, W., Zhao, J., Prakapenka, V.B., Meng, Y., Shu, J.F., Fei, Y.W., and Hemley, R.J. (2006) Iron-Rich Post-Perovskite and the Origin of Ultralow-Velocity Zones. Science, 312(5773), 564 - 565. DOI:10.1126/science.1123442.

Martin, C.D., Chaudhuri, S., Grey, C.P., and Parise, J.B. (2005) Effect of A-site cation radius on ordering of BX_6 octahedra in $(K,Na)MgF_3$ perovskite. American Mineralogist, 90(10), 1522-1533.

Mezouar, M., Crichton, W.A., Bauchau, S., Thurel, F., Witsch, H., Torrecillas, F., Blattmann, G., Marion, P., Dabin, Y., Chavanne, J., Hignette, O., Morawe, C., and Borel, C. (2005) Development of a new state-of-the-art beamline optimized for monochromatic single-crystal and powder X-ray diffraction under extreme conditions at the ESRF. Journal of Synchrotron Radiation, 12, 659-664.

Murakami, M., Hirose, K., Kawamura, K., Sata, N., and Ohishi, Y. (2004) Post-perovskite phase transition in $MgSiO_3$. Science, 304(5672), 855-858. DOI:10.1126/science.1095932.

Murakami, M., Hirose, K., Sata, N., and Ohishi, Y. (2005) Post-perovskite phase transition and mineral chemistry in the pyrolitic lowermost mantle. Geophysical Research Letters, 32(3), L03304. DOI:10.1029/2004GL021956.

O'Keeffe, M., Hyde, B.G., and Bovin, J.O. (1979) Contribution to the Crystal-Chemistry of Orthorhombic Perovskites - $MgSiO_3$ and $NaMgF_3$. Physics and Chemistry of Minerals, 4(4), 299-305.

Oganov, A.R., and Ono, S. (2004) Theoretical and experimental evidence for a post-perovskite phase of $MgSiO_3$ in Earth's D " layer. Nature, 430(6998), 445-448. DOI:10.1038/nature02701.

Ono, S., and Ohishi, Y. (2005) In situ X-ray observation of phase transformation in Fe_2O_3 at high pressures and high temperatures. Journal of Physics and Chemistry of Solids, 66(10), 1714-1720. DOI:10.1016/j.jpcs.2005.06.010.

Parise, J.B., Umemoto, K., Wentzcovitch, R.A., and Weidner, D.J. (2004) Post-perovskite transition in $NaMgF_3$. AGU Fall Meeting 2004 #MR23A-0188.

Rodi, F., and Babel, D. (1965) Ternare Oxide Der Ubergangsmetalle .4. Erdalkaliiridium(4)-Oxide - Kristallstruktur Von $CaIrO_3$. Zeitschrift Fur Anorganische Und Allgemeine Chemie, 336(1-2), 17.

Santillan, J., Shim, S.H., Shen, G.Y., and Prakapenka, V.B. (2006) High-pressure phase transition in Mn_2O_3: Application for the crystal structure and preferred orientation of the $CaIrO_3$ type. Geophysical Research Letters, 33(15), L15307(1-5).

Sata, N., Shen, G.Y., Rivers, M.L., and Sutton, S.R. (2002) Pressure-volume equation of state of the high-pressure B2 phase of NaCl. Physical Review B, 65(10). DOI:10.1103/PhysRevB.65.104114.

Schultz, E., Mezouar, M., Crichton, W., Bauchau, S., Blattmann, G., Andrault, D., Fiquet, G., Boehler, R., Rambert, N., Sitaud, B., and Loubeyre, P. (2005) Double-sided laser heating system for in situ high pressure-high temperature monochromatic X-ray diffraction at the ESRF. High Pressure Research, 25(1), 71-83.

Shen, G.Y., Prakapenka, V.B., Eng, P.J., Rivers, M.L., and Sutton, S.R. (2005) Facilities for high-pressure research with the diamond anvil cell at GSECARS. Journal of Synchrotron Radiation, 12, 642-649. DOI:10.1107/S0909049505022442.

Shieh, S.R., Duffy, T.S., Kubo, A., Shen, G.Y., Prakapenka, V.B., Sata, N., Hirose, K., and Ohishi, Y. (2006) Equation of state of the postperovskite phase synthesized from a natural $(Mg,Fe)SiO_3$ orthopyroxene. Proceedings of the National Academy of Sciences of the United States of America, 103(9), 3039-3043.

Sitepu, H., O'Connor, B.H., and Li, D. (2005) Comparative evaluation of the March and generalized spherical harmonic preferred orientation models using X-ray diffraction data for molybdite and calcite powders. Journal of Applied Crystallography, 38, 158-167.

Tateno, S., Hirose, K., Sata, N., and Ohishi, Y. (2006) High-pressure behavior of $MnGeO_3$ and $CdGeO_3$ perovskites and the post-perovskite phase transition. Physics and Chemistry of Minerals, 32(10), 721-725. DOI:10.1007/s00269-005-0049-7.

Thomas, N.W. (1998) New global parameterization of perovskite structures. Acta Crystallographica Section B-Structural Science, 54, 585-599.

Toby, B.H. (2001) EXPGUI, a graphical user interface for GSAS. Journal of Applied Crystallography, 34, 210-213.

Tsuchiya, T., Tsuchiya, J., Umemoto, K., and Wentzcovitch, R.A. (2004) Phase transition in $MgSiO_3$ perovskite in the earth's lower mantle. Earth and Planetary Science Letters, 224(3-4), 241-248.

Umemoto, K., Wentzcovitch, R.A., and Allen, P.B. (2006a) Dissociation of $MgSiO_3$ in the Cores of Gas Giants and Terrestrial Exoplanets. Science, 331(5763), 983 - 986. DOI:10.1126/science.1120865.

Umemoto, K., Wentzcovitch, R.M., Weidner, D.J., and Parise, J.B. (2006b) $NaMgF_3$: A low-pressure analog of $MgSiO_3$. Geophysical Research Letters, 33(15).

VonDreele, R.B. (1997) Quantitative texture analysis by Rietveld refinement. Journal of Applied Crystallography, 30, 517-525.

Wada, H., and Onoda, M. (1990) Preparation of New Compound $AgTaS_3$. Chemistry Letters(5), 705-706.

Zerr, A., Diegeler, A., and Boehler, R. (1998) Solidus of Earth's deep mantle. Science, 281(5374), 243-246.

Zhao, Y.S., Parise, J.B., Wang, Y.B., Kusaba, K., Vaughan, M.T., Weidner, D.J., Kikegawa, T., Chen, J., and Shimomura, O. (1994) High-Pressure Crystal-Chemistry of Neighborite, $NaMgF_3$ - an Angle-Dispersive Diffraction Study Using Monochromatic Synchrotron X-Radiation. American Mineralogist, 79(7-8), 615-621.

Zhao, Y.S., Weidner, D.J., Parise, J.B., and Cox, D.E. (1993) Thermal-Expansion and Structural Distortion of Perovskite - Data For $NaMgF_3$ Perovskite .1. Physics of the Earth and Planetary Interiors, 76(1-2), 1-16.

(a)

a (Å)	b	c	Volume (Å^3)
4.8904(13)	5.2022(6)	7.1403(8)	181.65(4)

	Na (4c)	Mg (4b)	F1 (4c)	F2 (8d)
x	0.9771(19)	0.0000	0.1019(25)	0.6750(17)
y	0.0802(13)	0.5000	0.4697(17)	0.3110(10)
z	0.2500	0.0000	0.2500	0.0619(12)

Octahedra Tilt	ϕ(°)	θ(°)	Φ(°)
	15.2(8)	17.8(7)	23.2(6)

Mg-F1 (x2)	Mg-F2 (x2)	Mg-F2 (x2)	V_B (Å^3)	V_A/V_B (Å^3)
1.860(4)	1.886(7)	1.917(8)	8.95(8)	4.07(5)

Residuals	χ^2	wRp	R(F^2)	Dwd
MAR345 (IP)	0.1190	0.0098	0.0588	0.5810

(b)

a (Å)	b	c	Volume (Å^3)
2.7145(14)	8.393(5)	6.8512(23)	156.09(7)

	Na (4c)	Mg (4a)	F1 (4c)	F2 (8f)
x	0.0000	0.0000	0.5000	0.5000
y	0.2567(13)	0.0000	0.4242(15)	0.1402(8)
z	0.2500	0.0000	0.2500	0.0676(12)

Mg-F1 x2	Mg-F2 x4	V_B (Å^3)	V_A/V_B (Å^3)
1.827(5)	1.855(6)	8.36(1)	3.66(8)

Residuals	χ^2	wRp	R(F^2)	Dwd
MAR CCD	0.0222	0.0038	0.0325	0.1120

(c)

a (Å)	b	c	Volume (Å^3)
2.7164(16)	8.381(5)	6.8487(25)	155.9(1)

	Na (4c)	Mg (4a)	F1 (4c)	F2 (8f)
x	0.0000	0.0000	0.5000	0.5000
y	0.2422(14)	0.0000	0.4433(12)	0.1385(10)
z	0.2500	0.0000	0.2500	0.0579(9)

Texture Index = 2.1429. C_l^{mn} as (l,m,n)

	(2,0,0)	(2,0,2)	(4,0,0)	(4,0,2)	(4,0,4)
	-1.1883	0.3942	-0.3545	-1.6891	-2.1180

Mg-F1 x2	Mg-F2 x4	V_B (Å^3)	V_A/V_B (Å^3)
1.777(3)	1.830(6)	7.881(82)	3.94(6)

Residuals	χ^2	wRp	R(F^2)	Dwd
MAR CCD	0.0136	0.0030	0.0196	0.1480

(d)

a (Å)	b	c	Volume (Å^3)
2.7143(9)	8.393(3)	6.846(2)	155.99(9)

	Na (4a)	Mg (4a)	F1 (4a)	F2 (4a)	F3 (4a)
x	0.0000	0.0000	0.0000	0.0000	0.0000
y	0.2531(6)	0.0129(13)	0.9251(7)	0.6286(10)	0.6554(8)
z	0.0036(7)	0.2556(18)	0.0000(7)	0.1551(9)	0.7902(13)

Mg-F1a	Mg-F1b	Mg-F2 x2	Mg-F3	V_B (Å^3)	V_A/V_B (Å^3)
1.900(15)	1.752(15)	1.805(10)	1.975(10)	8.44(1)	3.62(5)

Residuals	χ^2	wRp	R(F^2)	Dwd
MAR CCD	0.0188	0.0035	0.0325	0.1310

[Table 6.1] Structure parameters derived from Rietveld refinement of data for (**a**) $NaMgF_3$ perovskite at 27(1) GPa, (**b**) post-perovskite structure models of $NaMgF_3$ at 54(2) GPa without correction for preferred orientation as *Cmcm*, (**c**) with correction for preferred orientation as *Cmcm*, and (**d**) without correction for preferred orientation as *Cmc*2_1. V_A/V_B ratio was calculated considering, $V_A = (V_{UC}/Z)-V_B$.

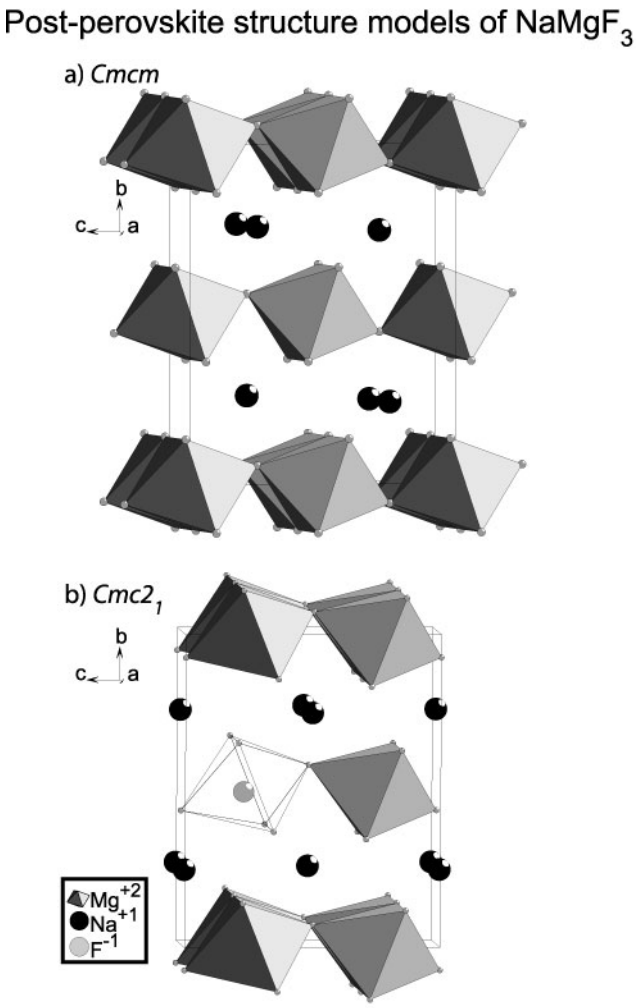

[Fig. 6.1] The orthorhombic post-perovskite structure of $NaMgF_3$ as (**a**) *Cmcm* and (**b**) *Cmc*2_1.

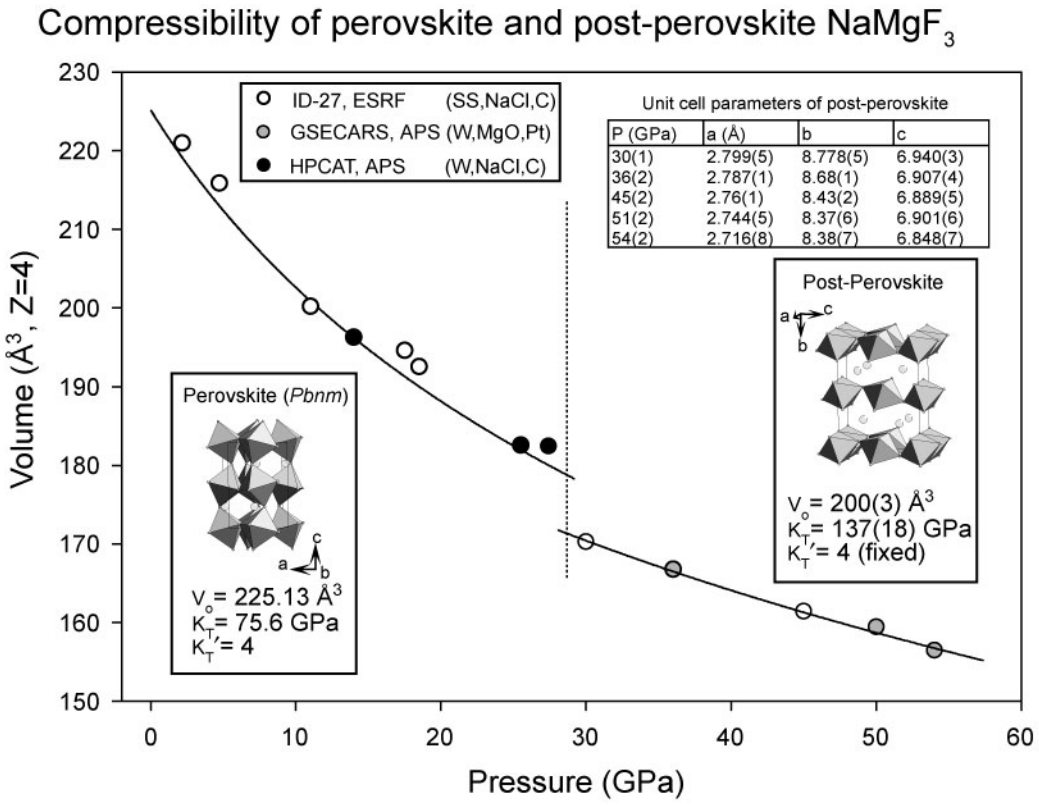

[Fig. 6.2] The 2nd order Birch-Murnaghan equations of state (EoS) of $NaMgF_3$ are compiled from three high pressure runs. Each high pressure run contained different materials to preclude reaction with the sample (SS, stainless steel; C, graphite).

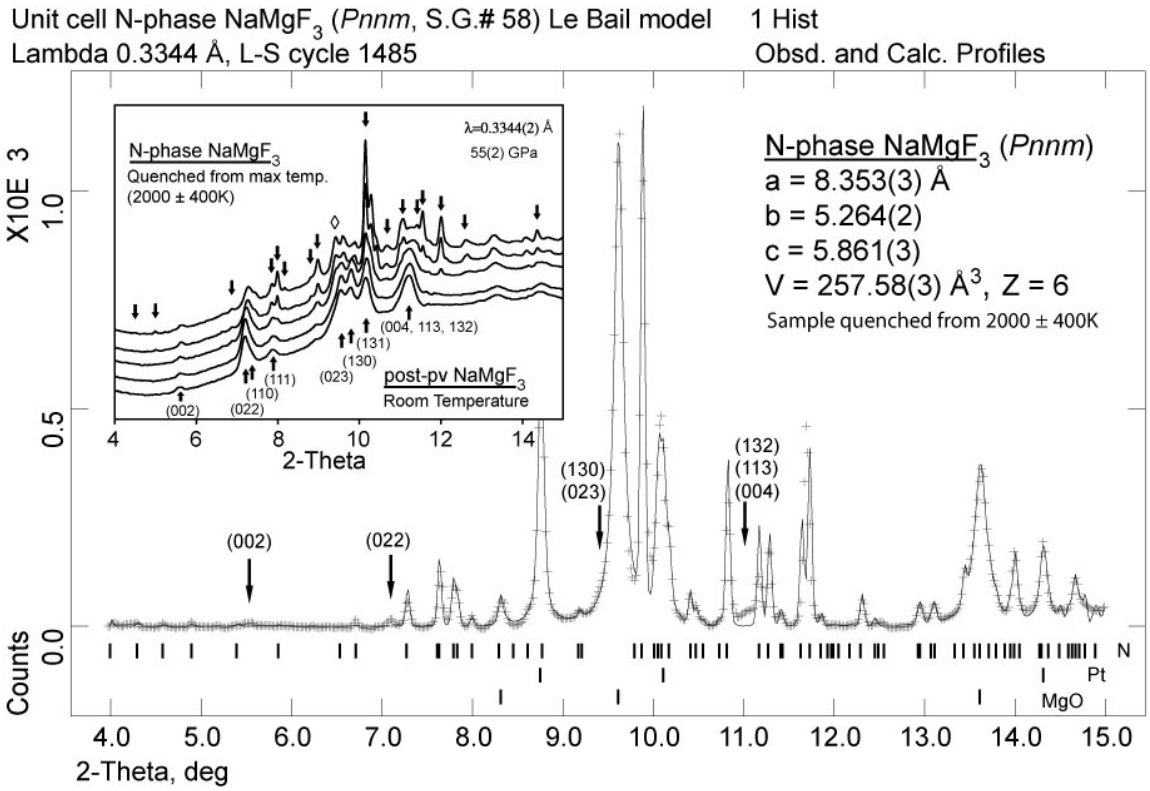

[Fig. 6.3] X-ray diffraction pattern of N-phase $NaMgF_3$ after laser heating at 37(1) GPa with Pt and MgO internal standards. The N-phase unit cell (Pnnm), Pt, and MgO are fit with a Le Bail model. Arrows pointing down indicate residual $CaIrO_3$-type $NaMgF_3$. Inset: X-ray diffraction patterns of $NaMgF_3$ at 55(2) GPa before and after laser heating. This data series (inset) was obtained by stepping the x-ray beam position away from the position of the heating laser, allowing the collection of x-ray diffraction patterns from sample heated to temperatures consecutively less than the maximum to room temperature. Arrows pointing up show indexed peak positions of the post-perovskite structure, while arrows pointing down highlight peaks of N-phase $NaMgF_3$. Sample also contains NaCl (◊) and graphite (no diffraction).

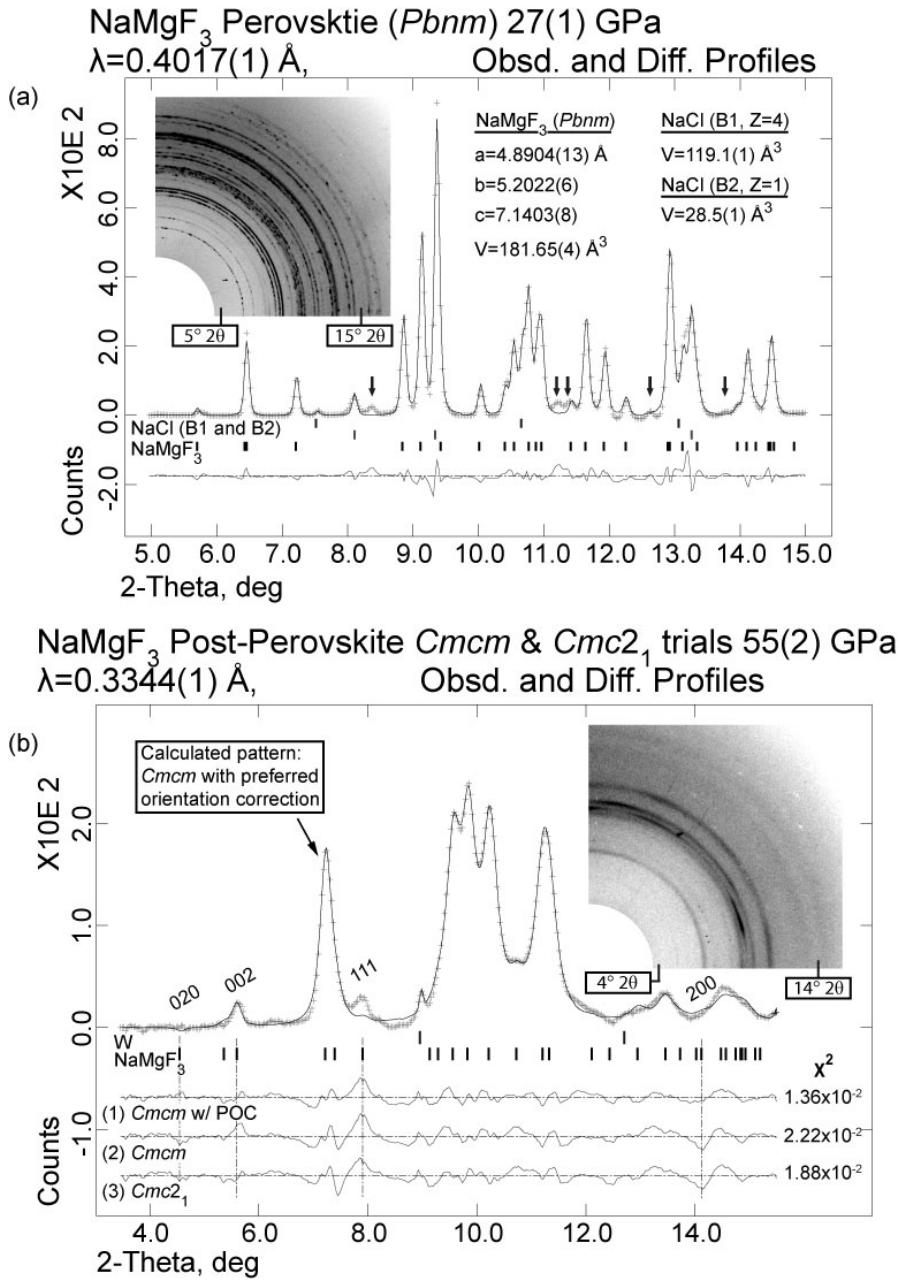

[Fig. 6.4] In-situ high pressure Rietveld structure modeling of (a) $NaMgF_3$ perovskite and (b) post-perovskite $NaMgF_3$. Portions of the raw two-dimensional data are inset in each plot to show sample texture. Difference curves of Rietveld structure models are plotted below the calculated (solid) and observed (dotted) background-subtracted X-ray diffraction patterns; (b) in descending order: (1) *Cmcm* with 4th order spherical harmonic preferred orientation correction (POC), (2) *Cmcm* without POC, (3) *Cmc*2_1 without POC. Weak reflections marked with an arrow are indexed as $NaMgF_3$ post-perovskite.

Chapter VII

Compression, thermal expansion, structure and bonding in $CaIrO_3$ at high pressure and temperature; the structure model of $MgSiO_3$ post-perovskite investigated with monochromatic X-ray and time-of-flight neutron powder diffraction.

MARTIN, C.D., CHAPMAN, K.W., CHUPAS, P.J., PRAKAPENKA, V.B., LEE, P.L., SHASTRI, S.D., AND PARISE, J.B. (2007, IN PRESS) COMPRESSION, THERMAL EXPANSION, STRUCTURE, AND INSTABILITY OF $CaIrO_3$, THE STRUCTURE MODEL OF $MgSiO_3$ POST-PEROVSKITE. AMERICAN MINERALOGIST.

MARTIN, C.D., SMITH, R.I., MARSHALL, W.G., AND PARISE, J.B. (2007, IN PRESS) HIGH PRESSURE STRUCTURE AND BONDING IN $CaIrO_3$; THE STRUCTURE MODEL OF $MgSiO_3$ POST-PEROVSKITE INVESTIGATED WITH TIME-OF-FLIGHT NEUTRON POWDER DIFFRACTION. AMERICAN MINERALOGIST.

7.1. Abstract

In this chapter we perform an analysis of monochromatic X-ray powder diffraction data from $CaIrO_3$, the structure model for post-perovskite $MgSiO_3$ and find the c-axis has a small compressibility and a large thermal expansion when compared to the other principle axes. Using Rietveld structure refinement we report changes in $CaIrO_3$ as a function of temperature and structure evolution in IrO_6 octahedra. We observe instability and dissociation of $CaIrO_3$ at high temperature. Rietveld structure refinement of $CaIrO_3$ (*Cmcm*) from neutron powder diffraction reveals structure changes occurring at high pressure and low temperature, separately. Evidence supporting deviation from space group *Cmcm* to $Cmc2_1$ is uncertain and discussed within. As $CaIrO_3$ (*Cmcm*) unit cell volume changes, refinements indicate deformation of cation-centered coordination polyhedra, rather than tilting. Structure models demonstrate Ca^{2+}-centered polyhedra are an order of magnitude more compressible than Ir^{4+}-centered octahedra. Bond valence

sums show significant chemical strain (over-bonding) of calcium and oxygen at ambient conditions. When pressure is increased, ions in $CaIrO_3$ accommodate chemical strain according to ion type and reduce chemical strain in proportion to strain value when temperature is increased. Implications for structure change in $MgSiO_3$ post-perovskite are discussed and a method for predicting Clapeyron slope between perovskite and post-perovskite phases is proposed.

7.2. Introduction

The composition and velocity structure of Earth's D" layer at the bottom of the lower mantle has recently been rationalized in terms of phase transition in $MgSiO_3$ perovskite (space group, *Pbnm*) to a post-perovskite structure believed to be isostructural with $CaIrO_3$ (*Cmcm*) (Murakami et al., 2004; Oganov and Ono, 2004). While this phase change may explain the D" seismic discontinuity, preferred orientation of $MgSiO_3$ post-perovskite (Merkel et al., 2006; Oganov et al., 2005) within the layer may explain many anomalous seismic observations which have puzzled the mineral physics and seismology communities for decades (Garnero, 2004; Lay et al., 1998). Until the physical properties of $MgSiO_3$ post-perovskite are known, those experimentally determined from analog materials are of great interest to Earth Science.

The $CaIrO_3$ structure (*Cmcm*) is very rare and $CaIrO_3$ itself is the only oxide known to crystallize with this structure at room pressure. The structure of $CaIrO_3$ (Fig 7.1), stoichiometry ABX_3, consists of single layers of IrO_6 octahedra normal to the b-axis. The octahedra share edges along the a-axis and corners along the c-axis, while calcium occupies sites between these layers (Rodi and Babel, 1965). Because of significant structural anisotropy, materials adopting this structure are expected to have very different physical properties from those crystallizing with structures related to perovskite. Recent experiments have focused primarily on the effects of element substitution in $MgSiO_3$ post-perovskite (Mao et al., 2006; Sinmyo et al., 2006) as well as changes in unit cell at high pressure using analog materials (Hirose et al., 2005; Kubo et al., 2006; Martin et al., 2006a; Tateno et al., 2006). However, few studies have investigated the effects of temperature on the post-perovskite ($CaIrO_3$) structure (Guignot et al., 2007; Hirose and Fujita, 2005; Tsuchiya et al., 2005).

Considering the large temperature gradient expected at the bottom of the lower mantle, knowledge of how structure and properties co-vary with temperature in materials with the post-perovskite structure is a necessity for geophysical modeling. In this study we report X-ray powder diffraction and Rietveld structure refinement that allow us to examine the compression, thermal expansion, stability and crystal structure of $CaIrO_3$ at high temperature. In order to extract differences between structure models under changing pressure conditions, we utilize Rietveld structure refinement with neutron powder diffraction since this data is sensitive to oxygen as well as most cations in a material. Understanding structure changes in $CaIrO_3$ as a proxy for post-perovskite structure, application of the bond valence concept provides a chemical foundation from which structure models, changes, and physical properties of materials may be understood in terms of crystal-chemistry. From a synthesis of the data presented in this study, we identify mechanisms controlling structure changes in $CaIrO_3$ which may prove useful to an understanding of the elastic, rheological, and chemical properties of post-perovskite $MgSiO_3$.

7.3. Experimental Methods

7.3.1. X-ray diffraction

Using a multi-anvil large-volume press (Gwanmesia et al., 1993), $CaIrO_3$ was synthesized from a stoichiometric mixture of [Ca_2IrO_4 + IrO_2] at high pressure and temperature. The mixture was loaded into a gold capsule and pressure was increased to 6.2(2) GPa before temperature was increased to 1223(50) K. Conditions were held for 12 hour prior to reducing temperature over 30 minutes and pressure over 6 hours. Several synthesis trials reacting a [CaO + IrO_2] mix at constant temperatures which ranged from 950 to 550 ˚C at room pressure from trial to trial, yield metastable synthesis of $CaIrO_3$ (Hirose and Fujita, 2005; McDaniel and Schneider, 1972) and further heating produces a pure [Ca_2IrO_4 + IrO_2] mix over time.

Monochromatic X-ray powder diffraction data were collected at high pressure using the diamond anvil cell at 1-ID-C (Martin et al., 2005; Shastri et al., 2002) and 13-ID-D (Shen et al., 2005) at the Advanced Photon Source (APS) at Argonne National Laboratory. Data were collected at 1-ID-C using monochromatic X-radiation with

wavelength 0.1240(2) Å to pressures of 7.6(1) GPa with a 4:1 methanol:ethanol pressure transmitting medium. Pressure was determined by ruby fluorescence, and data were collected on a MAR345 imaging plate detector to 10.5˚ 2θ (0.67 $Å^{-1}$). At 13-ID-D monochromatic X-rays had wavelength λ=0.3344(2) Å and $CaIrO_3$ was loaded with NaCl as an inert sample insulator and internal pressure standard (Decker, 1971; Sata et al., 2002). The dark $CaIrO_3$ sample itself absorbed the double-sided heating laser (Shen et al., 2001) and diffraction data were collected on a MAR CCD (2048x2048 pixels) to 17.0˚ 2θ (1.13 $Å^{-1}$), using laser annealing to quasi-hydrostatic pressures of 29(1) GPa.

X-ray diffraction suitable for Rietveld structure refinement were collected at room pressure and high temperature (Chupas et al., 2001) with $CaIrO_3$ in a 0.8 mm quartz capillary at 11-ID-B at the APS, where radiation had a wavelength of 0.1370(2) Å. Exposing for 180 seconds, a total of 74 temperature points were collected to 16.5˚ 2θ (0.48 $Å^{-1}$) on an amorphous silicon flat panel detector from General Electric Healthcare (Chupas et al.). Temperature increased between 332 and 1109 K over 383 minutes. For each temperature, Rietveld refinement converged with a χ^2 value (Larson and Von Dreele, 2000) less than 1.5.

Two-dimensional diffraction data collected during all three experiments were integrated and reduced to plots of intensity vs. 2θ using program FIT2D (Hammersley et al., 1996). Unit cell fitting and $CaIrO_3$ structure refinement was performed using program GSAS (Larson and Von Dreele, 2000) and user interface EXPGUI (Toby, 2001). After finding an appropriate mixture of Gaussian and Lorentzian terms to describe peak-shape in the lowest temperature pattern, during Rietveld refinement peak-shape was determined letting the Gaussian width refine at higher temperature. The background was fit with a 7 term Chebyschev polynomial and a common isotropic displacement parameter was used for both oxygen positions in the structure. A linear absorption coefficient, $\mu = 5.25\ cm^{-1}$, determined from the composition, atomic absorption cross sections at this energy, and likely packing density of the powder in the capillary was applied, but was found to have a negligible effect on structure parameters.

Equation of state parameters describing compressibility were obtained by fitting data to a 2nd order Birch-Murnaghan equation of state, while those describing thermal

expansion were obtained from fitting data according to integration of the thermodynamic definition using a reference temperature (T_o) of 300 K:

$$V(T) = V_O(T_O)\exp\int_{T_O}^{T}\alpha(T)dT \text{ , and } \alpha(T) = \alpha_0 + \alpha_1 T \quad (7.1)$$

7.3.2. Neutron diffraction

Using a piston-cylinder high pressure apparatus, $CaIrO_3$ was synthesized from a stoichiometric mixture of [Ca_2IrO_4 + IrO_2] at 2.0(1) GPa and 1150(75) K in a silver capsule surrounded by a ½ inch talc assembly. These conditions were sustained for 48 hours prior to quenching to room temperature. The resultant sample was found to contain ~96(1) wt.% $CaIrO_3$ with quantities of unreacted Ca_2IrO_4, IrO_2. The initial [Ca_2IrO_4 + IrO_2] mixture was prepared by firing an equal-molar quantity of $CaCO_3$ and IrO_2 (Alfa Aesar; Lot # E27P20) in a furnace at 850 ˚C for 48 hours at room pressure. Because platinum and iridium alloy, platinum was not used during sample preparation. This procedure is slightly different than that used for the X-ray measurements due to experimental constraints on the piston-cylinder press, which is needed for a large product volume.

Time-of-flight neutron powder diffraction data were collected on the POLARIS diffractometer at the ISIS pulsed spallation source Rutherford Appleton Laboratory, UK (Hull et al., 1992). For ambient pressure measurements, cylindrical pellets (~4 mm diameter x 2 mm high) were stacked in a thin-walled vanadium sample can and diffraction data were collected at room temperature, ~293 K, for 780 μAh proton beam current (~5 hours). For measurements below room temperature the sample, in the same sample can, was loaded into a helium flow cryostat and diffraction patterns collected at 2 K, 100 K and 250 K for between 1170 and 1250 μAh proton beam current (~7 hours). Data from the highest resolution, backscattering, detector bank $<2\theta>=145°$ were used in Rietveld profile refinement. Time-of-flight neutron powder diffraction patterns were collected from $CaIrO_3$ at high pressure using a type V2 Paris-Edinburgh press equipped with single toroid profile WC/Ni binder-cored anvils in conjunction with the POLARIS $2\theta=90^o$ detectors. The sample was confined within a null scattering TiZr capsule gasket (Marshall and Francis, 2002) with the powder moistened with deuterated

methanol:ethanol (4:1) pressure transmitting medium. Diffraction data were collected from the sample at hydraulic ram pressures of 70, 250, 500, 700, 850, and 800 bar, in sequential order. Judging by the bar/GPa trend and data trends with pressure, quasi-hydrostatic sample conditions were reached at 850 oil bars and data collected subsequently at 800 oil bar is considered representative of hydrostatic pressure conditions on the sample. Sample pressure was calculated using the known equation of state of $CaIrO_3$, with bulk modulus 180.2(28) GPa (Martin et al., 2007, In press).

Rietveld structure refinements were performed using the GSAS program suite (Larson and Von Dreele, 2000) and the user interface EXPGUI (Toby, 2001). While data were corrected for absorption according to the scattering cross-sections and relative abundances of each element, an additional correction was applied to data collected at high pressure according to neutron attenuation of the WC anvils of the Paris-Edinburgh press. Because of the significant neutron absorption of iridium and some uncertainly of the dependence on the instrumental absorption correction, isotropic displacement parameters calculated from high pressure data are overestimated.

Estimated uncertainties on refined parameters are included within our figures as grey areas and these are obtained from error propagation (Goodman, 1960) using the relation:

for function $Z(y,x,...)$,

$$\sigma_Z = \sqrt{\left(\partial Z/\partial y * \sigma_y\right)^2 + \left(\partial Z/\partial x * \sigma_x\right)^2 + \left(\partial Z/\partial ... * \sigma...\right)^2} \qquad (7.2)$$

where standard deviation (σ) is obtained directly from GSAS and/or through fitting.

7.4. Results

7.4.1. X-ray diffraction

Volume and unit cell lengths of $CaIrO_3$ are plotted as a function of pressure in Figure 7.2 and listed in Table 7.1. Pressure trends, observed to the maximum pressure values, are well defined by data collected below 8 GPa in the alcohol mixture. Consistent with previous studies of $CaIrO_3$-structured $MgGeO_3$ post-perovskite (Hirose et al., 2005; Kubo et al., 2006), the direction of greatest compressibility is the b-axis, followed by the a- and c-axis which are each significantly less compressible. While data indicate the

$CaIrO_3$ structure is stable beyond 50 GPa at room temperature, we find laser heating (1500±300 K) dissociates $CaIrO_3$ to products including iridium metal. Dissociation is visually marked by unknown translucent, presumably iridium depleted, crystals in the position of the laser after heating and breakdown appears with a positive slope in pressure-temperature space. It is difficult to determine whether sample dissociation in the diamond anvil cell under laser radiation is not a direct result of $CaIrO_3$ chemistry (McDaniel and Schneider, 1972). However, reduction of pure IrO_2 is not observed under these conditions (Ono et al., 2005). Thus, these unit cell data shown in Figure 7.2 have been fitted from raw data which include X-ray diffraction features from dissociation products.

A plot of the room pressure Rietveld refinement at maximum temperature is shown in Figure 7.3. Volume and unit cell lengths of $CaIrO_3$ are plotted as a function of temperature in Figure 7.4 and listed in Table 7.1. The data show a trend with increasing temperature divergent from that observed upon compression. While the b-axis (0 1 0) shows the most sensitivity to temperature, the c-axis (0 0 1) is significantly more sensitive to temperature than is the a-axis (1 0 0) and thermal expansion of the c-axis is comparable in magnitude to the b-axis. In the later stage of the high temperature experiment (T > ~650 K) very small peaks become visible, indicating metastability of $CaIrO_3$ and breakdown to [Ca_2IrO_4 + IrO_2]. This incipient dissociation is consistent with our inability to synthesize phase-pure $CaIrO_3$ at room pressure.

Through Rietveld refinement, we are able to determine the structural changes in $CaIrO_3$ as a function of temperature (Fig. 7.5). While the small X-ray scattering cross-section of oxygen relative to iridium makes precise determination (Chapman et al., 2006) of the oxygen position and displacement parameters (Fig. 7.6) difficult, fitting to the 74 temperatures included in our study provide accurate trends across this temperature range.

Using this structure data we may understand the effect of temperature on more complex and interesting structural features, which serve as indicators for phase transition. The first of these is the volume of the IrO_6 octahedron (B-site) relative to the polyhedron occupied by calcium (A-site). This value, known as the V_A/V_B ratio, is an independent structural variable describing rotation in perovskite BX_6 octahedra and an order parameter for perovskite/perovskite phase transitions (Thomas, 1998). Recently, V_A/V_B

was recognized as an indicator which may predict the pressure of a perovskite/post-perovskite phase transition (Martin et al., 2006b). To summarize, in perovskite structures $5 \geq V_A/V_B > \sim 4$, whereas in post-perovskite structures $V_A/V_B \leq \sim 4$. For reference, we list V_A/V_B in published post-perovskite structures, $MgSiO_3$, 4.01 (Murakami et al., 2004), 3.92 (Oganov and Ono, 2004); $NaMgF_3$, 3.94(6) (Martin et al., 2006b); $MgGeO_3$, 4.28 (Hirose et al., 2005), 3.59 (Kubo et al., 2006); $CaIrO_3$, 4.19 (Rodi and Babel, 1965); Fe_2O_3, 3.89 (Ono and Ohishi, 2005). Post-perovskite transitions occur in perovskites where $dV_A/dP > dV_B/dP$, thus pressure is required to stabilize the post-perovskite structure. Figure 7.7 shows the change in parameters V_A and V_B with changing temperature. The IrO_6 octahedra slightly decrease volume at high temperature, while the calcium polyhedron clearly increases with the V_A/V_B ratio.

By observing strain of the IrO_6 octahedra unit we understand how the octahedra volume may decrease with increasing temperature. Similar to the V_A/V_B ratio, the strain of BX_6 octahedra may be used to understand structure changes accompanying perovskite/perovskite phase transitions (Zhao et al., 1993). To measure strain we calculate the bias of the IrO_6 unit from a perfect octahedra (Fig. 7.8), where all Ir-O distances are equal and all O-Ir-O angles are 90˚. The data show that while the Ir-O bond lengths converge toward the mean Ir-O value at high temperature, the O-Ir-O bond angles diverge from 90˚, which decreases the volume of the octahedra.

7.4.2. Neutron diffraction

The refined unit cell parameters, atomic positions, and displacement parameters of $CaIrO_3$ at 1 bar pressure in space group *Cmcm* are listed in Table 7.2a at 2.0(1), 100.0(1), 250.0(1), and 293(2) K. Within error, relative length changes of each unit cell axis in this temperature range are consistent with those occurring at higher temperatures (Martin et al., 2007a) and while small, thermal expansion at low temperature is dominated by expansion in the [0 1 0] direction.

Bond valence (Brown and Altermatt, 1985; Brown and Shannon, 1973) provides a basis from which we may understand Rietveld structure models of $CaIrO_3$ at ambient conditions in terms of ideal ionic bonding. In Pauling's ionic bonding model, all bonds

between ions imply a charge-sum which may be compared to the ionic charge (formal valence) of the ion. This is expressed mathematically as:

$$V_i = \sum_j S_{ij} \tag{7.3}$$

where V_i is the formal valence of ion 'i' and S_{ij} is the 'bond strength', which is defined in terms of bond length (Brown and Altermatt, 1985; Brown and Shannon, 1973) as:

$$S_{ij} = \exp\left(\frac{R_0 - R_{ij}}{B}\right) \tag{7.4}$$

Thus, the bond strength is proportional to bond length and, for every bond between ions (R_{ij}), a standard distance (R_0) has been determined from systematic studies of crystal structures. The R_0 value for each bond must be known and the Ca^{2+}-O value, 1.967(2) Å (Brown and Altermatt, 1985), is better constrained than Ir^{4+}-O, 1.87(1) Å (Wills and Brown, 1999). The term B rarely deviates from 0.37 Å and we assume uncertainty ±0.01 Å.

Bond valence sums of each ion in room temperature $CaIrO_3$ structure are listed in Table 7.2b and while V_{Ir} and $V_{O[8f]}$ are in good accord with 4^+ and 2^-, both V_{Ca} and $V_{O[4c]}$ deviate significantly from 2^+ and 2^-, respectively. Deviations from formal ion valence are considered using the simple difference:

$$d_i = \sum_j S'_{ij} - |V_i| \tag{7.5}$$

where S'_{ij} is the experimentally determined bond strength. It is useful to normalize deviations as a percentage (P_i) in terms of the formal ion valence:

$$P_i = \frac{d_i}{|V_i|} * 100\% \tag{7.6}$$

Difference between the experimental valence sum and the formal ion valence is known as 'chemical strain' (Brown, 1992; Salinas-sanchez et al., 1992) and positive percentages imply over-bonding. At room temperature P_{Ir}, P_{Ca}, $P_{O[4c]}$, and $P_{O[8f]}$ in $CaIrO_3$ are approximately 1%, 13%, 13%, and 1%, respectively. Previous work (Brown, 1992; Salinas-sanchez et al., 1992) has developed a general measure to classify overall chemical strain in crystalline materials:

$$GII = \sqrt{\langle d_i^2 \rangle} \tag{7.7}$$

The root-mean-square of valence difference values for each ion site in a particular structure is referred to as the 'residual bond strain' or 'global instability index'. Our data indicate $CaIrO_3$ has a *GII* value of 0.16(2) valence units (dimensionless) at room temperature. Previous work finds *GII* > 0.1 in structures with significant residual bond strain and *GII* > 0.2 when the structure is unstable or has been assigned an incorrect space group (Brown, 1992; Salinas-sanchez et al., 1992; Wills and Brown, 1999). The large *GII* value for $CaIrO_3$ at ambient conditions might be considered consistent with observed metastability of the structure.

The *ab initio* structure solution of $TaAgS_3$ ($Cmc2_1$, S.G.# 36) (Wada and Onoda, 1990) was refuted (Marsh, 1993) and the most recently reported $TaAgS_3$ structure (*Cmcm*, S.G.# 63, $CaIrO_3$ structure-type) has large anisotropic thermal parameters for each ion (Kim et al., 1997). In view of the large residual bond strain found in space group *Cmcm* and previous work examining structure model trials of $NaMgF_3$ post-perovskite (Martin et al., 2006b), we have chosen to investigate structure model trials of $CaIrO_3$ in space group $Cmc2_1$.

The $CaIrO_3$ structure models in space group $Cmc2_1$ derived from the neutron diffraction data at 2 K, 293(2) K and 9.72(5) GPa are listed in (Table 7.3). The $Cmc2_1$ structural models are very similar to those in space group *Cmcm*, yet all ions show consistent displacement from the (0 0 1) mirror plane. While fluctuations in atomic position above and below this mirror plane between trial structures would best characterize statistical noise, deviations from *Cmcm* are relatively small. In addition, goodness of fit and residual bond strain of structure models in space group $Cmc2_1$ is unchanged relative to refinements in space group *Cmcm*. Deviations from the *Cmcm* structure model, if they exist, are within experimental error, and our analysis of the data taken at high pressure is limited to the *Cmcm* structure model.

Rietveld structure refinement (Fig. 7.9) reveals structure changes in $CaIrO_3$ at high pressure (Table 7.4, Fig. 7.10). Using these data together with data collected at high temperature (Martin et al., 2007a), we may investigate structure mechanisms that drive axial compression and thermal expansion of the unit cell. Mechanisms changing perovskite-type structures are commonly defined in terms of octahedra tilt and bond

length (Glazer, 1972; Glazer, 1975; Ross and Hazen, 1989; Zhao et al., 2004; Zhao et al., 1993). To describe mechanisms operating upon compression and expansion of the $CaIrO_3$ structure (ABX_3) we highlight relative changes in specific Ir-O bond lengths as well as volume changes of iridium- (V_B) and calcium-centered polyhedra (V_A) expressed as a ratio. Because it is useful to compare V_A/V_B between perovskite and post-perovskite structures (ABX_3), it is important to note the V_A/V_B ratio does not depend on the formal coordination number of the A-site (Thomas, 1998) and has the same definition in both perovskite and post-perovskite structure-types: all unit cell volume not occupied by the B-site octahedra is volume of the A-site.

The volume change of the Ca^{2+} site dominates compression and thermal expansion of the unit cell volume, thus, V_A/V_B increases with temperature (Martin et al., 2007a) and decreases with pressure (Fig. 7.11). Because of the A- and B-site configuration within the $CaIrO_3$ unit cell, the large compressibility and thermal expansion along the b-axis is understood considering pressure and temperature change the softer Ca-O distance along [0 1 0] between harder Ir-O layers of octahedra (Megaw, 1971). In addition, this understanding implies that the mechanism driving the small compressibility and large thermal expansion of the ***c***-axis relative to the ***a***-axis resides within the IrO_6 octahedra.

Octahedra in $CaIrO_3$-type structures are much more deformed (Martin et al., 2006b; Rodi and Babel, 1965) than octahedra found within perovskite-type (Zhao et al., 1993) structures. It is useful to measure deformation in contrast to perfect octahedra, having all Ir-O distances equal and all O-Ir-O angles at 90˚. The deformation in IrO_6 octahedra is plotted with increasing temperature (Martin et al., 2007a) and pressure (Fig. 7.12). We designate labels for bonds in the $CaIrO_3$ structure which correspond to the Wyckoff atom positions in the structure. The bond geometry of the Ca-site is such that $Ca\text{-}O_{[8f]}{}^{b}$ forms the bi-caps to the trigonal prism, which has $Ca\text{-}O_{[8f]}{}^{a}$ bonds to its base and $Ca\text{-}O_{[4c]}$ bonds to the prism apex. In order to understand how Ir-O bond lengths drive changes in the unit cell, it is important to note that $Ir\text{-}O_{[4c]}$ has unit cell vector components in only *y* and *z* (*b* and *c* axes) and $Ir\text{-}O_{[8f]}$ has significant unit cell vector components in only *x* and *y* (*a* and *b* axes) (Fig. 7.1).

Ir-O and Ca-O bond lengths are shown as a function of pressure in Figure 7.13a. With increasing pressure all bond lengths decrease and less change is observed in Ir-O bonds than in Ca-O bonds. In contrast, with increasing temperature, bond lengths increase as well as decrease (Fig. 7.13b) and the mechanism driving low compressibility and high thermal expansion of the ***c***-axis [0 0 1] relative to the ***a***-axis [1 0 0] can be understood in these terms: Because Ir-$O_{[4c]}$ shows strong thermal expansion (components in only *b* and *c*), while Ir-$O_{[8f]}$ contracts (significant components in only *a* and *b*), the Ir-O vector components sum to increase [0 0 1] relative to [1 0 0] and $\alpha_c > \alpha_a$. At high pressure however, rather uniform bond compression decreases [1 0 0] relative to [0 0 1] and $\beta_a > \beta_c$. The relative axial sensitivities are not preserved since Ir-$O_{[8f]}$ bonds would need to expand (or resist compression) at high pressure for $\beta_c > \beta_a$.

In diffraction studies, the bond length is computed from the distance between maxima in the atomic distribution at any two given sites in the crystal. Corrections can be applied to overcome possible artifacts driven by thermal motion, allowing approximation of real bond lengths within a crystal at high temperature (Busing and Levy, 1964). In this correction, a correlation between the vibrating atoms must be assumed and we are reluctant to do so here when bond lengths are uniquely defined by the pair distribution function (Chapman et al., 2005; Chupas et al., 2004; Martin et al., 2007b; Qiu et al., 2005) and that describing $CaIrO_3$ at high temperature has yet to be examined. However, after correcting the observed bond lengths for thermal motion following Busing and Levy (1964), we can calculate the upper (R_U) and lower (R_L) bounds of this approximation,

$$R_U = R_{ij} + \frac{\left(\sqrt{U_i} + \sqrt{U_j}\right)^2}{2R_{ij}} \tag{7.8}$$

$$R_L = R_{ij} + \frac{\left(\sqrt{U_i} - \sqrt{U_j}\right)^2}{2R_{ij}} \tag{7.9}$$

where R_{ij} is the observed length between atoms *i* and *j*, while U_i and U_j are the isotropic mean-square displacements (units $Å^2$) of atoms *i* and *j* from the crystallographic site. Considering the upper limit for the bond length approximation and the maximum isotropic mean-square displacements of each atom within uncertanty (Martin et al., 2007a),

$$U_{Ca} = 0.479(29)\cdot 10^{-2} + T\cdot 2.02(19)\cdot 10^{-5} - T^2\cdot 8.4(26)\cdot 10^{-9}$$
$$U_{Ir} = 0.112(5)\cdot 10^{-2} + T\cdot 7.99(35)\cdot 10^{-6} - T^2\cdot 4.6(47)\cdot 10^{-10} \quad (7.10)$$
$$U_{O} = 0.318(52)\cdot 10^{-2} + T\cdot 1.50(34)\cdot 10^{-5} - T^2\cdot 6.0(453)\cdot 10^{-10}$$

the corrected Ir-$O_{[8f]}$ and Ca-$O_{[4c]}$ bond lengths change at a rate of $-5.15\cdot10^{-6}$ and $-1.45\cdot10^{-5}$ (Å/K), respectively. Therefore, it appears that thermal motion cannot account for all of the observed reduction.

7.5. Discussion

Trends observed from systematic pressure-temperature studies of materials in the perovskite family (Finger and Hazen, 2000; Liu et al., 2005a; Ross and Hazen, 1989; Vanpeteghem et al., 2006; Zhao et al., 1993) show the axis with the least thermal expansion is generally the least compressible. This contrasts with our finding for $CaIrO_3$, where the c-axis (0 0 1) has a small compressibility (β or K^{-1}; see Table 7.1 caption) and a large thermal expansion. This characteristic of $CaIrO_3$ suggests the compressibility of the c-axis will increase with temperature at a faster rate than the compressibility of the a-axis ($d\beta_c/dT > d\beta_a/dT$), which implies there will be a large region in pT space at high temperature where $\beta_c \approx \beta_a$. The elasticity of a colder $MgSiO_3$ post-perovskite phase at the top of the D" may be very different than that found at the bottom of the layer where temperatures are expected to be much higher and in this respect, values and temperature derivatives of elastic moduli (Carpenter et al., 2006; Jackson et al., 2004; Liu et al., 2005b) of $MgSiO_3$ post-perovskite must be understood in order for studies of lattice preferred orientation (Merkel et al., 2006; Oganov et al., 2005) to place higher-order constraints on mineral models which address D" tomography and seismic anisotropy (Garnero et al., 2004; Lay et al., 1998; McNamara et al., 2002).

The structure of $CaIrO_3$ post-perovskite shows instability at high temperature, confirming previous observations (McDaniel and Schneider, 1972; Rodi and Babel, 1965). Using Rietveld refinement we observe structural changes that provide insight into the driving force behind phase transition in $CaIrO_3$ to what has been reported to be a metastable perovskite phase above 1173 K (Hirose and Fujita, 2005; McDaniel and Schneider, 1972). The V_A/V_B ratio of $CaIrO_3$ post-perovskite increases with temperature from a value of about 4.19 (Rodi and Babel, 1965) at room temperature to ~4.5 at 1100 K

and increasing V_A/V_B suggests instability of post-perovskite relative to a perovskite structure (Martin et al., 2006b). Because the volume of the iridium octahedra remains relatively constant with temperature, the structure evolution of $CaIrO_3$ is dominated by an increasing distance between IrO_6 layers. However, while the b-axis is indeed the most sensitive to temperature, this thermal expansion has a clear negative second-order dependence, indicating a slowing of expansion in this direction—a typical feature of many structures before high temperature phase transition. Considering this data we believe a transition to perovskite will follow at higher temperature.

While the $CaIrO_3$ phase transition to perovskite structure is controlled by V_A/V_B, the metastability behind dissociation of $CaIrO_3$ to [Ca_2IrO_4 + IrO_2] at room pressure could represent an instability which may be expected for all post-perovskite structures as temperature is increased. Recent studies suggest dissociation (Umemoto et al., 2006) in $MgSiO_3$ post-perovskite at high pressure and/or further phase transitions (Martin et al., 2006a) after heating post-perovskite. Considering how rare it is for a material to adopt the $CaIrO_3$ structure, it is reasonable to believe there may be an instability rooted in this structure which generally makes it energetically less favorable than another phase or a proportionate mixture of dissociation products at high temperature. This possibility should be explored in $MgSiO_3$ post-perovskite considering reported experimental temperatures under which this phase is experimentally synthesized (2000±500 K) in the diamond anvil cell do not match the much higher temperatures which may exist at the core-mantle boundary (Stixrude and Karki, 2005). If $MgSiO_3$ post-perovskite were to breakdown or undergo an additional phase transition below the D" discontinuity, reconciling recent observations of a doubling of the D" discontinuity (Flores and Lay, 2005; Hernlund et al., 2005) and ultra low velocity zones (Lay et al., 1998; Wang and Wen, 2004) within a mineral physics context may be challenged further.

The $CaIrO_3$ structure-type is rarely observed in ionic crystals and pressure is required to prevent amorphization and back-transformation of post-perovskite structured materials (Hirose et al., 2005; Kubo et al., 2006; Liu et al., 2005a; Martin et al., 2006a; Murakami et al., 2004; Oganov and Ono, 2004; Ono and Ohishi, 2005; Santillan et al., 2006; Tateno et al., 2006). This observation is understood considering the shared octahedral edges along [1 0 0] in $CaIrO_3$-type structures and is consistent with pressure

increasing overlap of the electron orbitals involved in bonding, leading to more covalent bonding in crystals. Pauling's third rule (Pauling, 1929) states, due to cation-cation repulsion in ionic crystals, edge-sharing polyhedra are less stable than corner-sharing polyhedra. Electronic structure modeling of ilmenite $Na^{+1}Sb^{+5}O_3$ finds covalent bonding (Sb-O, Sb *n*s, O 2p), stabilizes edge-sharing SbO_6 octahedra relative to perovskite structure, where bonding within corner-sharing octahedra have a strong ionic character (Mizoguchi et al., 2004). Considering that covalent bonding is expected in all the $CaIrO_3$-type structures which are stable at room pressure [$UFeS_3$, $TlPbI_3$, $UScS_3$, $CaInBr_3$, $TaAgS_3$, (Berndt, 1997)], perhaps we may expect bonding in post-perovskite $MgSiO_3$ to have a more covalent character and melting of a post-perovskite structure at higher temperatures than a perovskite-structured phase.

Results presented in this report show that pressure and temperature drive separate structural changes in $CaIrO_3$, thus the relative axial compressibility ($\beta_b > \beta_a > \beta_c$) and thermal expansion ($\alpha_b > \alpha_c > \alpha_a$) of the unit cell will change under simultaneous high pressure and temperature. Because α_c is large at room pressure, we might expect $\beta_c > \beta_a$ at sufficiently high temperatures where thermal effects may soften [0 0 1] at high pressure. If this is true, the elastic constants of $CaIrO_3$ at room temperature or below could be significantly different from those at high temperature at any given pressure.

The $CaIrO_3$ structure changes through deformation of coordination units, rather than tilting of nearly rigid octahedra, which takes place in perovskite structures. Increasing the tilt of perovskite octahedra (e.g., (Angel et al., 2005; Liu et al., 2005a) drives the structural phase transition to the post-perovskite structure ($CaIrO_3$-type) by decreasing V_A/V_B. Considering V_A/V_B is greater than 4 in perovskite structures, while less than ~4 in post-perovskite structures, the pressure-temperature region of perovskite/post-perovskite phase transition can be predicted based on extrapolation of V_A/V_B. Assuming the phase transition between $CaIrO_3$ and perovskite-type $CaIrO_3$ occurs at a constant V_A/V_B everywhere in pressure-temperature space, we can use our experimental values $\partial P/\partial(V_A/V_B)$ = 74070(1100) $MPa/(V_A/V_B)$, and $\partial T/\partial(V_A/V_B)$ = 4901(360) $°C/(V_A/V_B)$ (Martin et al., 2007a) to calculate a Clapeyron slope of 15(3) MPa/°C for the phase transition. This calculated value is in remarkable agreement with the experimentally determined value 17(3) MPa/°C (Hirose and Fujita, 2005). However,

we believe this number should not describe the Clapeyron slope of the phase transition in $MgSiO_3$ rather, we conclude it may be possible to estimate the Clapeyron slope between perovskite/post-perovskite phases of $MgSiO_3$ when $\partial P/\partial(V_A/V_B)$ and $\partial T/\partial(V_A/V_B)$ are experimentally determined for this material.

While V_A/V_B appears useful for predicting the phase transition between perovskite and post-perovskite structure, V_A/V_B implies a measure of relative ion valence between the two cation sites. Considering all $CaIrO_3$-type structures have very similar V_A/V_B ratios, we should expect cations in $CaIrO_3$-type structures of Fe_2O_3 and Mn_2O_3 to be 2^+:4^+ rather than 3^+:3^+ (Ono and Ohishi, 2005; Santillan et al., 2006). This observation implies a 4^+ oxidation state of Fe be stabilized in these high pressure structures. If Fe^{+4} were to exist in the lower mantle, perhaps we could expect iron to occupy both magnesium and silicon sites in $MgSiO_3$ post-perovskite during solid-solution and/or stabilization of a $CaIrO_3$-type $MgFeO_3$ structure.

References

Angel, R.J., Zhao, J., and Ross, N.L. (2005) General rules for predicting phase transitions in perovskites due to octahedral tilting. Physical Review Letters, 95(2), 025503(1-4).

Berndt, M. (1997) ICSC/RETRIEVE 2.01 Crystal Structure Database., Gmelin Institute/FIZ Karlsruhe, Germany.

Brown, I.D. (1992) Chemical and Steric Constraints in Inorganic Solids. Acta Crystallographica Section B-Structural Science, 48, 553-572.

Brown, I.D., and Altermatt, D. (1985) Bond-Valence Parameters Obtained from a Systematic Analysis of the Inorganic Crystal-Structure Database. Acta Crystallographica Section B-Structural Science, 41(AUG), 244-247.

Brown, I.D., and Shannon, R.D. (1973) Empirical Bond-Strength Bond-Length Curves for Oxides. Acta Crystallographica Section A, A 29(MAY1), 266-282.

Busing, W.R., and Levy, H.A. (1964) Effect of Thermal Motion on Estimation of Bond Lengths from Diffraction Measurements. Acta Crystallographica, 17(2), 142-&.

Carpenter, M.A., Sondergeld, P., Li, B.S., Liebermann, R.C., Walsh, J.W., Schreuer, J., and Darling, T.W. (2006) Structural evolution, strain and elasticity of perovskites at high pressures and temperatures. Journal of Mineralogical and Petrological Sciences, 101(3), 95-109. DOI:10.2465/jmps.101.95.

Chapman, K.W., Chupas, P.J., and Kepert, C.J. (2005) Direct observation of a transverse vibrational mechanism for negative thermal expansion in $Zn(CN)_2$: An atomic pair distribution function analysis. Journal of the American Chemical Society, 127 (44), 15630-15636

-. (2006) Compositional dependence of negative thermal expansion in the Prussian blue analogues $M^{II}Pt^{IV}(CN)_6$ (M = Mn, Fe, Co, Ni, Cu, Zn, Cd). Journal of the American Chemical Society, 128(21), 7009-7014. DOI:10.1021/ja060916r.

Chupas, P.J., Chapman, K.W., and Lee, P.L. (Submitted) Applications of an amorphous siliconbased area detector for high resolution, high sensitivity and fast time-resolved pair distribution function measurements. Journal of Applied Crystallography.

Chupas, P.J., Chaudhuri, S., Hanson, J.C., Qiu, X.Y., Lee, P.L., Shastri, S.D., Billinge, S.J.L., and Grey, C.P. (2004) Probing local and long-range structure simultaneously: An in situ study of the high-temperature phase transition of alpha-AlF_3. Journal of the American Chemical Society, 126(15), 4756-4757.

Chupas, P.J., Ciraolo, M.F., Hanson, J.C., and Grey, C.P. (2001) In situ X-ray diffraction and solid-state NMR study of the fluorination of gamma-Al_2O_3 with HCF_2Cl. Journal of the American Chemical Society, 123(8), 1694-1702.

Decker, D.L. (1971) High-Pressure Equation of State for NaCl, KCl, and CsCl. Journal of Applied Physics, 42(8), 3239.

Finger, L.W., and Hazen, R.M. (2000) Systematics of high-pressure silicate structures. High-Temperature and High-Pressure Crystal Chemistry, 41, p. 123-155.

Flores, C., and Lay, T. (2005) The trouble with seeing double. Geophysical Research Letters, 32(24), L24305. DOI:10.1029/2005GL024366.

Garnero, E.J. (2004) A new paradigm for Earth's core-mantle boundary. Science, 304(5672), 834-836. DOI:10.1126/science.1097849.

Garnero, E.J., Maupin, V., Lay, T., and Fouch, M.J. (2004) Variable azimuthal anisotropy in Earth's lowermost mantle. Science, 306(5694), 259-261. DOI:10.1126/science.1103411.

Glazer, A.M. (1972) Classification of Tilted Octahedra in Perovskites. Acta Crystallographica Section B-Structural Science, B 28(V15), 3384-3392.

-. (1975) Simple Ways of Determining Perovskite Structures. Acta Crystallographica Section a, 31(V1), 756-762.

Goodman, L. (1960) On the Exact Variance of Products. Journal of the American Statistical Association, 55(292), 708-713.

Guignot, N., Andrault, D., Morard, G., Bolfan-Casanova, N., and Mezouar, M. (2007) Thermoelastic properties of post-perovskite phase $MgSiO_3$ determined experimentally at core-mantle boundary P-T conditions. Earth and Planetary Science Letters, 256(1-2), 162-168.

Gwanmesia, G.D., Li, B.S., and Liebermann, R.C. (1993) Hot-Pressing of Polycrystals of High-Pressure Phases of Mantle Minerals in Multi-Anvil Apparatus. Pure and Applied Geophysics, 141(2-4), 467-484.

Hammersley, A.P., Svensson, S.O., Hanfland, M., Fitch, A.N., and Hausermann, D. (1996) Two-dimensional detector software: From real detector to idealized image or two-theta scan. High Pressure Research, 14(4-6), 235-248.

Hernlund, J.W., Thomas, C., and Tackley, P.J. (2005) A doubling of the post-perovskite phase boundary and structure of the Earth's lowermost mantle. Nature, 434(7035), 882-886. DOI:10.1038/nature03472.

Hirose, K., and Fujita, Y. (2005) Clapeyron slope of the post-perovskite phase transition in $CaIrO_3$. Geophysical Research Letters, 32(13), L13313(1-4). DOI:10.1029/2005GL023219.

Hirose, K., Kawamura, K., Ohishi, Y., Tateno, S., and Sata, N. (2005) Stability and equation of state of $MgGeO_3$ post-perovskite phase. American Mineralogist, 90(1), 262-265.

Hull, S., Smith, R.I., David, W.I.F., Hannon, A.C., Mayers, J., and Cywinski, R. (1992) The POLARIS Powder Diffractometer at ISIS. Physica B-Condensed Matter, 180 & 181, 1000-1002.

Jackson, J.M., Sinogeikin, S.V., Carpenter, M.A., and Bass, J.D. (2004) Novel phase transition in orthoenstatite. American Mineralogist, 89(1), 239-244.

Kim, C., Yun, H.S., Lee, Y., Shin, H., and Liou, K. (1997) Structure and electrical conductivity of $AgTaS_3$. Journal of Solid State Chemistry, 132(2), 389-393.

Kubo, A., Kiefer, B., Shen, G.Y., Prakapenka, V.B., Cava, R.J., and Duffy, T.S. (2006) Stability and equation of state of the post-perovskite phase in $MgGeO_3$ to 2 Mbar. Geophysical Research Letters, 33(12), L12S12(1-4). DOI:10.1029/2006GL025686.

Larson, A.C., and Von Dreele, R.B. (2000) General Structure Analysis System (GSAS). Los Alamos National Laboratory Report, 86-748.

Lay, T., Williams, Q., and Garnero, E.J. (1998) The core-mantle boundary layer and deep Earth dynamics. Nature, 392(6675), 461-468. DOI:10.1038/33083.

Liu, H.Z., Chen, J., Hu, J., Martin, C.D., Weidner, D.J., Hausermann, D., and Mao, H.K. (2005a) Octahedral tilting evolution and phase transition in orthorhombic

$NaMgF_3$ perovskite under pressure. Geophysical Research Letters, 32(4), L04304(1-5). DOI:10.1029/2004GL022068.

Liu, W., Kung, J., and Li, B.S. (2005b) Elasticity of San Carlos olivine to 8 GPa and 1073 K. Geophysical Research Letters, 32(16). DOI:10.1029/2005GL023453.

Mao, L.W., Mao, H.K., Sturhahn, W., Zhao, J., Prakapenka, V.B., Meng, Y., Shu, J.F., Fei, Y.W., and Hemley, R.J. (2006) Iron-Rich Post-Perovskite and the Origin of Ultralow-Velocity Zones. Science, 312(5773), 564 - 565. DOI:10.1126/science.1123442.

Marsh, R.E. (1993) The Space Group of $AgTaS_3$. Journal of Solid State Chemistry, 102(1), 283-283.

Marshall, W.G., and Francis, D.J. (2002) Attainment of near-hydrostatic compression conditions using the Paris-Edinburgh cell. Journal of Applied Crystallography, 35, 122-125.

Martin, C.D., Antao, S.M., Chupas, P.J., Lee, P.L., Shastri, S.D., and Parise, J.B. (2005) Quantitative high-pressure pair distribution function analysis of nanocrystalline gold. Applied Physics Letters, 86(6), 061910. DOI:10.1063/1.1856691.

Martin, C.D., Chapman, K.W., Chupas, P.J., Prakapenka, V.B., Lee, P.L., Shastri, S.D., and Parise, J.B. (2007a) Compression, thermal expansion, structure, and instability of $CaIrO_3$, the structure model of $MgSiO_3$ post-perovskite. American Mineralogist.

-. (2007, In press) Compression, thermal expansion, structure, and instability of $CaIrO_3$, the structure model of $MgSiO_3$ post-perovskite. American Mineralogist.

Martin, C.D., Chupas, P.J., Chapman, K.W., and Parise, J.B. (2007b) Local vs. average structure; a study of Neighborite ($NaMgF_3$) utilizing the pair-distribution function for quantitative structure determination. Journal of Applied Crystallography, 40, 441-448.

Martin, C.D., Crichton, W.A., Liu, H.Z., Prakapenka, V., Chen, J.H., and Parise, J.B. (2006a) Phase transitions and compressibility of $NaMgF_3$ (Neighborite) in perovskite- and post-perovskite-related structures. Geophysical Research Letters, 33(11), L11305. DOI:10.1029/2006GL026150.

Martin, C.D., Crichton, W.A., Liu, H.Z., Prakapenka, V.B., Chen, J., and Parise, J.B. (2006b) In-situ Rietveld structure refinement of perovskite and post-perovskite phases of $NaMgF_3$ (Neighborite) at high pressures. American Mineralogist, 91(10), 1703-1706.

McDaniel, C.L., and Schneider, S.J. (1972) Phase Relations in CaO-IrO_2-Ir System in Air. Journal of Solid State Chemistry, 4(2), 275-280.

McNamara, A.K., van Keken, P.E., and Karato, S.I. (2002) Development of anisotropic structure in the Earth's lower mantle by solid-state convection. Nature, 416(6878), 310-314. DOI:10.1038/416310a.

Megaw, H.D. (1971) Crystal Structures and Thermal Expansion. Materials Research Bulletin, 6(10), 1007-1018.

Merkel, S., Kubo, A., Miyagi, L., Speziale, S., Duffy, T.S., Mao, H.K., and Wenk, H.R. (2006) Plastic deformation of $MgGeO_3$ post-perovskite at lower mantle pressures. Science, 311(5761), 644-646. DOI:10.1126/science.1121808.

Mizoguchi, H., Woodward, P.M., Byeon, S.H., and Parise, J.B. (2004) Polymorphism in $NaSbO_3$: Structure and bonding in metal oxides. Journal of the American Chemical Society, 126(10), 3175-3184.

Murakami, M., Hirose, K., Kawamura, K., Sata, N., and Ohishi, Y. (2004) Post-perovskite phase transition in $MgSiO_3$. Science, 304(5672), 855-858. DOI:10.1126/science.1095932.

Oganov, A.R., Martonak, R., Laio, A., Raiteri, P., and Parrinello, M. (2005) Anisotropy of Earth's D" layer and stacking faults in the $MgSiO_3$ post-perovskite phase. Nature, 438(7071), 1142-1144. DOI:10.1038/nature04439.

Oganov, A.R., and Ono, S. (2004) Theoretical and experimental evidence for a post-perovskite phase of $MgSiO_3$ in Earth's D " layer. Nature, 430(6998), 445-448. DOI:10.1038/nature02701.

Ono, S., Kikegawa, T., and Ohishi, Y. (2005) High-pressure and high-temperature synthesis of a cubic IrO2 polymorph. Physica B-Condensed Matter, 363(1-4), 140-145. DOI:10.1016/j.physb.2005.03.014.

Ono, S., and Ohishi, Y. (2005) In situ X-ray observation of phase transformation in Fe_2O_3 at high pressures and high temperatures. Journal of Physics and Chemistry of Solids, 66(10), 1714-1720. DOI:10.1016/j.jpcs.2005.06.010.

Pauling, L. (1929) The principles determining the structure of complex ionic crystals. Journal of the American Chemical Society, 51, 1010-1026.

Qiu, X.Y., Proffen, T., Mitchell, J.F., and Billinge, S.J.L. (2005) Orbital correlations in the pseudocubic O and rhombohedral R phases of $LaMnO_3$. Physical Review Letters, 94(17), 177203.

Rodi, F., and Babel, D. (1965) Ternare Oxide Der Ubergangsmetalle .4. Erdalkaliiridium(4)-Oxide - Kristallstruktur Von $CaIrO_3$. Zeitschrift Fur Anorganische Und Allgemeine Chemie, 336(1-2), 17.

Ross, N.L., and Hazen, R.M. (1989) Single-Crystal X-Ray-Diffraction Study of $MgSiO_3$ Perovskite From 77-K to 400-K. Physics and Chemistry of Minerals, 16(5), 415-420.

Salinas-sanchez, A., Garcia-munoz, J.L., Rodriguez-carvajal, J., Saez-puche, R., and Martinez, J.L. (1992) Structural Characterization of R_2BaCuO_5 (R = Y, Lu, Yb, Tm, Er, Ho, Dy, Gd, Eu and Sm) Oxides by X-Ray and Neutron-Diffraction. Journal of Solid State Chemistry, 100(2), 201-211.

Santillan, J., Shim, S.H., Shen, G.Y., and Prakapenka, V.B. (2006) High-pressure phase transition in Mn_2O_3: Application for the crystal structure and preferred orientation of the $CaIrO_3$ type. Geophysical Research Letters, 33(15), L15307(1-5).

Sata, N., Shen, G.Y., Rivers, M.L., and Sutton, S.R. (2002) Pressure-volume equation of state of the high-pressure B2 phase of NaCl. Physical Review B, 65(10). DOI:10.1103/PhysRevB.65.104114.

Shastri, S.D., Fezzaa, K., Mashayekhi, A., Lee, W.K., Fernandez, P.B., and Lee, P.L. (2002) Cryogenically cooled bent double-Laue monochromator for high-energy undulator X-rays (50-200 keV). Journal of Synchrotron Radiation, 9, 317-322. DOI:10.1107/S0909049502009986.

Shen, G.Y., Prakapenka, V.B., Eng, P.J., Rivers, M.L., and Sutton, S.R. (2005) Facilities for high-pressure research with the diamond anvil cell at GSECARS. Journal of Synchrotron Radiation, 12, 642-649. DOI:10.1107/S0909049505022442.

Shen, G.Y., Rivers, M.L., Wang, Y.B., and Sutton, S.R. (2001) Laser heated diamond cell system at the Advanced Photon Source for in situ x-ray measurements at high pressure and temperature. Review of Scientific Instruments, 72(2), 1273-1282. DOI:10.1063/1.1343867.

Sinmyo, R., Hirose, K., O'Neill, H.S., and Okunishi, E. (2006) Ferric iron in Al-bearing post-perovskite. Geophysical Research Letters, 33(12), L12S13. DOI:10.1029/2006GL025858.

Stixrude, L., and Karki, B. (2005) Structure and freezing of $MgSiO_3$ liquid in Earth's lower mantle. Science, 310(5746), 297-299. DOI:10.1126/science.1116952.

Tateno, S., Hirose, K., Sata, N., and Ohishi, Y. (2006) High-pressure behavior of $MnGeO_3$ and $CdGeO_3$ perovskites and the post-perovskite phase transition. Physics and Chemistry of Minerals, 32(10), 721-725. DOI:10.1007/s00269-005-0049-7.

Thomas, N.W. (1998) New global parameterization of perovskite structures. Acta Crystallographica Section B-Structural Science, 54, 585-599.

Toby, B.H. (2001) EXPGUI, a graphical user interface for GSAS. Journal of Applied Crystallography, 34, 210-213.

Tsuchiya, J., Tsuchiya, T., and Wentzcovitch, R.M. (2005) Vibrational and thermodynamic properties of $MgSiO_3$ postperovskite. Journal of Geophysical Research-Solid Earth, 110(B2), B02204. DOI:10.1029/2004JB003409.

Umemoto, K., Wentzcovitch, R.A., and Allen, P.B. (2006) Dissociation of $MgSiO_3$ in the Cores of Gas Giants and Terrestrial Exoplanets. Science, 331(5763), 983 - 986. DOI:10.1126/science.1120865.

Vanpeteghem, C.B., Zhao, J., Angel, R.J., Ross, N.L., and Bolfan-Casanova, N. (2006) Crystal structure and equation of state of $MgSiO_3$ perovskite. Geophysical Research Letters, 33(3), L03306. DOI:10.1029/2005GL024955.

Wada, H., and Onoda, M. (1990) Preparation of New Compound $AgTaS_3$. Chemistry Letters(5), 705-706.

Wang, Y., and Wen, L.X. (2004) Mapping the geometry and geographic distribution of a very low velocity province at the base of the Earth's mantle. Journal of Geophysical Research-Solid Earth, 109(B10), B10305. DOI:10.1029/2003JB002674.

Wills, A.S., and Brown, I.D. (1999) VaList, CEA, France

Zhao, J., Ross, N.L., and Angel, R.J. (2004) Tilting and distortion of $CaSnO_3$ perovskite to 7 GPa determined from single-crystal X-ray diffraction. Physics and Chemistry of Minerals, 31(5), 299-305.

Zhao, Y.S., Weidner, D.J., Parise, J.B., and Cox, D.E. (1993) Thermal-Expansion and Structural Distortion of Perovskite - Data For $NaMgF_3$ Perovskite .1. Physics of the Earth and Planetary Interiors, 76(1-2), 1-16.

(a)

P (GPa)	a (Å)	b	c	Vol (Å^3)
0.30(1)	3.14525(15)	3.14525(15)	7.29729(32)	226.203(11)
1.40(1)	3.14059(14)	9.82932(48)	7.28711(32)	224.95(1)
2.60(6)	3.13427(13)	9.79502(43)	7.27512(29)	223.348(9)
3.60(8)	3.12996(14)	9.77099(47)	7.26582(31)	222.209(9)
4.2(1)	3.12709(13)	9.75465(46)	7.25995(31)	221.45(1)
4.9(1)	3.12454(14)	9.73877(48)	7.25483(32)	220.76(1)
5.7(2)	3.12147(14)	9.72240(48)	7.24889(32)	219.99(1)
6.30(5)	3.11914(14)	9.70761(48)	7.24371(33)	219.335(11)
6.90(5)	3.11749(15)	9.69789(52)	7.24088(35)	218.914(11)
7.6(1)	3.11502(27)	9.68520(92)	7.23709(61)	218.340(17)
12.5(5)	3.0906(21)	9.5824(56)	7.2117(47)	213.59(19)
7.2(5)	3.1102(8)	9.7148(27)	7.2374(16)	218.680(65)
11.9(5)	3.0891(27)	9.5903(81)	7.2060(62)	213.59(25)
20.4(8)	3.0593(13)	9.3861(35)	7.1424(30)	205.09(11)
29(1)	3.0487(27)	9.2580(73)	7.1180(62)	200.92(23)

(b)

	V_O(Å^3), L_O(Å)	K_T (GPa)
Vol	226.632(45)	180.2(28)
a	3.14685(36)	222.9(49)
b	9.8662(21)	116.7(32)
c	7.29947(60)	267.1(48)

(c)

T (K)	a (Å)	b	c	Vol (Å^3)
332(2)	3.14214(11)	9.8800(4)	7.29979(24)	226.616(14)
393	3.14332(11)	9.8877(4)	7.30400(24)	227.009(14)
465	3.14466(12)	9.8964(4)	7.30931(25)	227.471(14)
536	3.14466(12)	9.9055(4)	7.31469(25)	227.949(14)
608	3.14754(12)	9.9151(4)	7.31469(25)	228.456(15)
680	3.14911(12)	9.9240(4)	7.31469(25)	228.950(15)
751	3.15068(12)	9.9343(4)	7.33236(26)	229.500(15)
823	3.15220(12)	9.9437(4)	7.33853(27)	230.022(16)
894	3.15359(12)	9.9537(4)	7.34427(25)	230.535(15)
966	3.15503(12)	9.9624(4)	7.35021(26)	231.028(15)
1038	3.15669(13)	9.9624(4)	7.35640(27)	231.535(16)
1109	3.15863(11)	9.9827(4)	7.36487(24)	232.226(14)

(d)

	V_O(Å^3),L_O(Å)	α_0(K^{-1}x10^{-5})	α_1(K^{-2}x10^{-9})
Vol	226.3754(78)	2.841(34)	3.37(48)
a	3.14147(5)	1.716(46)	3.87(65)
b	9.87515(19)	4.056(55)	-1.85(77)
c	7.29711(11)	2.763(46)	7.96(65)

[Table 7.1] (a) Unit cell data from $CaIrO_3$ at high pressure. (b) Bulk modulus constants were obtained using a 2nd order Birch-Murnaghan equation of state. The cube of each unit cell length, i.e. a^3, has been fit to obtain a comparative bulk modulus. (c) The raw unit cell from every ~7th data in the high temperature series. (d) The fitted thermal expansion constants are listed with those obtained by fitting the cube of each unit cell length, i.e. a^3, to obtain a comparative thermal expansion.

(a)

Temperature (K)	2.0(1)	100.0(1)	205.0(1)	293(2)
a (Å)	3.13451(9)	3.13493(8)	3.13622(9)	3.13645(5)
b	9.87568(27)	9.87709(27)	9.88198(28)	9.88352(15)
c	7.29518(18)	7.29562(17)	7.29871(18)	7.29903(10)
V (Å^3)	225.825(10)	225.901(10)	226.202(11)	226.264(6)
Ca				
y	0.25019(13)	0.25019(13)	0.25034(15)	0.25035(9)
U	0.185(13)	0.219(13)	0.343(15)	0.576(10)
Ir				
U	0.113(6)	0.141(6)	0.185(7)	0.251(4)
$O_{[4c]}$				
y	0.42541(12)	0.42539(12)	0.42551(13)	0.42505(7)
U	0.217(12)	0.238(12)	0.303(14)	0.428(9)
$O_{[8f]}$				
y	0.12692(8)	0.12679(8)	0.12667(9)	0.12719(5)
z	0.05064(10)	0.05046(10)	0.05025(11)	0.05036(6)
U	0.192(8)	0.218(8)	0.280(9)	0.383(6)
χ^2	1.471	1.334	1.194	1.798
wRp	0.78%	0.74%	0.73%	2.06%
Rp	2.35%	2.21%	2.14%	6.25%

$wRp = 100\%*[\Sigma w(I_O - I_C)^2/\Sigma w I_O^2]^{1/2}$

$Rp = 100\%*\Sigma|I_O - I_C|/\Sigma I_O^2$

Terms I_O and I_C are observed and calculated profile intensities and *w* is weight associated with I_O.

(b)

293(2) (K)	Ca	Ir	$O_{[4c]}$	$O_{[8f]}$
S_{ij} (v.u.)	2.26(5)	4.03(9)	-2.27(5)	-2.01(4)
P_i (%)	13.0(24)	0.8(22)	13.7(24)	0.5(22)

*R*1 = 0.19(2)

[Table 7.2] Refined unit cell parameters, atomic coordinates, isotropic temperature factors (*U*), and refinement statistics are listed for $CaIrO_3$ (*Cmcm*) at several low temperatures in section (a), while the residual bond strain value (*R*1) of the structure, experimental bond valence sums (S_{ij}), and chemical strain (P_i) of each ion are listed at room temperature in section (b). (Ca: 0, y, 0; Ir: 0, 0, 0; O_{4c}: 0, y, 0.25; O_{8f}: 0, y, z)

Conditions	293(2) K	2.0(1) K	9.72(5) GPa
a	3.13642(6)	3.13450(9)	3.1010(4)
b	9.88337(20)	9.87576(27)	9.6588(13)
c	7.29891(13)	7.29521(18)	7.2111(9)
V	226.255(8)	225.827(10)	215.99(5)
$Ca_{[4a]}$			
y	0.25049(13)	0.25028(14)	0.2467(5)
z	-0.0100(14)	-0.0130(9)	-0.0051(24)
U	0.542(15)	0.163(16)	1.09(8)
$Ir_{[4a]}$			
y	0.00141(25)	0.0002(5)	0.0046(6)
z	0.2382(6)	0.2390(5)	0.2418(14)
U	0.221(7)	0.114(6)	0.73(4)
$O_{[4a]}$ (i)			
y	0.92506(10)	0.92547(12)	0.9228(5)
z	-0.0083(11)	-0.00793(71)	-0.0088(25)
U	0.361(8)	0.183(8)	1.05(4)
$O_{[4a]}$ (ii)			
y	0.62985(31)	0.62873(44)	0.6304(13)
z	0.1910(4)	0.19165(36)	0.1868(12)
U	0.361(8)	0.183(8)	1.05(4)
$O_{[4a]}$ (iii)			
y	0.62443(31)	0.62505(44)	0.6289(12)
z	0.7915(4)	0.79271(34)	0.7876(13)
U	0.361(8)	0.183(8)	1.05(4)
χ^2	1.785	1.469	0.882
wRp	2.09%	0.78%	2.63%
Rp	6.16%	2.35%	4.24%

[Table 7.3] Refined unit cell parameters, atomic coordinates, isotropic temperature factors (*U*), and refinement statistics are listed for $CaIrO_3$ ($Cmc2_1$) structure model trials at room pressure and low temperatures (2.0(1) and 293(2) K) with a trial at high pressure and room temperature (9.72(5) GPa). (Ca: 0, y, z; Ir: 0, y, z; O_{4c}: 0, y, z; O_{8f}: 0, y, z)

Presssure (GPa)	0.00(5), V_O	2.17(5)	5.40(5)	7.95(5)	9.72(5)	9.68(8)*
Oil bars to press	70	250	500	700	800	850
a	3.14341(35)	3.1332(4)	3.1193(4)	3.1084(4)	3.1011(4)	3.1015(4)
b	9.8816(11)	9.8271(14)	9.7505(13)	9.6931(14)	9.6587(13)	9.6551(14)
c	7.3021(8)	7.2805(10)	7.2496(9)	7.2280(10)	7.2111(9)	7.2141(10)
V	226.82(4)	224.17(5)	220.49(5)	217.78(5)	215.99(5)	216.03(5)
Ca						
y	0.2496(5)	0.2486(6)	0.2485(5)	0.2488(6)	0.2470(5)	0.2476(6)
U	1.45(7)	1.36(8)	0.90(4)	0.83(4)	0.81(4)	0.93(4)
Ir						
U	1.033(31)	0.94(4)	1.28(7)	1.26(7)	1.07(6)	1.12(7)
$O_{[4c]}$						
y	0.42512(42)	0.42505(53)	0.42450(50)	0.42346(52)	0.42290(47)	0.42423(54)
U	1.44(6)	1.36(8)	1.24(7)	1.25(7)	1.05(6)	1.26(7)
$O_{[8f]}$						
y	0.12673(26)	0.12747(31)	0.12817(30)	0.12897(31)	0.12965(29)	0.13035(30)
z	0.04994(34)	0.0496(4)	0.0503(4)	0.0508(4)	0.0506(4)	0.0511(4)
U	1.26(5)	1.05(5)	1.05(5)	1.03(5)	0.98(5)	0.86(5)
χ^2	0.8625	0.8563	0.8919	0.9177	0.8897	0.9236
wRp	2.77%	3.38%	3.04%	2.95%	2.65%	2.94%
Rp	4.32%	4.86%	4.84%	4.45%	4.25%	4.78%

*850 Oil bar pressure considered quasi-hydrostatic sample pressure.

[Table 7.4] Refined unit cell parameters, positional parameters, isotropic temperature factors (*U*), and refinement statistics are listed for $CaIrO_3$ (*Cmcm*) at high pressure.

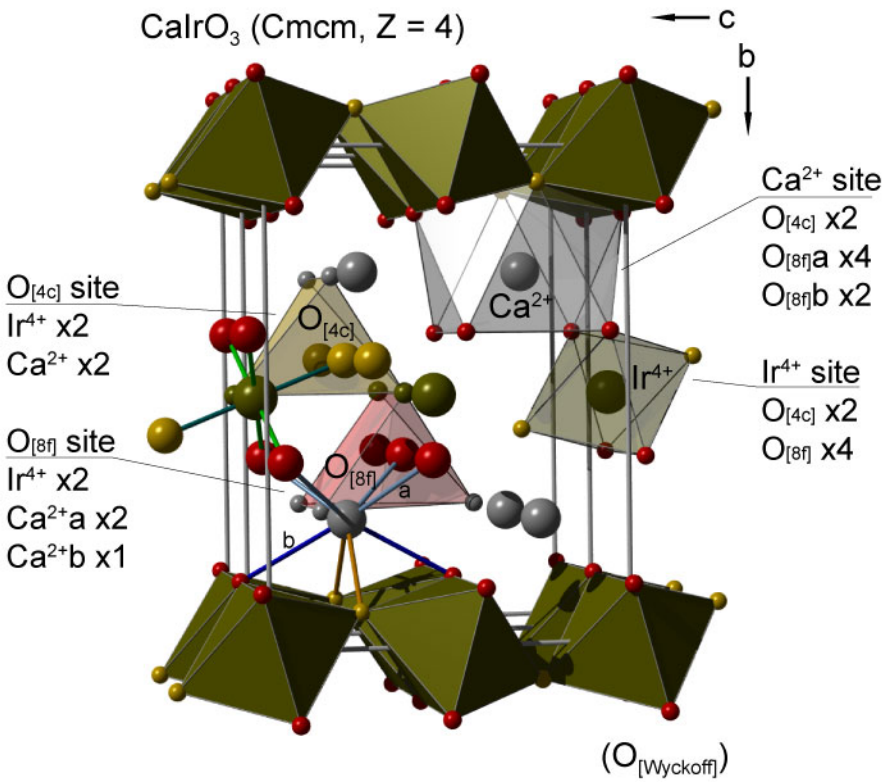

[Fig 7.1] Structure model of $CaIrO_3$ (*Cmcm*), showing coordination environment of each ion site. Each oxygen site is designated by the Wyckoff position symbol 4c or 8f. The number of each unique bond belonging to each ion environment is listed for clarity.

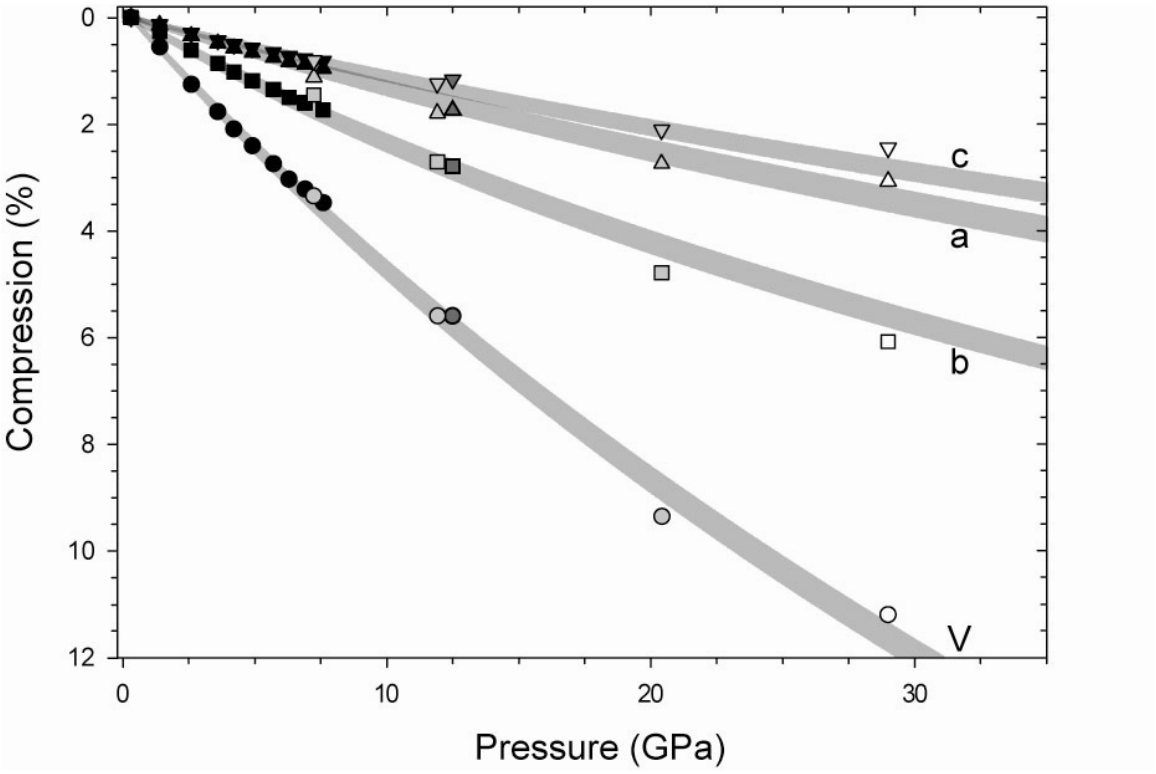

[Fig. 7.2] The unit cell parameters and volume of $CaIrO_3$ are plotted as a function of pressure. Data collected in an alcohol pressure medium (black) are plotted along side data collected from several sample runs (grey, dark grey, and white) in a NaCl pressure media after laser annealing (1500±300 K). All error bars are smaller than symbol size.

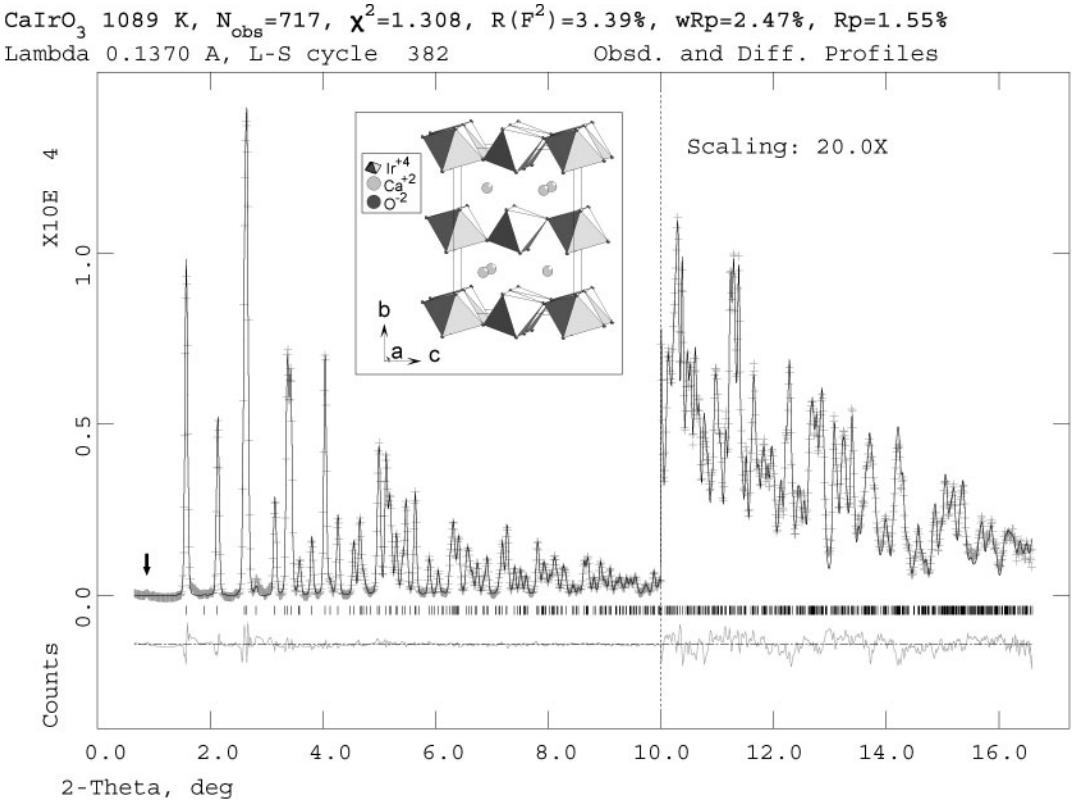

[Fig. 7.3] Results of a typical Rietveld refinement of $CaIrO_3$ showing the fit to the data collected at 1089 K. Data above 10˚ 2θ are magnified by a factor of 20 for clarity. The arrow pointing down indicates the I_o reflection from the dissociation product Ca_2IrO_4. A picture of the $CaIrO_3$ structural model is inset.

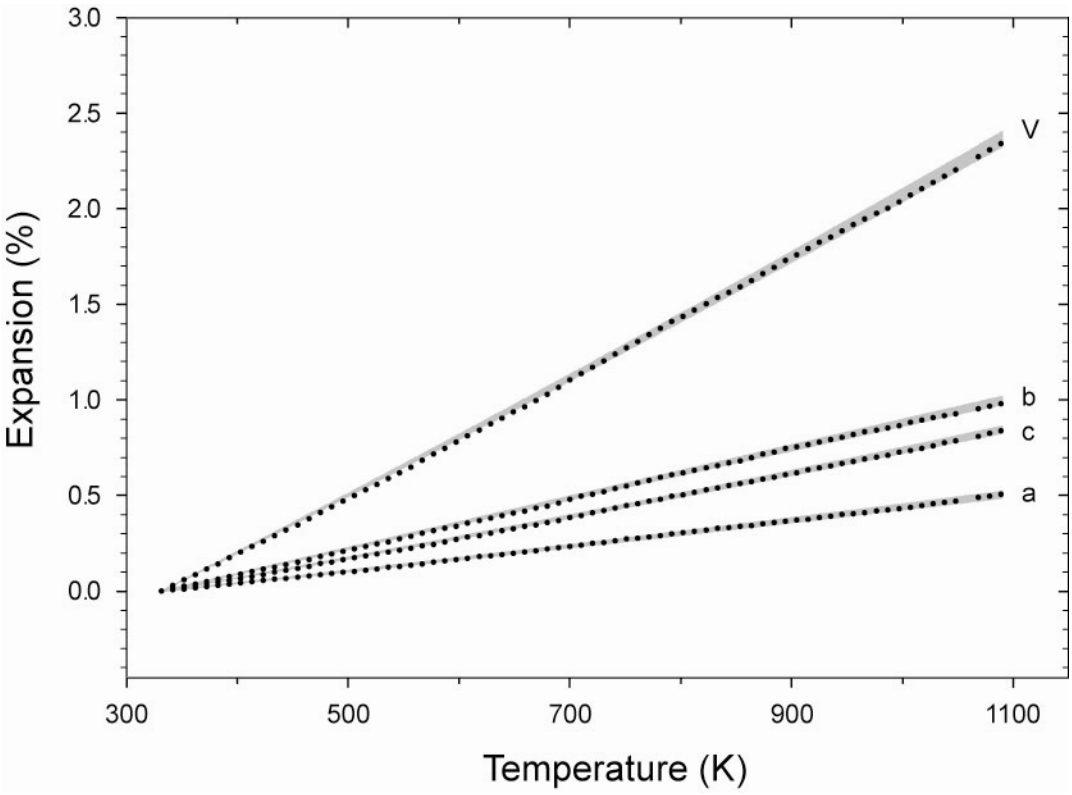

[Fig. 7.4] The unit cell parameters and volume of $CaIrO_3$ are plotted as a function of temperature. Error bars are smaller than symbol size.

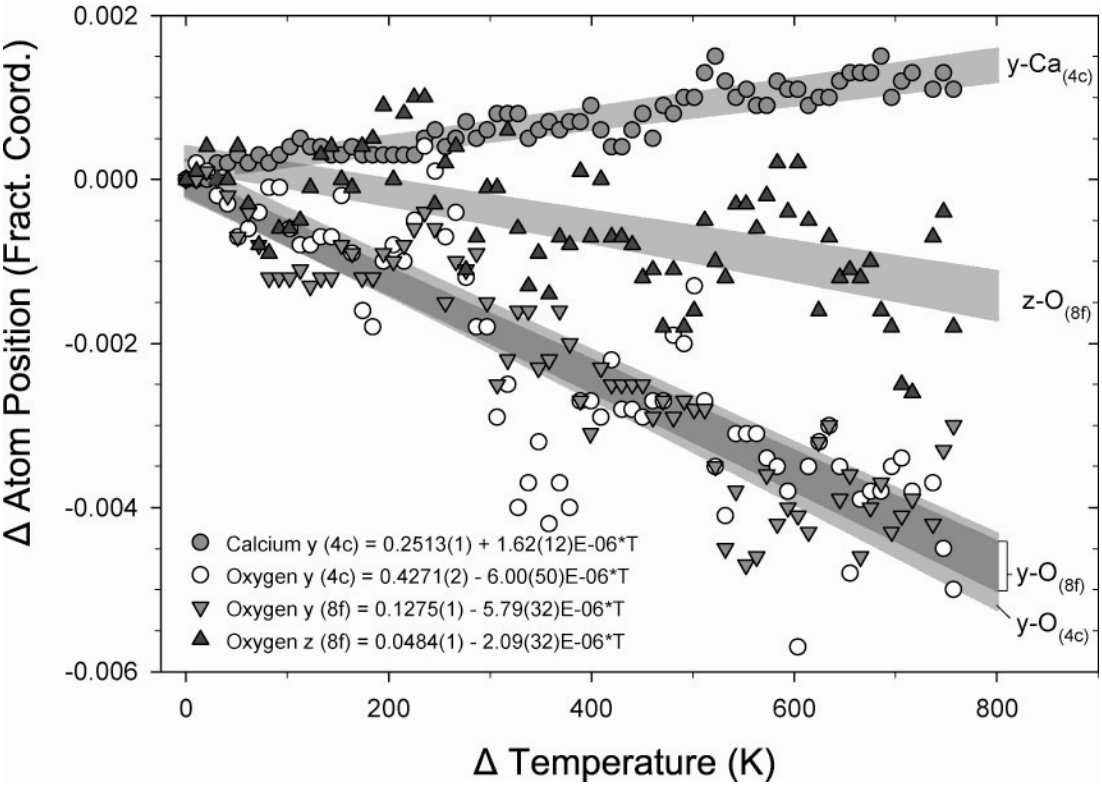

[Fig. 7.5] The change in atom positional parameters, in fractional coordinates, plotted as a function of the change in temperature increasing from 332 K. The asymmetric unit for the $CaIrO_3$ structure model in space group *Cmcm* has 4 independent atomic positional parameters; each is normalized according to their value at 332 K. Error bars are larger than symbol size and are not shown for clarity. Each parameter, with standard deviation, has been fit according to the linear equation displayed within the plot. Equations refer to the real atomic position within the unit cell (Ca: 0, y, 0; Ir: 0, 0, 0; O_{4c}: 0, y, 0.25; O_{8f}: 0, y, z) so the estimated structure may be calculated by the reader at any temperature, where T = 0 at 332 K. Atom labels contain the Wyckoff position of each atom (8f or 4c) in addition to the variable direction (y or z) within the unit cell.

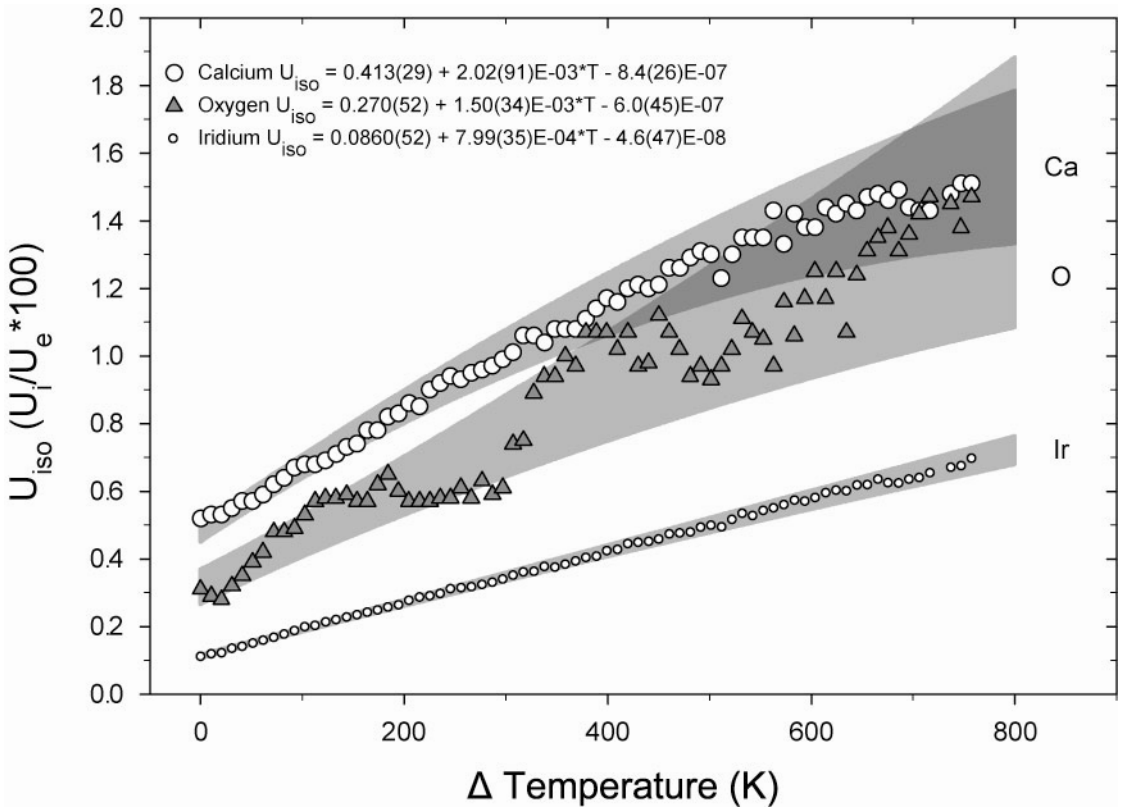

[Fig. 7.6] Isotropic displacement parameter for each atom is shown a function of change in temperature increasing from 332 K. Some error bars are larger than symbol size and not shown for clarity. Each parameter, with standard deviation, has been fit according to the second-order polynomial equation displayed within the plot.

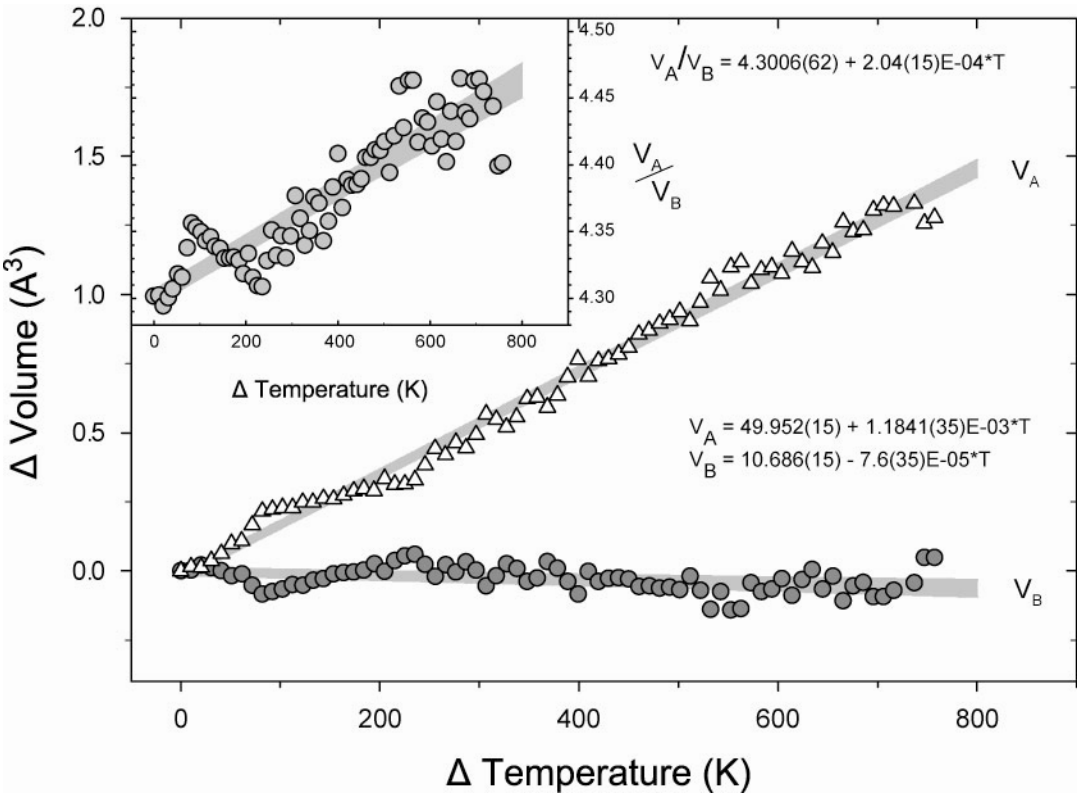

[Fig. 7.7] The volume of the Ca polyhedra (V_A), IrO_6 octahedra (V_B), and V_A/V_B ratio (inset) calculated from structure models derived from Rietveld refinement, along with the change in each parameter are plotted as a function of change in temperature increasing from 332 K. Error bars are smaller than symbol size and each parameter, with standard deviation, has been fit according to the linear equation displayed within the figure. The Ca polyhedra assumes: $V_A = (V_{UC}/4)-V_B$.

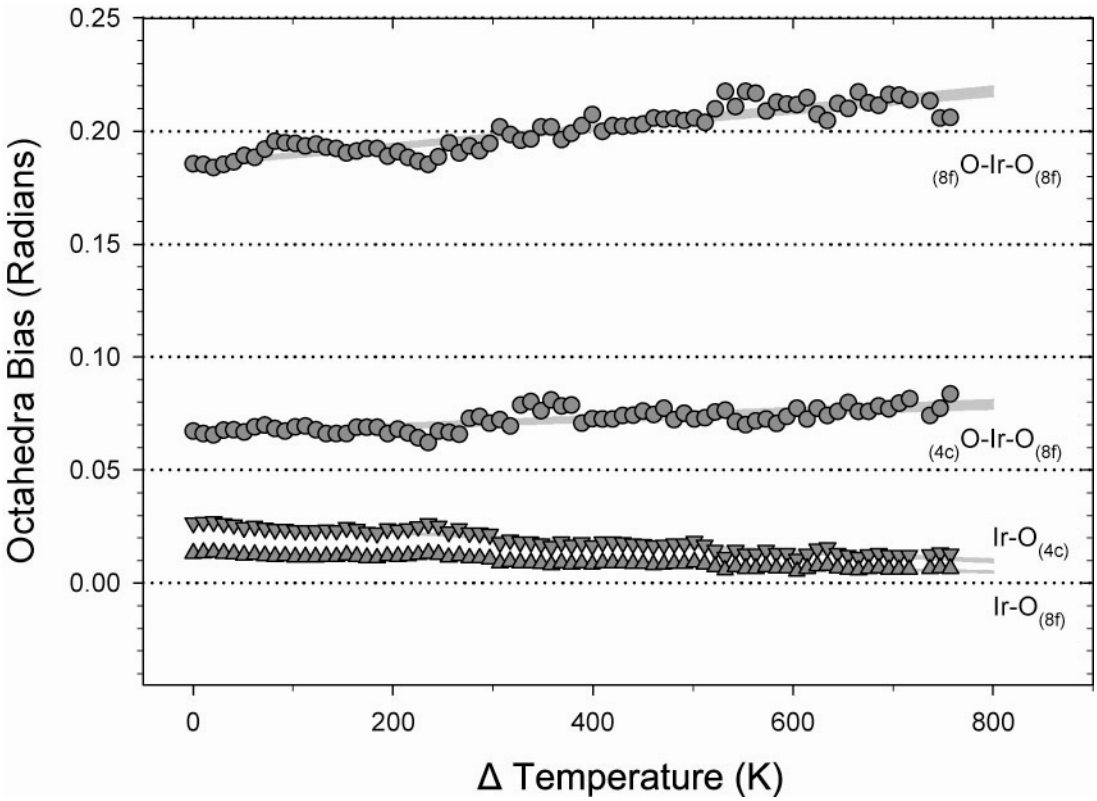

[Fig. 7.8] The deformation of IrO_6 octahedra as bias from a perfect octahedra plotted as a function of change in temperature increasing from 332 K. Oxygen labels contain the Wyckoff position of each atom (8f or 4c). Ir-O bias = $[(\text{Ir-O}) - (\text{Ir-O})_m] / (\text{Ir-O})_m$, while O-Ir-O bias = $\tan [(\pi/2) - (\text{O-Ir-O})]$.

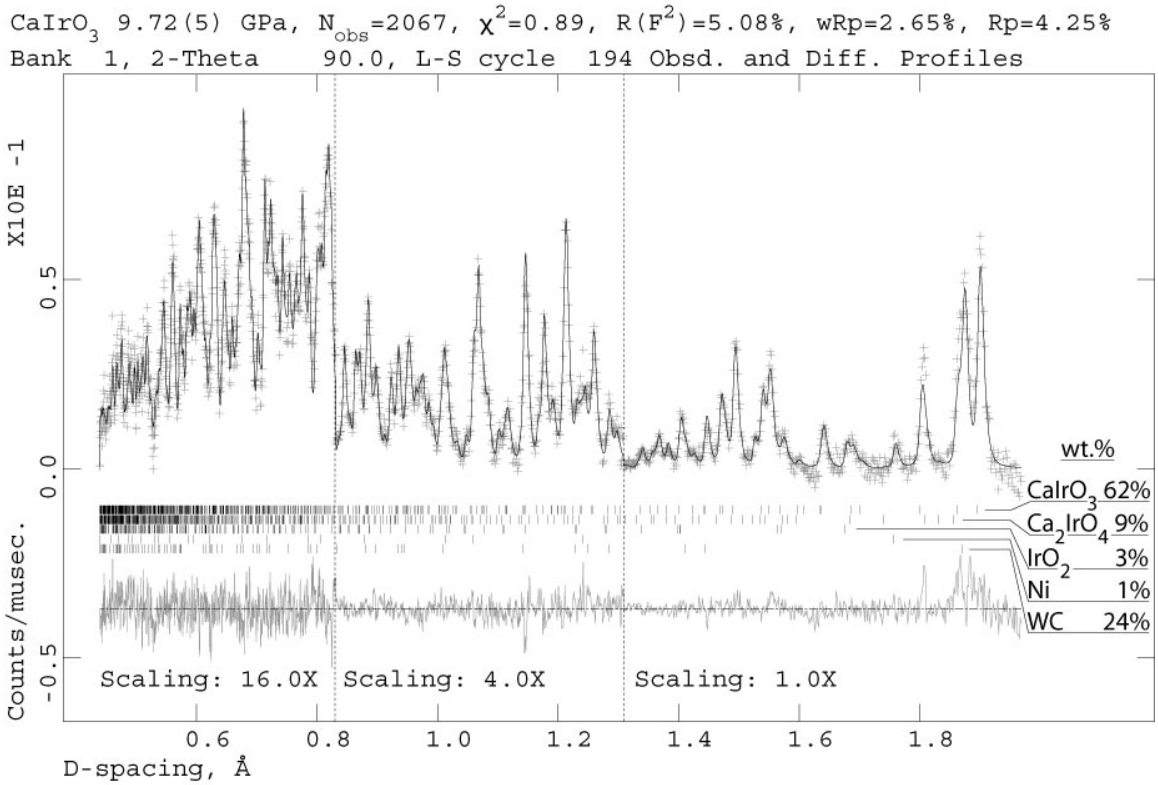

[Fig. 7.9] Rietveld structure refinement of $CaIrO_3$ showing the fit to the data collected at 9.72(5) GPa. Data below 1.3 Å d-spacing are magnified (counts-scale) by a factor of 4, while the intensities below 0.82 Å are magnified by a factor of 16. Weight fraction of each phase is refined and included in the plot at this pressure.

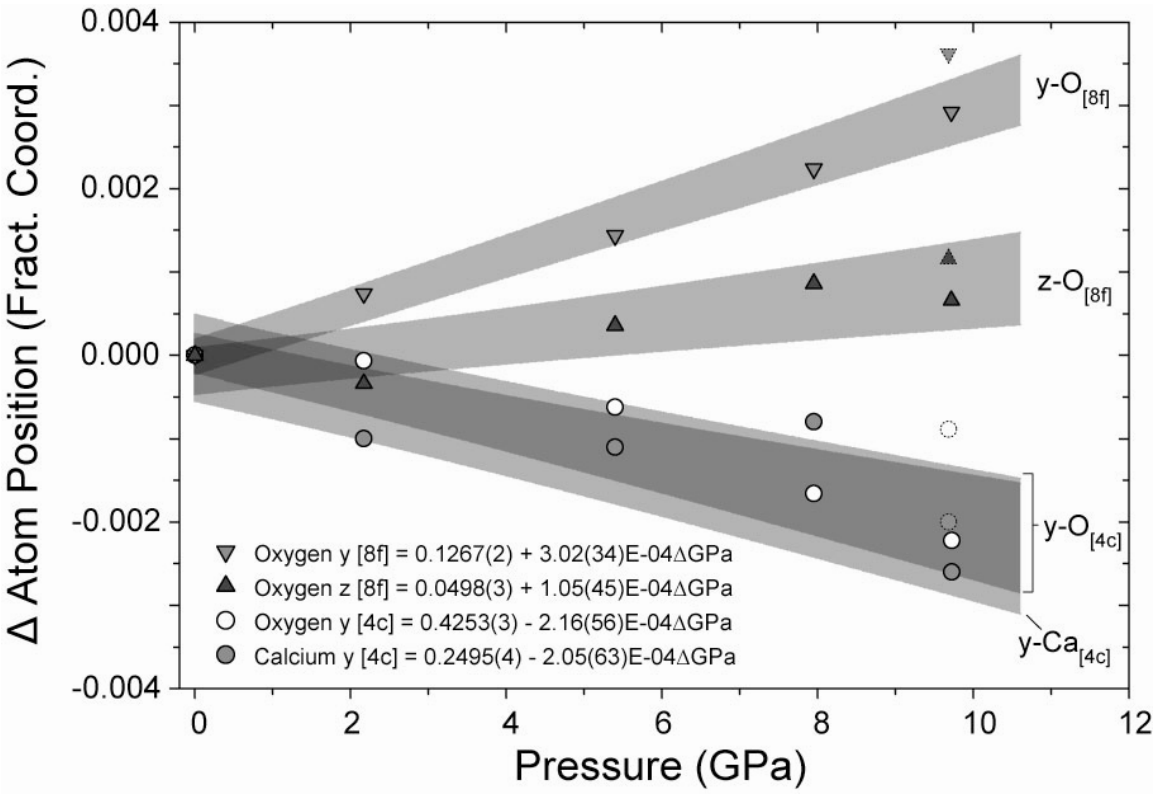

[Fig. 7.10] The change in atom positional parameters, in fractional coordinates, plotted as a function of pressure. The asymmetric unit of the $CaIrO_3$ structure model in space group *Cmcm* has 4 independent atomic positional parameters and each is normalized according to the 'room pressure' value (70 oil bar). Error bars are larger than symbol size and are not shown for clarity. Each parameter, with standard deviation, has been fitted according to the linear equation displayed within the plot. Quasi-hydrostatic data (850 bar) are shown as symbols with dotted line. Equations refer to the real atomic position within the unit cell (Ca: 0, y, 0; Ir: 0, 0, 0; O_{4c}: 0, y, 0.25; O_{8f}: 0, y, z).

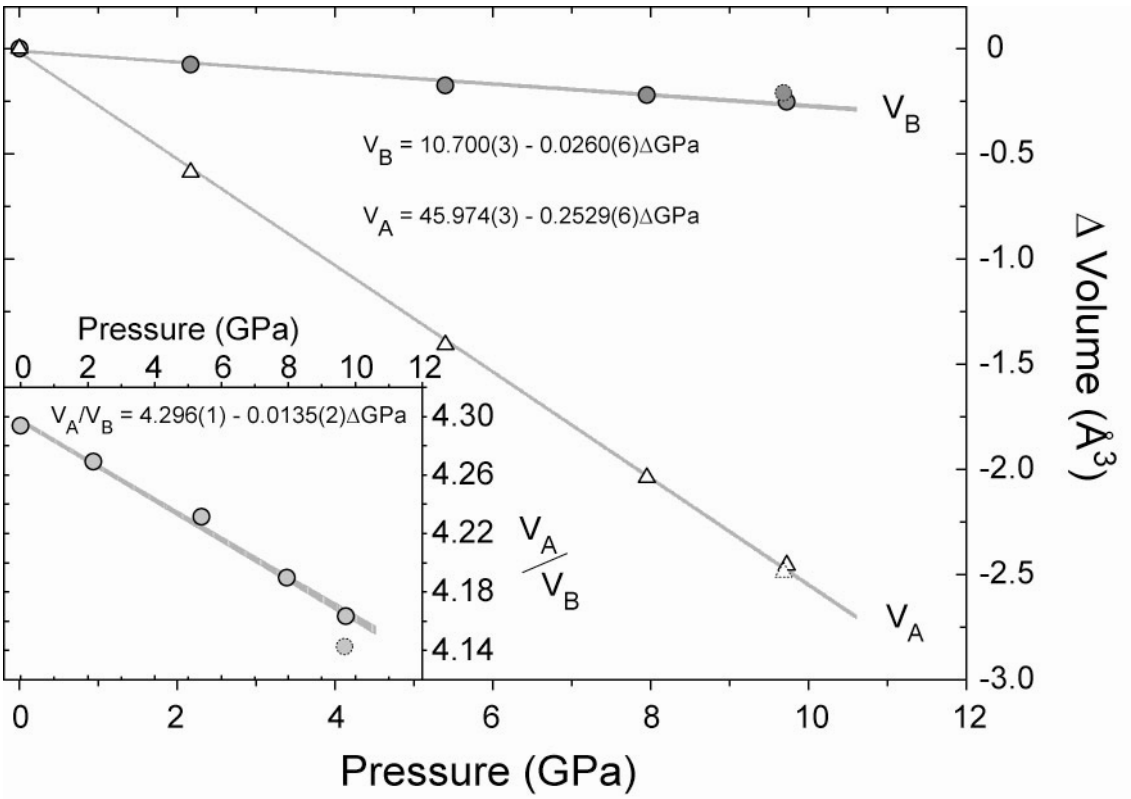

[Fig. 7.11] The volume of the Ca polyhedra (V_A), IrO_6 octahedra (V_B), and V_A/V_B ratio (inset) derived from Rietveld refinement are plotted as a function of pressure. Error bars are smaller than symbol size and each parameter, with standard deviation, has been fitted according to the linear equation displayed within the figure. Quasi-hydrostatic data (850 bar) are shown as symbols with dotted line. $V_A/V_B = [(V_{UC}/4)-V_B]/V_B$.

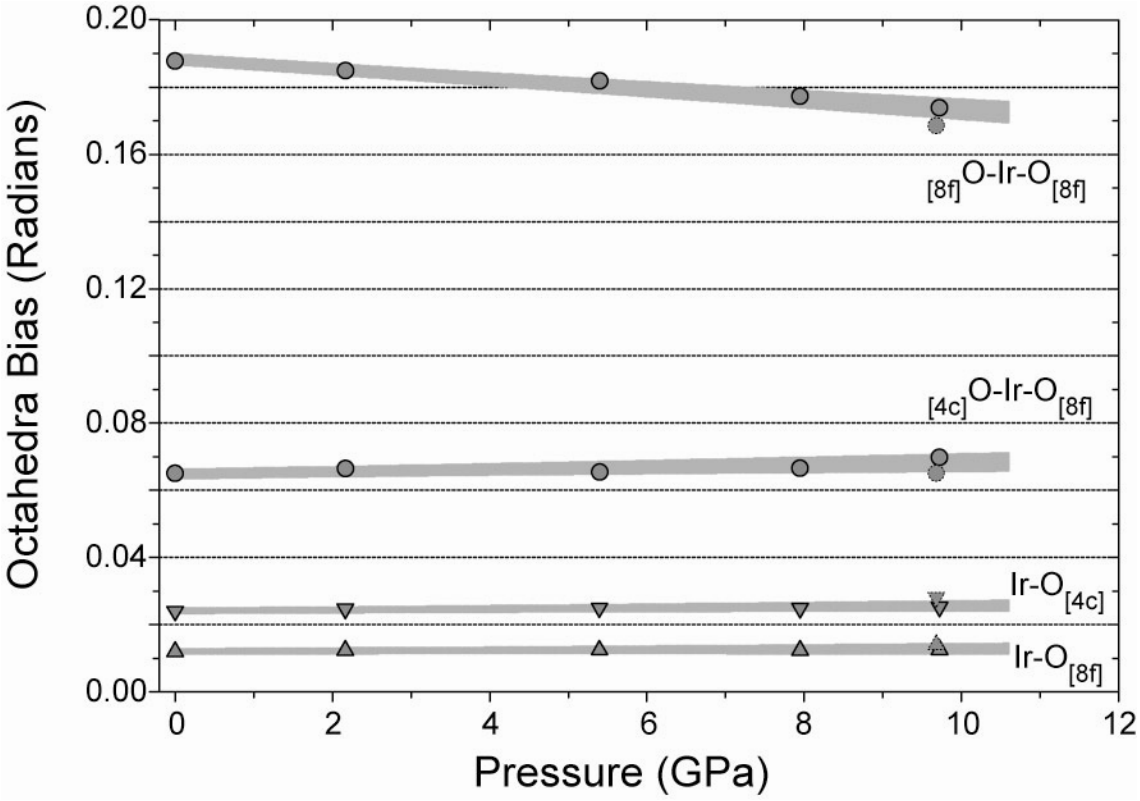

[Fig. 7.12] Strain of IrO_6 octahedra as bias from a perfect octahedra is plotted as a function of pressure. Quasi-hydrostatic data (850 bar) are shown as symbols with dotted line. Ir-O bias = $[(\text{Ir-O}) - (\text{Ir-O})_m] / (\text{Ir-O})_m$, while O-Ir-O bias = $\tan [(\pi/2) - (\text{O-Ir-O})]$.

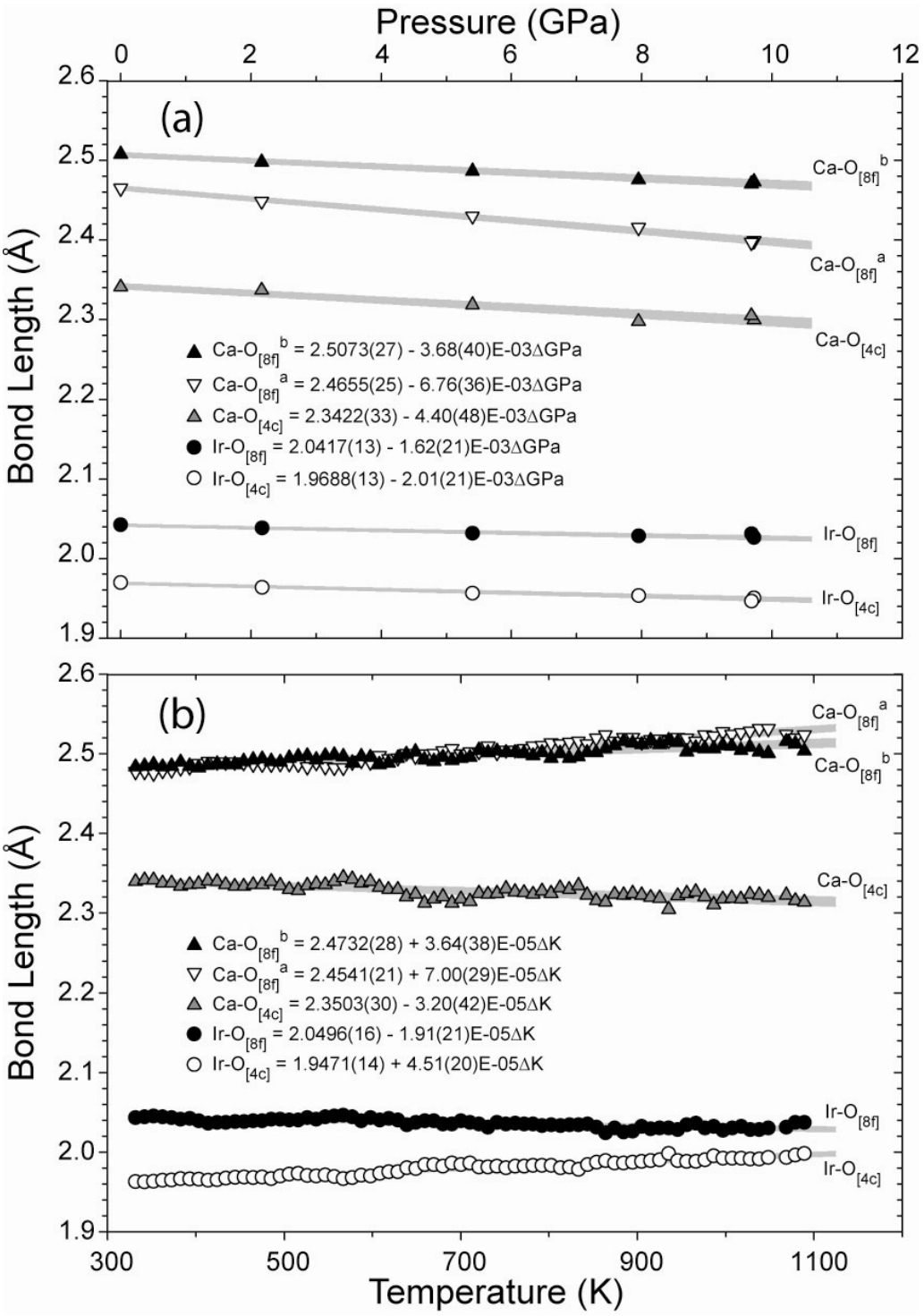

[Fig. 7.13] (a) Bond lengths within the $CaIrO_3$ structure plotted as a function of pressure and (b) as a function of temperature. Error bars are of the order of the symbol size and each parameter, with standard deviation, has been fitted according to the linear equation displayed within the figure.

Chapter VIII

Perovskite and Post-Perovskite: Structure Survey and Implications for $MgSiO_3$ in Earth's Lower Mantle.

SECTION 9.1 IN PREPARATION FOR SUBMISSION:

MARTIN, C.D., MENG, Y., PRAKAPENKA, V., AND PARISE, J.B. PEROVSKITE TO POST-PEROVSKITE PHASE TRANSITION AND A GRAPHITE GASKET INSERT FOR THE DIAMOND ANVIL CELL. JOURNAL OF APPLIED CRYSTALLOGRAPHY.

8.1. Predicting the post-perovskite phase transition.

8.1.1. Introduction

Underlying the theory for predicting the pressure of the phase transformation between perovskite and post-perovskite structures (Chapter 6) is the concept of bond valence (Chapter 7). As the bond valence concept applies to perovskites (ABX_3), where there exists a 1:2 charge-ratio (i.e., A^{+2}:B^{+4}, $Mg^{+2}Si^{+4}O_3$, $Ca^{+2}Ti^{+4}O_3$, $Na^{+1}Mg^{+2}F_3$) for the A- (dodecahedral site) and B-site (octahedral site), the longer A-X bonds are much more compressible than the shorter B-X bonds and corner-sharing octahedra tilt (Figure 3.2), collapsing the octahedra network into the A-site and reducing the volume of the A-site relative to the B-site (V_A:V_B ratio) when pressure is increased (Angel et al., 2005; Zhao et al., 2006). According to geometrical constraints imposed by the corner-sharing network, for cubic perovskites (*Pm*-3*m*) where no octahedral tilting occurs, $5 \equiv V_A:V_B$, thus $5 \geq V_A:V_B$ for perovskites in general, where corner-sharing BX_6 octahedra tilt (B-X-B bending from 180°) (Thomas, 1998). Increasing pressure will increase octahedral tilting and decrease the V_A:V_B ratio in perovskite structures where cations have a 1:2 charge-ratio. The V_A:V_B ratio in perovskite and post-perovskite structure-types is determined

according to $\frac{V_A}{V_B} = \frac{\frac{V_{UC}}{Z} - V_B}{V_B}$, where V_{UC} is the unit cell volume, Z is the number of formula units per unit cell, and V_B is calculated from structure information and program *CRYSTAL MAKER*. This relation implies V_A is all volume in the unit cell not occupied by V_B and this relation is independent of the formal coordination number of the A-site cation in either structure-type.

The research performed in Chapter 6 (Figure 8.1) suggests that the pressure where a post-perovskite phase transition occurs in a perovskite-structured material may be predicted by extrapolating the observed decrease in the V_A:V_B ratio value. Post-perovskite structures (*Cmcm*, $CaIrO_3$-type) become stable vs. perovskite structures when BX_6 octahedra tilt beyond a critical value and the V_A:V_B ratio is reduced below 4. In this section we survey V_A:V_B values from many perovskite structures cataloged in the International Crystal Structure Database [ICSD, (Berndt, 1997)]. In addition, we present new structure data obtained at high pressures using a strategy to maximize sample volume and improving powder statistics. This strategy allows re-evaluation of the $MgGeO_3$ post-perovskite structure, where literature reports of the values of V_A:V_B are in conflict: 4.28 (Hirose, et al., 2005) and 3.59 (Kubo, et al., 2006) (Chapter 7).

8.1.2. Results

8.1.2.1 Observations in the perovskite structure

In Table 8.1a we list a sample of 51 perovskite structures retrieved from the ICSD and we report the V_A:V_B ratio of each. These structures were not selected from the database for fitting any criteria other than that each atom must have complete site occupancy. Each structure represents the atomic configuration at room pressure and temperature unless otherwise noted. *First*, we observe that the rule, $5 \geq V_A$:V_B for perovskites, applies only to perovskites in general and a special exception exists in the case of the rare $NdFeO_3$ and $KCuF_3$ structures, where significant reduction of volume occurs in BX_6 octahedra as a result of deformation without tilting. *Second*, we observe that all 51 perovskite structures in the sample have a V_A/V_B greater than '4.00'. This result suggests that perovskite structures in general are not stable when V_A/V_B decreases below

'4.00'. Previously in Chapter 6, regarding the $NaMgF_3$ perovskite structure at 27 GPa before phase transition to post-perovskite structure at 30 GPa, we proposed that tilting of the octahedra (reduction of V_A/V_B), as pressure increases across the perovskite/post-perovskite phase transition ($V_A:V_B < 4$), causes some extra-octahedral anion-anion [$(X\text{-}X)_E$] distances to rival the average intra-octahedral anion-anion [$(X\text{-}X)_I$] distance and if a $(X\text{-}X)_E$ distance decreases below the average $(X\text{-}X)_I$ distance, repulsion between these poorly-screened like-charges would destabilize the perovskite-type corner-sharing network of octahedra. There are three unique $(X\text{-}X)_E$ distances that decrease and may rival the average $(X\text{-}X)_I$ distance as tilting of the octahedra increases in the orthorhombic (*Pbnm*) perovskite structure, while there is only one such distance in the rhombohedral ($R\bar{3}c$) perovskite structure. In Figure 8.2 we plot the ratio between specific $(X\text{-}X)_E$ distances and the average $(X\text{-}X)_I$ distance as a function of the $V_A:V_B$ ratio for each perovskite structure in the sample set and we consider both the shortest of the three $(X\text{-}X)_E$ distances as well as the average $(X\text{-}X)_E$ value.

8.1.2.2 Observations in the post-perovskite ($CaIrO_3$-type) structure

The data show that all perovskite structures in the sample have an average $(X\text{-}X)_I$ distance that is shorter than the $(X\text{-}X)_E$ distance. In addition, it is interesting to note the structure similarity between orthorhombic (*Pbnm*) structures with similar $V_A:V_B$ values. For instance, the $PrLuO_3$ structure ($V_A:V_B = 4.03$) duplicates both the $V_A:V_B$ ratio and octahedral tilt angle (Zhao et al., 1993) of the critical $NaMgF_3$ perovskite structure at 27(1) GPa before phase transition to post-perovskite structure at 30 GPa ($PrLuO_3$: $\varphi = 14.0°$, $\theta = 19.8°$ $\Phi = 24.1°$; $NaMgF_3$ (27 GPa): $\varphi = 15.2°$ $\theta = 17.8°$ $\Phi = 23.3°$). Also, using the $V_A:V_B$ ratio of the $MgSiO_3$ perovskite structure at room pressure with the $V_A:V_B$ ratio of the structure at extreme conditions (80 GPa and 1500 K) we calculate a post-perovskite phase transition should occur at 150 GPa by linear extrapolation of $V_A:V_B$ using $\partial P/\partial(V_A/V_B)$. While our calculation is in reasonable agreement with the actual phase transition pressure [120 GPa, (Murakami et al., 2004; Oganov and Ono, 2004)], the calculation could be improved if both structures were at constant temperature, since increasing the temperature is expected to increase the $V_A:V_B$ value of the structure (Angel et al., 2005) and, in the $MgSiO_3$ structure at extreme conditions, lead to an

overestimation of the calculated pressure where V_A:V_B is to equal 4. Overall, it appears that it is possible to increase V_A:V_B over 5 by deforming V_B, however, considering the geometry of the corner-sharing octahedra in the perovskite structure, it may not be possible to decrease the V_A:V_B ratio below 4 without decreasing a $(X\text{-}X)_E$ distance below the average $(X\text{-}X)_I$ distance and destabilizing the perovskite structure.

From examination of Table 8.1a & 8.1b it is clear that post-perovskite structures near the perovskite phase boundary have V_A:V_B = 4 and, with the exception of $CaIrO_3$ itself, all known $CaIrO_3$-type structures have V_A:$V_B \leq 4$. The fact that $CaIrO_3$ has a V_A:V_B slightly greater than 4 suggests that there is no geometrical constraint within the post-perovskite structure, such as $(X\text{-}X)_E$ vs. $(X\text{-}X)_I$ distances in the perovskite structure, that might otherwise limit the range of V_A:V_B in the critical $CaIrO_3$ structure-type.

8.1.2.3 Resolution of conflicting data on $MgGeO_3$

Recent studies addressing post-perovskite structure of $MgGeO_3$ (Table 8.1b) utilizing Rietveld structure refinement implement spherical harmonic preferred orientation corrections to observed x-ray diffraction intensities (Hirose et al., 2005; Kubo et al., 2006) without publishing raw 2-D images or spherical harmonic preferred orientation correction constants and readers are left without means to evaluate the validity of the correction and the strength of the Rietveld structure refinements are weakened. Both studies of $MgGeO_3$ post-perovskite report structures each with different V_A:V_B values of 4.28 (Hirose et al., 2005) and 3.59 (Kubo et al., 2006), suggesting one or both studies have over-fit or otherwise misinterpreted the diffraction pattern.

We are able to collect x-ray diffraction data from $MgGeO_3$ post-perovskite which show no evidence of lattice preferred orientation of sample powders (Figure 8.3) and structure models we obtain with Rietveld refinement from two X-ray separate diffraction patterns taken from different portions of the sample at 87 GPa (Figure 8.4) have V_A:V_B values of 4.01(3) and 4.02(3). Thus, it appears from our data that $MgGeO_3$ agrees with the theory that the V_A:V_B ratio in materials with ABX_3 stoichiometry is equal to 4 near the phase transformation between perovskite and post-perovskite structure.

8.2. Thesis Summary and Conclusion

To advance our understanding of $MgSiO_3$ in Earth's lower mantle, we have examined the structure of $NaMgF_3$, $CaIrO_3$, and $MgGeO_3$ analog materials at high pressure and temperature. As a result of our studies we have found:

(i) A difference develops between the short-range (< 20 Å) and average (> 100 Å) orthorhombic $NaMgF_3$ perovskite structure during evolution towards the 'cubic' structure when temperature is increased (Chapter 4) and when potassium is substituted for sodium (Chapter 3). This difference only becomes clear when probes sensitive to the local structure, such as nuclear magnetic resonance (Chapter 3) and pair distribution function analysis (Chapter 4), are used.

(ii) Dramatic attenuation of ultrasonic waves propagating through $NaMgF_3$ occurs when sample temperatures reach values consistent with those marking the onset of deviation of the short- from the long-range structure (Chapter 5).

(iii) While post-perovskite structures only crystallize at high pressures, the pressure value where the perovskite/post-perovskite phase transition occurs can be predicted for each individual composition by extrapolating the V_A:V_B ratio to a value of 4.00 (Chapter 6 & 8).

(iv) Assuming the V_A:V_B ratio of $CaIrO_3$ is constant in pressure-temperature space at the phase transition between perovskite and $CaIrO_3$-type structures, we calculate a Clapeyron slope for the phase transition which is in good agreement with the experimentally observed value [15(3) MPa/°C, (Chapter 7); 17(3) MPa/°C, (Hirose and Fujita, 2005)], using the $\partial P/\partial(V_A/V_B)$ and $\partial T/\partial(V_A/V_B)$ values we find from in situ Rietveld refinement.

(v) Tilting of corner-sharing octahedra composing the perovskite-structure framework is known to be the dominant mechanism of structure change as a result of changing pressure and temperature in orthorhombic (***P****bnm*) perovskites, however, from examination of the $CaIrO_3$ structure (***C****mcm*), we observe that octahedra deform rather than tilt upon application of pressure and temperature (Chapter 7).

As we discussed in the introductory chapter, one must be cautious when using results learned from an analog material to make conclusions about another. Considering

this we make the following conclusions which we believe apply to $MgSiO_3$ as well as all orthorhombic (*Pbnm*) perovskites (ABX_3) in general:

(i) If temperature drives average atomic positions to those consistent with that of a perovskite with cubic (*Pm*-3*m*) symmetry before the B-X bond lengths are equal to $V^{1/3}2^{-1}$, it is possible that attenuation of ultrasonic waves (MHz) traveling through the sample may occur as a result of coupling between the wave energy and domain wall (twin) motion. A similar coupling effect may not occur when partial element substitution drives the above structure phenomena, since crystal defects are found to 'pin' domain wall motion in $LaAlO_3$[*] (Harrison and Redfern, 2002).

(ii) The perovskite/post-perovskite phase transition occurs when the V_A:V_B ratio reaches a value of 4.0(1)[†].

(iii) Assuming the V_A:V_B ratio in perovskite and post-perovskite structures is constant at the phase transition (independent of actual V_A:V_B value), it may be possible to estimate the Clapeyron slope of the phase transition if $\partial P/\partial(V_A/V_B)$ and $\partial T/\partial(V_A/V_B)$ values are known for the perovskite or post-perovskite phase near the transition.

(iv) In the post-perovskite structure, B-X and A-X compression and expansion, rather than X-B-X bending, dominates structure change occurring upon application of pressure and temperature.

We believe the conclusions of this dissertation will prove useful to a subsequent understanding of the elastic, rheological, and crystal-chemical properties of perovskite and post-perovskite structures of $MgSiO_3$.

[*] Data suitable for pair distribution functions of $LaAlO_3$ at high temperature has been collected and a study of the structure behavior of this perovskite is underway.

[†] A function relating the $(X\text{-}X)_E$ distance to the $(X\text{-}X)_I$ distance as a function of V_A:V_B in a perovskite structure with un-deformed octahedra (simplest case) is underway and shall appear in the manuscript in preparation for Journal of Applied Crystallography.

References:

Angel, R.J., Zhao, J., and Ross, N.L. (2005) General rules for predicting phase transitions in perovskites due to octahedral tilting. Physical Review Letters, 95(2), 025503(1-4).

Berndt, M. (1997) ICSC/RETRIEVE 2.01 Crystal Structure Database., Gmelin Institute/FIZ Karlsruhe, Germany.

Harrison, R.J., and Redfern, S.A. (2002) The influence of transformation twins on the seismic-frequency elastic and anelastic properties of perovskite: dynamical mechanical analysis of single crystal $LaAlO_3$. Physics of the Earth and Planetary Interiors, 134(3-4), 253-272.

Hirose, K., and Fujita, Y. (2005) Clapeyron slope of the post-perovskite phase transition in $CaIrO_3$. Geophysical Research Letters, 32(13), L13313(1-4). DOI:10.1029/2005GL023219.

Hirose, K., Kawamura, K., Ohishi, Y., Tateno, S., and Sata, N. (2005) Stability and equation of state of $MgGeO_3$ post-perovskite phase. American Mineralogist, 90(1), 262-265.

Kubo, A., Kiefer, B., Shen, G.Y., Prakapenka, V.B., Cava, R.J., and Duffy, T.S. (2006) Stability and equation of state of the post-perovskite phase in $MgGeO_3$ to 2 Mbar. Geophysical Research Letters, 33(12), L12S12(1-4). DOI:10.1029/2006GL025686.

Murakami, M., Hirose, K., Kawamura, K., Sata, N., and Ohishi, Y. (2004) Post-perovskite phase transition in $MgSiO_3$. Science, 304(5672), 855-858. DOI:10.1126/science.1095932.

Oganov, A.R., and Ono, S. (2004) Theoretical and experimental evidence for a post-perovskite phase of $MgSiO_3$ in Earth's D " layer. Nature, 430(6998), 445-448. DOI:10.1038/nature02701.

Thomas, N.W. (1998) New global parameterization of perovskite structures. Acta Crystallographica Section B-Structural Science, 54, 585-599.

Zhao, J., Ross, N.L., and Angel, R.J. (2006) Estimation of polyhedral compressibilities and structural evolution of $GdFeO_3$-type perovskites at high pressures. Acta Crystallographica Section B-Structural Science, 62, 431-439.

Zhao, Y.S., Weidner, D.J., Parise, J.B., and Cox, D.E. (1993) Thermal-Expansion and Structural Distortion of Perovskite - Data For $NaMgF_3$ Perovskite .1. Physics of the Earth and Planetary Interiors, 76(1-2), 1-16.

(a) Perovskite-structured materials

Composition	ICSD #, reference	Space Group	V_A:V_B	Comment, p-T condition
$NdFeO_3$	78587	***P****bnm*	5.23	extreme BX_6 deformation
$KCuF_3$	21108	***I****4/mcm*	5.05	BX_6 deformation
$SrTiO_3$	23076	***P****m*-3*m*	5.00	No BX_6 tilt, V_A:V_B ≡ 5
$LaAlO_3$	90533	***R***-3*c*	4.95	
$LaNiO_3$	67717	***R***-3*c*	4.85	
$CaVO_3$	81056	***P****bnm*	4.80	
$KMgCl_3$	28291	***P****bnm*	4.77	
$NdGaO_3$	79633	***P****bnm*	4.76	
$LaCrO_3$	89098	***P****bnm*	4.75	
$LaGaO_3$	50388	***P****bnm*	4.73	
$SrSnO_3$	90846	***P****bnm*	4.73	
$CaGeO_3$	31338	***P****bnm*	4.72	
$CaFeO_3$	92330	***P****bnm*	4.70	
$KCdF_3$	201329	***P****bnm*	4.69	
$PrCoO_3$	88738	***P****bnm*	4.68	
$SrHfO_3$	84280	***P****bnm*	4.68	
$PrNiO_3$	69183	***P****bnm*	4.68	
$CsYbI_3$	72342	***P****bnm*	4.68	
$BaCeO_3$	2751	***P****bnm*	4.67	
$SrZrO_3$	650	***P****bnm*	4.66	
$LaVO_3$	73898	***P****bnm*	4.65	
$LaFeO_3$	28255	***P****bnm*	4.65	
$CaMnO_3$	50997	***P****bnm*	4.63	
$CaTiO_3$	62149	***P****bnm*	4.62	
$LaTiO_3$	202034	***P****bnm*	4.56	
$SmCoO_3$	90969	***P****bnm*	4.56	
$NdCrO_3$	80332	***P****bnm*	4.55	
$PrFeO_3$	27274	***P****bnm*	4.51	
$SmNiO_3$	69789	***P****bnm*	4.50	
$HoAlO_3$	39606	***P****bnm*	4.49	
$SrTbO_3$	89026	***P****bnm*	4.45	
$NaMgF_3$	94085	***P****bnm*	4.44	
$GdCrO_3$	38023	***P****bnm*	4.43	
$CdTiO_3$	62150	***P****bnm*	4.41	
$CaRuO_3$	75568	***P****bnm*	4.40	
$GdGaO_3$	492	***P****bnm*	4.37	
$TbCoO_3$	23657	***P****bnm*	4.36	
$NaUO_3$	202889	***P****bnm*	4.34	
$TlNiO_3$	93507	***P****bnm*	4.33	
$CaSnO_3$	59160	***P****bnm*	4.32	
$MgSiO_3$	68374	***P****bnm*	4.30	Quenched from 26 GPa
$GdFeO_3$	27278	***P****bnm*	4.30	
$SrCeO_3$	80271	***P****bnm*	4.26	
$TbMnO_3$	92078	***P****bnm*	4.24	
$NaCoF_3$	15622	***P****bnm*	4.23	
$GdNiO_3$	88040	***P****bnm*	4.21	
$MgSiO_3$	90065	***P****bnm*	4.14	80 GPa and 1500 K
$YTiO_3$	84608	***P****bnm*	4.09	
$NaMgF_3$	(Martin et al., 2006)	***P****bnm*	4.07(5)	27 GPa
$LiNbO_3$	28295	***R***-3*c*	4.06	
$PrLuO_3$	50758	***P****bnm*	4.03	

!! Continued on next page !!

!! Continued from last page !!

(b) Materials with $CaIrO_3$-type structure

Compositior	ICSD, reference	Space Group	V_A:V_B	Comment, p-T condition
$MgSiO_3$	(Murakami *et al*., 2004)	***C****mcm*	4.01	Post-perovskite, 121 GPa
—	(Oganov and Ono *et al*., 2004)	***C****mcm*	3.92	Post-perovskite, 120 GPa
$NaMgF_3$	(Martin et al., 2006)	***C****mcm*	3.94(6)	Post-perovskite, 30, 54 GPa
$MgGeO_3$	(Hirose *et al*., 2005)	***C****mcm*	4.28	Post-perovskite, 78 GPa
—	(Kubo *et al*., 2006)	***C****mcm*	3.59	Post-perovskite, 88 GPa
$CaIrO_3$	25524	***C****mcm*	4.19	
$CaInBr_3$	54138	***C****mcm*	4.09	
Mn_2O_3	(Santillan *et al*., 2006)	***C****mcm*	4.01	40.4 GPa
Fe_2O_3	(Ono and Ohishi *et al*., 2005)	***C****mcm*	3.89	68 GPa
$UScS_3$	2239	***C****mcm*	3.68	
$UFeS_3$	98	***C****mcm*	3.67	
$TlPbI_3$	1199	***C****mcm*	3.65	
$TaAgS_3$	73804	***C****mcm*	2.71	

[Table 8.1] (a) The perovskite structure sample from the ICSD includes 51 perovskite structures ordered according to V_A:V_B ratio and listed with (b) all materials known to adopt the $CaIrO_3$-type structure. Unless otherwise noted, the structures represent the atomic configuration at ambient conditions.

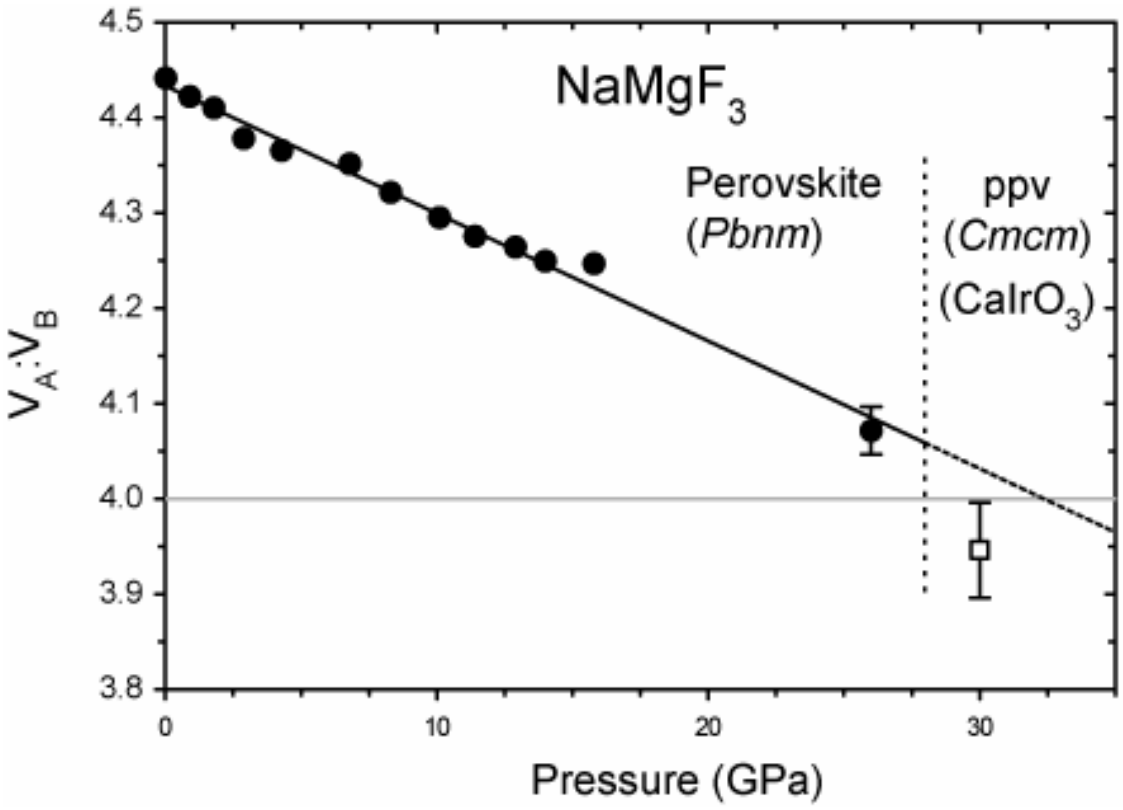

[Fig. 8.1] The V_A:V_B ratio of $NaMgF_3$ is plotted as a function of pressure. Data < 20 GPa are taken from Liu et al. (2005) and data > 20 GPa is from Chapter 6.

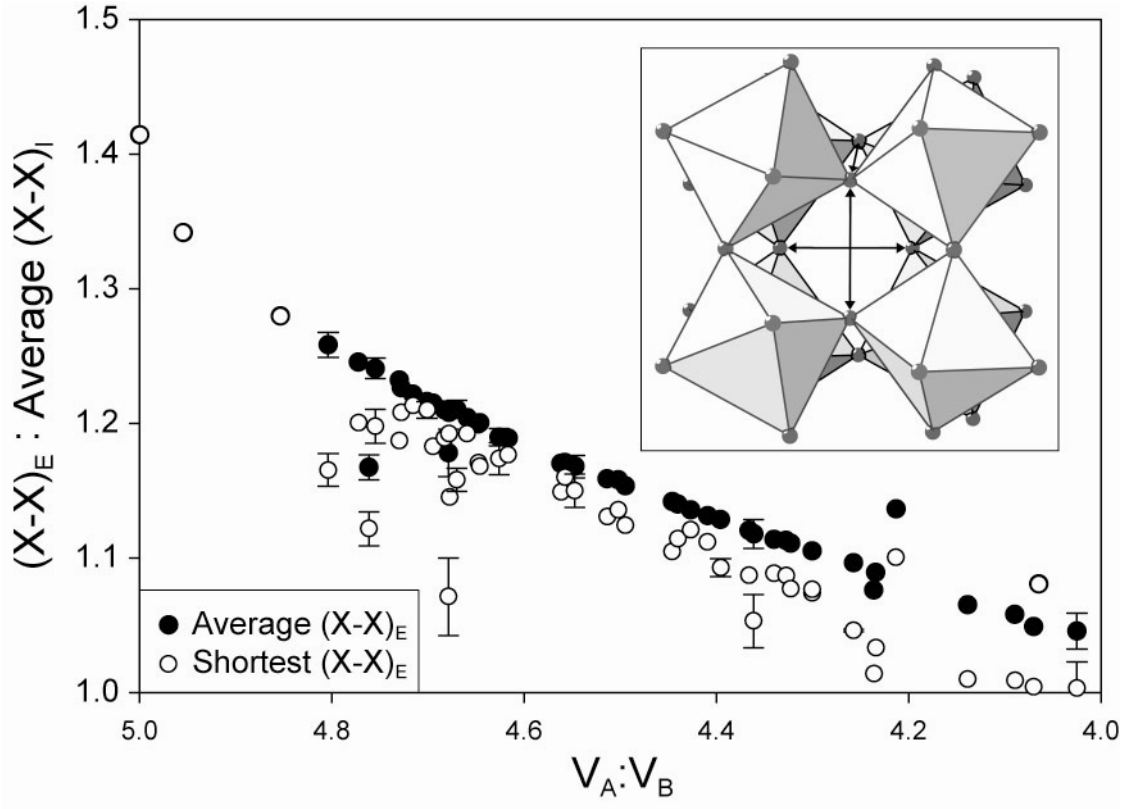

[Fig. 8.2] The ratio between specific extra-octahedral anion-anion distance [$(X\text{-}X)_E$] and the average intra-octahedral anion-anion [$(X\text{-}X)_I$] distance is plotted as a function of the V_A:V_B ratio. The average $(X\text{-}X)_E$ distance is used to calculate the data in black, while just the shortest $(X\text{-}X)_E$ distance is used to calculate the data in white. The data show that all perovskite structures in our sample have an average $(X\text{-}X)_I$ distance that is shorter than the $(X\text{-}X)_E$ distance. The three unique $(X\text{-}X)_E$ distances are indicated for the inset orthorhombic (*Pbnm*) perovskite structure. Errors bars are smaller than symbol size unless otherwise indicated or the standard deviations of raw structure parameters are not present in the ICSD.

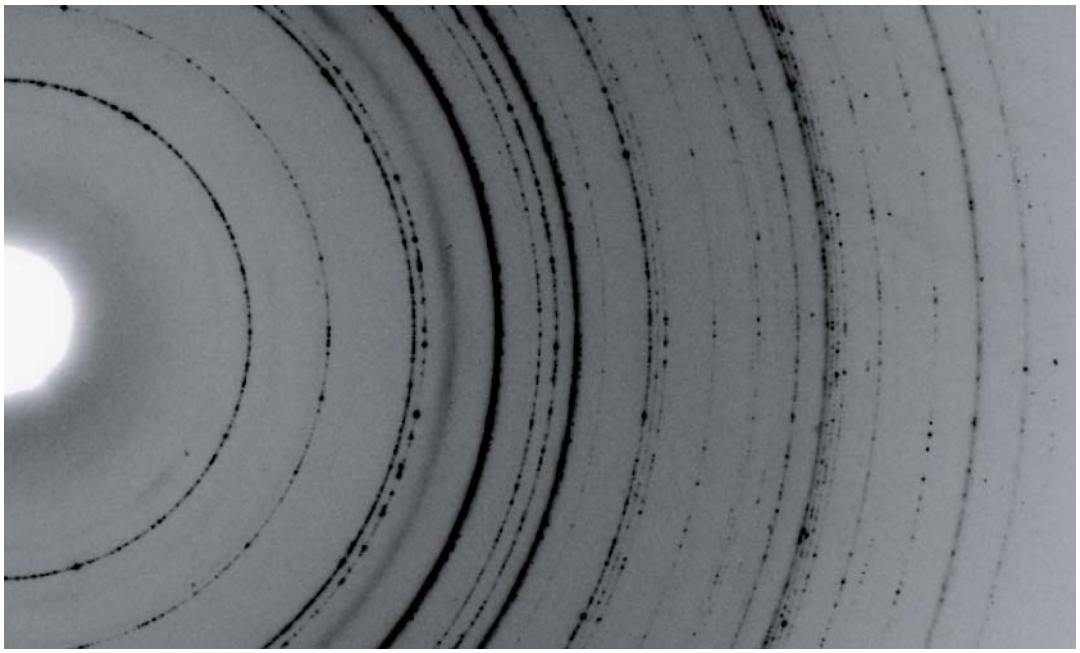

[Fig. 8.3] Raw area-detector image of x-ray diffraction from $MgGeO_3$ post-perovskite at 87 GPa after laser-heating at ~1500K. Data do not show texturing and the spotty texture may be overcome with integration around 360° chi.

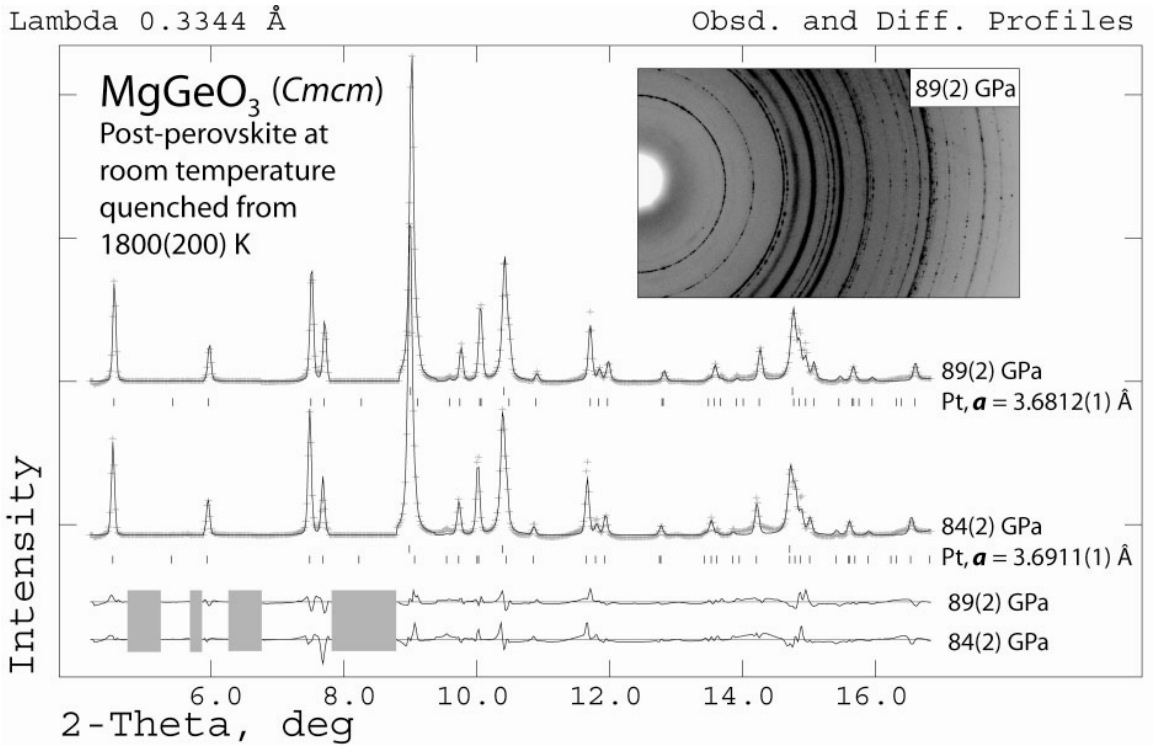

[Fig. 8.4] Rietveld refinements of $MgGeO_3$ post-perovskite, where data in grey is observed, data in black is calculated from the structure model, and data below is the difference which corresponds to each of the above diffraction patterns with respect to vertical position. Black ticks mark the position of sample reflections and upper-tier black ticks mark the position of reflections from platinum which is fit with a Le Bail model.

Appendix A

Quantitative Pair Distribution Function Analysis of Nanocrystalline Gold at High Pressure

MARTIN, C.D., ANTAO, S.M., CHUPAS, P.J., LEE, P.L., SHASTRI, S.D., AND PARISE, J.B. (2005) QUANTITATIVE HIGH-PRESSURE PAIR DISTRIBUTION FUNCTION ANALYSIS OF NANOCRYSTALLINE GOLD. APPLIED PHYSICS LETTERS, 86(6), 061910. DOI:10.1063/1.1856691.

A.1. Abstract

A complete knowledge of how the short vs. long range structure varies with pressure and temperature is necessary to solve long standing problems confronting Earth and materials science. Using a diamond anvil cell (DAC) coupled with high-energy monochromatic X-rays, high resolution data suitable for least-squares refinement of the pair distribution function (PDF) was obtained from nanocrystalline gold to pressure of 10 GPa in a hydrostatic alcohol pressure-medium. Without Kaplow-type corrections, high quality PDFs (G(r(Å))) were calculated through direct Fourier transformation of the structure function (S(Q(Å^{-1})). Quantitative analysis of each PDF has been performed by full-profile Rietveld-type modeling to determine lattice parameter, while a Gaussian distribution was fit to the first Au-Au correlation to extract structural information directly. The accuracy of the Au-Au bond distance and lattice parameter derived from this real space analysis are confirmed through comparison of parameters determined from Rietveld analysis of Bragg diffraction. The great quality of the high pressure PDFs obtained in this study and the successful execution of this analysis demonstrate the solidarity of the technique and opens a door to quantitative pair distribution function studies of liquids and disordered solids at high-pressure (QHP-PDF) in the DAC.

A.2. Introduction

Structural studies at high pressures and temperatures almost exclusively apply crystallographic techniques that make the assumption that the material under study possesses long range periodic order. An obvious consequence of the application of extreme pressure and temperature on materials is the introduction of disorder (both static and dynamic) into materials. Knowing the atomic arrangement in materials is the first step towards understanding and predicting inherent properties. A complete knowledge of how the short vs. long range structure varies with pressure and temperature is necessary to solve long standing problems confronting Earth and materials science (Lay et al., 1998; Mao et al., 1996; Mao et al., 2004; Price et al., 1998; Tolbert and Alivisatos, 1994). When materials of interest lack long range crystalline order, complete structural determination is impossible when employing classical methods of Bragg diffraction in combination with Rietveld/single crystal refinement. Quantitative analysis of the pair distribution function (PDF), has proven a reliable tool for the solution of structures with broken periodicity at various temperatures (Billinge, 2004; Egami and Billinge, 1994; Petkov et al., 2002; Proffen et al., 1999). With the exception of theoretical Monte Carlo calculations (Murugan et al., 2004), experimental PDF analysis at high pressures is subject to small scattering/background ratios and early truncations in scattering vector available for Fourier transform due to Compton scattering and geometrical limits imposed from experimental apparatus, respectively. Ultimately, these problems introduce noise and systematic errors in the structure function and final distribution function.

Previously, high pressure PDF analysis focused on pressure-quenched (ex-situ) structures (Sampath et al., 2003), in-situ qualitative analysis (Tsuji et al., 2004), or has utilized Kaplow-type iterative correction procedures (Kaplow et al., 1965) to improve the quality of the structure function and PDF. However, such iterations may introduce experimenter bias since behavior of the distribution function in the low-r region is forced to expected values, while these corrections are propagated to higher r-values in an attempt to improve over-all function quality (Eggert et al., 2002 ; Shen et al., 2003). These previous studies of amorphous materials were limited to truncation of the structure function at 15 $Å^{-1}$. Collecting diffuse scatter at larger vectors (~20-30 $Å^{-1}$) will significantly increase the quality and accuracy of the data and allow precise Monte Carlo simulations of high pressure liquids. In addition, Fourier transformation of the structure

function to 20 $Å^{-1}$ is sufficient to study high pressure PDFs of crystalline materials, where quantitative analysis via full-profile Rietveld-type least-squares fitting may be performed (QHP-PDF quantitative high pressure pair distribution function analysis). Such studies have far-reaching implications for simultaneously identifying inter-atomic mechanisms responsible for elevated/depressed/unchanged transition pressures observed in nanocrystals (Shen et al., 2001; Tolbert and Alivisatos, 1994; Vaughan et al., 2000) and studying the long vs. local structure of materials near high pressure phase transition. Due to the novelty of this technique and exclusive experimental configuration needed to perform QHP-PDF, no studies have yet been reported. We present a quantitative in-situ high pressure study of the long vs. short-range order in nanocrystalline gold via a comparison between Rietveld refinement of Bragg diffraction and full-profile fitting of the PDF from within the diamond anvil cell (DAC) to introduce the viability and integrity of the technique to the scientific community.

A.3. Methods

High-energy monochromatic X-ray scattering was performed at the Advanced Photon Source (APS) at Argonne National Laboratory. Experiments were conducted at beamline 1-ID where X-rays at 79.9562 keV (0.15507 Å) were selected using a unique cryogenically cooled bent double-Laue monochormator (Shastri et al., 2002). A beam 50 μm x 50 μm was used for all scattering measurements.

Pressure was generated with a Merril-Bassett type diamond anvil cell (DAC) with Be backs allowing for solid-angle scattering to 28˚ in 2θ. The DAC was outfitted with 600um culet anvils (type I) and a stainless steel gasket (250μm in thickness) was pre-indented to 120 μm. A sample chamber 200 μm in diameter was drilled into the pre-indented gasket by micro-EDM technique, creating a cavity of ~$3x10^{-3}$ mm^3. Nanocrystalline (50-100 nm) gold of 99.99% purity was purchased from Nanostructured & Amorphous Materials, Inc. NM and loaded into this sample chamber. An alcohol pressure medium of methanol:ethanol (4:1) was used to prevent/minimize deviatoric stress. The pressure medium filled about 15-20% of the total volume in the sample chamber. Two very small rubies (on the order of 500 $μm^3$) were placed at opposite edges of the sample container to determine pressure using the ruby fluorescence technique.

Diffraction patterns were collected using a 'mar345' flat imaging plate detector, carefully mounted orthogonal to and centered about the X-ray beam. Sample-detector distance was refined to 231.283 mm with the software Fit2D (Hammersley et al., 1996) using a NIST silicon diffraction standard loaded in a capillary. This sample-detector distance allows for scattering out to 20 $Å^{-1}$, however only 18.5 $Å^{-1}$ was used to preclude irregularities in the data caused by the detector and DAC angular limits. The tantalum beam stop used in the experiment was about 150 mm behind the sample and prevented detection of scattering between 0 and 0.7 $Å^{-1}$. Because of the small unit cell of Au, the beamstop did not eclipse any Bragg reflections to the detector in this configuration.

This study was performed using a conventional method of background subtraction. Thus, the background scatter from the hutch and DAC were collected at zero pressure without the sample in position and subtracted from exposures containing the sample at pressure. Scattering from the DAC included many single-crystal diamond spots (Fig. A.1) which were masked before data was reduced to angle vs. intensity using program Fit2D. These single crystal diamond spots are trivial, when they are carefully masked along with the added surrounding intensity. The imaging plate was exposed for ten 5-second exposures which were averaged to attain optimum counting statistics. The integrated data was processed to obtain PDFs using the program PDFgetX2 (Qiu et al., (submitted)), where standard corrections as well as those unique to the image plate geometry were applied (Chupas et al., 2003). Full profile fitting of the PDF was performed using program PDFFIT (Proffen and Billinge, 1999), while the program EXPGUI (Toby, 2001) for GSAS (Larson and Von Dreele, 2000) was used for Rietveld analysis of Bragg diffraction. Thinning of the stainless steel gasket did not alter the measurement of the background, as must be cautioned since a reduced gasket may allow more Compton scatter from the upstream diamond to be detected by the IP (Shen et al., 2003).

A.4. Results and discussion

When examining crystalline materials, the total structure function S(Q) must be measured to high values of momentum transfer to eliminate errors arising from the Fourier transformation of a finite Q range (Fig. A.2). However, this task is difficult at high pressure due to the anvil background and geometry imposed by the pressure

apparatus. In this study, measurements to 20 $Å^{-1}$ are used. While this range is of low resolution compared to some PDF measurements (Petkov et al., 1999), it is sufficient in the case of gold, to eliminate detrimental contamination from termination ripples (consistent short-wavelength oscillations) which may obstruct sample features in the PDF low-r(Å) region. Correction artifacts may also arise in the low-r(Å) region of the PDF as a result of long-wavelength systematic errors in S(Q) (much longer than oscillations arising from atomic correlation), such that the Fourier transform produces physically meaningless low-r(Å) peaks (often within atomic radius). These errors in S(Q) are easily introduced when making background corrections to data collected inside the DAC, where the primary background component consists of diamond anvil Compton scattering—a slowly varying function approximately 5 times the measured sample scattering intensity. Upon inspection of the low-r region, which shows only small ripples, it is clear that the gold PDFs obtained in the DAC are high quality. We have plotted the ambient pressure PDF of gold in the DAC against that of gold in a capillary and find no significant difference between the two (Fig. A.3). Thus, we are confident our high pressure data is properly corrected and the quality of the PDF data speaks to the accuracy of the background measurement used.

Table A.1 summarizes the gold unit cell and Au-Au distance at high pressure as determined by both Rietveld and PDF analysis; these results are plotted in Figure A.4. The long-range time-averaged unit cell length 'a ' is determined by Rietveld refinement from full profile fitting of Bragg reflections ($I(Q(Å^{-1}))$), while the 'average' Au-Au distance is obtained geometrically by a /1.414 (face-centered lattice). The unit cell length was also determined from full-profile fitting of the PDF using program PDFFIT over the range 1.5-20 Å. Lastly, we have independently fit the first Au-Au correlation in the PDF with a Gaussian to determine this position in real-space. By fitting the first Au-Au correlation directly, no additional structural information is assumed. The results obtained from Rietveld analysis and full profile fitting of the PDFs show the same linear decrease in lattice parameter (and thus a /1.414) with pressure as the Au-Au correlation position obtained from direct fitting of the PDF.

From our data it is necessary to first highlight the precision of our measurements. The standard error associated with each unit cell length and Au-Au value is about 0.003

Å (30 pm), whereas the error in pressure is typically on the order of 0.1 and 0.3 GPa at the largest values reached. Both PDF (G(r(Å)) short-range) and Rietveld (I(Q($Å^{-1}$)) long-range) methods arrive at the same unit cell when full profile fitting is applied. In addition, both techniques show an identical decrease in unit cell as pressure is increased. However, we find that the Au-Au distance, indicated by the position of the Gaussian fit to the first Au-Au correlation in the PDF, systematically underestimates the a/1.414 value (determined from full-profile refinement of Bragg diffraction and the PDF) by an average value of $6.4x10^{-3}$ Å (64 pm). At phase transition in some materials, Rietveld analysis may underestimate bond distance, while PDF methods may estimate the distance more accurately (Zhao, Weidner et al. 1993; Zhao, Weidner et al. 1993; Street, Wood et al. 1997; Tucker, Keen et al. 2001; Chupas, Chaudhuri et al. 2004). Here however, the Gaussian-fit PDF Au-Au distance is systematically underestimated (by about twice the standard error or 0.003 Å) for both data from the capillary and from within the DAC. Previous work fitting a Gaussian to the first Ni-Ni correlation in crystalline Ni metal has shown a similar offset of 0.006 Å at 300 K (Petkov et al., 2002; Proffen, 2004). This offset is due to the fact that the Au-Au peak is not a perfect Gaussian and PDFFIT software takes into account the asymmetry of the peak shape. The results from full-profile fitting of our data support this assertion, where the refinement difference plot is not asymmetric about the first Au-Au correlation (Fig. A.4). At the final pressure, the full width of half maximum (FWHM) of the first Au-Au correlation in the (PDF) widens, a result we attribute to deviatoric stress and quasi-hydrostatic sample conditions due to the expected pressure-freezing of the alcohol mixture (Piermari.Gj et al., 1973). Thus, this data point was not included in the linear regression.

A perhaps surprising outcome of this study is no diffuse scattering contributions from the methanol:ethanol:water (16:3:1) pressure transmitting medium are found in the data. We explain this as a result of the alcohol pressure transmitting medium having a much lower electron density than gold, while a large diamond Compton scatter contribution exists to the background which may washout weak C-H or C-C correlations. In addition, there is of course significantly less pressure transmitting medium in the beam than sample

References:

Billinge, S.J.L. (2004) The atomic pair distribution function: past and present. Zeitschrift Fur Kristallographie, 219(3), 117-121.

Chupas, P.J., Qiu, X.Y., Hanson, J.C., Lee, P.L., Grey, C.P., and Billinge, S.J.L. (2003) Rapid-acquisition pair distribution function (RA-PDF) analysis. Journal of Applied Crystallography, 36, 1342-1347.

Egami, T., and Billinge, S.J.L. (1994) Underneath the Bragg Peaks: Structural analysis of complex materials. Pergamon Press, Oxford.

Eggert, J.H., Weck, G., Loubeyre, P., and Mezouar, M. (2002) Quantitative structure factor and density measurements of high-pressure fluids in diamond anvil cells by x-ray diffraction: Argon and water. Physical Review B, 65(17).

Hammersley, A.P., Svensson, S.O., Hanfland, M., Fitch, A.N., and Hausermann, D. (1996) Two-dimensional detector software: From real detector to idealized image or two-theta scan. High Pressure Research, 14(4-6), 235-248.

Kaplow, R., Strong, S.L., and Averbach, B.L. (1965) Radial Density Functions for Liquid Mercury and Lead. Physical Review, 138(5A), A1336-A1345.

Larson, A.C., and Von Dreele, R.B. (2000) General Structure Analysis System (GSAS). Los Alamos National Laboratory Report, 86-748.

Lay, T., Williams, Q., and Garnero, E.J. (1998) The core-mantle boundary layer and deep Earth dynamics. Nature, 392(6675), 461-468. DOI:10.1038/33083.

Mao, H.K., Shu, J.F., Fei, Y.W., Hu, J.Z., and Hemley, R.J. (1996) The wustite enigma. Physics of the Earth and Planetary Interiors, 96(2-3), 135-145.

Mao, W.L., Shen, G.Y., Prakapenka, V.B., Meng, Y., Campbell, A.J., Heinz, D.L., Shu, J.F., Hemley, R.J., and Mao, H.K. (2004) Ferromagnesian postperovskite silicates in the D" layer of the Earth. Proceedings of the National Academy of Sciences of the United States of America, 101(45), 15867-15869.

Murugan, N.A., Jha, P.C., Yashonath, S., and Ramasesha, S. (2004) High pressure phase of biphenyl at room temperature: A Monte Carlo study. Journal of Physical Chemistry B, 108(13), 4178-4184.

Petkov, V., Jeong, I.K., Chung, J.S., Thorpe, M.F., Kycia, S., and Billinge, S.J.L. (1999) High real-space resolution measurement of the local structure of Ga1-xInxAs using X-ray diffraction. Physical Review Letters, 83(20), 4089-4092.

Petkov, V., Trikalitis, P.N., Bozin, E.S., Billinge, S.J.L., Vogt, T., and Kanatzidis, M.G. (2002) Structure of V2O5 center dot nH(2)O xerogel solved by the atomic pair distribution function technique. Journal of the American Chemical Society, 124(34), 10157-10162.

Piermari.Gj, Block, S., and Barnett, J.D. (1973) Hydrostatic Limits in Liquids and Solids to 100 Kbar. Journal of Applied Physics, 44(12), 5377-5382.

Price, D.L., Saboungi, M.L., and Barnes, A.C. (1998) Structure of vitreous germania. Physical Review Letters, 81(15), 3207-3210.

Proffen, T. (2004) Offset obtained from fitting Ni-Ni with a Guassian peak shape.

Proffen, T., and Billinge, S.J.L. (1999) PDFFIT, a program for full profile structural refinement of the atomic pair distribution function. Journal of Applied Crystallography, 32, 572-575.

Proffen, T., DiFrancesco, R.G., Billinge, S.J.L., Brosha, E.L., and Kwei, G.H. (1999) Measurement of the local Jahn-Teller distortion in LaMnO3.006. Physical Review B, 60(14), 9973-9977.

Qiu, X., Thompson, J.W., and Billinge, S.J.L. ((submitted)) PDFgetX2: A GUI driven program to obtain the pair distribution function from X-ray powder diffraction data. Journal of Applied Crystallography.

Sampath, S., Benmore, C.J., Lantzky, K.M., Neuefeind, J., Leinenweber, K., Price, D.L., and Yarger, J.L. (2003) Intermediate-range order in permanently densified GeO2 glass. Physical Review Letters, 90(11).

Shastri, S.D., Fezzaa, K., Mashayekhi, A., Lee, W.K., Fernandez, P.B., and Lee, P.L. (2002) Cryogenically cooled bent double-Laue monochromator for high-energy undulator X-rays (50-200 keV). Journal of Synchrotron Radiation, 9, 317-322. DOI:10.1107/S0909049502009986.

Shen, G.Y., Prakapenka, V.B., Rivers, M.L., and Sutton, S.R. (2003) Structural investigation of amorphous materials at high pressures using the diamond anvil cell. Review of Scientific Instruments, 74(6), 3021-3026.

Shen, G.Y., Rivers, M.L., Wang, Y.B., and Sutton, S.R. (2001) Laser heated diamond cell system at the Advanced Photon Source for in situ x-ray measurements at high pressure and temperature. Review of Scientific Instruments, 72(2), 1273-1282. DOI:10.1063/1.1343867.

Toby, B.H. (2001) EXPGUI, a graphical user interface for GSAS. Journal of Applied Crystallography, 34, 210-213.

Tolbert, S.H., and Alivisatos, A.P. (1994) Size Dependence of a First-Order Solid-Solid Phase-Transition - the Wurtzite to Rock-Salt Transformation in Cdse Nanocrystals. Science, 265(5170), 373-376.

Tsuji, K., Hattori, T., Mori, T., Kinoshita, T., Narushima, T., and Funamori, N. (2004) Pressure dependence of the structure of liquid group 14 elements. Journal of Physics-Condensed Matter, 16(14), S989-S996.

Vaughan, M.T., Chen, J., Li, L., Weidner, D.J., and Li, B.S. (2000) Use of X-ray image techniques at high pressure and temperature for strain measurements. In M.H. Manghnani, W.J. Nellos, and M.F. Nicol, Eds. Science and Technology of High Pressure, p. 1097-1098. Universities Press, Hyderadad.

Pressure (GPa)	Rietveld Cell	Rietveld Au-Au	PDF Cell	PDF Au-Au	FWHM of Gaussian Fit	PDFFIT R-weighted
Capillary	4.0798[1]	2.8842[1]	4.0789[1]	2.876[2]	0.283	0.0798
0	4.0772[1]	2.883[1]	4.0778[1]	2.8771[7]	0.283	0.1223
5.4[1]	4.0412[1]	2.8576[1]	4.0430[1]	2.8541[4]	0.285	0.1007
6.2[2]	4.0391[1]	2.8561[1]	4.0376[1]	2.8487[4]	0.285	0.1882
7.25[2]	4.0356[2]	2.8536[1]	4.0372[1]	2.8463[4]	0.285	0.1848
8.1[3]	4.0333[2]	2.8519[1]	4.0331[1]	2.8471[5]	0.286	0.1501
10.0[4]	4.0252[2]	2.8463[1]	4.0268[1]	2.8206[3]	0.292	0.2088

[Table A.1] Comparison of cell parameter and Au-Au distance as determined by Rietveld and PDF analysis. Estimated standard deviation (ESD) is listed to the right of their applicable variables.

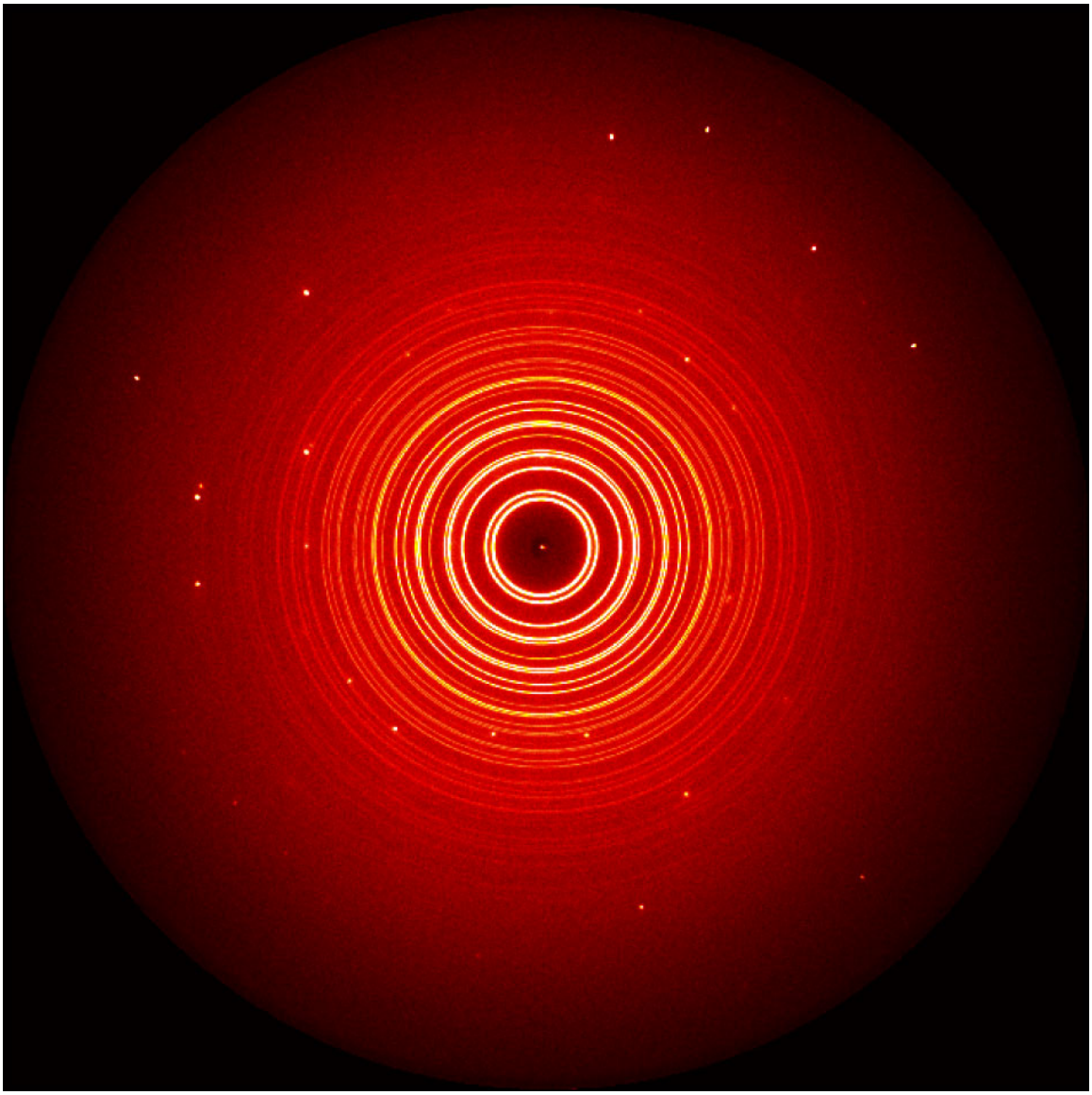

[Fig. A.1] Typical two-dimensional sample exposure illustrating the single crystal diamond spots along side sample powder diffraction. These spots, including the surrounding diffuse scatter, must be carefully masked prior to data integration. To avoid saturation of the detector and obtain optimal counting statistics, the bright spots from the diamond anvils demonstrate the need to average many short exposures. The intensity of parasitic DAC Compton scatter is best observed when comparing the central beamstop shadow with adjacent background intensity. The diamond anvil Compton scatter and sample diffuse scatter cannot be distinguished by eye.

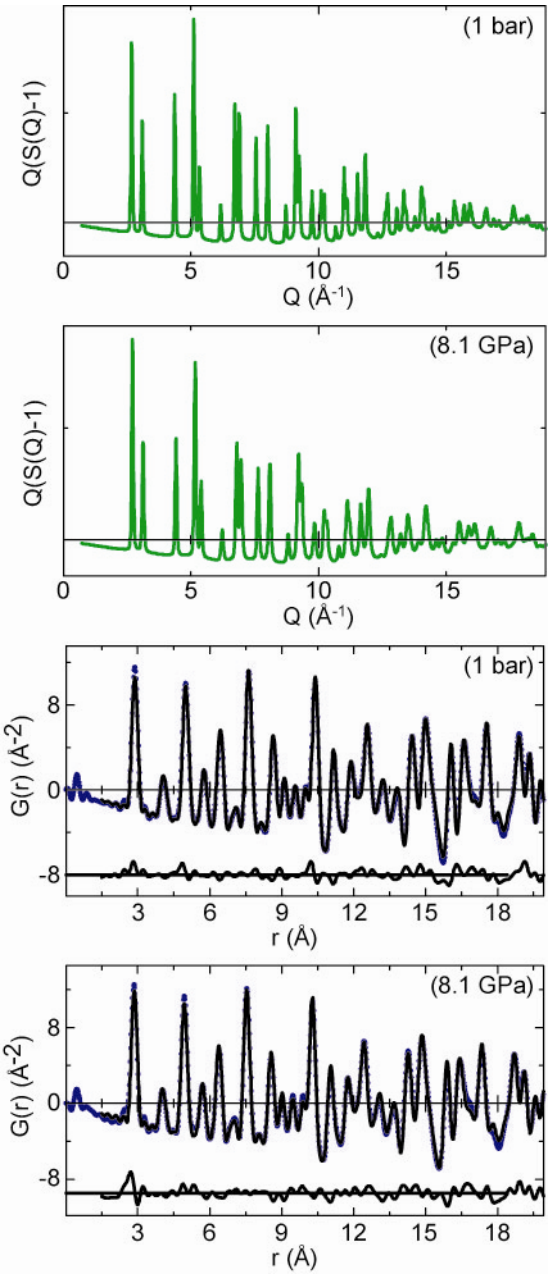

[Fig. A.2] Diagrams comparing S(Q) and G(r) for gold in the diamond anvil cell (DAC) at 1 bar, with Gold in the DAC at 8.1 GPa. Full-profile fitting plots of G(r) are represented with observed data (dashed blue), model data (solid black), and difference plot below (solid black).

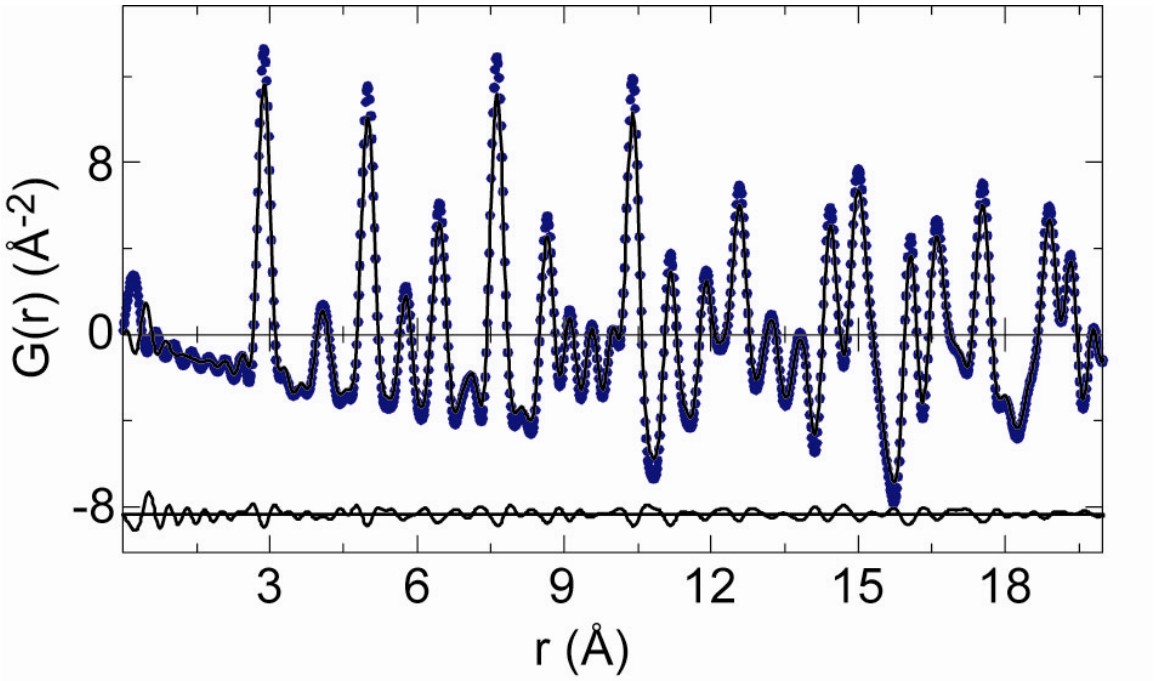

[Fig. A.3] A plot comparing the PDF of gold taken from a 1mm capillary (solid black) vs. that taken in the DAC at 1 bar (dash blue). The difference plot below (solid black) shows no asymmetry about PDF Au-Au correlations and we conclude our DAC background correction is valid.

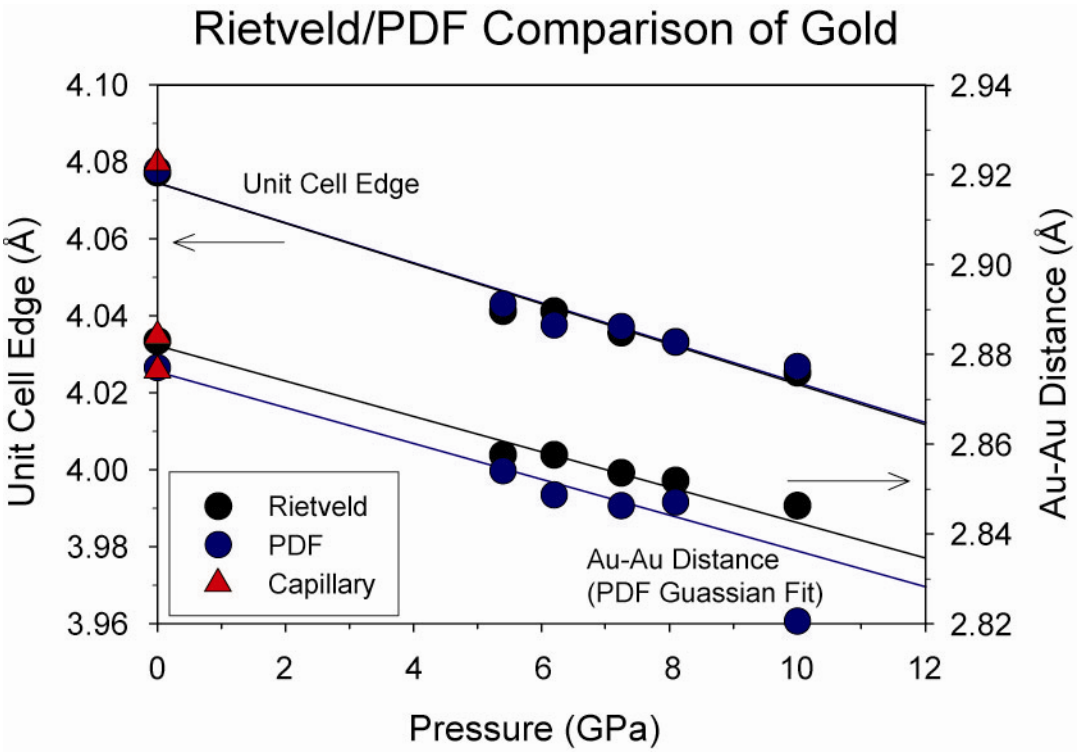

[Fig. A.4] Unit cell and Au-Au distance as determined by Rietveld and HPQ-PDF analysis. The PDF-derived unit cell values were fit from the entire G(r) profile (Program PDFFIT), while a Gaussian was fit to the first Au-Au correlation to independently derive this distance. The discrepancy between the Au-Au distances may be explained as an effect of imperfect Gaussian peak-shape. The data point at the final pressure shown in the Au-Au PDF analysis was not included in the regression, due to an increase in the full-width at half-maximum in the G(r) Au-Au correlation (indicating a deviatoric-stress).